Computational analysis and mitigation of micro-pressure waves in high-speed train tunnels

James Alexander Tebbutt

Department of Mechanical Engineering

Imperial College London

A thesis submitted for the degree of

Doctor of Philosophy of Imperial College London

2017

Abstract

Tunnels are increasingly used in high-speed rail projects to mitigate against issues such as environmental noise, land disputes, and unsuitable terrain. However, the trend for increasing train speeds will result in unacceptable noise emissions from tunnels without the use of effective countermeasures. Novel countermeasures for the propagation of pressure waves in tunnels and the emission of sound waves into the environment, commonly referred to as micro-pressure waves, were numerically investigated in this work.

This following countermeasures were considered: (1) the design and optimisation of an array of Helmholtz resonators embedded in redundant tunnel space; (2) a preliminary parametric study on the effect of modifying the junction geometry between the tunnel and side branches (e.g. ventilation shafts) for noise emissions from side branches.

Helmholtz resonators are used extensively in engineering disciplines where noise attenuation is an important factor (e.g. jet-engine liners). However, their ability to suppress noise emissions from tunnels has not been demonstrated. This work investigates the effectiveness of these countermeasures when applied to a representative tunnel system and compares their performance to existing ones (e.g. tunnel entrance hoods) using numerical techniques.

One and two-dimensional models were developed to predict the performance of these countermeasures, subject to realistic geometric constraints and operating conditions. The geometry of the array is optimised to provide robust performance over a range of operating conditions. The numerical predictions are validated against experimental data, and are benchmarked against analytical predictions and CFD. Finally, the combination with existing countermeasures is studied and enhancements to the models are proposed. Both countermeasures were found to work effectively for a physically representative system.

Declaration of Originality

This thesis submission is the author's own work, except where due acknowledgement has been made in the text. No part of this work has been submitted to any other institution of higher learning for a degree or an award.

Copyright Declaration

The copyright of this thesis rests with the author and is made available under a Creative Commons Attribution Non-Commercial No Derivatives licence. Researchers are free to copy, distribute or transmit the thesis on the condition that they attribute it, that they do not use it for commercial purposes and that they do not alter, transform or build upon it. For any reuse or redistribution, researchers must make clear to others the licence terms of this work.

Acknowledgements

To my supervisors, John Dear and Roderick Smith, for giving me the opportunity to undertake this project and a research placement at the Railway Technical Research Institute (RTRI) in Japan. This was an incredibly insightful experience into high-speed rail research.

To my mentors Tokuzo Miyachi, Sanetoshi Saito, and all of the other members of the Heat and Air Flow Analysis Laboratory at RTRI for their hospitality and guidance. I will never forget my experience of working and travelling in Japan.

To Mehdi Vahdati and Declan Carolan, for their continued guidance and interest in the project, which has been invaluable, and to Prathiban Sureshkumar for his advice on acoustics.

To High Speed Two Limited and EPSRC for providing the funding for this project, and for the many useful discussions I had with various staff at High Speed Two and Mott MacDonald, in particular, Mark Howard, Tim Smart, and Clive Pope.

To my friends, colleagues, and family who have helped support me during this time. Finally, to Shyeni for being there for me through the PhD.

Contents

List of Figures **19**

List of Tables **25**

Acronyms and Abbreviations **27**

Notation **29**

1 Introduction **33**

1.1 Motivation 33

1.2 Objectives 34

1.3 Outline of Thesis 35

1.3.1 Publications and Conferences 37

1.4 Research Placement at RTRI 37

2 Literature Review **39**

2.1 Introduction 39

2.2 Overview of Acoustics 39

2.2.1 Important Dimensionless Parameters 40

2.2.2 Basic Acoustics in Waveguides 42

2.3 Tunnel Aerodynamics Overview 44

2.3.1 Tunnel Entry 44

2.3.2 Tunnel Traversal 46

2.3.3 Tunnel Exit 47

2.4 Aerodynamic Issues in Tunnels 48

2.4.1 Micro-Pressure Waves 49
2.4.2 Passenger Aural Comfort 49
2.4.3 Aerodynamic Fatigue 50
2.4.4 Aerodynamic Drag 51
2.5 Existing MPW Countermeasures 51
2.5.1 Entrance Hood and Train Nose Optimisation 51
2.5.2 Ballasted Track 54
2.6 Novel MPW Countermeasures 54
2.6.1 Helmholtz Resonator Array 55
2.6.2 Tunnel Exit Silencer 56
2.6.3 Branch MPWs 56
2.7 Numerical Methods for PDEs 57
2.7.1 Semi-Discretisation 57
2.7.1.1 Finite Difference Method 58
2.7.1.2 Finite Volume Method 59
2.7.1.3 Finite Element Method 60
2.7.1.4 Pseudo-Spectral Methods 60
2.7.1.5 Summary 62
2.7.2 ODE Integration 62
2.7.3 Overview of OpenFOAM 63
2.8 Optimisation Algorithms 65
2.9 Conclusions 66

3 Numerical Model for an Array of Helmholtz Resonators 67
3.1 Introduction 67
3.2 Physical Model Development 68
3.2.1 System Overview 68
3.2.1.1 Idealised Helmholtz Resonator Array 68
3.2.1.2 End Corrections 69
3.2.1.3 Representative System 70
3.2.2 Assumptions 71

3.2.2.1 Summary 76
3.2.3 Continuum Near-Field Model 77
3.2.4 Continuum Far-Field Model 80
3.2.4.1 Limit Cases 81
3.3 Numerical Treatment 83
3.3.1 Fractional Derivatives 83
3.3.1.1 Conventional Methods 83
3.3.1.2 Diffusive Representation 84
3.3.1.3 Optimisation of Quadrature Coefficients 86
3.3.1.4 Comparison of Numerical Methods 89
3.3.2 First-Order System 90
3.3.3 Discretisation 91
3.3.3.1 KT Scheme 92
3.3.3.2 WENO Scheme 95
3.3.3.3 Dissipative terms 97
3.3.4 Space Marching 99
3.3.4.1 Comparison with Near-Field Treatment 100
3.3.5 Initial Conditions 101
3.3.6 Boundary Conditions 102
3.4 Physical Model Improvements 104
3.4.1 Discrete Far-Field Model 104
3.4.1.1 Model Derivation 105
3.4.1.2 Space Marching 107
3.4.1.3 Comparison of Continuum and Discrete Models . . 109
3.5 Conclusions 110

4 Experimental Validation and Numerical Benchmarking 115
4.1 Introduction 115
4.2 Experimental Validation 116
4.2.1 Experimental and Numerical Configuration 116
4.2.2 Results and Discussion 117

4.3 3-D CFD Benchmarking . . . 120
4.3.1 Overview . . . 120
4.3.2 Model Configuration . . . 120
4.3.2.1 Solver and Time Marching . . . 120
4.3.2.2 Mesh Generation . . . 122
4.3.2.3 Initial Condition . . . 122
4.3.2.4 Boundary Conditions . . . 125
4.3.2.5 Solver Settings . . . 126
4.3.3 Mesh Sensitivity and Flux Limiter Selection . . . 127
4.3.4 Model Cases . . . 128
4.3.5 Results . . . 130
4.3.6 Discussion . . . 134
4.4 Conclusions . . . 136

5 1-D Model Application for a Demonstrative Array 139
5.1 Introduction . . . 139
5.2 Array Specification . . . 140
5.2.1 Overview . . . 140
5.2.2 Optimisation Variables . . . 141
5.3 Initial Condition . . . 144
5.3.1 Characteristic Wavefront . . . 144
5.3.2 Comparison with Other Initial Conditions . . . 146
5.3.3 Non-Uniform Grid . . . 148
5.4 Scale Analysis . . . 149
5.5 Optimisation Strategy . . . 151
5.5.1 Objective Function . . . 151
5.5.2 Optimisation Procedure . . . 153
5.5.2.1 Modified Optimisation Procedure . . . 155
5.5.3 Non-linear Constraints . . . 156
5.6 Objective Function Sensitivity Analysis . . . 157
5.6.1 Overview . . . 157

5.6.2 Results and Discussion . . . 158
5.7 Optimisation Results . . . 159
5.7.1 Regular Geometry . . . 161
5.7.2 Irregular Geometry . . . 165
5.8 Sensitivity to Operating Conditions . . . 167
5.9 Effect of Train Entry Speed on MPWs . . . 171
5.9.1 Analytical Model . . . 172
5.9.2 Demonstrative Case . . . 176
5.10 Comparison of MPW Countermeasures . . . 178
5.10.1 Array Versus a Hood . . . 180
5.10.2 Array Combined with a Hood . . . 180
5.11 Multi-Peak Waveforms . . . 182
5.11.1 Overview . . . 182
5.11.2 Modelling of Branch Waves . . . 182
5.11.3 Initial Comparison of Waveforms . . . 185
5.11.4 Optimisation . . . 186
5.12 Conclusions . . . 190

6 Branch Micro-Pressure Waves 193
6.1 Introduction . . . 193
6.2 Overview of Branch MPWs . . . 194
6.3 Branch Geometry Parametric Study . . . 197
6.4 Boundary Conditions . . . 198
6.4.1 Mesh Motion . . . 200
6.4.1.1 Methods for Mesh Motion . . . 200
6.4.1.2 Implementation . . . 200
6.4.2 Other Boundary Conditions . . . 202
6.5 Initial Conditions . . . 204
6.6 Solver Settings . . . 206
6.7 Results and Validation . . . 209
6.7.1 Overview . . . 209

6.7.2 Validation . . . 210
6.7.3 Main Results . . . 211
6.8 Conclusions and Future Work . . . 216

7 Conclusions and Future Direction **219**
7.1 An Array of Helmholtz Resonators . . . 219
7.2 Branch Micro-Pressure Waves . . . 221
7.3 Future Work . . . 222

Bibliography **225**

A Research Placement at RTRI **243**
A.1 Overview of Placement . . . 243
A.2 Experimental Overview . . . 244
A.3 Results and Discussion . . . 247
A.4 Conclusions . . . 249

B An Exit Silencer for MPWs **251**
B.1 Introduction . . . 251
B.2 Exit Silencer Overview . . . 252
B.3 1-D Model . . . 253
B.3.1 Physical Model . . . 253
B.3.2 Numerical Implementation . . . 254
B.3.3 Initial and Boundary Conditions . . . 256
B.3.4 Demonstrative Silencer System . . . 257
B.4 Parametric Study . . . 258
B.5 Optimisation strategy . . . 260
B.6 3-D Benchmarking . . . 261
B.7 Proposed Work . . . 263

C Continuum Model with Wave Reflection **265**
C.1 Introduction . . . 265
C.2 Physical Model . . . 266

C.3 Comparison of One and Two-way Propagation 267

D OpenFOAM Pseudo-Code **269**

D.1 OpenFOAM 3-D Model Configuration 269

D.2 OpenFOAM 2-D Model Configuration 271

D.2.1 Top-Level Parametrised Script 271

D.2.2 Primary Branch Wave 271

D.2.3 Secondary Branch Wave 272

E Array Optimisation - Additional Results **275**

E.1 Initial Condition Parameters 275

E.2 Results 275

List of Figures

2.1 Process leading to the emission of a micro-pressure wave from the tunnel exit. 44

2.2 Optimised train nose profile on the Shinkansen N700-A train-set. . . 52

2.3 A hood that has been fitted on a tunnel entrance in Japan. 52

3.1 Idealised array of Helmholtz resonators connected to a duct. 71

3.2 Demonstrative tunnel cross-section with resonators under side walkway. 71

3.3 Normalised acoustic pressures for the first two non-planar cut-on frequencies for the demonstrative tunnel cross-section. 73

3.4 Illustration of the underlying assumptions of a continuum distribution of resonators and negligible interaction between neighbouring resonators. 76

3.5 Illustration of the flow field in the resonator neck. 78

3.6 A comparison of the half-order derivatives obtained for the reference initial condition by using the diffusive representation and FIT. . . . 87

3.7 Convergence analysis of the diffusive representation for the original and modified objective functions. 88

3.8 Local stencil for the cell edge flux reconstruction for MUSCL schemes. 92

3.9 Overview of the fifth order accurate upwinded ENO/WENO stencil, S, and sub-stencils, S_i. 95

3.10 Comparison of shock capturing schemes for a steep incident wavefront on a uniform grid, with and without an arbitrary array of resonators. 98
3.11 Comparison of numerically derived Jacobian sparsity patterns for a fixed value of $N_{\mathfrak{I}}$. 101
3.12 Illustration of a backward weighted stencil which requires one ghost cell at the right-hand side boundary. 103
3.13 The effect of various upstream boundary conditions for an arbitrary array. 103
3.14 Interpolation of an arbitrary data set, which is representative of a space-dependent far-field coefficient, using linear, piece-wise cubic, and spline interpolation. 105
3.15 Resonator coupling coefficient versus resonator location for a demonstrative array, in order to compare the discrete model and continuum models. 109
3.16 Dimensionless pressure waveforms for varying values of σ for an array of identical and equispaced resonators for the continuum and discrete far-field models. 111
3.17 Dimensionless pressure waveforms as a function of σ for an irregular array of resonators, using the continuum and discrete far-field models. 112

4.1 Experimental set-up showing the resonator lattice and one resonator. 116
4.2 Normalised numerical and experimental pressure-time histories in the scale model waveguide. 119
4.3 Power Spectral Density (PSD) for the initial condition in Figure 4.2a. 119
4.4 Overview of the 3-D mesh for Case 3. 123
4.5 Power Spectral Density versus frequency for the scaled initial pressure waveform. 124
4.6 Vertical cut through the length of the 3-D model at $t = 0$, showing the location of the IC, array and the upstream and downstream boundaries. 125

4.7 Mesh sensitivity study for Case 4 using the van Leer flux limiter and 2nd order accurate least-squares gradient discretisation. 128
4.8 Pressure-time histories for Case 4, for a range of flux limiters and gradient discretisation methods. 129
4.9 Comparison of the predicted 3-D and 1-D pressure waveforms for the demonstrative array configurations. 132
4.10 Velocity magnitude field and streamlines for one of the resonator cavities at $t = 0.12$ s in Case 6. 134
4.11 Pressure contours for Case 1, overlayed with the pressure-distance plot over the length of the array for various time points. 135

5.1 Characteristic pressure wave generated by train-nose entry into a tunnel. 146
5.2 Box plot for an order-of-magnitude analysis of the continuum far-field equations. 151
5.3 EE sensitivity analysis for $1 \leq N_c \leq 20$. 159
5.4 EE sensitivity analysis for $N_c = 20$. 160
5.5 Pareto set under the typical regime, extreme envelope, and extended extreme envelope, for regular resonator geometry. 162
5.6 Maximum rate of change of pressure versus equivalent array length for the Pareto optimal configurations with and without an array, with reference to Table 5.3. 163
5.7 Pressure waveforms and corresponding resonator response for $\alpha_a = 0.61$ in Figure 5.5, under typical operation for regular geometry. . . 164
5.8 Pressure waveforms for $\alpha_a = 0.65$ in Figure 5.5 for lower and upper bounds of the extreme operating envelope for regular geometry. . . 164
5.9 Pareto set under the operating regimes considered, for irregular resonator geometry. 165
5.10 Pressure waveform and resonator response for $\alpha_a = 0.65$ for the Pareto plot in Figure 5.9, under typical operation for irregular geometry. 166

5.11 Pressure waveforms for $\alpha_a = 0.71$ in Figure 5.9 for lower and upper bounds of the extreme operating envelope for irregular geometry. . . 167

5.12 Comparison of the pressure waveforms and resonator response for $\tilde{l_a} \approx 13$ on the Pareto fronts for the extreme envelope (with 2 optimisation points) with regular and irregular resonator geometry. . . 168

5.13 Sensitivity of the objective function to the initial condition, for $\tilde{l_a} \approx 13$ and $\tilde{L} = 2 \pm 50\%$, with regular resonator geometry. 169

5.14 Sensitivity of the objective function to the initial condition, for $\tilde{l_a} \approx 13$ and $\tilde{L} = 2 \pm 50\%$, with irregular resonator geometry. 170

5.15 Train time-speed profile for tunnel passage for a train with a speed reduction on tunnel entry and a constant speed. 176

5.16 The effect of reducing the train speed (from 380 km/h) on the added journey time (for one tunnel) and the change in the analytical maximum MPW SPL. 177

5.17 The effect of reducing the train speed (from 380 km/h) on the maximum MPW SPL for $l_t = 1$ km, based on numerical modelling of wave steepening. 178

5.18 Comparison of the relative reduction in the maximum rate of change of pressure for an entrance hood and array of resonators with countermeasure length, for various operating speeds. 181

5.19 Maximum rate of change of pressure versus train velocity for different combinations of an optimised entrance hood and array of resonators. 183

5.20 Normalised maximum rate of change of pressure as a function of train velocity for different combinations of an optimised entrance hood and array ($\tilde{l_h} = 3$, $\tilde{l_a} \approx 20$). 184

5.21 Example of the effect of a series of closed side branches on an idealised entry compression wave. $\tilde{L} = 1$, $u_z = 400$ km/h, $\theta = 0.2$, $l_b = 3$ m, with a branch spacing of 100 m. 185

5.22 Tunnel pressure waveforms and corresponding time-derivative profiles for an incident characteristic pressure wave preceded by side branches, after 190 m with, and without an array of resonators. . . 187
5.23 Optimised dimensionless tunnel pressure waveforms and corresponding time-derivative profiles, for a characteristic incident pressure wave preceded by side branches, after $\sim$ 190 m with, and without an array of resonators. 189

6.1 Illustration of the generation of the Primary branch wave before and after the entry wave has reached the branch, and the Secondary branch wave before and after the train nose and tail have passed the branch, respectively. 195
6.2 The effect of train speed on the maximum MPW amplitude with $\theta = 0.1$, and θ on the maximum branch MPW amplitude. 196
6.3 Overview of the branch wave model boundary conditions. 199
6.4 Example of the mesh for the Secondary branch wave model. 203
6.5 Dimensionless Primary branch waveforms predicted using the 2-D and semi-analytical models, with $\tilde{r_{\mathrm{bj}}} \approx 0$. 211
6.6 Normalised maximum overpressure in the branch versus θ, for comparison of the analytical model with 2-D predictions. 212
6.7 Example of the static pressure field in the branch region for $u_{\mathrm{z}} = 400$ km/h, $\tilde{r_{\mathrm{bj}}} = 0.5$ and $\theta = 0.5$. 213
6.8 Example of predicted fields in the region around the idealised train, with reference to Figure 6.7. 213
6.9 Dimensionless pressure waveforms for the Primary and Secondary branch waves for a selection of the branch radii. 214
6.10 Maximum rate of change of pressure for the Primary and Secondary branch waves versus branch junction radius, for a range of train speeds. 215

A.1 Scale train model and microphone set-up in the open and the train nose against a simple tunnel entrance hood. 246

A.2 Pressure coefficient waveforms versus measurement distance from the train model in an open environment. 247
A.3 Variation of maximum MPW amplitude with train entry speed from experimental measurements. 248
A.4 Comparison of experiments and a semi-empirical model for the maximum rate of change of pressure in the duct versus train entry speed. 249

B.1 Cross-section of an axi-symmetric silencer with N_c baffle chambers, with variable heights and lengths. 253
B.2 The axial variation of cross-sectional area across a duct contraction and expansion, with the pre and post smoothed non-uniform grid. . 256
B.3 Effect of the number of expansion chambers on the transmitted pressure waveform and the reduction in the normalised maximum rate of change of pressure. 259
B.4 Effect of $\tilde{l}$ on the transmitted pressure waveform and the normalised maximum rate of change of pressure. 260
B.5 Effect of $\tilde{h}$ on the transmitted pressure waveform and the normalised maximum rate of change of pressure. 260
B.6 Example of 2-D axis-symmetric meshes for the silencer model in OpenFOAM. 262

C.1 Dimensionless pressure waveforms for an arbitrary array using the uni-directional and bi-directional continuum far-field models. 268

E.1 Pareto set under the typical regime, extreme envelope, and extended extreme envelope, for reference $\tilde{L} = 1$. 277
E.2 Sensitivity of the objective function to the initial condition, for $\tilde{l_a} \approx 15$ and $\tilde{L} = 1 \pm 50\%$, with regular resonator geometry. 278
E.3 Sensitivity of the objective function to the initial condition, for $\tilde{l_a} \approx 15$ and $\tilde{L} = 1 \pm 50\%$, with irregular resonator geometry. 279

List of Tables

3.1 Reference physical and constant geometric parameters for the demonstrative tunnel section. 110

4.1 Physical and fixed geometric parameters used for experimental validation, with reference to Figure 3.1. 118

4.2 Array configurations used for the 1-D and 3-D model comparative study. 130

4.3 Dimensionless parameters for the 1-D modelling assumptions for the comparative study. 130

5.1 Summary of normalised optimisation variables and corresponding lower and upper bounds, with reference to Figure 3.2. 143

5.2 Summary of normalised geometric variables and corresponding lower and upper bounds for the order of magnitude analysis. 149

5.3 Optimisation points for evaluation of the objective function for reference $\tilde{L} = 2 \pm 50\%$. 161

5.4 Variation of optimised resonator dimensions with non-dimensional array length, based on the Pareto front in Figure 5.5, for regular resonator geometry. 161

5.5 Statistics for the sensitivity of the different operating regimes as a function of the number of optimisation points. 167

5.6 Normalised dimensions for the array test cases, with reference to § 5.2 and with $l_{\mathrm{a}} = 190$ m for all cases. 186

5.7 Normalised dimensions for the optimised arrays, with reference to § 5.2, and with $l_a \approx 190$ m. 188

6.1 Fixed side-branch and tunnel geometric parameters for parametric study. 209

A.1 Experimental scale model configurations. 246

B.1 Summary of normalised optimisation variables and corresponding lower and upper bounds, with reference to Figure B.1. 258

B.2 Normalised geometric variables used for the silencer in the parametric study for regular expansion chamber geometry. 259

E.1 Optimisation points for evaluation of the objective function for reference $\tilde{L} = 1$. 275

E.2 Statistics for the sensitivity of the different operating regimes as a function of the number of optimisation points. 276

Acronyms and Abbreviations

Re	Reynolds number
Pr	Prandtl number
stdev	Standard Deviation
3-D	Three-Dimensional
ACMI	Arbitrarily Coupled Mesh Interface
BC	Boundary Condition
BDF	Backward Differentiation Formulas
CFD	Computational Fluid Dynamics
CFL	Courant-Friedrichs-Lewy
D/FFT	Discrete/Fast Fourier Transform
DAE	Differential Algebraic Equation
EE	Elementary Effects
F D/V/E M	Finite Difference/Volume/Element Method
FOAM	Field Operation and Manipulation
FV	Fixed-Value
FVM	Finite Volume Method
He	Helmholtz number
IC	Initial Condition
KT	Kurganov & Tadmor
LB	Lower Bounds
LS	Least Squares

MOGA	Multi-Objective Genetic Algorithm
MOL	Method of Lines
MPI	Message Passing Interface
MPW	Micro-Pressure Wave
MUSCL	Monotonic Upstream-Centered Schemes for Conservation Laws
NRBC	Non-Reflective Boundary Condition
ODE	Ordinary Differential Equation
PDE	Partial Differential Equation
PIMPLE	PISO-SIMPLE
PISO	Pressure Implicit with Splitting of Operator
RANS	Reynolds-Averaged Navier-Stokes
RHS	Right-Hand Side
RK	Runge-Kutta
RMS	Root-Mean-Square
RTRI	Railway Technical Research Institute
SIMPLE	Semi-Implicit Method for Pressure Linked Equations
SPL	Sound Pressure Level
SQP	Sequential Quadratic Programming
STL	Standard Triangle Language
TVD	Total Variation Diminishing
UB	Upper Bounds
UD	Upwinded Differencing
WENO	Weighted Essentially Non-Oscillatory
ZG	Zero-Gradient

Notation

Greek Characters

α	eigenvalue; differential order; reduction factor
β	train-tunnel area ratio; smoothness indicator
χ	inter-cavity spacing
δ	length correction; boundary layer thickness
ϵ	acoustic non-linearity parameter
η	quadrature weight
γ	ratio of specific heats
κ	cavity smallness parameter
λ	characteristic wavelength
μ	dynamic viscosity
ν	kinematic viscosity
Ω	far-field coefficient
ω	characteristic angular frequency
ϕ	train nose & tunnel entrance shape empirical factor; flux limiter
ψ, ξ	diffusive variables
ρ	density
σ	continuum distribution parameter
θ	quadrature abscissa; branch-tunnel area ratio
υ	characteristic linear frequency
φ	plane wave parameter
ϖ	lumped element parameter

Lower-Case Italic Characters

a	speed of sound
b	half-range of IC in x
c	constant
d	diameter
e	error
f	far-field tunnel variable
g	far-field cavity variable
h	height

i	imaginary number; counter
l	length
p	pressure
q	$\partial g/\partial \mathcal{T}$
r	radius
t	time
u	velocity
w	width; weighting factor
x, y, z	spatial variables

Miscellaneous Characters

$\mathcal{C}$	dissipation in boundary layer
$\mathcal{F}$	advective flux; Fourier transform
$\mathcal{R}$	specific gas constant
$\mathcal{T}$	dimensionless far-field time
$\mathcal{X}$	dimensionless far-field space
$\Re$	Real number
T	dimensional far-field time
X	dimensional far-field space

Operators

$\bar{}$	averaged quantity
$\cdot$	equivalent circular/bore diameter
$\sim$	dimensionless parameter
N	index number, e.g. $i = 1, N$
D	material derivative

Subscripts

0	equilibrium, initial value
a	array
b	branch
c	cavity; cut-on/off
ch	characteristic
e	effective; exit
g	ghost
h	hood
i	incident
j	junction
n	neck; nose
o	observer
r	reflected
s	sample
t	tunnel
z	train (zug)

Upper-Case Italic Characters

$A - J$	near-field equation coefficients, see Equation 3.17
C^n	Continuous n-order derivative
K, U, W	far-field equation coefficients, see Equation 3.24
L	characteristic length
M	Mach number

Q	linear dispersion relation	V	volume
S	cross-sectional area	X	far-field space
T	far-field time		
T	temperature	Z	far-field equation coefficient

Chapter 1

Introduction

1.1 Motivation

Attempts to reduce greenhouse emissions and facilitate greater mobility are expected to require a modal shift from private road and air transport to public transport, including electrified trains (SDS, 2014). New high-speed rail projects will likely require the construction of tunnels, particularly where the construction of rail infrastructure above ground is infeasible (e.g. mountainous terrain). Tunnels also offer the advantage of minimising the environmental impact from noise pollution and the destruction of natural landscapes. However, they are costly to construct and create new problems, many of which are related to aerodynamic phenomena. Aerodynamic effects are an important consideration for high-speed train operations (greater than $200 - 250$ km/h) in tunnels.

New aerodynamic problems are encountered for train operations in tunnels, compared to an open environment. These are related to the interaction of compression and expansion waves generated by the train as it enters the tunnel and passes discontinuities (e.g. side branches). These pressure waves can cause aural discomfort for passengers (Montenegro Palmero and Vardy, 2014), mechanical fatigue of the car bodies (Lee et al., 2002; Wang et al., 2012), increased power requirements for the train, and the generation of environmental noise from the tunnel exit (Vardy, 2008) and other connections to the atmosphere (Miyachi et al., 2014;

Saito et al., 2010).

The micro-pressure wave (MPW) phenomena was first recognised in Japan with the introduction of the Shinkansen service between Tokyo and Osaka in 1964. An impulse noise, similar in sound to a sonic boom and of the order of 50-100 Pa at 200 km/h (Maeda, 1999), could be heard from tunnel exits shortly after a train had entered the tunnel. This became an environmental issue for people living nearby (Aoki et al., 1999; Ogawa and Fujii, 1996). Consequently, efforts have been made to tackle the issues related to the aforementioned pressure wave phenomena by refining the design of the trains and tunnels using experimental and computational techniques. These developments have been applied in different parts of the world, such as in Europe, where high speed rail networks have been built in countries such as France, Spain and Germany.

In the UK there are plans to build a new high speed rail link (High Speed Two) between London and Birmingham (Phase 1) with a maximum design speed of 400 km/h and with around 50% of the route in tunnels. Careful consideration of the issues mentioned above will be required in the design process. It is anticipated that existing countermeasures for MPWs will need to be augmented with new ones for increasing operating speeds, particularly in long tunnels.

1.2 Objectives

The original theme of this work was the optimisation of the safety and sustainability of high-speed rail operations in tunnel environments. This broad research scope was subsequently narrowed down to the theme of pressure wave phenomena and counteracting noise emissions from tunnels portals, after discussions with High Speed Two Ltd. and experts in the field.

This work presents a numerical investigation of several new countermeasures for the emission of micro-pressure waves in a physically representative tunnel system, which are: (1) an array of Helmholtz resonators embedded in the tunnel structure; (2) the modification of the geometry of a tunnel-branch junction connected to atmosphere (e.g. ventilation shafts); (3) a reactive silencer/muffler installed at

the exit of the tunnel (or branch openings). These countermeasures have not been employed in any commercial tunnel systems (to the author's knowledge as of 2017). The objectives of this work were to:

- Develop a fast and accurate low order numerical modelling framework for predicting the transmitted pressure wave due to an array of Helmholtz resonators;
- Validate and benchmark the framework against experimental data and 3-D computational fluid dynamics (CFD), respectively, in order to identify the limitations of the underlying assumptions;
- Apply the framework to a realistic tunnel system scenario, in order to identify the potential of this countermeasure to railway engineers, and to develop an optimisation procedure to maximise the robustness of the array across a range of operating conditions (e.g. future increases in trains speeds);
- Conduct a preliminary parametric study on the effectiveness of modifying the tunnel-branch junction geometry on the amplitude of micro-pressure waves emitted from side branches, and to identify if further work is warranted to investigate this countermeasure.

An outline of the work carried out to support these objectives is now presented.

1.3 Outline of Thesis

In Chapter 2 a brief overview of relevant acoustic principles and terminology for pipe flows is provided before introducing the relevant physical phenomena and acoustic issues related to the aerodynamics of high-speed train operations in tunnels. Existing countermeasures for these issues are discussed, as well as new countermeasures which have not been implemented in any high-speed tunnel system. A brief overview of optimisation algorithms and numerical solution techniques are outlined, which are required for the numerical solution and optimisation of the countermeasures.

Chapter 3 presents the physical and numerical model development for a duct connected to an array of Helmholtz resonators, in order to predict the transmitted pressure wave. A brief overview of the theory of Helmholtz resonators is provided before a physical model for an array of Helmholtz resonators is presented. An efficient and accurate numerical scheme is then applied to the system, for intended use in an optimisation procedure. Finally, improvements to the model are proposed by removing several underlying assumptions.

The 1-D modelling framework is first validated against data from shock tube experiments in Chapter 4. It is then benchmarked against a full scale and physically representative array embedded in the tunnel structure for a range of resonator geometries and train operating conditions, using 3-D CFD in OpenFOAM (Weller and Tabor, 1998). The array geometries are selected to compare any differences between the 1-D and CFD predictions in scenarios where the assumptions of the 1-D model are no longer expected to be valid.

In Chapter 5 the numerical model developed in Chapter 3 is applied to a demonstrative tunnel system in order to predict the effectiveness and robustness of an array of Helmholtz resonators, subject to different train operating regimes. A procedure to optimise the geometry of an array of resonators is proposed to maximally attenuate the amplitude of emitted micro-pressure waves from the tunnel exit. Both regular (uniform) and irregular (non-uniform) resonator geometry are considered. A sensitivity analysis of the geometric optimisation variables is performed in order to identify non-influential factors and reduce the complexity of optimisation. The array is also combined with an entrance hood in order to analyse their combined effect over a range of operating speeds. Finally, the effectiveness of the array to different incident waveform shapes is analysed, as a result of the distortion of the wavefront as it passes a series of side-branches. A simple inviscid analytical model is presented for the distortion of an idealised entry wave in a concrete slab track tunnel in order to support the work in this chapter.

In Chapter 6 a preliminary parametric study is conducted on the effect of modifying the geometry of the junction formed between the tunnel and an open

side-branch (e.g. ventilation shaft, pressure relief duct) on the amplitude of MPWs emitted from the branch portal. The effect of modifying the branch geometry is studied for the case of the compression wave generated as the train enters the tunnel when it reaches the branch, and the pressure waves formed in the branch as the train nose and tail passes. The study is conducted using 2-D CFD in openFOAM with sliding mesh motion to mimic the movement of an idealised train past a branch.

The overall conclusions of this work are provided in Chapter 7 and suggestions for future work are proposed.

1.3.1 Publications and Conferences

The following peer-reviewed journal paper has been published based on the work carried out in Chapters 3, 4 and 5:

J. A. Tebbutt, M. Vahdati, D. Carolan, and J. P. Dear. Numerical investigation on an array of Helmholtz resonators of micro-pressure waves in modern and future high-speed rail tunnel systems. *Journal of Sound and Vibration*, 400:606-625, 2017.

The author also had the opportunity to provide oral presentations at the following conferences:

J. A. Tebbutt. The Effect of Ventilation Shaft Geometry on Shaft Micro-Pressure Wave Emissions. In *9th World Congress on High Speed Rail*, Tokyo, 2015.

J. Zhou, J. A. Tebbutt, and R. A. Smith. High speed rail and questions of energy. In *High Speed Rail: Celebrating Ambition*, Birmingham, 2014. University of Birmingham.

1.4 Research Placement at RTRI

The author is grateful for being given the opportunity to undertake a three-month research placement at the Railway Technical Research Institute (RTRI) in Japan,

in 2014. Experiments were carried out under the supervision of Dr. Tokuzo Miyachi and Dr. Sanetoshi Saito (Heat and Air Flow Analysis Laboratory), in order to investigate the pressure transients generated by a scale moving train model in an open environment and inside a short tunnel. An analytical model was validated against these results, which can be used to assess the noise impact of a train on the surrounding environment.

The project also involved visiting several high-speed rail related sites, such as the RTRI Maibara Large-scale Low-noise wind tunnel and Hitachi Kasado Railway Works. An overview of the work carried out at RTRI is provided in Appendix A. This placement was partially funded by a Special Engineering Experience Award from the Institute of Mechanical Engineers.

Chapter 2

Literature Review

2.1 Introduction

This chapter provides the relevant background theory to train tunnel aerodynamics and identifies the research topic of this work. A brief overview of relevant acoustic principles and terminology for pipe flows is provided in § 2.2. The physical phenomena and aeroacoustic issues related to the aerodynamics of high-speed train operations in tunnels are presented in § 2.3 and § 2.4, respectively. Existing countermeasures for these issues are discussed and several novel countermeasures are suggested in § 2.5 and § 2.6, respectively. Finally, optimisation algorithms and numerical solution techniques are briefly described in § 2.8 and § 2.7. These are required for the design and optimisation of the countermeasures.

2.2 Overview of Acoustics

An overview of relevant and basic acoustic principles for pipe flows is provided before discussing the specific physical phenomena related to train operations in tunnels. Relevant dimensionless parameters are first defined in § 2.2.1 and a brief overview of fluid dynamic concepts relating to linear and non-linear acoustics in pipes is provided in § 2.2.2. The reader is directed towards a more detailed review of acoustics (Rienstra and Hirschberg, 2004; Skulina, 2005) and fluid mechan-

ics (Ferziger and Peric, 2012; Moukalled et al., 2015).

2.2.1 Important Dimensionless Parameters

Dimensionless parameters are produced when the conservation equations for mass, momentum and energy are written in a dimensionless form. These parameters are useful for performing parametric studies for engineering problems and identifying physical phenomena depending on the flow regime. For example, incompressible, compressible, porous flows, etc.

Reynolds number

The Reynolds number is a measure of the balance between kinetic energy and viscous damping and is defined as the ratio of inertial forces (momentum, gravity, pressure gradients) to viscous forces:

$$\mathrm{Re} = \frac{\rho u L}{\mu} \tag{2.1}$$

where ρ is the fluid density, u is a characteristic velocity, μ is the dynamic viscosity and L is a characteristic length scale. The duct diameter, d, is typically used as the length scale. The flow velocity is taken as the acoustic velocity amplitude of the fluid ($u = p/\rho_0 a_0$), where p is the pressure perturbation and a_0 is the ambient speed of sound. The Reynolds number conveys the boundary layer characteristics of the fluid flow, such as whether it is laminar, turbulent or in a transition state. It is a useful tool for comparing flows with different speeds and/or length scales, based on equivalent Reynolds numbers.

The boundary layer consists of the region where stream-wise velocity varies from $u = 0$ at the wall (no-slip condition) up to where the velocity is the free-stream value. A laminar flow regime is expected for pipe flow with $\mathrm{Re} < 2000$ and is characterised by smooth layered flow where the stream-wise velocity increases uniformly moving away from the wall. The point of transition, as defined by the critical Reynolds number, is dependent on the wall roughness for pipe flows and must be determined experimentally. It is expected to be in the range $2000 <$

$\mathrm{Re}_{\mathrm{crit}} < 4000$. The turbulent regime is expected for flows with $\mathrm{Re} > 4000$ and is characterised by unsteady mixing inside the boundary layer. The reader is directed towards the literature for more information on boundary layer theory (e.g. Schlichting and Gersten, 2000).

Mach number

The Mach number is a measure of the compressibility of a fluid flow (by how much the density changes) and is given by the ratio between the local flow velocity and the speed of sound:

$$M = \frac{u}{a_0} \tag{2.2}$$

Compressibility is assumed to be negligible for $M \ll 1$, or more specifically for $M < M_{\mathrm{crit}} \approx 0.3$. Below this threshold the density change due to the flow velocity is less than $\sim 10\%$, which is taken as sufficiently small to be assumed as constant. The flow can then be modelled using simplified incompressible equations (incompressible Navier-Stokes), where the finite wave propagation speed through the domain is ignored and only pressure and velocity are considered as variables. Conversely, for $M > M_{\mathrm{crit}}$ changes in the fluid temperature, T and density are no longer negligible. The addition of an equation of state for the gas is now required (e.g. the ideal gas law with $p = \rho \mathcal{R} T$, where $\mathcal{R}$ is the specific gas constant) and the equations for the conservation of mass and energy.

Helmholtz number

The Helmholtz number is the ratio of the characteristic length scale to the characteristic acoustic wavelength:

$$\mathrm{He} = \frac{l_{\mathrm{ch}}}{\lambda} = \frac{l_{\mathrm{ch}} \upsilon}{a_0} \tag{2.3}$$

where υ is a characteristic frequency, $\upsilon = a_0/\lambda$. Flows with $\mathrm{He} \ll 1$ are defined as acoustically compact, which can occur at low frequencies where time derivatives

become small, or near a singularity where spatial gradients become large. The acoustic flow can then be locally approximated as an incompressible potential flow with an irrotational velocity field. A compact source can be treated as a radiating point.

2.2.2 Basic Acoustics in Waveguides

Acoustic theory is concerned with small perturbations in pressure and density ($p,\ \rho$) around a mean equilibrium state ($p_0,\ \rho_0$), for which a stagnant ($u_0 = 0$) and uniform fluid (i.e. a quiescent fluid) is assumed. For example, $p' \simeq p_0 + p$ and $\rho' \simeq \rho_0 + \rho$. Second order terms can be neglected upon substituting these perturbations into the conservation equations for mass and momentum, assuming a low Mach number (see § 1 Rienstra and Hirschberg, 2004). If pressure and density fluctuations are approximated by a linear relationship for isentropic flow (e.g. $p = a_0^2\rho$) then the conservation equations eventually simplify to the inhomogeneous linear wave equation:

$$\frac{\partial^2 p}{\partial t^2} = a_0^2 \nabla^2 p \tag{2.4}$$

where t and x are time and space, respectively. This equation permits the advection of waves with no distortion at the ambient speed of sound, a_0.

Non-linear flow effects must be considered at sufficiently high acoustic amplitudes and Mach numbers. These are usually satisfactorily captured by including second (and possibly third) order terms in the process outlined above. An important phenomenon of acoustic non-linearity is wave steepening in waveguides (defined by $d \sim O(\lambda)$ and $l \gg d$, where l is the length of the waveguide), where the acoustic energy cannot spread out as it would be able to in an open environment. Non-linear wave steepening is captured by the inviscid Burgers' equation, which is given in its conservation form in a frame of reference moving with the

wavefront by:

$$\frac{\partial u}{\partial t} = \frac{\partial}{\partial x}\left(\frac{u^2}{2}\right) \tag{2.5}$$

The solution of Equation 2.5 reveals that a compression wave (an increase in pressure) will steepen as it propagates, whilst a rarefaction (a reduction in pressure) will reduce in gradient. Consequently, a compression wave can steepen into a shock wave, given a sufficient propagation distance in a waveguide. However, it is noted that visco-thermal effects (e.g. wall friction, sound diffusivity) will counteract this process as the wave steepens.

Another source of non-linearity at high acoustic velocities is the dissipation of kinetic energy through vortex shedding due to jet formation around sudden changes in cross-sectional area, e.g. baffles, duct junctions. At sufficiently high Reynolds numbers the effects of the viscous boundary layer on the flow are confined to a thin region close to the wall. Flow separation can still occur at open ends or sudden changes in area, even for low Reynolds numbers.

Acoustic propagation in a duct can be accurately described by plane waves if the frequency is below the plane wave cut-off frequency ($\upsilon < \upsilon_c$). The cut-on modes and frequencies are dependent on the geometry of the waveguide. If $\upsilon \geq \upsilon_c$ then higher modes of propagation are cut-on (e.g. circumferential and radial modes), which would have otherwise decayed exponentially with distance from the source (i.e. they are evanescent). The cut-on modes can be combined to represent the complete sound field in the duct. A lower frequency bound for the plane wave approximation is given by the assumption of a thin viscous boundary layer relative to the wetted diameter of the waveguide:

$$\delta/d = (2\nu/\omega)^{1/2}/d \ll 1 \tag{2.6}$$

where $\nu = \mu/\rho$ is the kinematic viscosity of the fluid and $\omega = 2\pi\upsilon$ is the characteristic angular frequency. The reader is directed to § 4 of Rienstra and Hirschberg (2004) for more detail on the topic of non-linear acoustics in waveguides.

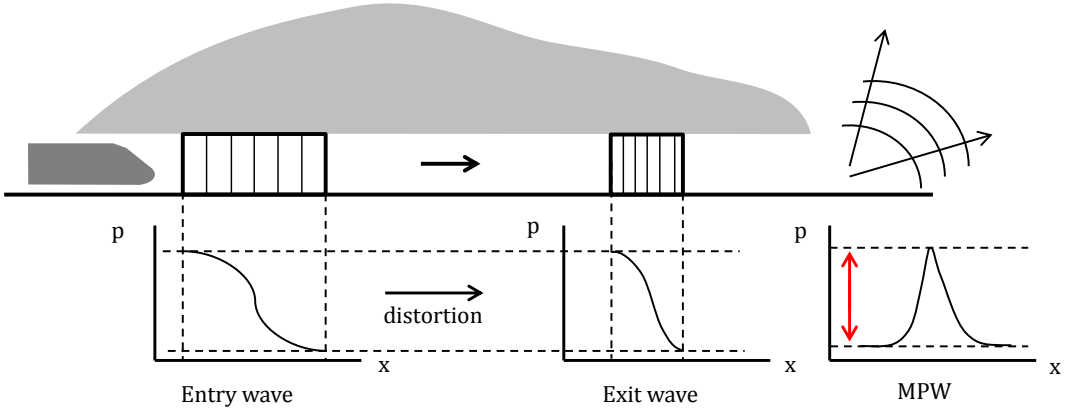


Figure 2.1: Process leading to the emission of a micro-pressure wave from the tunnel exit.

2.3 Tunnel Aerodynamics Overview

An overview of the relevant physical phenomena related to train operations in tunnels is provided in order to familiarise the reader with the causes of the main aerodynamic and acoustic problems encountered in tunnels. The processes are divided into the regions of tunnel entry in § 2.3.1, passage in § 2.3.2, and exit in § 2.3.3.

2.3.1 Tunnel Entry

A train operating in an open environment will displace the air ahead of it in all directions. However, the train can only displace the column of air ahead of it when it enters a tunnel. A compression wave is generated due to the geometric discontinuity between the open air and the tunnel as the train enters (also referred to as the Primary wave), as illustrated in Figure 2.1. A portion of the air ahead of the train is able to escape to the outside through the annulus created between the train and the tunnel in a vortex jet (Bellenoue, 2002). Similarly, a rarefaction (expansion wave) is generated as the tail of the train enters the tunnel.

Dissipative processes can be neglected during the initial wavefront generation period as the train nose enters the tunnel, due to the large Reynolds number. A convenient consequence of this assumption is that the dynamic processes scale on

Mach number and so the entry wave can be accurately replicated using small-scale experiments with moving models of trains. Facilities of this type exist at the Railway Technical research Institute (RTRI) in Japan and the Centre for Railway Research at the University of Birmingham. The amplitude of the primary compression wave generated at train entry is predicted by Hara (1961) using steady, compressible inviscid flow under adiabatic conditions:

$$p_1 \approx \frac{1}{2}\rho_0 u_z^2 \frac{1-(1-\beta)^2}{(1-M_z)(M_z+(1-\beta)^2)} \tag{2.7}$$

where u_z is the train speed, $0 < \beta = S_z/S_t < 1$ is the blockage ratio between the train and tunnel cross-sectional areas, $M_z = u_z/a_0$ is the Mach number of the train, and a_0 and ρ_0 are the speed of sound and density of air at ambient conditions, respectively.

It is clear that the amplitude of the entry wave is primarily governed by the entry speed and tunnel blockage ratio. However, Vardy (1996) showed that the amplitude may vary slightly depending on the streamlining of the nose and the associated stagnation pressure losses. For example, a larger region of local separation (bubble) is generated around the end of a "blunt" nose, which artificially increases the blockage ratio. Although the characteristics of the primary wave are largely governed by inertial effects, it will also be affected to a much smaller degree by friction from the tunnel wall and train body.

The tunnel entry pressure waveform is strongly influenced by the shape of the train nose and tunnel entrance. The characteristic frequency of the entry compression wave, $\upsilon = a_0/\lambda$, is estimated to be in the order of 1-10 Hz (Sugimoto, 1992). Such low frequencies are less affected by dissipation and it is posited that non-linear steepening over the course of propagation could result in the emergence of shock waves. Vardy (2008) approximates the maximum wave-front steepness due to the entry of the train into the tunnel as:

$$\left(\frac{\partial p}{\partial t}\right)_{\max} \approx \frac{p_1}{(1/u_z - 1/a_0)\phi d_t} \tag{2.8}$$

where d_t is the hydraulic diameter of the tunnel and ϕ is an empirical coefficient typically in the range of $0.75 < \phi < 1.25$, which accounts for the profile of the train nose and tunnel entrance.

2.3.2 Tunnel Traversal

The region around the train and tunnel entrance is dominated by three-dimensional (3-D) aerodynamics. Multiple sources of aeroacoustic noise over a large frequency range can be identified, and are related to the geometry of the train and tunnel entrance (e.g. pantograph and inter-car spaces). High frequencies are rapidly attenuated further away from the train (or noise source) owing to dissipation, resulting in near one-dimensional (1-D) propagation in the far field. Bellenoue (2002) found that the distance corresponding to the transition from the near (3-D flow region) to far (1-D plane wave region) field was roughly four times the tunnel diameter from scale model experiments.

Part of the primary compression wave generated at tunnel entry will be reflected from discontinuities in the tunnel, such as shafts/branches and changes in cross-sectional area. In addition, weaker secondary compression and expansion waves will be generated as the train passes these discontinuities. Small effects described by non-linear acoustic theory will cause the pressure wave gradient to steepen over large distances. Conversely, dispersive effects from ballast track (or other dispersive sources) will counteract steepening and smear out gradients, while visco-thermal losses from the tunnel walls will attenuate the wavefront. The steepening rate of the compression wave increases with the acoustic amplitude of the entry wave (see § 5.9).

Additional drag is experienced by trains in tunnels, compared to in an open environment due the piston effect. The train must "push" the column of air ahead of it towards the exit. The piston effect can be significant for high blockage ratios as less air is able to pass through the annulus between the train and tunnel.

2.3.3 Tunnel Exit

The compression waves are reflected as rarefactions back towards the tunnel entrance at the exit portal. A portion of the energy is radiated into the environment as an impulse wave, or MPW. The interaction of reflected waves in the tunnel can affect the performance of the train as well as passenger comfort. The MPW amplitude can be modelled as a point monopole in the low-frequency and far-field approximations (Yamamoto, 1977):

$$p_{\mathrm{MPW}}(r_{\mathrm{o}}, t) \approx \frac{2S_{\mathrm{t}}}{\Omega a_0 r_{\mathrm{o}}} \cdot \frac{\partial p_2}{\partial t}\left(t - \frac{r_{\mathrm{o}}}{a_0}\right) \tag{2.9}$$

where p_2 is the acoustic pressure at the exit of the tunnel and r_{o} is the distance from the centre of the tunnel exit to the observer. The solid angle, Ω, is defined as the surface area of a unit sphere covered by the surface's projection onto the sphere. Its value depends on the geometry of the terrain around the tunnel exit. A first approximation of semi-infinite space (i.e. a hemisphere) with $\Omega = 2\pi$ is representative of many tunnel exits and is useful for preliminary design calculations. The far-field approximation is valid provided that the observation distance is much greater than the equivalent radius of the exit portal. A or C-weighting can be applied to the spectrum of Equation 2.9 to determine the relative loudness of the MPW to the human ear.

Clearly, the MPW amplitude is proportional to the rate of change of pressure at the exit of the tunnel. Therefore, the main principle of control is to reduce the gradient of the pressure wave reaching the tunnel exit. The maximum MPW amplitude will generally be dominated by low-frequency components. However, higher frequencies within the audible range are of greater importance and therefore should have stricter limits on their amplitude. More complex equations can provide better MPW predictions for steep incident wavefronts (Blake, 2012), or if the topography around the exit portal is known (Miyachi, 2011, 2017).

In practice and for initial design purposes it is assumed that the maximum amplitude is limited by the low frequency components (Vardy, 2008) and the exact topography is unknown, for which Equation 2.9 is generally adequate. Several

conclusions can be drawn from the basic equations and underlying theory used to estimate the strength and shape of the entry wave and resultant MPW:

- Reducing the tunnel diameter in order to reduce constructions costs will result in an increase in the amplitude and steepness of generated pressure waves. The restricted airflow and high pressure wave amplitudes could impact the performance of the train, resulting in increased operating costs. Additional costs will be incurred due to the requirement for more substantial countermeasures for micro-pressure waves.

- Future increases in train speeds will require greater consideration for pressure wave problems in tunnels, such as MPWs. Consequently, the cost of installing commonly used countermeasures, such as tunnel entrance hoods and longer train noses (see § 2.5) will likely increase, particularly for very long tunnels. As a result, complementary countermeasures may be required.

2.4 Aerodynamic Issues in Tunnels

Several issues have been identified in the literature (e.g. Baker, 2014; Raghunathan et al., 2002; Vardy, 2008) relating to the aerodynamics of high-speed train operations in tunnels and the phenomena described in the previous section. The main ones are listed below:

- Micro-pressure waves from tunnel portals, e.g. tunnel exit, ventilation shafts, etc.;

- Passenger aural comfort and safety;

- Aerodynamically induced mechanical fatigue of the train body and tunnel infrastructure;

- Heat and smoke ventilation;

- Aerodynamic drag and the associated train power requirements.

These issues are to a varying degree related due to a dependency on pressure wave phenomena. Therefore, they should be considered concurrently during the design process. For example, countermeasures for MPWs may also be effective for reducing pressure transients on the train and the passengers. A combination of methods can be used to counteract MPWs, which will be discussed in greater detail in this section.

2.4.1 Micro-Pressure Waves

The micro-pressure wave phenomena first became a problem in Japan with the introduction of the Shinkansen service. An impulse noise (see Raghunathan et al., 1998), similar in sound and amplitude to a sonic boom could be heard from tunnel exits shortly after a train had entered the tunnel. This noise became an environmental issue for people living nearby (see Aoki et al., 1999; Ogawa and Fujii, 1996). The low frequency noise can also cause objects to rattle and may disturb nearby wildlife.

MPWs are a particular concern in Japan, where many of the tunnel exits on the Tokaido Shinkansen are located nearby to populated areas. The amplitude of MPWs is approximately proportional to u_z^3 (Sakurai et al., 2008) for short concrete slab and ballast track tunnels. MPWs can be clearly audible, even at distances of approximately 1 km from the exit portal (Degen et al., 2008). MPWs are the main environmental noise issue associated with high-speed train operations in tunnels and place limitations on the minimum size of the tunnel bore and maximum train operating speed.

2.4.2 Passenger Aural Comfort

Aerodynamic pressures acting on the passengers arise from the complex interference of pressure waves in the tunnel. The area of passenger comfort and safety is complex due to the subjective human aspect (see Glöcke and Pfretzschner, 1988). Aural comfort is affected by the rate of change of pressure and how quickly passengers can adjust to the changes (Montenegro Palmero and Vardy, 2014), rather

than the absolute change in pressure. This is in turn dependent on the train operating conditions, tunnel geometry, and changes in elevation.

The maximum permissible pressure gradient according to the guidelines in UIC-779-11 (UIC, 2005) is 1 kPa in 1 s for a sealed train. Similarly, the European Rail Research Institute states that the maximum pressure difference that can be experienced in a tunnel is 10 kPa. These requirements place constraints on the design of tunnels. However, the use of countermeasures which are also effective for MPWs may also help to reduce the severity of the pressure transients experienced by passengers.

2.4.3 Aerodynamic Fatigue

Aerodynamic forces on the train cars arise from the complex interference of pressure waves generated in the tunnel. For example, a stress analysis for a Korea high-speed train passenger car found that fatigue damage in tunnels was considerably higher than in the open (Lee et al., 2002). Nonetheless, the required fatigue strength was still satisfied for the extreme case of crossing trains with speeds of 350 km/h. Increasing operating speeds will likely require the implementation of more effective train sealing in order to maintain passenger comfort. This would place greater demands on the car sealing and ventilation systems. For example, the magnetically levitating (Maglev) Shinkansen will operate largely in tunnels and with a maximum speed of approximately 500 km/h when opened between Tokyo and Osaka (Railway Gazette, 2013).

Information about the area of train body/sealing fatigue has been difficult to acquire. Much of the related research is carried out by rolling stock manufacturers and is proprietary. It was recognised from discussions with engineers at RTRI and Hitachi Kasado Rolling Stock Works that the capability already exists to model the stresses on a train vehicle due to the pressure transients experienced in a tunnel. The issues of aerodynamic fatigue did not seem to be of particular concern. Despite this, rolling stock manufacturers, such as Hitachi, have a full scale fatigue testing machine which can mimic the pressure transients experienced

by a train car in a tunnel (Hitachi, 2013).

2.4.4 Aerodynamic Drag

The additional power requirements experienced by the train due to the piston effect can be reduced through various methods of pressure relief. Constructing ducts to the atmosphere in shallow tunnels, and/or providing regular cross-passages between tunnel bores in deep tunnels are effective methods of pressure relief (Baron et al., 2001). The cross-passages also provide a positive benefit to trains moving in opposite directions and can help to reduce the amplitude of MPWs by partially reflecting the incident compression wave.

Building this additional infrastructure increases overall construction costs, particularly for long and deep tunnels. It also introduces more potential sources of environmental noise. The amplitude of MPWs emitted from pressure relief ducts and ventilation shafts into the atmosphere is less than those from the tunnel exit (Miyachi et al., 2014). However, branch MPWs could become an issue with increasing operating speeds and/or an increase in the tunnel blockage ratio (see Chapter 6).

2.5 Existing MPW Countermeasures

2.5.1 Entrance Hood and Train Nose Optimisation

Most efforts to reduce the amplitude of MPWs from the tunnel exit have focussed on reducing the maximum rate of change of pressure of the primary compression wave at the point of generation (see Equation 2.9). Tunnel entrance hoods (Howe et al., 2003a,b), and/or the optimisation and elongation of the nose profile (Iida et al., 1996a,b; Kwon et al., 2001; Maeda et al., 1993; Muñoz-Paniagua et al., 2014) are commonly used for this purpose. Examples of these countermeasures for the Japanese Shinkansen are shown in Figures 2.2 and 2.3.

A well-designed entrance hood and train nose provides a smoother transition from the outside into the tunnel, compared to without these measures. Successive



Figure 2.2: Optimised train nose profile on the Shinkansen N700-A train-set (Tokyo Railway Labyrinth, 2013), with a length of $\sim$ 11 m (Ueno et al., 2008).



Figure 2.3: A hood that has been fitted on a tunnel entrance in Japan (JR-EAST, 2016).

small compression waves are generated as the train nose passes the staggered change in cross-sectional area of the hood, smearing out the effective length of the compression wave. A significant portion of the energy of the generated compression waves is temporarily trapped in the hood due to reflections. It is noted that the overall amplitude of the entry compression wave is not affected by the hood.

Hoods can be very effective, particularly for short tunnels of up to about 1 km as a first approximation (Vardy, 2008). It may be necessary to use a longer hood in longer tunnels to account for non-linear wave steepening between the entrance and exit portals, in order to meet MPW loudness criteria. For example, Howe et al. (2008) predict that entrance hoods of 200 m or more in length will be required to suppress non-linear steepening for Maglev trains operating at $\sim$ 500 km/h. Recent developments (Sakurai et al., 2008) have demonstrated that the length of an entrance hood can be reduced by integrating a series of ducts into the hood. For example, a 9 m reduction in hood length can be achieved by incorporating ducts into a 49 m long unventilated hood.

Experiments performed by Takayama et al. (1995) indicate that an entrance hood becomes less effective for suppressing MPWs with increasing operating speeds. New countermeasures, which are effective at higher operating speeds, will be needed to augment tunnel entrance hoods. Non-linear steepening in modern concrete slab track tunnels can cause the micro-pressure wave amplitude to be greater than 50 Pa (a sound pressure level of $\sim$ 130 dB) near the exit. This is comparable to the amplitude of the sonic boom from a supersonic aircraft (Howe et al., 2000). Increasing the nose length and optimising its shape for longer tunnels reduces the availability of passenger seating and may require longer platforms. A simple method which has been suggested is to temporarily reduce the speed of the train as it enters the tunnel (see § 5.9). However, the resultant penalty on the journey time would need to be considered.

2.5.2 Ballasted Track

Ballast (pebble bed) has been shown to dramatically reduce the amplitude of MPWs (Ozawa et al., 1993; Vardy, 2008; Vardy and Brown, 2000), compared to concrete slab track. Ballast acts as a porous acoustic liner by counteracting the wave steepening process in long tunnels through dispersion and friction. Current models describe ballast as analogous to an array of Helmholtz resonators. Air from the pressure wave flows into the ballast where it is subsequently released behind the pressure wave, eroding the pressure wave front. Despite this, the use of concrete slab track in modern rail infrastructure is more practical:

- Reduced maintenance and a longer design life. For example, ballast can resettle and must be replaced.
- The issue of ballast flight is negated. Ballast can be thrown-up at the underside of the train or onto the railheads at high speeds. This can cause damage to the train (Baker, 2010; Kwon and Park, 2006), and also the railhead and wheels due to ballast pitting as the particles are crushed (Quinn et al., 2010).
- Overall construction costs are reduced, by approximately 30% according to Miura et al. (1998). Slab is lighter and requires less space, and so the tunnel cross-section can be reduced.

Therefore, a method of combining the practicality of slab track with the dissipative properties of ballast is desired (see § 2.6.1).

2.6 Novel MPW Countermeasures

It is anticipated that increasing train speeds and a modal shift to high-speed rail will require the construction of new tunnel infrastructure, particularly with increasing urbanisation across the world. Existing countermeasures for MPWs will need to be augmented by new ones as train speeds increase, particularly in long tunnels where existing entrance countermeasures are likely to become less cost effective.

Several countermeasures for the MPW problem were investigated in this work. Although some of these methods have established roles in other applications, their application and effectiveness in high-speed rail infrastructure has not been explored in much detail. An overview of these countermeasures is provided in the next subsections.

2.6.1 Helmholtz Resonator Array

It has been suggested by some authors (Sugimoto, 1992; Vardy, 2008) that an array of Helmholtz resonators could be used in a slab track tunnel, combining the dispersive qualities of ballast with the practicality of slab track. A brief overview of the theory of Helmholtz resonators is presented in § 3.2.1.1. The resonator cavities would need to be large in order to disperse low frequency pressure waves (Vardy, 2008), which could be prohibitively expensive. Therefore, the aim would be to incorporate the cavities into redundant tunnel space, if available. Vardy (2008) notes that safety refuges with restricted openings to the tunnel might exhibit the characteristics of Helmholtz resonators. The Grauholtz tunnel in Switzerland is cited as a potential example for the absence of steepening wavefronts.

Acoustic absorbing panels have been developed and retrofitted in the Euerwang and Irlahull tunnels on the ICE high-speed line from Nuremburg to Ingolstadt (see Tielkes, 2006). The panels were retrofitted due to unacceptable MPW levels at the tunnel exits after a decision was made to change from ballast track to concrete slab track, without modifying other aspects of the tunnel design. The sound absorbing plates (with the brand name LIAKUSTIK) were originally designed to attenuate rail vibration noise. Tielkes et al. (2008) found that they were also effective at reducing the pressure wave steepening process.

Model and full scale experiments performed by Takayama et al. (1995) on the Tohoku Shinkansen showed that a 200 m long section with a perforated wall reduced the MPW overpressure by around 30%. However, it became less effective at lower operating speeds. On the other hand, an entrance hood becomes less effective at higher operating speeds. Combing the two countermeasures was suggested

as an effective approach over a range of operating speeds.

2.6.2 Tunnel Exit Silencer

A reactive silencer consists of a series of baffles and expansion chambers, e.g. a firearm suppressor or an exhaust muffler. The discontinuous change in duct cross-sectional area (and hence acoustic impedance) results in the successive reflection of the incident pressure wave and the attenuation of the transmitted wave. Aoki et al. (1999) conducted a parametric study on a simple antisymmetric silencer with one chamber by solving the 2-D Euler equations and found that up to a 30% reduction in the maximum amplitude of MPWs was possible.

The silencer can be fitted to both the tunnel exit and other connections to the atmosphere (i.e. side branches), such as ventilation shafts. An optimisation study on the geometry of a tunnel exit silencer was planned in order to refine its design when applied to a representative tunnel system. This work has been started and is included in Appendix B.

2.6.3 Branch MPWs

It has been mentioned that unacceptable MPWs could be generated not just from the tunnel exit, but from side branches connected to the atmosphere (e.g. ventilation shafts and pressure relief ducts) with increasing train speeds. Existing countermeasures (see § 2.5) and an array of Helmholtz resonators (see Chapter 3) are effective for reducing the amplitude of branch MPWs in the case of the Primary compression wave generated as the train enters the tunnel. However, these countermeasures are ineffective for the pressure waves generated by a train passing a branch, except for the train nose shape.

The simplest method to reduce the branch MPW amplitude is to reduce the branch area, but this may conflict with ventilation and pressure relief requirements. In this work it is proposed that the geometry of the tunnel-branch junction could be modified to reduce the steepness of generated branch waves in a manner similar to the functionality of a tunnel entrance hood. The effect of modifying the branch

geometry is considered in Chapter 6.

2.7 Numerical Methods for PDEs

The models used in this work require the numerical solution of a system of time-dependent partial differential equations (PDEs). The PDE must be discretised to produce a system of algebraic equations in order to be solved numerically. An overview of the methods used to discretise and solve PDE systems is provided.

2.7.1 Semi-Discretisation

The method of lines (MOL) is an established technique for numerically evaluating a system of time-dependent PDEs. Semi-discretisation is used so that the PDE is discretised in all but one independent variable. Typically, the boundary value derivatives (usually space) are discretised, resulting in a system of first order ordinary differential equations (ODEs). This system can be solved using standard ODE integration routines. This process is demonstrated for a simple linear advection initial value problem with a uniform grid in space, x:

$$\frac{\partial u}{\partial t} = a\frac{\partial u}{\partial x} \tag{2.10}$$

where a is the linear wave propagation speed. For example, discretising the terms on the right-hand side (RHS) in space using a simple equispaced and second order accurate central difference scheme yields:

$$\frac{\mathrm{d}u}{\mathrm{d}t} = a\left(\frac{u_{i+1} - u_{i-1}}{2\Delta x}\right) \tag{2.11}$$

where $i = 1, n$ and n is the number of grid points, resulting in a system of n ODEs. Many techniques can be used to discretise Equation 2.11, as outlined in § 2.7.1. This system of first order algebraic equations can be integrated using the techniques discussed in § 2.7.2. ODEs can be generalised to differential algebraic

equations (DAEs), containing an unknown function and its derivatives:

$$F\left(t, x, x'\right) = 0 \tag{2.12}$$

where $x = x(t)$ and $F = F(t, u, v)$. It is possible that the Jacobian (the first order partial derivative of a function with respect to all the variables) of the DAE is singular, resulting in an implicit system. An important class of DAEs is the semi-explicit Hessenberg index-1 type:

$$u' = f\left(t, u, v\right) \tag{2.13}$$

$$0 = g\left(t, u, v\right) \tag{2.14}$$

This DAE is closely related to implicit ODEs (see § 2.7.2). DAEs are more complex to solve than ODEs as they typically require the use of iterative techniques, such as a Newton method. They also require consistent initial values to be generated for all the variables, which typically requires the derivative of some functions of the DAE.

Several methodologies are available for the semi-discretisation of the RHS of an ODE/DAE system. A brief overview of several of the most popular techniques is provided in the following sections. A detailed review of numerical methods for ODEs and DAEs is provided by Ascher and Petzold (1998).

2.7.1.1 Finite Difference Method

The finite difference (FD) method is based on the differential form of the PDE. Derivatives are approximated using a Taylor series expansion, which is truncated to give the required order of accuracy. The solution is directly obtained at the nodal points. Finite differences are relatively simple to implement for 1-D and structured grids. Formal higher order accuracy can be achieved by extending the stencil to include more nodes. Despite this, finite differences do not easily scale-up to multiple dimensions and complex geometries, particularly for unstructured

grids. This limits their use for many practical engineering applications.

The FDM has been commonly used for meteorology, astrophysics and computational fluid dynamics (CFD). The reader is directed to consult LeVeque (2007) and Strikwerda (2004) for further details. The FDM can be adapted for conservation laws by evaluating convective fluxes at the "cell" edges (i.e. $u_{i+\frac{1}{2}}$ and $u_{i-\frac{1}{2}}$, see Figure 3.9), rather than at the nodal points.

2.7.1.2 Finite Volume Method

The finite volume (FV) method is based on the integral form of the PDE. The domain is divided into control volumes, or cells, where the unknown quantity is calculated as the volume average of each cell. For example, the volume average value of $u_i(t) = u(x,t)$ for cell i is given by

$$\bar{u_i} = \frac{1}{x_{i+\frac{1}{2}} - x_{i-\frac{1}{2}}} \int_{x_{i-\frac{1}{2}}}^{x_{i+\frac{1}{2}}} u(x,t)\mathrm{d}x \tag{2.15}$$

where locations $x_{i\mp\frac{1}{2}}$ represent the left/right cell boundaries, respectively. Volume integrals containing divergence terms are then converted to surface integrals using the divergence (also known as Gauss') theorem. The FVM is conservative as fluxes are specified through the cell surfaces using piece-wise approximations.

The FVM can be applied to an arbitrary grid, making it particularly useful for the complex geometries involved in many engineering applications. All dimensions are implicitly treated simultaneously for 2-D and 3-D meshes by integrating over the FV, while each direction must be treated independently in the FDM. It is also suitable for problems containing discontinuities due to the use of non-linear slope/flux reconstruction. The FVM has historically been used for CFD, heat transfer and chemical engineering. Additional details on the FV discretisation procedure is provided in the literature (see Ferziger and Peric, 2012; Jasak, 1996; Moukalled et al., 2015), and is not discussed further here.

2.7.1.3 Finite Element Method

In the finite (FE) element method the PDE is represented in the weak form by multiplying the integral form by a smooth weight function and integrating over the domain. The domain is divided into elements, where continuous or weakly continuous approximations for the fields are assumed using linear or quadratic polynomials. The contributions from all elements are assembled into a large sparse global matrix. It is relatively easy to increase the order of the elements by using higher-order polynomial approximations for the weight functions.

The FEM is generally more computationally and memory intensive compared to the FD and FV methods, and is more complex to implement. The FEM is traditionally used in structural/solid mechanics engineering applications, but it is becoming more prevalent in multi-physics and CFD. The reader is directed towards the literature for more information (e.g. Barth et al., 2003).

2.7.1.4 Pseudo-Spectral Methods

Spectral methods are based on global approximations by using very high-order polynomials, or the Fourier transform (FT). Conversely, standard finite difference/volume approximations make use of local approximations, e.g. typically low order polynomials. Therefore, spectral methods represent the limit of finite differences in terms of order of accuracy. Spectral methods provide a very simple treatment of derivatives in the frequency domain as they are transformed into algebraic equations:

$$\mathcal{F}\left\{\frac{\mathrm{d}^{\alpha}u(x)}{\mathrm{d}x^{j}}\right\} = (i\omega)^{\alpha}\,\hat{u}(\omega) \tag{2.16}$$

where α is the order of the derivative (which is not just limited to integers) and $\mathcal{F}$ is the FT. This method significantly simplifies the treatment of fractional-order derivatives/integrals compared to the time domain, where the function must be integrated using the Riemann-Liouville (RL) integral (Oldham and Spanier, 1974):

$$\mathcal{D}_t^{-\alpha} u(t) = \frac{\partial^\alpha}{\partial t^\alpha} u(t) = \frac{1}{\Gamma(\alpha)} \int_a^t (t-\tau)^{\alpha-1} u(\tau) \mathrm{d}\tau \tag{2.17}$$

where $\Gamma(\alpha)$ is the gamma function and $\mathcal{D}$ is the differential operator. The use of the fast Fourier transform (FFT) (Cooley and Tukey, 1965) allows spectral methods to be implemented efficiently, with $O(n \log n)$ scaling in computational complexity (n is the bin size), compared to $O(n^2)$ for the discrete Fourier transform (DFT).

The FT assumes periodic boundaries. A non-periodic boundary represents a discontinuity, which yields non-physical high-frequency Gibbs phenomena in the frequency domain. Several options are available to overcome this limitation, the simplest of which is to mirror the signal in order to make it periodic, or to use a windowing function. However, this may not always be feasible or practical. A more involved alternative is based on the use of Chebyshev polynomials, which increases the concentration of grid points near the boundaries.

Spectral methods can be applied to non-linear problems by using the split-step Fourier method, based on the semi-discrete form of the PDE. Non-linear terms are treated in the time domain, and linear terms are treated in the frequency domain. This method benefits from the simple and efficient treatment of derivatives as algebraic equations in the frequency domain. Spectral methods also suffer from non-physical oscillations (i.e. the Gibbs phenomenon) near discontinuities, posing difficulties for hyperbolic PDEs involving shocks, such as Burgers' equation. Godunov's theorem (Godunov, 1954) states that linear numerical schemes for solving partial differential equations, having the property of not generating new extrema (i.e. a monotone scheme), can be at most first-order accurate. On the other hand, spectral methods are essentially $O((\Delta x)^n)$ accurate. Filtering methods can be used as a post-process to remove these non-physical oscillations. A more detailed review of pseudo-spectral methods is provided by Fornberg (1998).

2.7.1.5 Summary

An overview of the main discretisation schemes has been carried out. The FD, FV and FE methods are in some cases equivalent for 1-D equispaced grids. The FDM is the simplest discretisation strategy to implement for 1-D non-linear problems. Higher-order accuracy can easily be achieved by extending the stencil size to include more nodes. Spectral methods using the FT offer excellent numerical accuracy and computational efficiency. They are very simple to implement for linear, periodic and discontinuity-free systems. The FVM is desirable when scaling to two and three dimensions for both linear and non-linear problems involving conservation laws, particularly for complex geometries.

2.7.2 ODE Integration

A system of ODEs is produced once the RHS of the PDE system has been discretised (see Equation 2.11) using any of the methods listed in § 2.7.1. The simplest ODE integration technique is the first order accurate explicit Euler method. Increased stability (discussed at the end of this section) can be obtained at the expense of increased computational cost by using the implicit Euler method, which requires the solution of a system of equations at each iteration. Implicit methods allow for a larger stable step size to be taken compared to explicit methods and are more robust in the presence of numerical stiffness (as discussed below).

The Euler method belongs to the family of implicit/explicit Runge-Kutta methods (see Ascher and Petzold, 1998; Ferziger and Peric, 2012). These methods require multiple intermediate steps in order to reach the next step, which are then disregarded for subsequent calculations. Alternatively, linear multi-step methods may be more efficient for computationally expensive problems, as they re-use the information from previous time steps. Examples of multi-step methods are the backwards differentiation formulas (BDF) (Gear, 1971) and Adams-Bashforth/Moulton.

The limitation of explicit techniques is poor performance and stability in the presence of stiffness, typically leading to the requirement of an extremely small

time step. A stiff system is generally characterised by the inclusion of terms which lead to rapid variations in the solution. The step size is constrained by the stability requirements of these rapidly varying terms, rather than accuracy. The issue of numerical stiffness is covered in greater detail by Shampine and Gear (1979).

One measure of the stability of a system is its A-stability. This requires that the test problem, $\mathrm{d}u/\mathrm{d}t = ku$, where k is a constant, subject to $\Re(k) < 0$ with the initial condition $u(0) = 1$ tends to zero as $t \to \infty$. A more stringent condition is L-stability, where the solution to this problem approaches zero in a single step, as $\Delta t \to \infty$. The L-stability regions of implicit methods tend to be much larger than explicit methods.

Amongst the most popular implicit multi-step methods for the solution of stiff systems is the family BDFs, the simplest of which is the implicit Euler method. These are zero-stable (i.e. the numerical approximation does not diverge away from the true solution when small perturbations are applied to the initial conditions) up to 6th order accuracy. However, A-stability is only possible to attain for up to second order accuracy for linear multi-step methods.

2.7.3 Overview of OpenFOAM

OpenFOAM (Open source Field Operation and Manipulation) (Weller and Tabor, 1998) is used in this work for the purpose of 2-D and 3-D CFD modelling. It is an open source, object-orientated, FV based C++ library for the numerical solution of PDEs. Even though OpenFOAM is most well-known for CFD applications, it has been applied to other disciplines (e.g. fluid-structure interaction, solid mechanics), and it has been adopted by academic institutions and industries.

Proprietary codes which are commonly used for CFD include ANSYS Fluent, CD-adapco STAR-CCM+, and COMSOL Multiphysics. In comparison, OpenFOAM has no licensing restrictions and provides a greater degree of flexibility in how it is used. For example, the source code can be reviewed and modified in order to incorporate new functionality, which can be provided back to the research community.

OpenFOAM includes pre and post-processing utilities, as well as solvers for a wide range of problems (e.g. compressible, incompressible, multiphase, mesh motion, fluid-structure interaction, etc.). The syntax for the treatment of tensors and PDEs is similar to the equations being solved. For example, the equation (Greenshields, 2015):

$$\frac{\partial \rho \mathbf{U}}{\partial t} + \nabla \cdot \phi \mathbf{U} - \nabla \cdot \mu \nabla \mathbf{U} = -\nabla p \tag{2.18}$$

where $\mathbf{U}$ is a vector field, and ϕ and ρ are scalar fields, is represented by the code:

```
solve
 (
     fvm::ddt(rho, U)
   + fvm::div(phi, U)
   - fvm::laplacian(mu, U)
     ==
   - fvc::grad(p)
 );
```

where the `fvm::` finiteVolumeMethod and `fvc::` finiteVolumeCalculus classes distinguish between functions which calculate implicit and explicit derivatives, respectively.

The drawbacks of OpenFOAM over the proprietary codes mentioned above include a steep learning curve due to the absence of a graphical user interface (although proprietary versions support this, e.g. Engys HELYX and simFlow) and inconsistent documentation. In addition, experience with object orientated programming and C++ is required if the user wishes to add new functionality. More information relating to pre and post-processing utilities, as well as code structure, discretisation implementation, and so on can be found in the literature (e.g. Jasak, 1996; Moukalled et al., 2015).

2.8 Optimisation Algorithms

Optimisation is used in this work to refine the geometry of the countermeasures listed in § 2.6 for a specific tunnel system. This section is intended to briefly acquaint the reader with the most relevant aspects of this mathematical discipline. The reader is directed to the literature (see Chong and H. Zak, 2013) for a more detailed review. The goal of optimisation is to find the value of the independent variables which maximise or minimise an objective function. By systematically varying the input parameters it may be possible to find local minima, or the global minimum of the function across the search-space. Clearly, the greater the number of variables (higher dimensionality), the more complex the optimisation problem will become and the longer it will take to converge.

For simplicity, optimisation algorithms are divided into two classes in this work: deterministic (finitely terminating and convergent) and heuristic algorithms. Deterministic algorithms are able to guarantee convergence towards the global minimum within a certain tolerance. Deterministic algorithms typically make use of additional information about the objective function, such as the Jacobian (first order partial derivative of a vector function), or the Hessian (second order partial derivative of a scalar function), in order to dictate the direction of search where the minimum is likely to be located. Popular deterministic algorithms include linear/non-linear programming, the simplex algorithm and Newtons method.

Alternatively, heuristic methods do not guarantee convergence to the minima but can provide a solution which is sufficient for the user, given the complexity of the problem. Examples of heuristic optimisation algorithms include Evolutionary algorithms and Simulated annealing. These particular techniques also come under the umbrella of stochastic methods. Many practical engineering problems tend to involve highly non-linear and discontinuous objective functions, where it may not be possible to infer more information about the underlying nature of the algorithm, e.g. the gradient or the Hessian. In these cases, the objective function is essentially a “black box” and derivative-free optimisation methods must be used.

2.9 Conclusions

A comprehensive overview of the relevant pressure wave related phenomena of high-speed rail operations in tunnels has been carried out. The following topics have been discussed: (1) aerodynamic phenomena in tunnel operations and the resultant operational issues; (2) relevant numerical and optimisation techniques that are employed in this work. A summary of the existing countermeasures for pressure wave related phenomena in tunnel operations is provided and their limitations are identified. New countermeasures for the emission of micro-pressure waves from the tunnel exit and other connections to atmosphere are suggested, namely: (1) an array of Helmholtz resonators; (2) modifying the tunnel-branch junction geometry; (3) installing a reactive silencer at tunnel portals.

It is proposed that these new countermeasures will be particularly useful for future high-speed rail projects involving long concrete slab track tunnels (due to non-linear steepening) and very high operating speeds. This work seeks to find out if existing countermeasures (e.g. nose shape optimisation and tunnel entrance hoods) may be efficiently augmented using the aforementioned countermeasures under these conditions.

An array of Helmholtz resonators has been proposed for counteracting non-linear wave steepening and environmental noise in tunnels in the literature (see § 2.6.1). However, the application and effectiveness of this concept has not been explored in much detail from a practical standpoint. Countermeasures for branch MPWs have been considered in the literature (see § 2.6.3). Modifying the tunnel-branch geometry is suggested in this work as a way to mitigate the issue of ventilation posed by other potential countermeasures. Finally, installing a reactive silencer at the tunnel exit (or branch portals) has been proposed in the literature and is already used in other fields (e.g. firearm suppressors, exhaust mufflers). However, the effectiveness of a tunnel exit silencer in a real-world application has not been considered in much detail.

Chapter 3

Numerical Model for an Array of Helmholtz Resonators

3.1 Introduction

In Chapter 2 an array of Helmholtz resonators was proposed as an effective countermeasure for the emission of micro-pressure waves from the exit of concrete slab track tunnels. The array allows for the dispersive properties of ballast track to be combined with the superior maintainability of concrete slab track.

This chapter presents the development of a numerical framework for predicting the propagation of pressure waves in a tunnel connected to an array of Helmholtz resonators. The model must be accurate and fast, in order to allow for optimisation to be used. The layout and aims of the chapter are as follows. An overview of the theory of Helmholtz resonators and a reduced-order physical model for an array of Helmholtz resonators is presented in § 3.2. The assumptions of the model are justified in the context of high speed rail operations in tunnels. An efficient and accurate numerical scheme is then applied to the system in § 3.3. Finally, improvements to the model are proposed in § 3.4, in order to remove several underlying assumptions.

3.2 Physical Model Development

3.2.1 System Overview

The system studied in this chapter consists of a duct connected via a neck to an array of Helmholtz resonators. The geometric parameters of the resonator array are the hydraulic diameter, d; length, l; and height, h. The radius, r, is expressed as half of the hydraulic diameter. Derived parameters are the volume, V and cross-section area, S. Subscripts are used to denote the cavity, c; neck, n; tunnel, t; array, a; and the train, z.

The calculated physical parameters of the model are the thermal dissipation in the boundary layer, $\mathcal{C}$; density at equilibrium, ρ_0; linear speed of sound, a_0; characteristic angular frequency, ω; diffusivity of sound, ν_d; and the linear acoustic pressure in the tunnel, p_t, These parameters are defined by:

$$\begin{aligned} &\mathcal{C} = 1 + \frac{\gamma - 1}{\sqrt{\mathrm{Pr}}}, \quad \rho_0 = \frac{p_0}{\mathcal{R} T_0}, && a_0 = \sqrt{\frac{\gamma p_0}{\rho_0}}, \\ &\omega = 2\pi\upsilon, && \nu_\mathrm{d} = \nu\left(\frac{4}{3} + \frac{\mu_\mathrm{d}}{\mu} + \frac{\gamma - 1}{\mathrm{Pr}}\right), \quad \frac{p_\mathrm{t}}{p_0} = \gamma\frac{u}{a_0} \end{aligned} \tag{3.1}$$

where $\mathcal{R}$ is the individual gas constant, T_0 is the ambient temperature, γ is the ratio of specific heats, υ is the linear characteristic frequency, Pr is the Prandtl number, μ_d/μ is the ratio of shear and bulk viscosities, ν is the kinematic viscosity and u is the particle velocity in the tunnel.

3.2.1.1 Idealised Helmholtz Resonator Array

Helmholtz resonance occurs when a fluid passes over a port opening connected to a closed cavity. The fluid volume near to, and in the neck, vibrates due to the alternating compression and expansion of the fluid in the cavity. A Helmholtz resonator is analogous to a lumped mass-spring-damper system (see Figure 3.1), assuming that the maximum dimension of the resonator is much less than the acoustic wavelength. The compressible fluid in the cavity represents a spring connected to the fluid mass in the neck, while damping occurs through friction in

the neck. The linear ODE for this system, assuming a harmonic response, is:

$$M\frac{\mathrm{d}z^2}{\mathrm{d}t^2} + C\frac{\mathrm{d}z}{\mathrm{d}t} + Kz = Fe^{iwt} \tag{3.2}$$

where z and $M = \rho_0 S_\mathrm{n} l_\mathrm{e}$ are the displacement and mass of the fluid in the neck, $K = (\rho_0 a_0^2 S_\mathrm{n}^2)/V_\mathrm{c}$ and C are the stiffness and damping coefficients and F is the forcing amplitude. The un-damped natural angular frequency of the resonator under no excitation force is then:

$$\omega_0^2 = \frac{K}{M} = \frac{S_\mathrm{n} a_0^2}{l_\mathrm{n} V_\mathrm{c}} \tag{3.3}$$

3.2.1.2 End Corrections

The angular frequency of the resonator in Equation 3.3 must be corrected to account for evanescent higher-order modes, which are excited when sound waves encounter a discontinuous change in cross-sectional area (e.g. between the resonator neck and the cavity). These high frequency waves decay exponentially with distance from the source when they are cut-off (see § 2.2.1). Under plane wave propagation the effect of the evanescent modes are observed as a phase shift in the reflection coefficient ($R = p_\mathrm{r}/p_\mathrm{i}$, where p_r and p_i are the reflected and incident wave amplitude, respectively) and can be incorporated as an acoustic end correction. The effective neck length including the end corrections is given by:

$$l_\mathrm{e} = l_\mathrm{n} + \delta_\mathrm{nt} + \delta_\mathrm{nc} \tag{3.4}$$

where δ_nc and δ_nt are the neck-cavity and neck-tunnel end corrections, respectively. The effective natural angular frequency of the resonator is given by replacing l_n with l_e in Equation 3.3:

$$\omega_\mathrm{e}^2 = \frac{S_\mathrm{n} a_0^2}{l_\mathrm{e} V_\mathrm{c}} \tag{3.5}$$

The neck-cavity correction length for a circular un-flanged end is defined in the

limit of $k_0 r_\mathrm{n} \to 0$ (where $k_0 = \omega/a_0$ is the wave number) by (Levine and Schwinger, 1948):

$$\frac{\delta_\mathrm{nc}}{r_\mathrm{n}} = 0.6133 \tag{3.6}$$

This correction is used for the geometry in Figure 3.2. Alternatively, the correction for a concentric flanged end (as seen in Figure 3.1a) is given for $r_\mathrm{n}/r_\mathrm{c} \leq 0.4$ by (Equation 21 of Selamet and Ji, 2000):

$$\frac{\delta_\mathrm{nc}}{r_\mathrm{n}} = 0.82\left(1 - 1.33\frac{r_\mathrm{n}}{r_\mathrm{c}}\right) \tag{3.7}$$

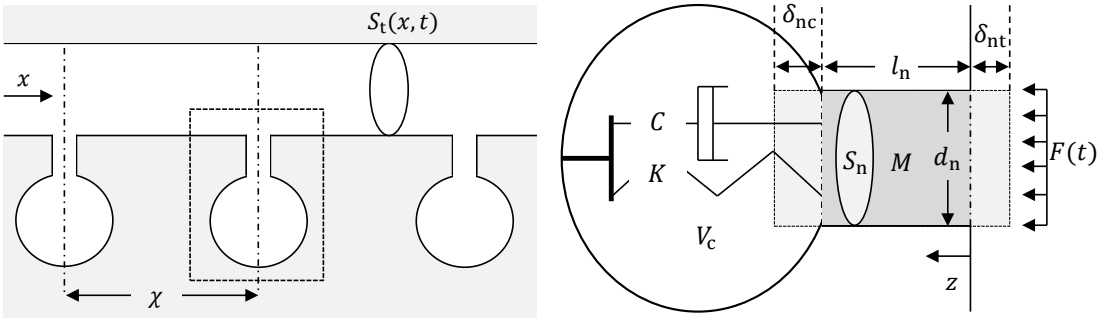
where r_c is the radius of the cavity, which is assumed as half the hydraulic diameter for a non-circular cavity. The neck-tunnel correction length for a flanged can be calculated empirically by (Ji, 2005):

$$\frac{\delta_\mathrm{nt}}{r_\mathrm{n}} = \begin{cases} 0.8216 - 0.0644\left(r_\mathrm{n}/r_\mathrm{t}\right) - 0.694\left(r_\mathrm{n}/r_\mathrm{t}\right)^2, & \text{if } r_\mathrm{n}/r_\mathrm{t} \leq 0.4. \\ 0.9326 - 0.6196\left(r_\mathrm{n}/r_\mathrm{t}\right), & \text{if } r_\mathrm{n}/r_\mathrm{t} > 0.4. \end{cases} \tag{3.8}$$

The simple resonator model in this section is extended to account for the difference in the flow pattern either side of the neck and adiabatic compression in the cavity in § 3.2.3. The Helmholtz resonator functions as a band-stop filter by attenuating the sound power over a frequency range. Attenuation is minimal outside of the resonator bandwidth frequency and the reflection coefficient is approximately zero. In contrast, the attenuation of the incident wave is maximised at the natural frequency.

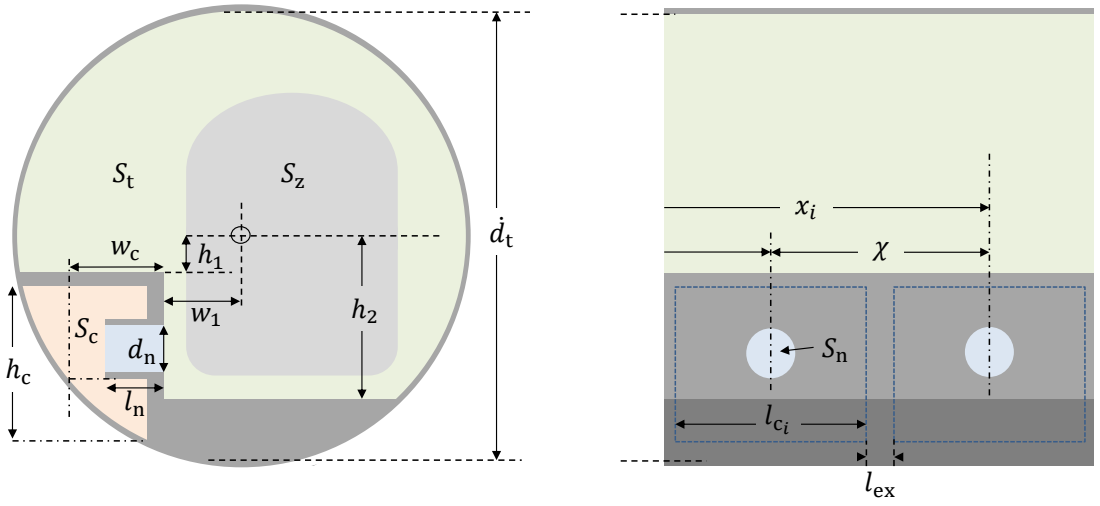
3.2.1.3 Representative System

The representative system considered in this work consists of a tunnel connected via a neck to an array of Helmholtz resonators (see Figure 3.2). Note that the



(a) Overview of array (b) Equivalent lumped parameter resonator

Figure 3.1: Idealised array of Helmholtz resonators connected to a duct.



(a) front, $y-z$ (b) side, $x-y$, $i=1,N_c$

Figure 3.2: Demonstrative tunnel cross-section (not to scale) with resonators under side walk-way. The necks are located at the centre of the cavity. Note: $\dot{d}_t$ refers to the bore diameter and not the hydraulic diameter. Refer to § 5.2.2.

geometry of the cross-section is not to scale and the size of the cavities has been exaggerated for illustrative purposes. The resonators are embedded in redundant tunnel space (e.g. beneath maintenance access walkways, or under the track, given sufficient space) to avoid reducing the cross-section of the tunnel, S_t. More information is provided regarding the design of the array in § 5.2.

3.2.2 Assumptions

The modelling approach follows the work of Sugimoto (1992) and Lombard and Mercier (2014). Several assumptions are made which allow the full physical com-

plexity of this problem to be reduced without comprising the physical accuracy of the predictions. Therefore, simplified 1-D models can be used instead of 3-D CFD. The assumptions of the physical model are stated in this section and dimensionless parameters are introduced to indicate whether they are satisfied. The validity of the assumptions are then considered for the full-scale tunnel system in Figure 3.2.

Plane wave propagation

Plane wave (1-D) propagation under the low frequency approximation can be assumed provided the characteristic acoustic frequency is less than the first non-planar cut-on frequency (see § 2.2.2). The plane wave cut-off frequency for a circular duct, $\upsilon_c = 1.84a_0/(\pi d_t)$ (Munjal, 2014), is used for simplicity. The plane wave parameter is then given by:

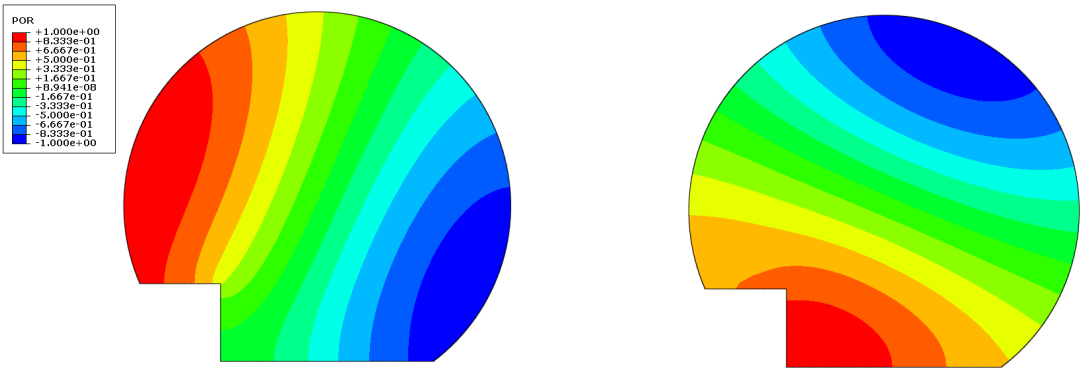
$$\varphi = \frac{\upsilon}{\upsilon_c} \approx 1.71\frac{d_t}{\lambda} < 1 \tag{3.9}$$

The plane wave cut-off frequency for a circular duct was found to be within $\sim 10\%$ of the value predicted from a 2-D eigenvalue analysis for the tunnel section in Figure 3.2, with the geometric parameters in Table 3.1. The eigenvalue analysis was carried out using Abaqus standard (Dassault Systèmes, 2011). The first two non-planar modes and corresponding cut-on frequencies (see Figure 3.3) are nearly identical to the circular duct modes.

Further consideration of the cut-on frequencies is required for tunnel sections which strongly differ from a circle. The first non-planar cut-on mode/frequency can be found using an eigenvalue analysis of the tunnel section. This is compared to a frequency decomposition of the expected incident wavefront in order to assess whether the dominant frequencies (i.e. the characteristic frequency) lie below the plane wave cut-off frequency.

Weak acoustic non-linearity

The framework of weakly non-linear acoustic theory can be used on the condition that the amplitude of a pressure disturbance from the ambient pressure is relatively



(a) $\upsilon_c = 26.0$ hz (b) $\upsilon_c = 29.4$ hz

Figure 3.3: Normalised acoustic pressures (by the maximum pressure) for the first two non-planar cut-on frequencies for the reference tunnel cross-section, with the dimensions given in Table 3.1.

small ($p/p_0 \ll 1$, see § 2.2.2). Therefore, the acoustic Mach number must also be small ($M \ll 1$). The Mach number is multiplied by $\frac{1}{2}(\gamma+1)$ for convenience when considering the propagation of weakly non-linear waves in a duct (see § 3.2.3). The weak non-linearity parameter is then given by:

$$\epsilon = \frac{\gamma+1}{2} M \ll 1 \tag{3.10}$$

To relate Equation 3.10 to tunnel operations, the acoustic Mach number is replaced by the linear acoustic pressure in the tunnel, as given by Equation 3.1. It is assumed that $p_t \approx p_1$, where p_1 is the maximum pressure rise of the entry compression wave, which gives:

$$\epsilon \approx \frac{\gamma+1}{2\gamma} \frac{p_1}{p_0} \tag{3.11}$$

The value of p_1 is predicted using Equation 2.7 and so the non-linearity parameter is now a function of the tunnel blockage ratio, β, and the train velocity, u_z. In most high-speed rail tunnel systems $\beta < 0.3$, whilst 600 km/h is approximately the maximum speed record (as of 2015) set by the magnetically levitating Shinkansen being developed in Japan (BBC, 2015). Therefore, $\epsilon \approx 0.13$ for this extreme operating regime. The validity of the 1-D model for large values of the non-linearity parameter is considered in Chapter 4.

Negligible reflection and interaction between resonators

The original model proposed by Sugimoto (1992) considers cavities with a very small volume, V_c, compared to the waveguide, per axial spacing between the resonator necks, χ (see Figure 3.1a). This is quantified by the parameter:

$$\kappa = \frac{V_c}{S_t \chi} \ll 1 \tag{3.12}$$

A sufficiently small value of κ indicates that the array is acoustically compact and so there is a negligible degree of interaction between neighbouring resonators. The size of the equation system can then be reduced by disregarding the effect of reflected waves propagating in the upstream direction. Additionally, the reflected waves are not of interest for the purpose of this work. This assumption is expected to be conservative as realistically a portion of the acoustic energy is reflected by each resonator, attenuating the transmitted waves.

A worst-case (conservative) approximation for the value of κ is derived in order to justify this assumption for the tunnel geometry considered in this work (see Figure 3.2). The volume of the cavity accounting for the resonator neck is given by $V_c = S_c l_c - S_n l_n$. The cavity spacing interval for a constant (or near-constant) cavity length is $\chi = l_c + l_{ex}$, where l_{ex} is additional spacing between two successive cavity boundaries. Substituting these equations into Equation 3.12 gives after some rearrangement:

$$\kappa = \frac{V_c}{S_t \chi} = \left(\frac{S_c}{S_t}\right)\left(\frac{l_c}{l_c + l_{ex}}\right)\left[1 - \frac{S_n l_n}{S_c l_c}\right]$$

where $(S_n l_n)/(S_c l_c) = V_n/V_c < 1$. A conservative assumption of $V_n/V_c \ll 1$ gives:

$$\kappa \approx \left(\frac{S_c}{S_t}\right)\left(\frac{1}{1 + l_{ex}/l_c}\right)$$

If $l_{ex}/l_c \ll 1$ (i.e. negligible inter-cavity spacing), then a simple to interpret and

conservative approximation for κ is obtained:

$$\kappa \approx \frac{S_c}{S_t} \tag{3.13}$$

It is anticipated that the cross-sectional area of the cavities of the type shown in Figure 3.2 will be restricted for most tunnel systems, and so $S_c/S_t \ll 1$. As a result, the volume of the cavities is largely controlled by the cavity length, l_c. The effect of parameter κ on the solution is considered in § 4.3.

Continuum distribution of resonators

The original model of Sugimoto (1992) simplifies the discrete response of each resonator to a spatially averaged distribution along the length of the array, on the condition that the spacing between then resonators is much smaller than the characteristic wavelength:

$$\sigma = \frac{\chi}{\lambda} \ll 1 \tag{3.14}$$

Consequently, wave interactions between the resonators are ignored and the array responds in unison to local pressure disturbances. This is acceptable for the purpose of this work, provided that the acoustic power of the reflected waves is smaller than the transmitted waves (governed by parameter κ) and we are only interested in waves propagating downstream. An illustration of the relation between parameters κ and σ is shown in Figure 3.4. The effect of parameter σ on the solution is studied in greater detail in § 3.4.1.

Lumped parameter model for the resonator response

The predicted response of the resonator is valid provided that its maximum dimension is much less than the characteristic wavelength:

$$\varpi = \frac{1}{\lambda} \max(l_c, h_c, w_c) \ll 1 \tag{3.15}$$

This parameter has been introduced specifically for the tunnel geometry in Fig-

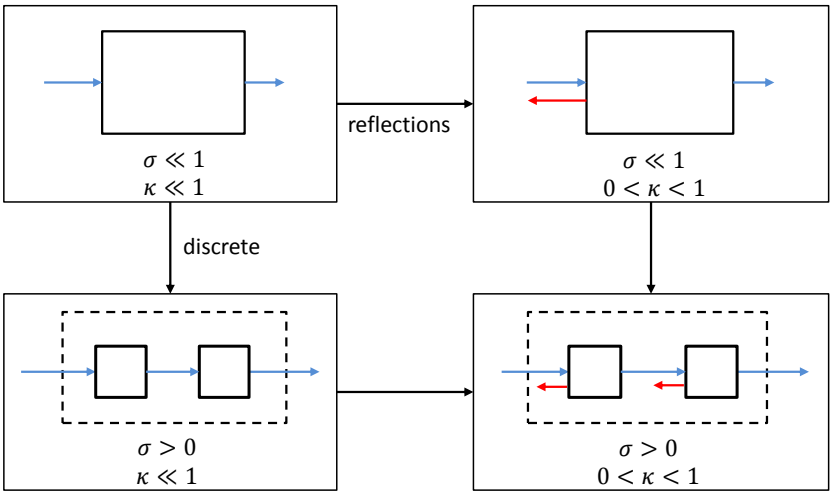


Figure 3.4: Illustration of the underlying assumptions of a continuum distribution of resonators and negligible interaction between neighbouring resonators.

ure 3.2, as the characteristic wavelength of the incident waveform may be comparable to the cavity length. The cavity length is the main parameter for controlling the cavity volume, due to the limited cross-sectional area of the cavities. This assumption simplifies the spatio-temporal response of each resonator to a time dependent ODE and ignores the finite wave propagation time in the cavity. The response of the cavity is also assumed to be independent from its internal geometry. Standing waves can occur when the length of the cavity is equal to an odd integer number of quarter wavelengths of the resonator natural frequency. The effect of violating the lumped element approximation is considered in § 4.3.4.

3.2.2.1 Summary

The threshold of these dimensionless parameters for which the assumptions no longer hold depends on the required accuracy of the simulation. This can be found through comparison with experiments, 3-D CFD, or the 1-D model where the assumptions have been removed. These parameters are considered in greater detail in § 4.2.2 and § 4.3.

3.2.3 Continuum Near-Field Model

The basic system consists of two coupled fractional order differential equations: a non-linear PDE describing the downstream propagation of acoustic waves in a waveguide, and a non-linear ordinary differential equation (ODE) describing oscillations within a Helmholtz resonator (Lombard and Mercier, 2014; Sugimoto, 1992):

$$\frac{\partial u}{\partial t} + \frac{\partial}{\partial x}\left(Au + B\frac{u^2}{2}\right) = \bar{C}\frac{\partial^{-1/2}}{\partial t^{-1/2}}\frac{\partial u}{\partial x} - \bar{Q}u|u| + D\frac{\partial^2 u}{\partial x^2} - \bar{E}\left(1 - 2Hp_\mathrm{c}\right)\frac{\partial p_\mathrm{c}}{\partial t} \tag{3.16a}$$

$$\frac{\partial^2 p_\mathrm{c}}{\partial t^2} + F\frac{\partial^{3/2} p_\mathrm{c}}{\partial t^{3/2}} + Gp_\mathrm{c} - H\frac{\partial^2 p_\mathrm{c}^2}{\partial t^2} + I\left|\frac{\partial p_\mathrm{c}}{\partial t}\right|\frac{\partial p_\mathrm{c}}{\partial t} = Ju \tag{3.16b}$$

where u and p_c are the acoustic velocity in the waveguide and the pressure in the resonator cavity, respectively. Wave propagation in the tunnel (Equation 3.16a) accounts for:

- linear and weakly non-linear advection, A and B, respectively;
- viscous losses due quasi-steady and unsteady friction, C and Q, respectively;
- the diffusivity of sound due to viscosity and heat conduction, D;
- source term due to an array of Helmholtz resonators, E.

The non-linear resonator response in Equation 3.16b accounts for:

- unsteady viscous losses from the boundary layer of the neck of the resonator, F;
- adiabatic compression in the cavity up to second order non-linearity, H;
- dissipation from the periodic formation of jets at the ends of the resonator neck, I.

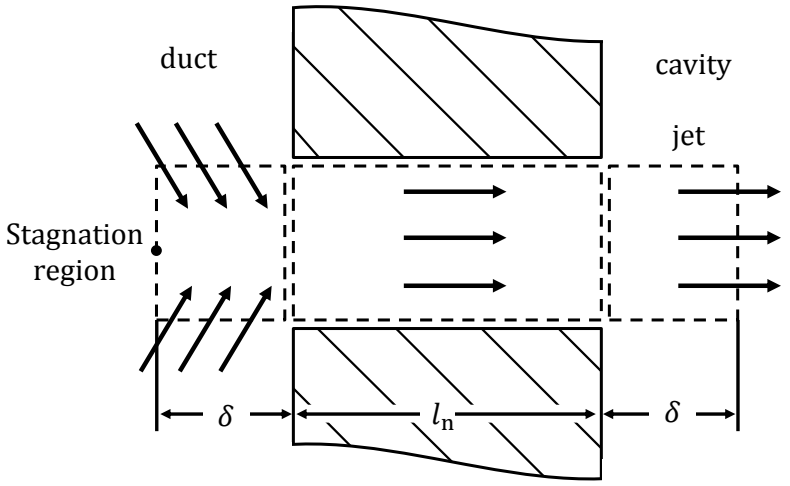


Figure 3.5: Illustration of the flow field in the resonator neck.

Coupling between the two equations can be removed by setting coefficient $E = 0$, which implies no resonators are attached. The definition of weak acoustic non-linearity in Equation 3.10 can be rationalised by considering the advection term in Equation 3.16a, where $\epsilon = (Bu)/A \ll 1$.

Equation 3.16a differs from Sugimoto's original form through the incorporation of quasi-steady friction from the model of Ozawa et al. (1993). Ozawa's model is used to predict the distortion of compression waves in a tunnel with ballast track. It is noted that Equation 3.16b may under-predict dissipation for a rough neck surface, as quasi-steady friction in the resonator neck is not considered. The unsteady friction accounts for the laminar boundary layer to a first-order approximation.

The term with coefficient I accounts for the difference in the inflow and outflow patterns at the resonator neck by incorporating a length correction (see Figure 3.5). Absolute values are used for the operators with coefficients Q and I, in order to account for the alternating flow direction in the neck. Viscous forces arising from jet formation are of second order in magnitude and can be neglected (see Zinn, 1970).

Coefficients C, Q, and E use the over-bar to show that they are averaged over the interval of the resonators ($x = -\chi/2$ to $\chi/2$, also see Equation 3.65), in order to fulfil the continuum approximation. A general form of Equation 3.16a considering

a discrete treatment of the resonators and bi-directional wave propagation is given by Mercier and Lombard (2016) (see § 3.4.1). The coefficients are defined by:

$$\begin{aligned} A &= a_0, & B &= \frac{\gamma+1}{2}, & \bar{C} &= \frac{\mathcal{C} a_0 \sqrt{\nu}}{r_\mathrm{t}^*}, & D &= \frac{\nu_\mathrm{d}}{2} \\ \bar{E} &= \frac{V_\mathrm{c}}{2\rho_0 a_0 S_\mathrm{t} \chi}, & F &= \frac{2 l_\mathrm{n}' \nu^{1/2}}{l_\mathrm{e} r_\mathrm{n}}, & G &= \omega_\mathrm{e}^2, & H &= \frac{\gamma-1}{2\gamma p_0} \\ I &= \frac{V_\mathrm{c}}{S_\mathrm{n} l_\mathrm{e} \rho_0 a_0^2}, & J &= \frac{\omega_\mathrm{e}^2 \gamma p_0}{a_0}, & \bar{Q} &= \frac{f_\mathrm{D}}{8 r_\mathrm{t}^*} \end{aligned} \tag{3.17}$$

where $l_\mathrm{n}' = l_\mathrm{n} + 2r_\mathrm{n}$ incorporates viscous end corrections due to the inertia of the oscillating mass of fluid in the neck (see Figure 3.5). The reduced tunnel radius, r_t^*, accounts for the effect of a continuous distribution of resonator connections on the boundary layer of the tunnel:

$$r_\mathrm{t}^* = r_\mathrm{t} \Big/ \left(1 - \frac{r_\mathrm{n}^2}{2\chi r_\mathrm{t}}\right) \tag{3.18}$$

Therefore, $r_\mathrm{t}^* \to r_\mathrm{t}$ as $\chi \to \infty$ for the case of sparsely distributed resonator necks. However, large values of χ violate the continuum distribution and/or the lumped element approximations (for long cavities). The half-order fractional integral is given by the RL integral in Equation 2.17, with $\alpha = 1/2$:

$$\frac{\partial^{-1/2}}{\partial t^{-1/2}} u(t) = \frac{1}{\sqrt{\pi}} \int_0^t (t-\tau)^{-1/2} \, u(\tau) \mathrm{d}\tau \tag{3.19}$$

Derivatives of orders 1/2 and 3/2 are found by differentiating Equation 3.19 once and twice respectively, with respect to t. The fractional derivative is causal (non-local) as it requires the entire time-history to be integrated. In contrast, integer-order derivatives can be evaluated using a local stencil over adjacent nodal points. The evaluation of fractional order derivatives is discussed in greater detail in § 3.3.1.

The Darcy-Weisbach friction factor, f_D in coefficient Q, is found for fully developed turbulent flows (Re $>$ 4000) by using the implicit equation given by

(Colebrook and White, 1937):

$$\frac{1}{\sqrt{f_\mathrm{D}}} = -2\log\left(\frac{h_\mathrm{wall}}{3.7d_\mathrm{t}} + \frac{2.51}{\mathrm{Re}\sqrt{f_\mathrm{D}}}\right) \tag{3.20}$$

where h_wall is the effective roughness height of the tunnel surface. This value is estimated to range from 0.3 to 5 mm for various concrete finishes (The Engineering Toolbox, 2016). The region of the boundary layer excited by the compression wave may be undergoing transition, due to the short time-scales involved. In the turbulent regime the steady friction component is proportional to p_t^2 ($p_\mathrm{t} = u$ for a plane wave), as used in Equation 3.16a. However, for a purely laminar boundary layer, steady friction is proportional to the acoustic pressure in the tunnel. Miyachi et al. (2016) considered a "quasi-laminar model" to account for this discrepancy, which matches well with experimental data for pressure waves in tunnels.

3.2.4 Continuum Far-Field Model

This study is only interested in the local distortion of the initial pressure wave as it propagates along the array. It is assumed that the tunnel is infinitely long and that there are no sources of wave reflection, except for the array. Therefore, a change in the reference frame to one moving with the ambient speed of sound (called the far field from here-on) can be used. This confines the domain to the region around the propagating wavefront. The resulting system is written in $(\mathcal{X}, \mathcal{T})$ coordinates, where $\mathcal{X}$ and $\mathcal{T}$ are dimensionless retarded space and time variables, respectively:

$$\mathcal{T} = \omega\left(t - \frac{x}{a_0}\right), \qquad \mathcal{X} = \epsilon\omega\frac{x}{a_0} \tag{3.21}$$

The dimensionless variables f and g of $O(1)$ are also used:

$$f = \frac{1}{\epsilon}\frac{\gamma+1}{2}\frac{u}{a_0} = \frac{1}{\epsilon}\frac{\gamma+1}{2\gamma}\frac{p_\mathrm{t}}{p_0}, \quad g = \frac{1}{\epsilon}\frac{\gamma+1}{2\gamma}\frac{p_\mathrm{c}}{p_0} = \frac{p_\mathrm{c}}{p_\mathrm{t}}f \tag{3.22}$$

Under the approximation of weak non-linearity the substitution of the linear ad-

vection equation in the downstream direction, $\partial u/\partial x = -(1/a_0)\partial u/\partial t$, is made in terms with coefficients B, $\bar{C}$, and D in Equation 3.16. The change of variables in Equation 3.22 is then made, giving a modified form of the PDE system originally proposed by Sugimoto (1992):

$$\frac{\partial f}{\partial \mathcal{X}} - f\frac{\partial f}{\partial \mathcal{T}} = -\bar{\delta}_\mathrm{t}\frac{\partial^{1/2} f}{\partial \mathcal{T}^{1/2}} - \bar{\tau} f|f| + \beta\frac{\partial^2 f}{\partial \mathcal{T}^2} - \bar{K}\left(1 - 2U\epsilon g\right)\frac{\partial g}{\partial \mathcal{T}} \tag{3.23a}$$

$$\frac{\partial^2 g}{\partial \mathcal{T}^2} + \delta_\mathrm{n}\frac{\partial^{3/2} g}{\partial \mathcal{T}^{3/2}} + \Omega g = \Omega f + \epsilon\left[U\frac{\partial^2 g^2}{\partial \mathcal{T}^2} - W\left|\frac{\partial g}{\partial \mathcal{T}}\right|\frac{\partial g}{\partial \mathcal{T}}\right] \tag{3.23b}$$

with the new parameters:

$$\begin{aligned} \bar{\delta}_\mathrm{t} &= \frac{\mathcal{C}}{\epsilon r_\mathrm{t}^*}\sqrt{\frac{\nu}{\omega}}, \quad \beta = \frac{\nu_\mathrm{d}\omega}{2\epsilon a_0^2}, \quad \bar{K} = \frac{V_\mathrm{c}}{2S_\mathrm{t}\chi\epsilon}, \quad \delta_\mathrm{n} = \frac{2l'_\mathrm{n}}{l_\mathrm{e} r_\mathrm{n}}\sqrt{\frac{\nu}{\omega}} \\ \Omega &= \left(\frac{\omega_\mathrm{e}}{\omega}\right)^2, \quad U = \frac{\gamma - 1}{\gamma + 1}, \quad W = \frac{2V_c}{(\gamma+1)\,S_\mathrm{n} l_\mathrm{e}}, \quad \bar{\tau} = \frac{f_\mathrm{D} a_0}{4r_\mathrm{t}^*\omega(\gamma+1)} \end{aligned} \tag{3.24}$$

where δ_t and δ_n are the ratios of the boundary-layer thickness to the tunnel and neck radius, respectively. The over-bar is used again to denote spatially averaged quantities for K, τ, and δ_t over the resonator interval. The linear resonator response is recovered when $U = W = 0$ in Equation 3.23b and the neck length corrections are discounted (i.e. $l_\mathrm{e} = l'_\mathrm{n} = l_\mathrm{n}$).

A scale analysis of the dissipative terms β, δ_t, and δ_n has been studied in the linear regime by Sugimoto (1991, 1992), where the effect of β was found to be negligible. The system was found to be governed mainly by the ratio of geometric dispersion, K, and the tuning parameter, Ω. A scale analysis of the non-linear system is carried out based on full-scale tunnel geometry in § 5.4.

3.2.4.1 Limit Cases

Sugimoto (1992) identified three extreme cases for the inviscid far-field system, assuming a linear resonator response. Firstly, in the absence of the resonators $\bar{K} \ll 1$ or $\Omega \ll 1$. This leads to the inviscid Burgers' equation and the emergence

of shock waves over a sufficiently large propagation distance:

$$\frac{\partial f}{\partial \mathcal{X}} - f\frac{\partial f}{\partial \mathcal{T}} = 0 \tag{3.25}$$

Realistically, visco-thermal effects from the diffusivity of sound and the boundary layer of the tunnel will attenuate the wavefront and counteract wave steepening, particularly for steep wavefronts. In the second regime, $\bar{K} \gg 1$ and the system is dominated by the effect of the resonator array, giving the linear dispersive equation:

$$\frac{\partial f}{\partial \mathcal{X}} + \bar{K}\frac{\partial f}{\partial \mathcal{T}} + \frac{1}{\Omega}\frac{\partial^3 f}{\partial \mathcal{T}^2 \partial \mathcal{X}} = 0 \tag{3.26}$$

However, it is noted that the assumption of small resonator interaction ($\kappa \ll 1$) is violated for large values of κ, and hence $\bar{K}$. Finally, the Korteweg-de Vries equation (see Chapter 7 Linares and Ponce, 2014) is obtained when the characteristic frequency is much smaller than the natural frequency of the resonators ($\Omega \gg 1$). This equation permits the existence of acoustic solitary waves where dispersion (represented by the third-order derivative) competes with non-linear steepening:

$$\frac{\partial f}{\partial \mathcal{X}} + \bar{K}\frac{\partial f}{\partial \mathcal{T}} - f\frac{\partial f}{\partial \mathcal{T}} = \frac{\bar{K}}{\Omega}\frac{\partial^3 f}{\partial \mathcal{T}^3} \tag{3.27}$$

Equation 3.27 is similar to the equation used by Ozawa et al. (1993) (excluding viscous terms) to describe the propagation of compression waves through a tunnel with ballast track. The dispersive effect of ballast is comparable to the steepening process, whilst viscothermic losses are small for $\Omega \gg 1$ (Lombard and Mercier, 2014). Lombard et al. (2014) expanded Equation 3.27 to account for non-linear attenuation in the resonators, assuming that the volume of the resonator cavity is much larger than the neck ($W \gg U$):

$$\frac{\partial f}{\partial \mathcal{X}} + \bar{K}\frac{\partial f}{\partial \mathcal{T}} - f\frac{\partial f}{\partial \mathcal{T}} = \frac{\bar{K}}{\Omega}\frac{\partial^3 f}{\partial \mathcal{T}^3} + \frac{2\bar{K}W}{\Omega}\left|\frac{\partial f}{\partial \mathcal{T}}\right|\frac{\partial^2 f}{\partial \mathcal{T}^2} \tag{3.28}$$

Solitons are still expected to exist for solutions of this equation, but will be attenuated as they propagate.

3.3 Numerical Treatment

The far-field system has been identified as being more suitable for optimisation, as this study is primarily interested in the distortion of the initial pressure disturbance over the course of propagation. The number of grid-points required is generally reduced compared to the near-field model, as the entirety of the resonator array does not need to be modelled throughout the simulation. An efficient treatment of the fractional derivatives in Equation 3.23 is desired. At the same time, the computational cost should be minimised to make the scheme suitable for repeated function calls in optimisation.

MATLAB (2017) is used for the 1-D numerical treatment and optimisation procedure, due to its efficiency for code prototyping and excellent debugging capabilities. Alternative codes with support for differential algebraic equation (DAE) solvers and derivative free optimisation can also be used. It may be advantageous to port the code to a more computationally 'efficient' and non-proprietary programming language/environment in the future.

3.3.1 Fractional Derivatives

Several strategies are considered for evaluating the fractional derivatives in Equations 3.23 and 3.16.

3.3.1.1 Conventional Methods

The RL integral (Equation 3.19) and its derivatives (of orders 1/2 and 3/2) can be approximated using a quadrature scheme for an unknown function $u(t)$. For example, Oldham and Spanier (1974) proposed the L1 scheme for a uniform step size, Δt, and with an approximation accuracy of $O((\Delta t)^{2-\alpha})$ for $0 \leq \alpha \leq 1$ (Langlands and Henry, 2005). The L1 scheme is given by (Marinov et al., 2013):

$$\frac{\partial^\alpha}{\partial t^\alpha} u(t) \approx \frac{\Delta t^{-\alpha}}{\Gamma(2-\alpha)} \left[\frac{(1-\alpha)\, u(0)}{N^\alpha} + \sum_{i=1}^{N} a_i \left(u(t_{i+1}) - u(t_i) \right) \right] \tag{3.29}$$

where N is the number of data points and a_i are the quadrature weights for $i = 1, \ldots, N$, which are defined by:

$$a_i = (N - i + 1)^{1-\alpha} - (N - i)^{1-\alpha} \tag{3.30}$$

This algorithm is used by the Fractional Integration Toolbox (FIT) (Marinov et al., 2013) in MATLAB. FIT can re-use the calculated weights in order to improve the performance of the algorithm when it is called repeatedly (e.g. a simulation). Limitations of the L1 algorithm include a fixed step size and order of accuracy, as well as a high memory requirement and arithmetic cost per iteration, particularly for large datasets. Podlubny (1998) proposed the "short memory principle" to reduce the memory requirement, by excluding values in the past that are more than a pre-specified distance from the current time point. This gives a more efficient but generally inaccurate algorithm, as most of the time-history needs to be included to achieve reasonable accuracy.

Miyachi et al. (2016) and Sugimoto (1991) eliminate the singular point around $\tau = 0$ in Equation 3.19 by locally fitting a quadratic function to u. However, the methods used by these authors are limited to $O(\Delta\tau)$ and $O(\Delta\tau)^3$ accuracy, respectively. Alternatively, a simple and accurate method, on the condition of periodic boundaries, is to take the Fourier transform of the function, as described in § 2.7.1.4. Podlubny (2000) proposed the fractional differentiation matrix (see § 3.3.3.3), which can take advantage of MATLAB's efficient matrix calculus. This is currently limited to first order accuracy and uniform grids.

3.3.1.2 Diffusive Representation

A novel approach based on the diffusive representation of the fractional derivative was employed by Lombard and Mercier (2014), based on the method of Yuan and Agrawal (2002) and Diethelm (2008). The diffusive representation is an efficient technique for simplifying time non-local formulations into ones with simple numerical approximations based on diffusion equations (see Casenave and Montseny,

2010). It is valid for Caputo-type fractional differential operators of the order $\alpha > 0$, $\alpha \notin \mathbb{N}$, and assuming $u \in C^{\lceil \alpha \rceil}[0,t]$ (Diethelm, 2008). The diffusive representation of the half-order integral operator ($\alpha = 1/2$) is given by (Diethelm, 2008):

$$\frac{\partial^{-1/2}}{\partial t^{-1/2}} u(t) = \int_0^{+\infty} \psi(\theta, t) d\theta \tag{3.31}$$

where the diffusive variable ψ is defined by:

$$\psi(\theta, t) = \frac{2}{\pi} \int_0^t e^{-(t-\tau)\theta^2} u(\tau) d\tau \tag{3.32}$$

The diffusive representations for the derivatives of order 1/2 and 3/2 in Equation 3.23 can be approximated using a quadrature scheme with $l = 1, N_l$ integration points:

$$\frac{\partial^{1/2} f}{\partial \mathfrak{T}^{1/2}} = \int_0^{+\infty} \left(-\theta^2 \psi + \frac{2}{\pi} f \right) d\theta \simeq \sum_{l=1}^{N_l} \eta_l \left(-\theta_l^2 \psi_l + \frac{2}{\pi} f \right) \tag{3.33a}$$

$$\frac{\partial^{3/2} g}{\partial \mathfrak{T}^{3/2}} = \int_0^{+\infty} \left(-\theta^2 \xi + \frac{2}{\pi} g' \right) d\theta \simeq \sum_{l=1}^{N_l} \eta_l \left(-\theta_l^2 \xi_l + \frac{2}{\pi} \frac{\partial g}{\partial \mathfrak{T}} \right) \tag{3.33b}$$

where η_l and θ_l are the quadrature weights and abscissa, respectively. The diffusive variables ψ and ξ satisfy the first order ODEs:

$$\begin{aligned} &\frac{\partial \psi}{\partial \mathfrak{T}} = -\theta^2 \psi + \frac{2}{\pi} f \\ &\psi(\theta, 0) = 0 \end{aligned} \tag{3.34}$$

$$\begin{aligned} &\frac{\partial \xi}{\partial \mathfrak{T}} = -\theta^2 \xi + \frac{2}{\pi} g' \\ &\xi(\theta, 0) = 0 \end{aligned} \tag{3.35}$$

The values of η_l and θ_l can be most easily found by using a suitable quadrature

scheme for improper integrals, such as Gauss-Laguerre, or Gauss-Jacobi with a change in integration limits (Diethelm, 2008; Lombard and Mercier, 2014). However, these standard quadrature schemes tends to converge slowly with an increasing number of integration points.

3.3.1.3 Optimisation of Quadrature Coefficients

An improvement to the standard quadrature schemes is proposed by Richoux et al. (2015). A non-linear optimisation procedure based on the linear dispersion relation of Equation 3.16a is used to find the weights and abscissa. Fractional derivatives obtained using the optimisation approach were found to converge faster with respect to N_l compared to the aforementioned quadrature schemes. The objective function for this procedure is defined by:

$$\mathcal{J}(\{\eta_l, \theta_l\}; N_l, N_k) = \sum_{k=1}^{N_k} |Q - 1|^2 \tag{3.36}$$

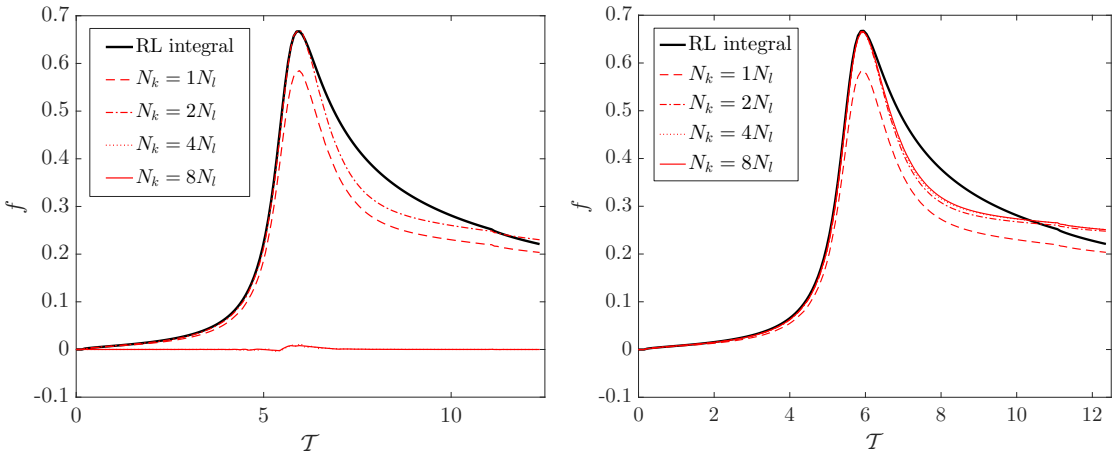
where $k = 1, N_k$ is the number of angular frequencies (as chosen by the user), and Q is based on the linear dispersion relation of Equation 3.16a (Lombard and Mercier, 2014):

$$Q(\omega_k) = \frac{2}{\pi} \sum_{l=1}^{N_l} \eta_l \frac{(i\omega_k)^{1/2}}{\theta_l^2 + i\omega_k} \tag{3.37}$$

The angular frequencies, ω_k, are defined linearly on a logarithmic scale on the interval $[\omega_{\min}, \omega_{\max}]$:

$$\omega_k = \omega_{\min} \left(\frac{\omega_{\max}}{\omega_{\min}} \right)^{\frac{k-1}{N_k - 1}} \tag{3.38}$$

The summation on N_l in Equation 3.37 is evaluated efficiently using the matrix product in MATLAB. A modification to the objective function in Equation 3.36



(a) Original objective function

(b) Modified objective function

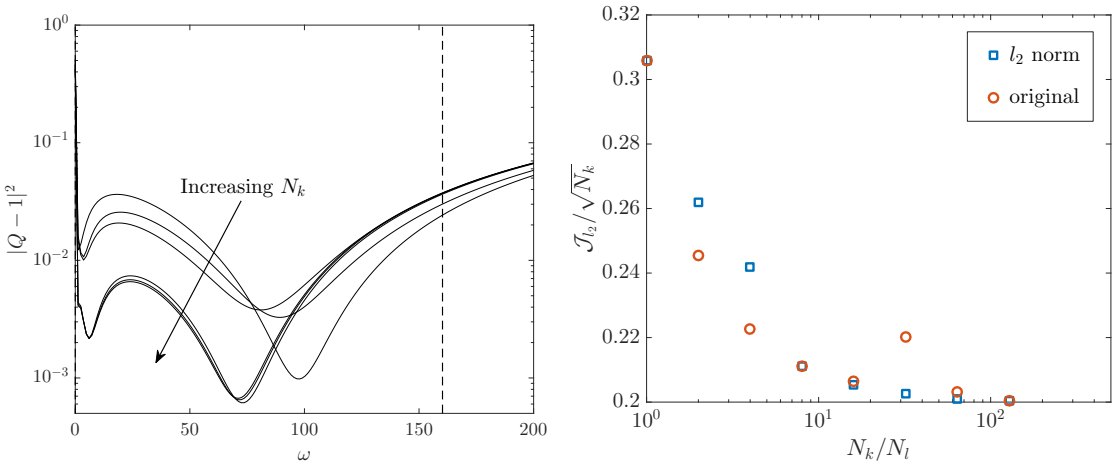
Figure 3.6: A comparison of the half-order derivatives obtained using the diffusive representation and conventional methods (FIT), for the reference initial condition in § 5.3, with $L = d_\mathrm{t}$, $u_\mathrm{z} = 400$ km/h, $N_l = 4$.

is proposed in this work so that it is less susceptible to divergence for small values in the range $0 < |Q - 1|^2 < 1$. This is achieved by evaluating the l^2-norm:

$$\mathcal{J}(\{\eta_l, \theta_l\}; N_l, N_k)_{l_2} = \sqrt{\mathcal{J}(\{\eta_l, \theta_l\}; N_l, N_k)} \tag{3.39}$$

Figure 3.6 demonstrates the improvement in convergence properties for the modified objective function for relatively few integration points ($N_l = 4$ in this case). It is noted that this is not enough integration points to represent the derivative accurately. The accuracy of the solution increases with the value of N_k, as shown in Figure 3.7. The solution appears to have converged sufficiently for $N_k \approx 16N_l$, as judged by the root-mean-square (RMS) of the objective function. The computational cost of increasing N_k is negligible, as it only impacts the calculation of the diffusive coefficients and has no effect on the size of the DAE system (see § 3.3.2). The size of the DAE system is only impacted by the value of N_l.

Derivatives calculated using the optimisation approach are sensitive to the values of ω_min and ω_max used in Equation 3.38. Lombard and Mercier (2014) suggest using a narrow interval of $\omega_\mathrm{min} = \omega/2$ and $\omega_\mathrm{max} = 3\omega/2$ when solving with the array, as the frequency content of the initial disturbance is maintained by



(a) Error versus ω_k for the modified objective. Dashed line is the upper bound of ω_k

(b) RMS error versus N_k for the original and modified objectives

Figure 3.7: Convergence analysis of the diffusive representation for the original and modified objective functions. $N_k/N_l = 2^n$ with $n = 0, 5$ and $N_l = 6$.

the existence of solitary waves. However, these constraints resulted in predictions which were inconsistent with those from FIT for the reference initial condition (see § 5.3). Increasing the frequency range to $\omega_{\min} = 0.01$ and $\omega_{\max} = 2\omega$ improved convergence, indicating that the estimated characteristic frequency of the initial condition is likely higher than the true value.

The complexity of the optimisation problem and the likelihood of divergence increases with the frequency bounds and the dimensionality of the search space (N_l). In the case of the tunnel without the array, the frequency content of the signal is no longer bounded. Therefore, the upper bound is changed to $\omega_{\max} = \mathcal{N}\omega$, where $\mathcal{N}$ is the number of harmonics of interest. Lombard and Mercier (2014) use a value of $\mathcal{N} = 20$ for numerical experiments, which is retained in the current work.

The `fmincon` function (MathWorks, 2017a) is used for the optimisation procedure to find the minimum of a constrained, non-linear, and multi-variable function. The sequential quadratic programming algorithm (SQP) (Boggs, 1996) was used as it was generally found to provide superior convergence properties compared to the default interior-point algorithm, i.e. a smaller error on the objective function in fewer function iterations. The non-linear iterative method of Shor (2012) was

also tested, using the `solveOpt` function (Kappel and Kuntsevich, 2000). The convergence properties of `fmincon` were found to be more reliable for different values for N_l and the constraint bounds.

Initial values for η_l and θ_l are provided using modified Gauss-Jacobi quadrature (see Birk and Song, 2010; Lombard and Mercier, 2014), while the constraints $\theta_l \geq 0$, $\eta_l \geq 0$ and $\theta_l \leq \theta_{\max}$ are imposed to ensure positivity and reduce the likelihood of divergence, respectively. The result is very sensitive to the value of $\theta^2_{\max}$, which is taken as the maximum value from Equation 3.38.

3.3.1.4 Comparison of Numerical Methods

The diffusive representation of the fractional derivatives provides greater flexibility in terms of order of accuracy and programming implementation with ODE solvers, compared to the methods described in § 3.3.1.1. The approximation accuracy error of the diffusive representation is difficult to define. It is affected by the number of integration points, the step size, the ODE solver and the discretisation approach used in Equations 3.34 and 3.35. Diethelm (2008) approximates the accuracy as of $O(N_l^{\bar{\alpha}-1})$ for Gauss Laguerre quadrature, where $\bar{\alpha} = 2\alpha - 2\lceil\alpha\rceil + 1 \equiv 0$ for $\alpha = 1/2$ and $3/2$. Therefore, the order of approximation accuracy is of $O(N_l^{-1})$.

Several disadvantages of the diffusive representation have been identified in this work and include:

- A greater impact on computational cost with increasing N_l due to the increase in the size of the sparse Jacobian matrix, which is required for DAE integration routines (see § 3.3.4). Therefore, optimisation of the quadrature coefficients is necessary in order to accelerate convergence and reduce the size of the Jacobian matrix.

- The convergence of the optimisation method is very sensitive to the constraints, initial values, and value of N_l. Achieving accurate results requires tuning these parameters through a process of trial and error, and is dependent on the frequency content of the incident pressure waveform. Further

difficulty arises if the characteristic frequency of the initial condition is not accurately known.

- Increased numerical stiffness of the ODE system presented in § 3.3.2 with increasing N_l. This increases the computational cost of integration and the likelihood of convergence failure.

In light of the points above, it is recommended that the fractional derivatives are evaluated using a simpler approach, such as the L1 algorithm, or the fractional differential matrix, if the user wants to avoid these complexities.

3.3.2 First-Order System

The method of lines provides a high degree of flexibility in terms of temporal and spatial discretisation approaches (see § 2.7.1). Equation 3.23 must be re-written as a system of first-order partial DAEs, with all temporal terms moved to the right-hand side (RHS). Firstly, the second order derivative of g^2 in Equation 3.23b is re-written using the product rule as:

$$\frac{\partial^2 g^2}{\partial \mathfrak{T}^2} \equiv 2\left[g\frac{\partial^2 g}{\partial \mathfrak{T}^2} + \left(\frac{\partial g}{\partial \mathfrak{T}}\right)^2\right] \tag{3.40}$$

If a diffusive representation of the fractional derivatives is sought then Equation 3.33 is substituted into Equation 3.23. Equations 3.34 and 3.35 must also be included to provide closure for the diffusive variables, ψ and ξ. Finally, all temporal derivatives in Equation 3.23 are moved to the RHS, which gives after some rearrangement:

$$\frac{\partial f}{\partial \mathcal{X}} = \frac{\partial \mathcal{F}}{\partial \mathcal{T}} - \bar{\delta}_{\mathrm{t}} \sum_{l=1}^{N_l} \eta_l \left(-\theta_l^2 \psi_l + \frac{2}{\pi} f \right) - \bar{\tau} f |f| + \beta \frac{\partial f^2}{\partial \mathcal{T}^2} - \bar{K} \left(1 - 2U\epsilon g \right) q \quad (3.41a)$$

$$0 = q - \frac{\partial g}{\partial \mathcal{T}} \quad (3.41b)$$

$$0 = \frac{\partial q}{\partial \mathcal{T}} - \left[\Omega \left(f - g \right) + \epsilon q \left(2Uq - W |q| \right) - \delta_{\mathrm{n}} \sum_{l=1}^{N_l} \eta_l \left(-\theta_l^2 \xi_l + \frac{2}{\pi} q \right) \right] / \left(1 - 2U\epsilon g \right) \quad (3.41c)$$

$$0 = -\theta_l^2 \xi_l + \frac{2}{\pi} q - \frac{\partial \xi_l}{\partial \mathcal{T}} \quad (3.41d)$$

$$0 = -\theta_l^2 \psi_l + \frac{2}{\pi} f - \frac{\partial \psi_l}{\partial \mathcal{T}} \quad (3.41e)$$

where the $(3 + 2N_l)\, N_{\mathcal{T}}$ unknowns to be solved are $(f, g, q, \xi_1, \cdots, \xi_{N_l}, \psi_1, \cdots, \psi_{N_l})^T$, and $\mathcal{F}(f) = f^2/2$ is the advection-Burgers' flux for the conservation form:

$$\frac{\partial \mathcal{F}^{\pm}}{\partial \mathcal{T}} = \frac{1}{\Delta \mathcal{T}} \left\{ \mathcal{F}^{\pm}_{i+1/2} - \mathcal{F}^{\pm}_{i-1/2} \right\} \quad (3.42)$$

The superscripts $\pm$ denote wave propagation in the downstream/upstream directions, respectively. Shock capturing schemes are required for the conservation form, in order to physically represent the wavefront speed and any discontinuities which may emerge in the solution. The discretisation of the RHS terms, including the conservation form of the advection term is discussed in the next section. Note that Equations 3.41d and 3.41e are disregarded when not using the diffusive representation for the fractional derivatives.

3.3.3 Discretisation

Many techniques are available for the discretisation of semi-discrete systems, for which a brief overview is provided in § 2.7.1. Two of the most popular high-resolution schemes for the treatment of conservative fluxes are Monotonic Upstream-Centered Schemes for Conservation Laws (MUSCL) (van Leer, 1979) and Weighted

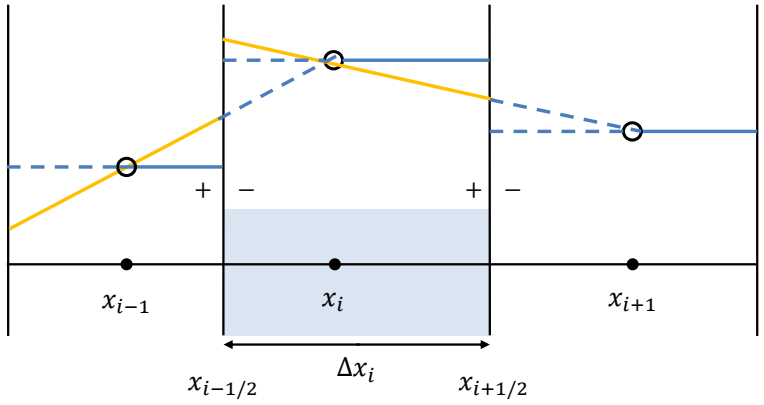


Figure 3.8: Local stencil for the cell edge flux reconstruction for MUSCL schemes, where + and − represent the left and right edges of the cell boundary.

Essentially Non-Oscillatory (WENO) schemes (Liu et al., 1994). Both methods have been implemented in this work. For MUSCL, the scheme of Kurganov and Tadmor (2000) (KT) has been used with both piece-wise linear (KT-L) and parabolic (KT-P) reconstruction. The near-field space variable, x, is used for this section, in-keeping with convention in the literature. A description of the KT scheme is provided first.

3.3.3.1 KT Scheme

The limited extrapolated cell edge variables for the 2nd order accurate KT-L scheme are given with reference to Figure 3.8 and for a non-uniform grid by:

$$\begin{aligned} f^+_{i+1/2} &= f_i + \frac{\Delta x_i}{2}\phi\left(r_i\right)\nabla f_{i-\frac{1}{2}} \\ f^-_{i+1/2} &= f_{i+1} - \frac{\Delta x_i}{2}\phi\left(r_{i+1}\right)\nabla f_{i+\frac{1}{2}} \\ f^+_{i-1/2} &= f_{i-1} + \frac{\Delta x_i}{2}\phi\left(r_{i-1}\right)\nabla f_{i-\frac{1}{2}} \\ f^-_{i-1/2} &= f_i - \frac{\Delta x_i}{2}\phi\left(r_i\right)\nabla f_{i+\frac{1}{2}} \end{aligned} \tag{3.43}$$

where $f_i = f(x_i, t)$ and the gradients, ∇, are given by:

$$\begin{aligned} \nabla f_{i+\frac{1}{2}} &= \frac{f_{i+1} - f_i}{x_{i+1} - x_i}, \qquad \nabla f_{i-\frac{1}{2}} = \frac{f_i - f_{i-1}}{x_i - x_{i-1}} \\ \nabla f_{i+\frac{3}{2}} &= \frac{f_{i+2} - f_{i+1}}{x_{i+2} - x_{i+1}}, \quad \nabla f_{i-\frac{3}{2}} = \frac{f_{i-1} - f_{i-2}}{x_{i-1} - x_{i-2}} \end{aligned} \tag{3.44}$$

The grid spacing, Δx_i, is evaluated at the cell boundaries using:

$$\mathrm{d}x_i \approx \Delta x_i = x_{i+1/2} - x_{i-1/2} = \frac{x_{i+1} - x_{i-1}}{2} \tag{3.45}$$

The cell edge variables for the 3rd order accurate KT-P scheme are given by (Kermani et al., 2003):

$$\begin{aligned}
f^+_{i+\frac{1}{2}} &= f_i + \frac{\Delta x_i}{4}\phi\left(r_i\right)\left[\left(1-\kappa\right)\nabla f_{i-\frac{1}{2}} + \left(1+\kappa\right)\nabla f_{i+\frac{1}{2}}\right] \\
f^-_{i+\frac{1}{2}} &= f_{i+1} - \frac{\Delta x_i}{4}\phi\left(r_{i+1}\right)\left[\left(1-\kappa\right)\nabla f_{i+\frac{3}{2}} + \left(1+\kappa\right)\nabla f_{i+\frac{1}{2}}\right] \\
f^+_{i-\frac{1}{2}} &= f_{i-1} + \frac{\Delta x_i}{4}\phi\left(r_{i-1}\right)\left[\left(1-\kappa\right)\nabla f_{i-\frac{3}{2}} + \left(1+\kappa\right)\nabla f_{i-\frac{1}{2}}\right] \\
f^-_{i-\frac{1}{2}} &= f_i - \frac{\Delta x_i}{4}\phi\left(r_i\right)\left[\left(1-\kappa\right)\nabla f_{i+\frac{1}{2}} + \left(1+\kappa\right)\nabla f_{i-\frac{1}{2}}\right]
\end{aligned} \tag{3.46}$$

where $\kappa = 1/3$. The flux limiter, ϕ, in Equations 3.43 and 3.46 is a function of the ratio of successive gradients, r:

$$r_i = \frac{\nabla f_{i-\frac{1}{2}}}{\nabla f_{i+\frac{1}{2}}} \tag{3.47}$$

Flux limiting constrains the flux of the piece-wise approximations to ensure the solution is total variation diminishing (TVD) (Harten, 1983). The TVD condition limits the accuracy to first order around a discontinuity or local extrema in order to avoid non-physical and spurious oscillations (Gibbs phenomena) appearing in the solution, in-line with Godunov's theorem (Godunov, 1954).

The choice of flux limiter is problem specific and no 'best' limiter exists for all applications. However, the monotonized central (MC, also referred to as the MUSCL limiter) (Van Leer, 1977) and van Leer (van Leer, 1974) limiters are popular choices for general applications. For piecewise parabolic reconstruction a modified van Albada limiter was proposed by Kermani et al. (2003). The MC, van

Leer, and modified van Albada limiters are defined respectively by:

$$\begin{aligned}
\phi_{\mathrm{mc}}(r) &= \max\left[0, \min\left(2r, 0.5(1+r), 2\right)\right]; \quad \lim_{r\to\infty} \phi_{\mathrm{mc}}(r) = 2 \\
\phi_{\mathrm{vl}}(r) &= \frac{r+|r|}{1+|r|}; \quad \lim_{r\to\infty} \phi_{\mathrm{vl}}(r) = 2 \\
\phi_{\mathrm{va2}}(r) &= \frac{2r}{r^2+1}; \quad \lim_{r\to\infty} \phi_{\mathrm{va2}}(r) = 0
\end{aligned} \tag{3.48}$$

where $\phi(r) = 0$ results in a 1st order accurate scheme. It should be noted that piecewise parabolic reconstruction with the modified van Albada limiter is no longer TVD, in order to allow for higher than 1st order accuracy at smooth extrema. The reconstructed cell edge fluxes for the semi-discrete form of the KT scheme (accounting for the wind direction) are given by the Rossanov (also known as local Lax-Friedrichs) flux:

$$\mathcal{F}_{i\mp\frac{1}{2}} = \frac{1}{2}\left\{\left[\mathcal{F}\left(f^{-}_{i\mp\frac{1}{2}}\right) + \mathcal{F}\left(f^{+}_{i\mp\frac{1}{2}}\right)\right] - a_{i\mp\frac{1}{2}}\left[f^{-}_{i\mp\frac{1}{2}} - f^{+}_{i\mp\frac{1}{2}}\right]\right\} \tag{3.49}$$

where $\mathcal{F}(f)$ is the flux and $a_{i+\frac{1}{2}}$ is the local propagation speed:

$$a_{i+\frac{1}{2}} = \max\left[\rho\left(\frac{\partial\mathcal{F}}{\partial f}\left(f^{+}_{i+1/2}\right)\right), \rho\left(\frac{\partial\mathcal{F}}{\partial f}\left(f^{-}_{i+1/2}\right)\right),\right] \tag{3.50}$$

In the case of the 1-D Burgers' flux the spectral radius, ρ, of the Jacobian matrix, $\partial\mathcal{F}(f)/\partial f$, reduces to:

$$\rho = \max\left|\frac{\partial\mathcal{F}(f)}{\partial f}\right| = \max|f| \tag{3.51}$$

In practice, Equations 3.49 and 3.50 are not required for the numerical models used in this work as the wind directions are treated separately (see Equation 3.62). The KT scheme is written for a non-uniform grid, which is a generalisation of the uniform case: $\Delta x_i = x_{i+1} - x_i = x_i - x_{i-1}$. A non-uniform grid permits the mesh to be refined in regions where large gradients are expected.

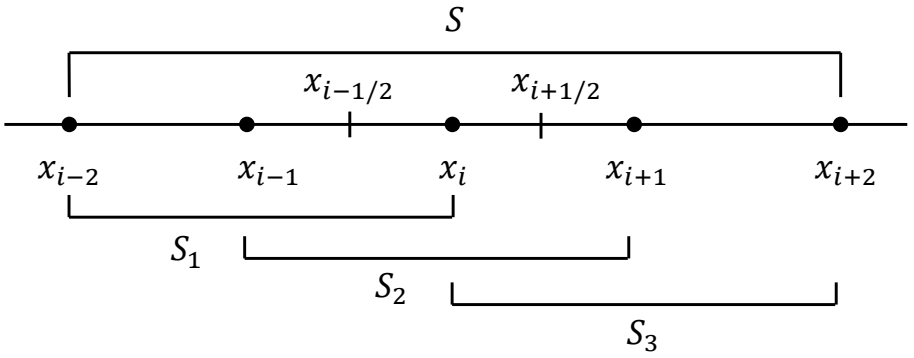


Figure 3.9: Overview of the fifth order accurate upwinded ENO/WENO stencil, S, and sub-stencils, S_i.

3.3.3.2 WENO Scheme

The scheme for WENO reconstruction is now presented for a uniform grid (see Liu et al., 1994). Non-uniform WENO and ENO schemes are available (e.g. Wang et al., 2008), however they have not been incorporated due to their complexity. The main principle behind ENO schemes is to apply an adaptive procedure to automatically choose the smoothest stencil from a set of overlapping sub-stencils (see Figure 3.9). The other sub-stencils are then disregarded. WENO schemes build on this approach by applying a non-linear weighting factor between all the sub-stencils, which favours the smoothest sub-stencil.

WENO schemes can achieve an arbitrarily high order of accuracy in smooth regions and 'essentially' non-oscillatory behaviour (hence the name) around discontinuities. WENO schemes relax the TVD criterion in order to achieve these properties, at the potential cost of generating (hopefully small and imperceptible) non-physical oscillations in the solution. For the third/fifth order accurate ENO/WENO scheme, the three sub-stencils are given by $\{S_1, S_2, S_3, \cdots, S_i\}$, with reference to Figure 3.9:

$$\begin{aligned} f^{(1)}_{i+\frac{1}{2}} &= \frac{1}{3}f_{i-2} - \frac{7}{6}f_{i-1} + \frac{11}{6}f_i \\ f^{(2)}_{i+\frac{1}{2}} &= -\frac{1}{6}f_{i-1} + \frac{5}{6}f_i + \frac{1}{3}f_{i+1} \\ f^{(3)}_{i+\frac{1}{2}} &= \frac{1}{3}f_i + \frac{5}{6}f_{i+1} - \frac{1}{6}f_{i+2} \end{aligned} \tag{3.52}$$

which are third order accurate. The union of the three sub-stencils produces a centred global stencil, S, which is fifth order accurate, on the condition that the function is globally smooth:

$$f_{i+\frac{1}{2}} = \frac{1}{30}f_{i-2} - \frac{13}{60}f_{i-1} + \frac{47}{60}f_i + \frac{9}{20}f_{i+1} - \frac{1}{20}f_{i+2}, \tag{3.53}$$

The index of the sub-stencils can be shifted by one so that the global stencil is upwind biased. The global stencil is redefined as a convex combination of the three sub-stencils:

$$f_{i+\frac{1}{2}} = \gamma_1 f^{(1)}_{i+\frac{1}{2}} + \gamma_2 f^{(2)}_{i+\frac{1}{2}} + \gamma_3 f^{(3)}_{i+\frac{1}{2}} \tag{3.54}$$

where $\sum_i \gamma_i = 1$ are referred to as the linear weights. For this particular scheme the weights are: $\gamma_1 = 1/10, \gamma_2 = 6/10, \gamma_3 = 3/10$. In the presence of a discontinuity the ENO scheme would select the locally smoothest stencil, providing third order accuracy on the condition that at least one of the sub-stencils is smooth. On the other hand, the WENO scheme approximates a convex combination of the three sub-stencils:

$$f_{i+\frac{1}{2}} = w_1 f^{(1)}_{i+\frac{1}{2}} + w_2 f^{(2)}_{i+\frac{1}{2}} + w_3 f^{(3)}_{i+\frac{1}{2}} \tag{3.55}$$

where w_i are the non-linear weights. It is required that $w_i \approx \gamma_i$ if the function is smooth across all sub-stencils, and $w_i \approx 0$ if a discontinuity is present in one of the sub-stencils, S_i. The non-linear weights are defined by:

$$w_i = \frac{\tilde{w}_i}{\sum_i \tilde{w}_i}, \qquad \tilde{w}_i = \frac{\gamma_i}{\sum_i (\varepsilon + \beta_i)^2} \tag{3.56}$$

where ε is a small positive number chosen to be $O(10^{-16})$, which is used to avoid zero-division. The smoothness indicators, β_i, for the fifth order accurate WENO

scheme are:

$$\begin{aligned}\beta_1 &= \frac{13}{12}\left(f_{i-2} - 2f_{i-1} + f_i\right)^2 + \frac{1}{4}\left(3f_{i-2} - 4f_{i-1} + f_i\right)^2 \\ \beta_2 &= \frac{13}{12}\left(f_{i-1} - 2f_i + f_{i+1}\right)^2 + \frac{1}{4}\left(3f_{i-1} - f_{i+1}\right)^2 \\ \beta_3 &= \frac{13}{12}\left(f_i - 2f_{i+1} + f_{i+2}\right)^2 + \frac{1}{4}\left(f_i - 4f_{i+1} + f_{i+2}\right)^2\end{aligned} \tag{3.57}$$

The WENO-Z+ scheme (Acker et al., 2016) uses modified weights to provide improved resolution in smooth regions and reduced numerical dissipation, with only a minimal increase in computational cost compared to the original WENO scheme. The modified weights are given by:

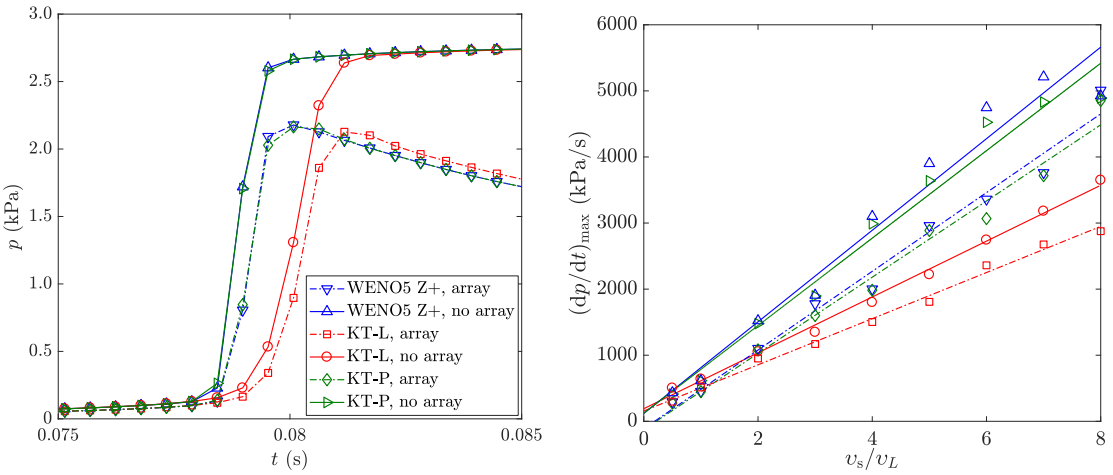
$$\tilde{w}_i = \gamma_i \left[1 + \varrho_i^2 + \frac{\lambda}{\varrho_i}\right], \qquad \varrho_i = \frac{\tau + \varepsilon}{\beta_i + \varepsilon} \tag{3.58}$$

where $\tau = |\beta_3 - \beta_1|$ and $\lambda = \Delta x^{2/3}$, based on numerical experiments. The 3rd order accurate KT-P scheme is advantageous over the 5th order accurate WENO-Z+ scheme for the purpose of optimisation due to the non-uniform grid implementation. This can significantly reduce the number of grid points required, as the mesh can be coarsened away from high gradients (for example, see § 5.3.3).

Figure 3.10 compares the accuracy of the 5th order accurate WENO Z+ scheme, the 3rd order KT-P scheme with the modified van Albada limiter, and the 2nd KT-L scheme with the van Leer limiter, for a steep incident wavefront, i.e. a characteristic wavefront length $\tilde{L} = 0.1$ in Figure 5.1, so that $(\mathrm{d}p/\mathrm{d}t)_{\max} > 100$ kPa/s. Steep gradients are most accurately resolved across a range of sample frequencies by the WENO Z+ scheme (see Figure 3.10b). The 3rd order KT-P scheme offers similar performance to the WENO scheme, while the KT-L scheme is much worse.

3.3.3.3 Dissipative terms

Other derivatives with respect to $\mathcal{T}$ (e.g. source term, dissipation, etc.) use finite differences with an order of accuracy at least equal to that used for the treat-



(a) Pressure waveforms with $\upsilon_s/\upsilon_L = 4$.

(b) Maximum pressure rate versus normalised sample frequency.

Figure 3.10: Comparison of shock capturing schemes for a steep incident wavefront on a uniform grid, with and without an arbitrary array of resonators. $l_a \approx 100$ m, $\tilde{L} = 0.1$, $u_z = 400$ km/h, $\upsilon_L = a_0/L \approx 450$ Hz.

ment of the advective flux. The derivatives can be evaluated efficiently using the differentiation matrix approach:

$$\frac{\mathrm{d}\mathbb{f}}{\mathrm{d}\mathcal{T}} = \mathbb{D}\mathbb{f} \tag{3.59}$$

where $\mathbb{D}$ is a matrix containing the differencing weights. The `fdcoeffF` function (LeVeque, 2007) is used based on Fornberg's method (Fornberg, 1988), which can achieve an order of accuracy up to $O(\Delta t)^n$ on a non-uniform grid. The differentiation matrix approach is well suited to MATLABs inherent efficiency in matrix operations. At least one stencil point either side of the current operating point i was found to be necessary to maintain stability (see Figure 3.9), particularly for large values of $\Delta\mathcal{T}$ (see § 3.3.6).

The accuracy of the numerical model can be improved for fewer grid points by using pseudo-spectral methods based on the Chebyshev differentiation matrix (Trefethen, 2000) to treat the source term and the diffusive representation of the resonator response. This method permits non-periodic boundary conditions to be applied, compared to spectral methods based on the Fourier transform. The

advection term would still need to be treated using an appropriate shock capturing scheme (e.g. WENO or TVD schemes), or by applying spectral filtering to remove non-physical Gibb's phenomena as a post-process around discontinuities.

3.3.4 Space Marching

A suitable DAE solver is required for space marching, for which a brief overview is provided in § 2.7.2. The MATLAB solvers `ode15s` (semi-explicit index-1 DAE) and `ode15i` (fully implicit DAE) (Shampine and Reichelt, 1997) have been tested. These solvers are based on the numerical and backwards differentiation formulas (BDF) (see Ascher and Petzold, 1998) and can take advantage of a variable step size and order of accuracy (from 1 to 5th order). They are particularly well suited to stiff problems (see § 2.7.2). `ode15s` was generally found to exhibit faster convergence, while `ode15i` was less likely to fail in the presence of moderate stiffness. Therefore, `ode15i` is called in cases in which a first attempt using `ode15s` fails. It is noted that implicit multi-step methods, including the BDF family, are A-stable only up to 2nd order accuracy (see Chapter 7 LeVeque, 2007).

The Jacobian sparsity pattern is provided in order to accelerate the solvers (see Figure 3.11) by reducing the number of finite differences which must be evaluated in order to calculate the numerical Jacobian matrix. Providing the sparsity pattern is beneficial when using the diffusive representation of the fractional derivatives, as the diffusive representation significantly increases the number of variables and hence the size of the Jacobian matrix. An analytical sparsity pattern is difficult to implement for this system and instead is estimated prior to running the solver based on the numerical calculation of the Jacobian via finite differences by using the MATLAB function `odenumjac` (Salane, 1986; Shampine and Reichelt, 1997). This approach is valid as long as the sparsity pattern does not change with the space step. A more efficient alternative to a numerical Jacobian sparsity pattern may be to provide the analytical Jacobian by using automatic differentiation (see Griewank and Walther, 2008), for which several MATLAB toolboxes are available.

Six integration points ($N_l = 6 - 10$, see § 3.3.1.2) provide a compromise be-

tween the desired accuracy of the fractional derivatives and the solver speed. The accuracy of the diffusive representation is also highly sensitive to the optimisation constraints, which are dependent on the initial condition, as discussed in § 3.3.1. The local error calculated by the ODE solver at each step must satisfy:

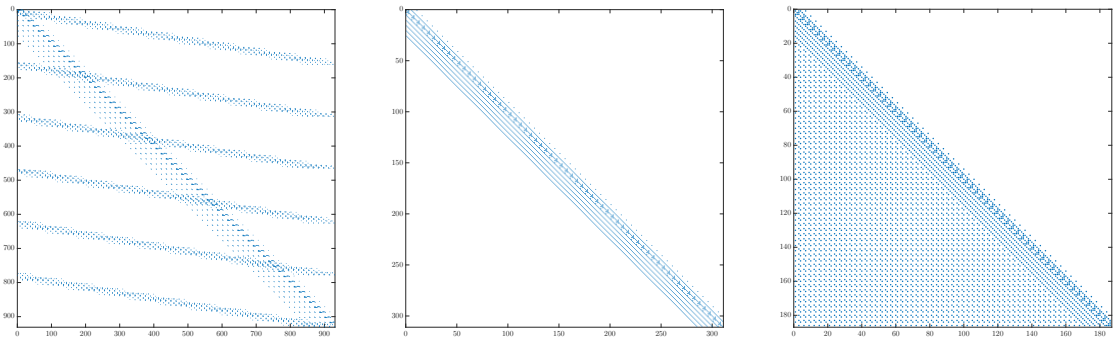
$$|e_i| \leq \max(\text{RelTol} \cdot |y_i|, \text{AbsTol}) \tag{3.60}$$

where y_i is the i-th component of the solution. Relative (dimensionless) and absolute (with dimensions of the variable) integration tolerances of 1e-3 and 1e-6, respectively were found to provide adequate spatial convergence over a range of cases. The solvers must take smaller steps in order to satisfy smaller tolerances, which increases the simulation time. The value of these tolerances may need to be reconsidered if using the near-field system in § 3.2.3, as the magnitude of the discretised PDE terms may vary considerably in comparison to the far-field system where the dimensionless terms are all of $O(1)$.

3.3.4.1 Comparison with Near-Field Treatment

A comparison is made with the numerical treatment of the near-field system in § 3.2.3. Richoux et al. (2015) use 2nd order accurate Strang operator splitting (Strang, 1968) in order to decompose the near-field system into a propagative part (which also includes diffusion) and forcing part (source term and friction). The two parts are then treated separately using an explicit and implicit integration routine, respectively. Strang splitting is an efficient technique for stiff problems with operators with very different time scales. The computational overhead of integration is reduced by avoiding the use of an implicit integration technique for the entire system (both the propagative and forcing parts). In contrast, the entire far-field system must be integrated using a semi-explicit DAE solver and operator splitting cannot be used.

It is more difficult to use the far-field system with a discrete treatment of the resonators, or irregular resonator geometry (see § 3.4.1), particularly with the



(a) $N_l = 6$ (b) $N_l = 1$ (c) RL (FIT)

Figure 3.11: Comparison of numerically derived Jacobian sparsity patterns for a fixed value of $N_{\mathcal{T}}$.

incorporation of bi-directional wave propagation. These modifications significantly increase the stiffness of the system due to the discontinuous change in the value of the equation coefficients as a function of space. As a result, more function calls of the RHS of the DAE system must be made in order to achieve the desired accuracy around discontinuities (where a small step size is required).

In summary, the choice between the near and far-field systems is respectively one between efficient numerical integration (fewer integration steps) but with a potentially expensive RHS evaluation cost, versus expensive numerical integration but with a smaller RHS evaluation cost. The far-field system becomes more attractive for longer arrays, as the number of grid points is almost entirely independent of the propagation distance.

3.3.5 Initial Conditions

The initial condition (incident pressure waveform) is applied at $f(0, \mathcal{T}) = f_0$ after performing a change to the far-field variables using Equations 3.21 and 3.22 for t and p, respectively. Initial conditions for the remaining variables are found by solving the system of ODEs representing the resonator response (Equation 3.41b-3.41e) by time-marching using a stiff ODE solver (e.g. `ode15s` in MATLAB), subject to $f(0, \mathcal{T}) = f_0$ and zero-valued starting points at $\mathcal{T} = 0$ for all other variables. These values (at $\mathcal{X} = 0$) are then provided as an initial guess to the `decic` function (MathWorks, 2017a), which is used to generate consistent initial

conditions for implicit ODE systems with algebraic constraints.

This approach was found to be more reliable than providing null starting points for the `decic` function for the remaining variables, which would occasionally fail or take a comparatively long time to converge. The ODE solver can take advantage of an adaptive step size when considering only the ODE system for the resonator response. In contrast, the `decic` function is limited to the predefined grid, and so may fail to converge if the grid spacing is too large.

3.3.6 Boundary Conditions

Boundary conditions (BCs) are implemented using "ghost" points. These are non-physical grid points added outside of the boundary of the physical domain in order to satisfy the finite difference stencil. The principle of ghost cells is illustrated in Figure 3.12 for the example of a backward biased stencil with one forward point at the right boundary of a 1-D grid. A larger stencil (with a higher order of accuracy) may require additional ghost points to be added. The ghost points simply take the prescribed boundary value for a Dirichlet BC. For Neumann and mixed-type BCs the values of the ghost points are calculated using a stencil which is weighted in the direction of the interior points (i.e. backwards biased stencil at the right boundary).

The order of accuracy of the stencil is consistent with that used for calculating the derivatives of the interior points. For example, the 2nd order accurate central difference scheme for a uniform grid (see the RHS of Equation 2.11) can be rearranged to calculate the value of the ghost point at the right boundary for a Neumann BC (see Figure 3.12):

$$u_{\mathrm{g,r}} = u_{i+1} = u_{i-1} + 2\Delta x \frac{\partial u}{\partial x}\Big|_{x=x_n} \tag{3.61}$$

A disadvantage of the far-field regime is the complexity of implementing physically representative BCs. All variables are null-valued at $\mathcal{T} = 0$, assuming undisturbed air at ambient conditions downstream of the wavefront. The solution is not affected by reflections from the upstream boundary at $\mathcal{T} = \mathcal{T}_{\mathrm{end}}$, as only down-

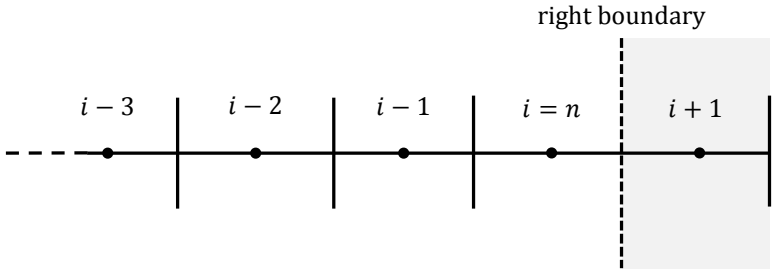


Figure 3.12: Illustration of a backward weighted stencil which requires one ghost cell at the right-hand side boundary, for a grid with n cells.

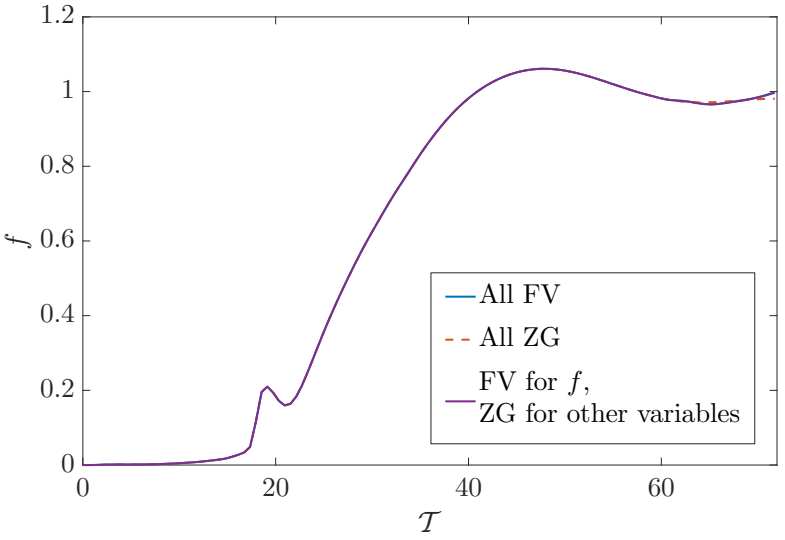


Figure 3.13: The effect of various upstream (RHS) boundary conditions for an arbitrary array with a length of $\tilde{l_a} = l_a/\dot{d}_t = 65$, subject to the initial condition specified in § 5.3.

stream propagation is modelled in Equation 3.23.

The use of backwards differencing (downwind biasing) for dissipative terms helps to localise non-physical boundary effects at the upstream boundary. This is demonstrated in Figure 3.13 for fixed-value Dirichlet (FV) and zero-gradient Neumann (ZG) BCs at the upstream boundary. The choice of the upstream BC has a negligible and very localised effect on the solution. The FV BC takes the value at the boundary for the initial condition, e.g. $f(\mathcal{X}, \mathcal{T}_{\text{end}}) = f(0, \mathcal{T}_{\text{end}})$. Boundary effects can be minimised by placing the boundary sufficiently far from the wavefront. Zero-gradient boundary conditions were chosen for the upstream boundary for all variables.

3.4 Physical Model Improvements

Modifications to the far-field model in § 3.2.4 are implemented in order to remove some assumptions of the physical model (see § 3.2.2), namely a continuum distribution of resonators and negligible interaction between neighbouring resonators. Test cases are then used in order to identify the threshold where the assumptions of the original model in § 3.2.4 are no longer valid. The far-field model accounting for bi-directional wave propagation is included in Appendix C rather than in the main body of this work, due to convergence issues which were encountered in its numerical implementation.

3.4.1 Discrete Far-Field Model

The previous sections have described the development of a model for the downstream propagation of pressure waves in a tunnel, based on the assumption of a continuum distribution of resonators. This assumption is expected to be less reliable for cases where the distance between the resonator openings, χ, approaches the characteristic wavelength, λ.

Although the continuum model was developed to work with equidistant and identical resonators, it is possible to use it with irregular resonator geometry and spacing. The PDE coefficients are now space-dependent, i.e. $\bar{K}(\mathcal{X})$, $\bar{\delta}_{\mathrm{t}}(\mathcal{X})$, $\bar{\tau}(\mathcal{X})$, $W(\mathcal{X})$, $\Omega(\mathcal{X})$ and $\delta_{\mathrm{n}}(\mathcal{X})$ in Equation 3.23. Equation 3.23 can be used with irregular geometry by interpolating the coefficients between the discrete resonator positions at each space step. A smoothly differentiable interpolation algorithm is required in order to minimise the likelihood of convergence failure around large changes in the equation coefficients between neighbouring resonators. Therefore, shape-preserving piecewise cubic hermite interpolation (Fritsch and Carlson, 1980) (function `pchip` in MATLAB) is used, which is more representative than spline interpolation for non-oscillatory functions (see Figure 3.14). Despite this, the stiffness of the system can still be a problem, particularly if the resonator properties change rapidly over a short space interval. In this case, convergence failure occurs as the step size tends to zero ($\Delta\mathcal{X} \to 0$), in order to sufficiently resolve sudden

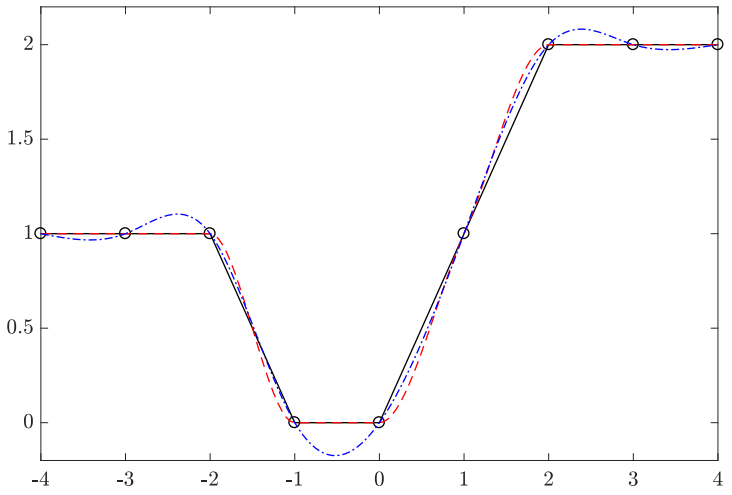


Figure 3.14: Interpolation of an arbitrary data set (∘) which is representative of a space-dependent far-field coefficient, using: linear C^0 (—); piece-wise cubic C^1 (– – –); and spline C^2 (– · – ·) interpolation.

changes in the equation coefficients.

In this section, a discrete far-field model is presented in order to see: (i) if there is an improvement in convergence properties for the case of irregular resonator geometry; (ii) at what value of the continuum approximation parameter, σ the continuum approximation diverges from the discrete treatment of the resonators.

3.4.1.1 Model Derivation

This section presents the far-field model including a discrete treatment of the resonators. The system in Equation 3.16 can be generalised to account for a discrete distribution of resonators and bi-directional wave propagation (Mercier and Lombard, 2016):

$$\frac{\partial u^{\pm}}{\partial t} + \frac{\partial}{\partial x}\left[\pm A u^{\pm} + B\frac{(u^{\pm})^2}{2}\right] = \pm C(x)\frac{\partial^{-1/2}}{\partial t^{-1/2}}\frac{\partial u^{\pm}}{\partial x} \mp Q(x)u^{\pm}|u^{\pm}| + D\frac{\partial^2 u^{\pm}}{\partial x^2} \mp E(x)\left(1-2Mp_{\mathrm{c}}\right)\frac{\partial p_{\mathrm{c}}}{\partial t} \tag{3.62a}$$

$$\frac{\partial^2 p_{\mathrm{c}}}{\partial t^2} + F\frac{\partial^{3/2} p_{\mathrm{c}}}{\partial t^{3/2}} + G(x)p_{\mathrm{c}} - H\frac{\partial^2 p_{\mathrm{c}}^2}{\partial t^2} + I(x)\left|\frac{\partial p_{\mathrm{c}}}{\partial t}\right|\frac{\partial p_{\mathrm{c}}}{\partial t} = J(x)\left(u^{+}-u^{-}\right) \tag{3.62b}$$

where the steady skin friction term has been added in this work. The superscripts

$[+,-]$ denote "right" running waves propagating downstream and "left" running waves propagating upstream, respectively. The new near-field space-dependent coefficients are defined by:

$$\begin{aligned} C(x) &= C_0 Z(x), \quad E(x) = E_i l_i(x), \quad Q(x) = Q_0 Z(x) \\ J(x) &= \frac{\gamma p_0}{a_0} G(x), \quad I(x) = \frac{V_{ci}}{S_{\mathrm{n}i} l_{\mathrm{e}} \rho_0 a_0^2} \end{aligned} \tag{3.63}$$

with:

$$E_i = \frac{V_{ci}}{\rho_0 a_0 S_{\mathrm{t}} S_{\mathrm{n}i}}, \qquad C_0 = \frac{\mathcal{C} a_0 \sqrt{\nu}}{r_{\mathrm{t}}}, \qquad Q_0 = \frac{f_{\mathrm{D}}}{8 r_{\mathrm{t}}}$$

Coefficients G, J and I are functions of the resonator index, $i = 1, N_{\mathrm{c}}$, which is a function of x. The other coefficients remain unchanged from Equation 3.16. Function $Z(x)$ in Equation 3.63 is geometry dependent and scales terms associated with the boundary layer of the duct to account for the junction formed with the resonator neck. Mercier and Lombard (2016) define Z for a circular duct where the neck junction is represented by a flat disc:

$$Z(x) = \left[1 - \frac{1}{\pi} \arcsin\left(\frac{l_i(x)}{r_{\mathrm{t}}} \right) \right]$$

where the length of the disc at location x is given by:

$$l_i(x) = \begin{cases} 0, & \text{if } r_{\mathrm{n}} < |x - x_i| \leq \chi \\ \sqrt{r_{\mathrm{n}}^2 - (x - x_i)^2}, & \text{if } |x - x_i| \leq r_{\mathrm{n}} \end{cases} \tag{3.64}$$

Function $Z(x)$ needs to be modified for the tunnel geometry considered in Figure 3.2, particularly as the profile of the tunnel becomes less like a circular duct (i.e. for large values of κ). The continuum approximation is recovered by calculating the mean values of $C(x)$, $E(x)$ and $Q(x)$ over the resonator interval, χ. For

example:

$$\bar{E} = \frac{1}{\chi} \int_{x=-\chi/2}^{\chi/2} E(x) \tag{3.65}$$

The discrete far-field system is derived under the same assumptions (see § 3.2.2) as the continuum far-field model in Equation 3.23. The assumption of negligible resonator interaction ($\kappa \ll 1$) is maintained by only considering the forward direction of propagation in Equation 3.62, i.e. $u^- = 0$. Applying the change of variables in Equation 3.22 to the discrete near-field system results in the following new space-dependent coefficients for the far-field system in Equation 3.23a, which remains otherwise unchanged:

$$\delta_{\mathrm{t}}(\mathcal{X}) = \frac{C_0 F(\mathcal{X})}{a_0 \epsilon \sqrt{\omega}}, \quad \tau(\mathcal{X}) = Q_0 F(\mathcal{X}) \frac{2a_0}{\omega(\gamma+1)}, \quad K(\mathcal{X}) = l_i(\mathcal{X}) \frac{V_{ci}}{S_{\mathrm{t}} S_{\mathrm{n}} \epsilon} \tag{3.66}$$

$$F(\mathcal{X}) = \left[1 - \frac{1}{\pi} \arcsin\left(\frac{l_i(\mathcal{X})}{r_{\mathrm{t}}} \right) \right] \tag{3.67}$$

$$l_i(\mathcal{X}) = \begin{cases} 0, & \text{if } r_{\mathrm{n}} < |\zeta(\mathcal{X})| \leq \chi \\ \sqrt{r_{\mathrm{n}}^2 - \zeta(\mathcal{X})^2}, & \text{if } |\zeta(\mathcal{X})| \leq r_{\mathrm{n}} \end{cases} \tag{3.68}$$

where $\zeta(\mathcal{X}) = a_0/(\epsilon\omega)\,(\mathcal{X} - \mathcal{X}_i)$. The ODE for the resonator response remains unchanged from Equation 3.23b. However, the coefficients are now dependent on the resonator index and remain constant valued on the interval $|\zeta(\mathcal{X})| \leq r_{\mathrm{n}}$.

3.4.1.2 Space Marching

The modified far-field model presented in the previous section has space-dependent PDE coefficients. Therefore, a modified space marching procedure from § 3.3.4 is required. The space-dependent coefficients can significantly increase the stiffness of the system as the DAE solver attempts to refine the step-size around the points where the resonators are activated/deactivated (i.e. through a non-zero value of

K at the interval endpoints of $|\zeta(\mathfrak{X})| \leq r_\mathrm{n}$ in Equation 3.68). As a result, most DAE solvers are likely to fail at the space point corresponding to the activation of the first resonator, as the space steps-size tends to zero (see Figure 3.15). Two techniques have been employed to resolve this issue, which are described below.

Firstly, the value of K is set to a small value (e.g. 1e-6) outside of the resonator intervals, rather than zero (see Equation 3.68). This was found to aid convergence, with no noticeable effect on the accuracy of the solution when compared to the continuum model with an identical equispaced array. $K(\mathfrak{X}) > 0$ implies that the resonator response is always active, even if the current space-step corresponds to a position where there is no resonator neck. The corresponding non-physical resonator coefficients are found by piecewise cubic interpolation in the regions outside of the resonator intervals (see Figure 3.14).

Secondly, the DAE solver is re-initialised at the start and end of each resonator interval (see Figure 3.15). The end state from the previous run is used as the initial condition for the next until the end of the array is reached. This process is implemented in MATLAB using the function `odextend` (MathWorks, 2017a). There are $2N_\mathrm{c} + 1$ solver restarts, in order to model the array. The process of restarting the solver multiple times is defined as a local approach, compared to the global approach of running the DAE solver only once over the entire length of the array.

The local solver approach was found to be more reliable and efficient than the global approach. The global approach often poorly resolves or entirely misses the location of the resonators, particularly as the neck diameter decreases relative to the resonator interval. Reducing the maximum step size can help to remedy this issue, at the expense of significantly increasing the total number of steps taken by the global approach. For example, the global approach is limited to small steps even in regions where much larger steps can be taken to achieve the required solution accuracy, such as outside of the resonator intervals. The reduction in the total number of steps required by the local approach more than offsets the additional computational cost of re-initialising the DAE solver at the start and

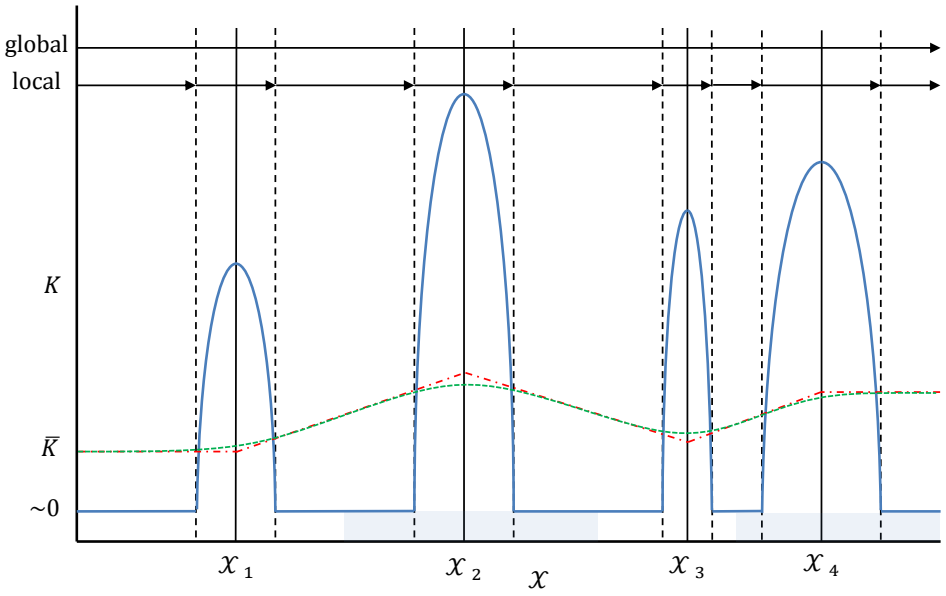


Figure 3.15: K versus $\mathcal{X}$ for a demonstrative array (not to scale) with four irregular resonators (neck diameter and spacing), in order to compare the discrete (——); continuum (linear interpolation) (- - - -), and continuum (piecewise-cubic interpolation) (– – –) models. The arrows at the top denote restarts for the local and global DAE solvers.

end of each resonator interval.

3.4.1.3 Comparison of Continuum and Discrete Models

The far-field continuum and discrete models are compared for different values of the continuum parameter, σ, for an array of regular (identical and equispaced) resonators. The constant geometric and physical parameters of the array are given in Table 3.1, with reference to Figure 3.2. Other parameters for the array are $\tilde{l}_{\mathrm{c}} = 0.3$, $N_{\mathrm{c}} = 20$, $N_{\mathrm{n}} = 1$, $\tilde{l}_{\mathrm{n}} = 0.3$, $\tilde{d}_{\mathrm{n}} = 0.3$, which are dimensionless and are defined in § 5.2. The parameters of the initial condition are $\tilde{L} = 1.0$ and $u_{\mathrm{z}} = 400$ km/h, with reference to § 5.3. The value of σ is controlled solely by varying the spacing between the cavity walls, l_{ex}.

Figure 3.16 shows that there is only a small difference in the dimensionless tunnel pressure waveforms between the discrete and continuum resonator models, even for large values of the continuum distribution parameter (i.e. $\sigma > 2$). Small differences between the continuum and discrete model predictions may be due in

γ	p_0 (Pa)	T_0 (K)	μ ($\mathrm{kg\,m^{-1}s^{-1}}$)	μ_v/μ	Pr	$\mathcal{R}$ ($\mathrm{J\,kg^{-1}K^{-1}}$)
1.40	1.0e5	300	1.846e-5	0.6	0.707	287.1
$\dot{d}_\mathrm{t}$ (m)	β	w_1 (m)	h_1 (m)	h_2 (m)		
7.6	0.15	1.90	1.52	3.04		

Table 3.1: Reference physical and constant geometric parameters (unless stated otherwise), with reference to the demonstrative tunnel section in Figure 3.2.

part to the different automatic step sizes used by the DAE solver. For example, the discrete model uses a much smaller step size to resolve the discrete resonator positions compared to the continuum model, but then switches to a relatively large step size outside of the resonator interval.

The continuum and discrete models have also been compared for irregular resonator geometry (neck diameter and cavity length) in Figure 3.17, for $\tilde{d_{\mathrm{n},0}} = 0.3$, $\tilde{d_{\mathrm{n},1}} = 0.9$, $\tilde{l_{\mathrm{c},0}} = 0.9$ and $\tilde{l_{\mathrm{c},1}} = 0.3$, with reference to Table 5.1 and § 5.2.2. Differences between the continuum and discrete predictions are very small, even for $\sigma > 1$. The predicted waveforms for the irregular resonator geometry are significantly less oscillatory than those for the regular geometry. The resonators for the irregular geometry are excited for a range of natural frequencies, rather than at just one natural frequency for regular geometry. It is also important to note that the value of σ is an estimate, as the characteristic wavelength of the initial condition is not accurately known (see § 5.3).

3.5 Conclusions

An array of Helmholtz resonators has been proposed as a countermeasure to the problem of non-linear wave steepening in long concrete slab track tunnels. Non-linear steepening will increase the severity of pressure transients in the tunnel and the environmental noise emitted from the exit portals. A numerical modelling framework has been developed in this chapter to predict the propagation of pressure waves through a tunnel with an array of Helmholtz resonators. The assumptions of the physical model are justified within the context of high-speed

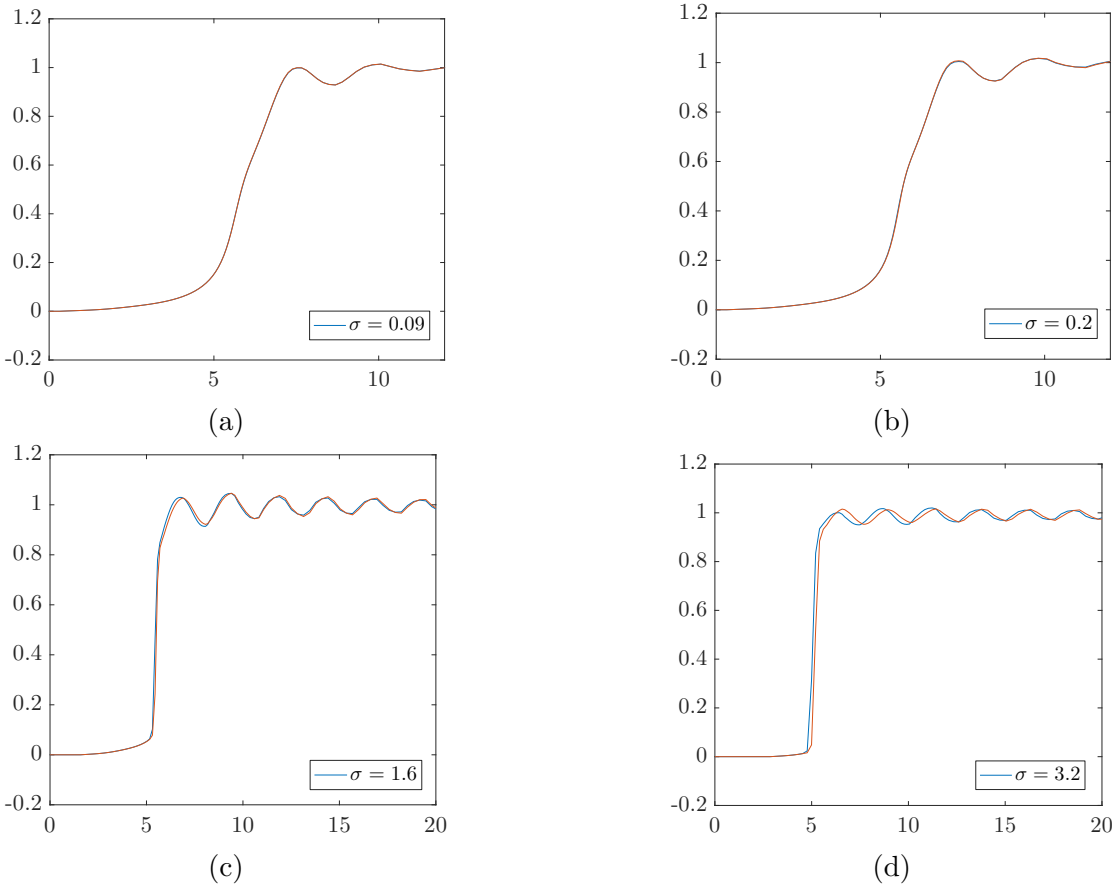
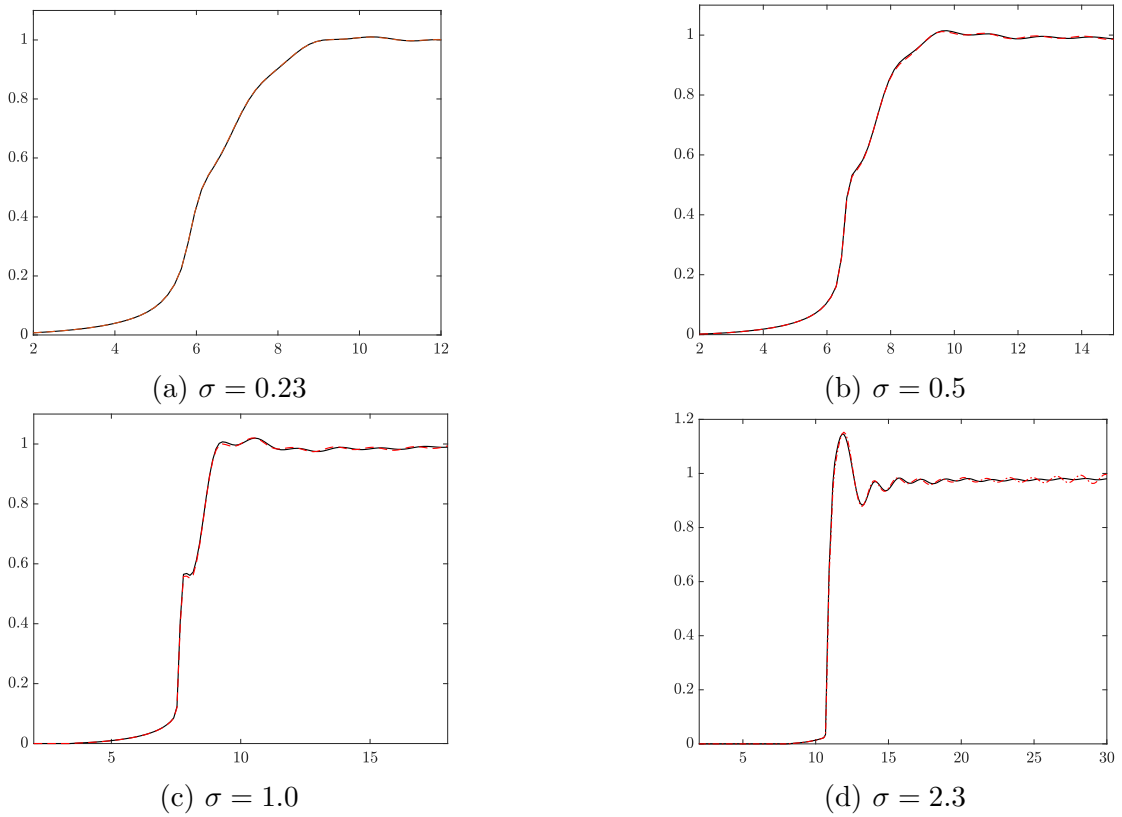


Figure 3.16: Dimensionless pressure waveforms for varying values of σ for an array of identical and equispaced resonators for the continuum (—); and discrete (—) far-field models.



(a) $\sigma = 0.23$

(b) $\sigma = 0.5$

(c) $\sigma = 1.0$

(d) $\sigma = 2.3$

Figure 3.17: Dimensionless pressure waveforms as a function of σ for an irregular array of resonators, using the continuum (——); and discrete (– – –) far-field models.

train aerodynamics in tunnels, i.e. plane wave propagation, negligible interaction between the resonators, a continuum distribution of resonators, weak acoustic non-linearity, and a lumped element approximation for the resonator response.

A fast and accurate numerical model is implemented. For example, high-order stencils including Weighted Essentially Non-Oscillatory schemes for shock capturing, and non-uniform grids are used. Non-local fractional derivatives, which represent the effect of the laminar boundary layer in the tunnel and resonator necks, are efficiently treated using a diffusive representation. However, the flexibility of the diffusive representation comes at the cost of additional fine-tuning by the user in order achieve accurate results, compared to conventional methods of evaluating fractional-order derivatives.

Several assumptions of the basic model are removed to account for bi-directional wave propagation and a discrete distribution of resonators, at the expense of increased computation time. Preliminary numerical tests indicate that the initial simplified model is adequate for the tunnel geometry considered. The numerical model presented in this chapter provides a framework for rapidly predicting the performance of an array of resonators. This can then be used as the basis of an optimisation procedure in long tunnels. It is proposed that the attenuation properties of the physical model could be improved by incorporating the following features as part of future work:

- The effect of porous media in the cavities (e.g. steel wool/foam), in order to increase viscous dissipation. This would be most effective against higher frequency pressure components (see Selamet et al., 2005).

- Remove the lumped element approximation for the resonator response, in order to allow long cavities to be accurately modelled (discussed in the next chapter).

- Increase the surface roughness of the tunnel wall, and/or more easily the neck of the resonators, in order to increase frictional losses. Quasi-steady friction in the resonator neck would need to be incorporated in the physical

model.

- Multiple sub-cavities, in order to break-up the pressure wave entering the cavity. This modification is only worth considering for long cavities and would require the lumped element approximation to be removed, but it may be more effective against lower frequency wave components compared to porous media.

Finally, it is suggested that the modelling framework is ported to a more efficient and non-proprietary programming environment/language, such as C++ or Python.

Chapter 4

Experimental Validation and Numerical Benchmarking

4.1 Introduction

A 1-D numerical model was developed in Chapter 3 to efficiently predict the distortion of a pressure wave propagating in a duct connected to an array of Helmholtz resonators. In this chapter the 1-D model is first validated against experimental data from a shock tube connected to a lattice of identical and equispaced Helmholtz resonators in § 4.2. The 1-D model is then benchmarked against a full scale and physically representative array embedded in the tunnel structure in § 4.3, for a range of resonator geometries and train operating conditions.

Constructing and testing an array Helmholtz resonators embedded in a full sized-tunnel system is impractical given the time and cost constraints of the project. Thus, it is necessary to use 3-D CFD. The array geometries are selected to compare differences between the 1-D and CFD predictions when the simplifying assumptions associated with the 1-D model are no longer expected to be valid.

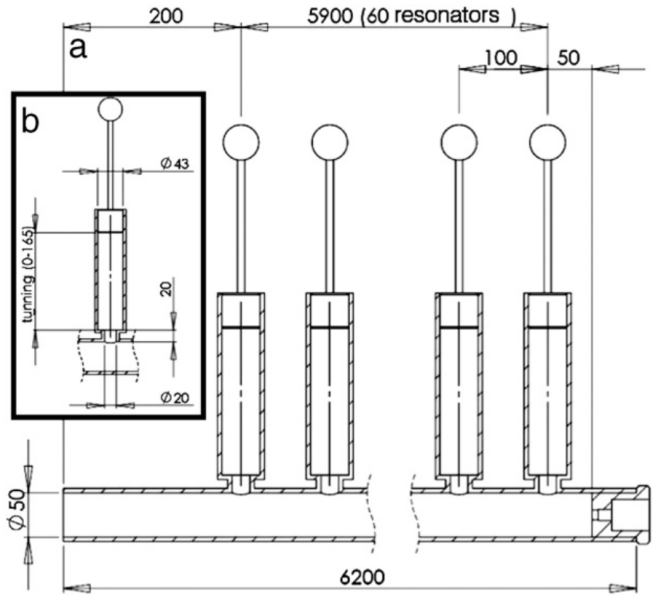


Figure 4.1: Experimental set-up (from Richoux et al., 2015) showing (a) the resonator lattice, and (b) one resonator. All dimensions are in mm.

4.2 Experimental Validation

4.2.1 Experimental and Numerical Configuration

The 1-D numerical models in § 3.2.4 and § 3.4.1 have been validated against experimental data kindly provided by Olivier Richoux of the Université du Maine, Le Mans, and Bruno Lombard of the Laboratoire de Mécanique et d'Acoustique, Centrale Marseille. A full description of the experimental configuration and equipment used is provided by Richoux et al. (2015).

The test rig consists of a waveguide connected to a lattice of equidistant and identical resonators (see Figure 4.1). The measured input pressure signal at $x = 0$ (see Figure 4.2a) is generated by the explosion of a latex balloon. It can be described as a gate signal with a maximum amplitude of 38.5 kPa and a width of approximately 1.5 ms, followed by a tail due to reflection from the end of the tube.

The input signal is sampled at $\upsilon_{\mathrm{s}} = 10$ kHz using linear interpolation and is converted to the far-field system variables using Equation 3.21 and 3.22, in order to be used as the initial condition to the far-field system in Equation 3.41.

Predictions from the far-field model after the initial pressure wave has propagated the full length of the array are time-shifted to account for the distance between the input signal and measurement position. The time shift is estimated from the advection speed in Equation 3.16a as:

$$\Delta t_{\text{init}} \approx \sum_{i=1}^{N_x-1} \frac{\Delta x_i}{A + B\overline{u_i}} = \sum_{i=2}^{N_x} \frac{x_i - x_{i-1}}{a_0\left(1 + \epsilon|\overline{f_i}|\right)} \tag{4.1}$$

where A and B are defined in Equation 3.17, Δx_i is the space step taken by the ODE solver at point i, N_x is the total number of steps and $\overline{u_i}$ is the mean axial particle velocity behind the wavefront at each space step (calculated using Equation 3.22). The accuracy of Equation 4.1 increases with the value of N_x.

The results are normalised by the magnitude of the sampled initial condition, p_{s}. The roughness height, h_{wall}, in Equation 3.20 is set to 0.0, in order to only simulate the effect of a laminar boundary layer in a smooth-walled duct. The power spectrum of the initial disturbance is plotted in Figure 4.3, where the frequency range excited by the source is mostly less than $\sim$ 800 Hz. Therefore, the characteristic frequency is approximated as the midpoint, $\upsilon \approx 400$ Hz, compared to $\sim$ 650 Hz from the width of the initial pulse. As is evident from the spectra, the use of a single characteristic frequency is no longer appropriate for accurately describing a signal excited over a large range of frequencies. This should be considered when calculating the non-dimensional parameters in § 3.2.2. For example, for this type of signal it may be more suitable to consider a range of characteristic frequencies. The physical and constant geometric parameters of the experimental configuration are given in Table 4.1.

4.2.2 Results and Discussion

A comparison of the experimental results and 1-D predictions are presented in Figure 4.2 for the waveguide with:

1. the initial pressure waveform at $x = 0$ - Figure 4.2a;

γ	p_0 (Pa)	μ ($\mathrm{kg\,m^{-1}s^{-1}}$)	ρ_0 ($\mathrm{kg\,ms^{-3}}$)	μ_v/μ	Pr
1.403	1.0e5	1.576e-5	1.177	0.6	0.708
r_t (m)	χ (m)	r_n (m)	l_n (m)	r_c (m)	h_c (m)
0.025	0.1	0.01	0.02	0.0215	0.07

Table 4.1: Physical and fixed geometric parameters used for experimental validation, with reference to Figure 3.1 and Figure 4.1. h_c and r_c are the height and radius of the cylindrical cavities.

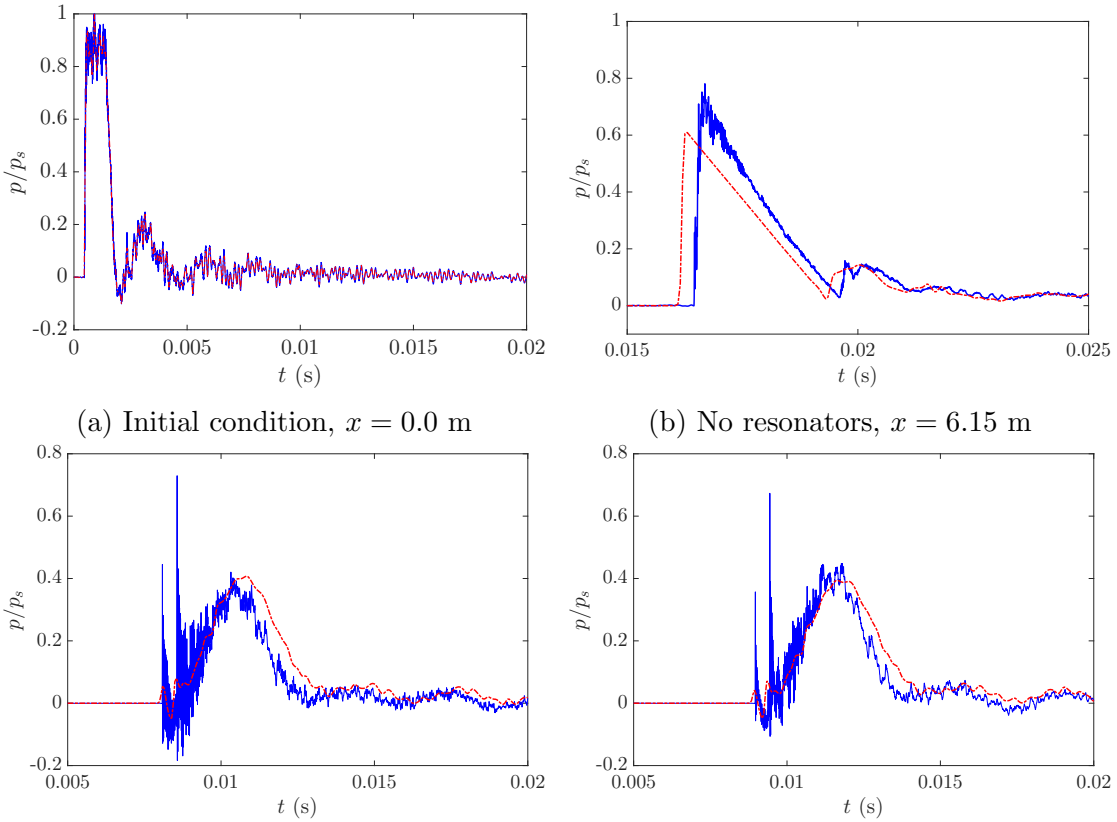
2. no resonators attached, with measurements at 6.15 m from the source - Figure 4.2b;

3. an array, with measurements at 2.8 m from the source - Figure 4.2c;

4. an array, with measurements at 3.1 m from the source - Figure 4.2d.

Good agreement with experiments is obtained for all of the test cases. Figure 4.2b reveals that the initial disturbance evolves towards a shock without the presence of the resonator array. Viscothermic losses from the laminar boundary layer are insufficient to prevent shock formation, but slightly erode the amplitude of the initial disturbance. In contrast, Figures. 4.2c and 4.2d show that the wavefront has evolved into a soliton with the presence of the array, due to the cancellation of dispersive effects and non-linear steepening. The presence of acoustic solitons is confirmed by Sugimoto (1992) and Sugimoto et al. (2004) in the inviscid regime with $\Omega \gg 1$ ($\Omega \approx 1.9$) in Equation 3.23, resulting in the Korteweg-de Vries equation (see § 3.2.4.1). A shock wave can no longer propagate in this case.

The values of the dimensionless parameters (defined in § 3.2.2) for this system with the resonators attached are: $\varphi \approx 0.08$, $\epsilon = 0.32$, $\kappa = 0.52$, $\sigma \approx 0.12$ and $\varpi \approx 0.08$. Parameters φ, σ and ϖ are stated as approximate values, due to the uncertainty in the value of the characteristic frequency. Good agreement with experiments is still obtained even with relatively large values for κ and ϵ (the model is valid for $\kappa \ll 1$ and $\sigma \ll 1$), which supports the results in § 3.4.1.3 and § C.3. These values are much larger than those expected for high-speed train operations in tunnels (see § 3.2.2).



(a) Initial condition, $x = 0.0$ m

(b) No resonators, $x = 6.15$ m

(c) With resonators, $x = 2.8$ m

(d) With resonators, $x = 3.1$ m

Figure 4.2: Normalised pressure-time histories in the waveguide. The lines in (a) represent raw experimental data sampled at 250 kHz (——); and sampled data at 10 kHz (- - - -). The lines in (b)-(d) represent experimental data (——); and predictions (- - - -).

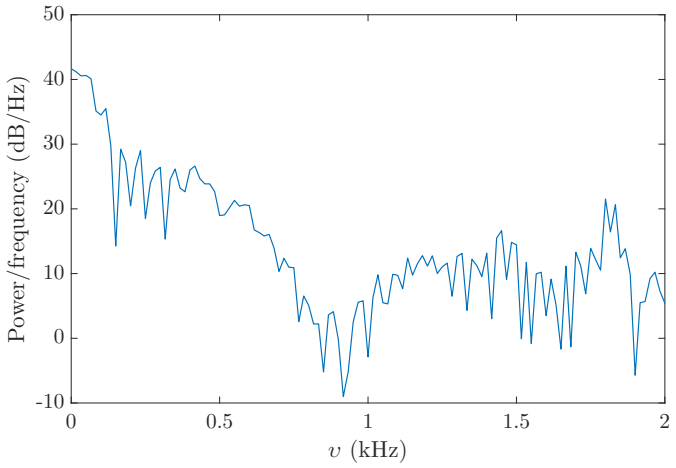


Figure 4.3: Power Spectral Density (PSD) for the initial condition in Figure 4.2a.

4.3 3-D CFD Benchmarking

4.3.1 Overview

The far-field model has been validated against small-scale shock tube experiments in Section 4.2. However, it is infeasible to validate the model against a real high speed train-tunnel system, considering the time and cost constraints of the project. Therefore, the 1-D predictions have been benchmarked against CFD in order to provide insight into the validity of the underlying assumptions. OpenFOAM 3.0.x (Weller and Tabor, 1998) has been used to mesh and solve the 3-D CFD models for a variety of test cases (refer to § 2.7.3 for an overview of OpenFOAM).

As far as the author is aware, the only case of an array of Helmholtz resonators being tested in a full scale tunnel system was on a small section of the Tohuku Shinkansen (see Takayama et al., 1995). Perforated aluminium side walls (1.5 m wide and 30 mm thick) were installed either side of the tunnel for a length of 200 m. Up to a 30% reduction in the MPW overpressure was measured for a wavefront with an amplitude of 2 kPa, generated by a train operating at 200 km/h. This result demonstrates the potential effectiveness of this countermeasure, even over a relatively short stretch of the total tunnel length.

4.3.2 Model Configuration

4.3.2.1 Solver and Time Marching

The propagation of pressure waves in the tunnel is modelled using the semi-implicit solver `pisoCentralFoam` (Kraposhin et al., 2015), which blends the compressible Pressure Implicit with Splitting of Operator (PISO) algorithm (see Issa, 1986; Moukalled et al., 2015) for coupling between velocity and pressure with the density based central-upwind scheme of Kurganov and Tadmor (2000) (KT) for evaluating convective non-oscillatory fluxes. The solver blends the fluxes of the two methods depending on the local Mach number and Courant-Friedrichs-Lewy (CFL) condition (see Ferziger and Peric, 2012) across each cell. The hybrid scheme can operate efficiently over a wide range of Mach numbers, compared to using either scheme

alone. The KT scheme is implemented independently in `rhoCentralFoam` (Greenshields et al., 2010), and the compressible PISO scheme is implemented in the blended PISO-SIMPLE solver, `rhoPimpleFoam`.

Schemes which have been tested for time marching include the 1st order backwards Euler, 2nd order Crank-Nicolson and 2nd order upwind (Adams-Moulton) (see Ferziger and Peric, 2012; Jasak, 1996). A second order accurate scheme is desirable in order to accurately resolve transient phenomena with minimal numerical diffusion. The unbounded Adams-Moulton (second order backwards difference) and Crank-Nicolson schemes were found to introduce non-physical pressure oscillations, which is associated with dispersion from the 3rd order derivative in their Taylor expansions. Instead, a blended (1st - 2nd order) Euler-Crank-Nicolson scheme is used to provide physical boundedness, i.e. prevent non-physical quantities in the solution. Pressure oscillations with non-physical amplitudes were not apparent in the solution with a blending factor of less than 0.4 (0 is pure Euler and 1.0 is Crank-Nicolson). The time-step size is given by:

$$\Delta t = \min\left(\frac{1}{10\upsilon_{\mathrm{s}}}, \Delta t_{\mathrm{CFL}}\right) \tag{4.2}$$

which provides at least 10 points over the period of the sample frequency, υ_{s}, and satisfies the acoustic CFL condition for numerical stability. This solver is able to reproduce acoustic waves, provided that CFL < 1 and the mesh resolution is greater than 20 cells per resolved wavelength (Kraposhin, 2016). CFL ≤ 0.4 was generally found to be necessary to maintain stability and physical boundedness with the blended 1st - 2nd order time marching scheme. $\upsilon_{\mathrm{s}} = 10\max(\upsilon_0, \upsilon_L)$ was chosen in order to encompass the natural frequency of the resonators, υ_0, and characteristic frequency of the initial condition, where $\upsilon_L = a_0/L$ (see § 5.1).

The Reynolds number for the flow in the tunnel and the resonator necks is estimated to be $O(1-10\mathrm{e}6)$ and $O(1-10\mathrm{e}5)$, respectively. Therefore, it is assumed that the bulk flow is fully developed and the models can be solved in the inviscid regime. For example, a pressure drop of less than 0.5% is predicted due to steady wall friction over the length of the array ($\tilde{l_{\mathrm{a}}} < 5$) by using the Colebrook-White

equations (see Equation 3.20) with a concrete roughness height of $h_{\text{wall}} = 1.0$ mm (The Engineering Toolbox, 2016).

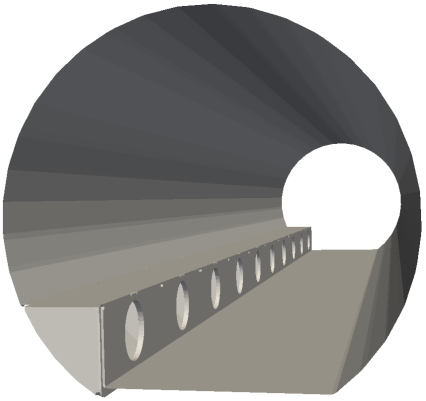
4.3.2.2 Mesh Generation

The 3-D models have been created in the SolidWorks (Dassault Systèmes, 2013) computer-aided design (CAD) software based on the representative array geometry in Figure 3.2, and meshed using the `snappyHexMesh` tool provided with OpenFOAM. The structured mesh is composed of hexahedra and split-hexahedra cells. All internal walls have a nominal thickness of 0.05 m. In comparison, it is assumed for convenience that the walls are infinitesimally thin for the 1-D model.

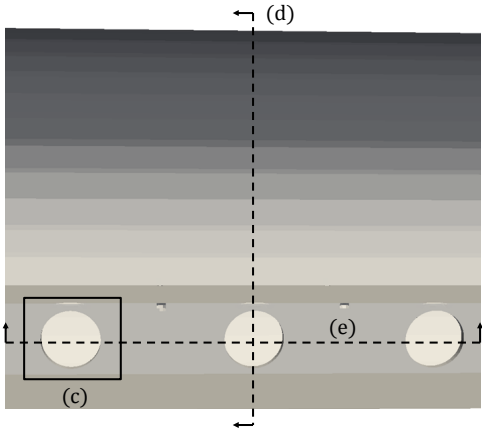
The maximum cell size is given by $\Delta x_{\max} = L/10$, which provides at least 10 cells over the steepest part of the wavefront for the initial condition (see Figure 5.1). Additional mesh refinement is prescribed around the resonator necks and tunnel walls (see Figure 4.4), with a minimum cell size of $\Delta x_{\max}/128$ (approx. 5 mm for $L = d_{\text{t}}$ m). A mesh convergence test for Case 4 (defined in Table 4.2) indicates that this mesh definition provides adequate spatial accuracy for the purpose of benchmarking the 1-D models (see § 4.3.3). The geometry of the array is defined using the Standard Triangle Language (STL) file format. Three STL files are used for each case so that different levels of mesh refinement can be prescribed for different parts of the array, which are: (1) the resonator necks; (2) the region preceding the array for the initial condition and (3) the tunnel section containing the array.

4.3.2.3 Initial Condition

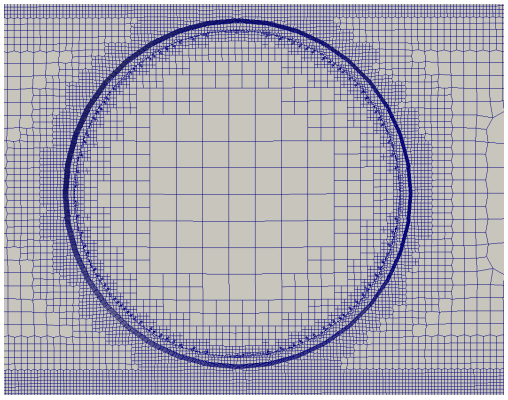
The scaled form of the characteristic entry compression wave generated by a high-speed train entering a tunnel (see § 5.3.1) is prescribed as a 1-D planar pressure field, $p_0 + p(x)$, at $t = 0$, in a region just upstream of the array (see Figure 4.6). The corresponding initial velocity field is given by the linear approximation $u(x) = p(x)/\rho_0 a_0$, with $u(y) = u(z) = 0$ (i.e. a planar wave), assuming no disturbance has propagated upstream. This is based on the approach used by Aoki et al. (1999)



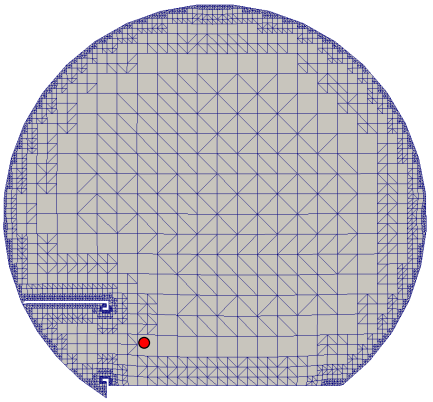
(a) 3-D overview of the array



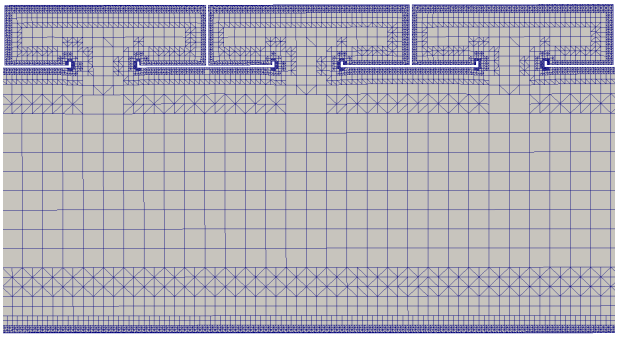
(b) Vertical cut along the centre of the tunnel



(c) Close-up of the neck

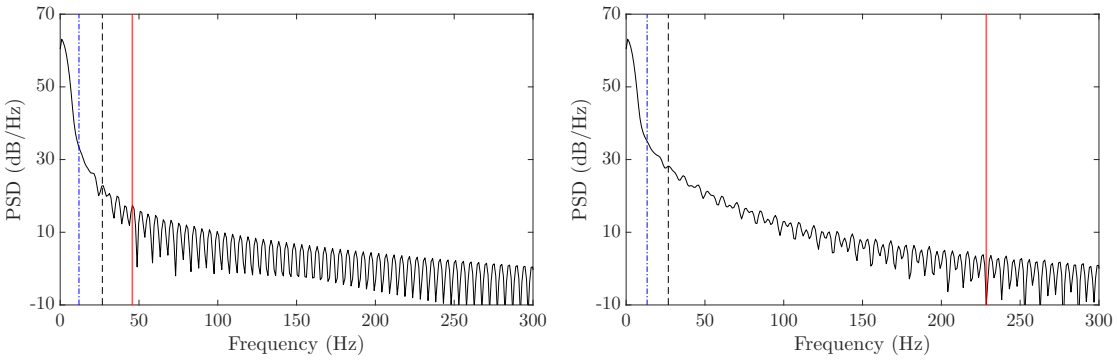


(d) Cut across the tunnel diameter



(e) Horizontal cut along the tunnel

Figure 4.4: Mesh for Case 3 (see Table 4.2). The dot near the resonator neck in (d) is the position of a pressure-distance line plot through the tunnel length.



(a) $\tilde{L} = 1.0$, $\upsilon_s = 457$ Hz (b) $\tilde{L} = 0.2$, $\upsilon_s = 2288$ Hz

Figure 4.5: PSD versus frequency for the scaled initial pressure waveform. The vertical lines denote the: estimated characteristic frequency (----); first non-planar cut-on frequency for a circular duct (– – –); frequency corresponding to the wavefront length (L) (—).

for the propagation of pressure waves through an expansion chamber mounted at the exit of a tunnel.

Alternatively, the initial condition could be prescribed as a time-dependent boundary condition at the upstream boundary. Defining the IC as a BC would significantly reduce the size of the mesh, as the large region upstream of the array reserved for the IC ($0 \leq x \leq 2b$ in Figure 4.6) could be removed. However, the author is unaware of a simple way to combine a time-dependent and non-reflective boundary condition in OpenFOAM (as of February 2017), which is necessary in order to prevent non-physical reflections from the upstream boundary.

Power Spectral Density (PSD) plots of the initial pressure waveforms used in the 3-D analysis (see Figure 4.5, with reference to Table 4.2), indicate that the signal energy is distributed over a wide range of frequencies (0 - 150 Hz). A single characteristic frequency may not be adequate to describe this type of signal. A large proportion of the signal power appears to be contained in frequencies below both the approximate characteristic frequency (calculated using Equation 5.8) and the first non-planar cut-on frequency for a circular duct (see § 3.2.2). Therefore, the continuum distribution (σ), lumped element (ϖ), and non-planar cut-on frequency (φ) parameters (calculated using Equations 3.9 - 3.15) are likely to be overestimated.

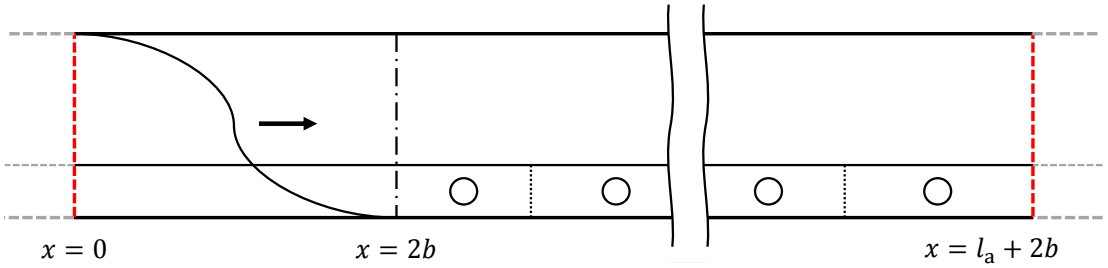


Figure 4.6: Vertical cut through the length of the 3-D model (not to scale) at $t = 0$, showing the location of the IC ($0 \leq x \leq 2b$), array ($2b < x \leq l_a + 2b$) and the upstream ($x = 0$) and downstream ($x = l_a + 2b$) boundaries. Also, see Figure 4.4b.

4.3.2.4 Boundary Conditions

Non-reflective boundaries conditions (NRBCs) are used both up and downstream from the array for all fields. NRBCs are implemented using the `waveTransmissive` BC, which solves the following condition for the outgoing characteristics in 1-D at the boundary (Poinsot and Lele, 1992):

$$\frac{\mathrm{D}}{\mathrm{D}t}(\psi, u) = 0 \tag{4.3}$$

where D is the material derivative and ψ is the field being solved. This BC implies that there are no reflections from the far-field into the working section, i.e. an infinitely long and smooth tunnel outside of the boundaries. A direct comparison with the BCs in the 1-D model cannot be made, as the BCs are prescribed on time in the 1-D model (see § 3.3.6). However, the 1-D far-field model can be considered to be analogous to spatial boundaries which are moving at approximately the same acoustic speed as the wavefront.

At the walls, zero-gradient boundary conditions are assigned for pressure and temperature, while the slip condition is prescribed for velocity, i.e. $u \cdot \mathrm{n} = 0$. The zero-gradient condition is a special case of the Neumann boundary condition where the gradient normal to the boundary is set to zero. The wall shear stress is zero for the slip condition, as required for inviscid flow.

The number of grid points and hence the simulation time of the 3-D models could be significantly reduced if the initial condition is applied as a time-dependent

boundary condition at the upstream boundary, instead of as an initial pressure and velocity field upstream of the array. This was not possible, as the functionality does not currently exist in OpenFOAM (as of March 2017) to combine a time-dependent and non-reflective boundary condition.

4.3.2.5 Solver Settings

The linear equation system is solved using the iterative diagonal incomplete-Lower-Upper preconditioned Bi-conjugate gradient stabilised solver (PBi-CGSTAB) (van der Vorst, 1992) for all fields, except density which is solved explicitly. The Bi-CGSTAB solver provides greater flexibility than the Bi-CG and CG solvers, with no requirement for the matrix being Symmetrical Positive Definite. Corrections are applied for skewed and non-orthogonal meshes by evaluating gradients using the method of least-squares (see § 4.3.3) and applying one non-orthogonal correction loop on the pressure equation (Ferziger and Peric, 2012; Jasak, 1996; Moukalled et al., 2015). Highly skewed and non-orthogonal meshes can introduce significant error and numerical diffusion into the solution (Rhoads, 2014).

A TVD flux limiter (described in § 3.3.3.1) is used for the evaluation of the convective fluxes to avoid non-physical oscillations around discontinuities (see § 4.3.3). Similarly, multi-dimensional gradient limiters are used for the velocity field in order to maintain physical boundedness (see Nozaki, 2014). The gradient limiter ensures that the face-extrapolated cell values using the gradient are physically bounded by the minimum and maximum values of the neighbouring cells.

The models, with between 1-4 million cells each were solved in parallel on an 8-core Intel Xeon processor. OpenFOAM uses domain decomposition to partition the mesh and the associated fields to be solved on each processor. The Open-MPI (Gabriel et al., 2004) implementation of the message passing interface (MPI) is used for parallelisation. The parallel-threaded PT-scotch algorithm (Chevalier and Pellegrini, 2008) is used to minimise the number of processor boundaries, and hence the communication overhead between the processors. A batch script is used to automate the model set-up, where the steps for pre and post-processing are

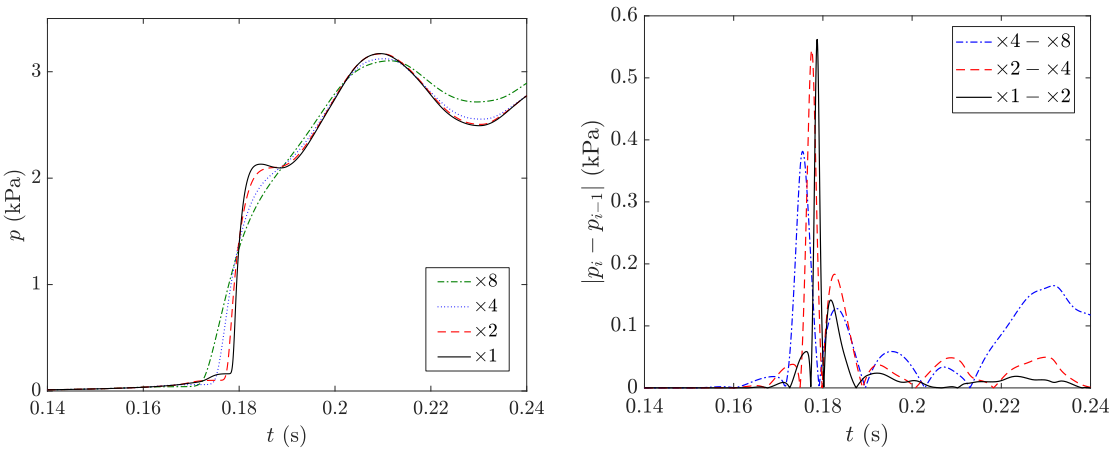
provided in § D.1.

4.3.3 Mesh Sensitivity and Flux Limiter Selection

A mesh sensitivity analysis has been carried out for Case 4 in Table 4.2. This represents the most severe case, as it features a combination of steep gradients and large amplitude smooth oscillatory behaviour (see Figure 4.7). The mesh sensitivity is measured using the area-weighted average pressure-time profile across the downstream boundary. The reference mesh is referred to as $\times 1$, which permits a maximum cell length of $\Delta x_{\max} = L/10$ m, in order to adequately resolve waves of length L m (see § 5.3.1). Comparisons are then made against meshes where the cells are two-times ($\times 2$), four-times ($\times 4$) and eight-times ($\times 8$) longer than the maximum cell size of the reference mesh.

Figure 4.7b plots the residuals between two successive pressure waveforms (for example, the absolute value of the difference between the waveforms for $\times 1$ and $\times 2$). Therefore, there are three residual waveforms in Figure 4.7b and four pressure waveforms in Figure 4.7a. The pressure residuals decrease relatively quickly with a reduction in mesh size in the smoothly varying regions, compared to the steepest part of the wavefront. Additional mesh refinement (e.g. $\times 0.5$) would significantly increase the simulation time for cases with a steep incident wave (i.e. a total number of cells of $O(10e6)$). The current mesh ($\times 1$) is deemed to be sufficiently accurate to act as a quantitative benchmark for the 1-D numerical model, based on these tests.

The effect of the choice of flux limiter (refer to § 3.3.3.1) for the convective terms and the discretisation scheme of the gradient terms is plotted in Figure 4.8, for Case 4. The standard Green-Gauss linear scheme (Moukalled et al., 2015) for gradients provides formal 2nd order accuracy, but only on purely orthogonal grids. On the other hand, least-squares (LS) discretisation provides greater flexibility in the order of accuracy on arbitrary grids. However, it is known to incur a greater computational cost than Green-Gauss gradients, as the stencil weights must be calculated during execution. The difference in simulation time for Case



(a) Pressure-time histories

(b) Pressure residuals

Figure 4.7: Mesh sensitivity study for Case 4 using the van Leer flux limiter and 2nd order accurate least-squares gradient discretisation.

4, solved with least-squares and Gauss linear gradients for a range of grid sizes was negligible. The choice of 2nd or 4th order accurate least-squares gradient discretisation (LS2 and LS4, respectively) does not appear to make much difference to the solution when coupled with the Superbee limiter (Roe, 1986), at least for the cell sizes considered.

The Superbee limiter resolves the steepest part of the wavefront as effectively as the van Leer limiter on a mesh where the maximum cell length is four times larger. However, the Superbee limiter introduces artificial sharpening/squaring in smooth oscillatory regions. This phenomenon is a well documented downside of this limiter (Berger et al., 2005; Kemm, 2011). The MC (known as MUSCL) limiter (van Leer, 1974) (defined in § 3.3.3) performs similarly to the van Leer limiter for the same mesh resolution.

4.3.4 Model Cases

Table 4.2 lists the dimensions of the array configurations used for the comparative study, based on the tunnel geometry in Figure 3.2. The corresponding dimensionless parameters used to quantify the validity of the assumptions of the 1-D model (see § 3.2.2) are provided in Table 4.3. The resonator geometry and incident wavefront shapes have been chosen in order to test the 1-D modelling assumptions

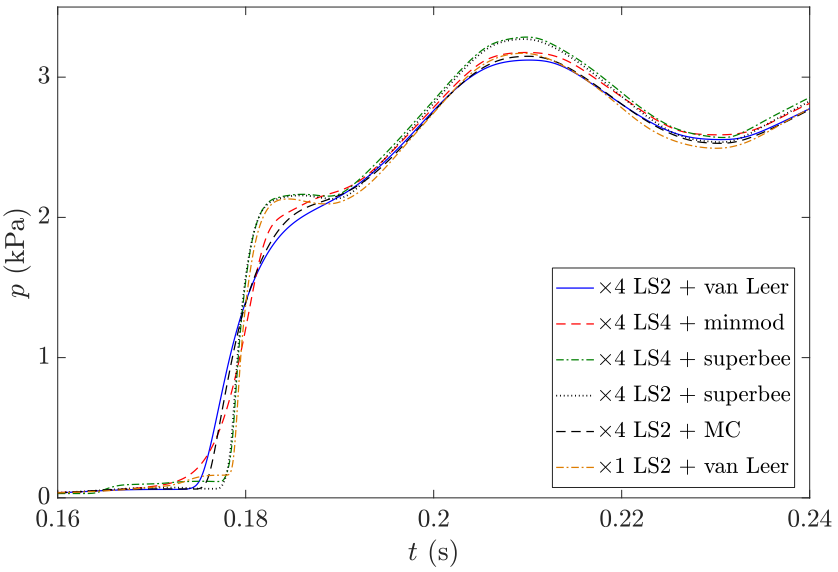


Figure 4.8: Pressure-time histories for Case 4, for a range of flux limiters and gradient discretisation methods.

when applied to a demonstrative tunnel system (see Table 3.1):

- The continuum distribution approximation (σ) is tested in Cases 1 & 2 by varying the cavity interval distance, χ.
- Case 1 also attempts to violate the lumped element approximation (ϖ) by using long cavities, but maintains the same cavity interval distance as Case 2.
- Cases 3 & 4 are geometrically identical and compare the effect of the steepness of the initial wavefront, which is controlled by parameter L (see Figure 5.1).
- Cases 5 & 6 test the assumptions of weak acoustic non-linearity and negligible wave reflection, respectively. Case 5 is geometrically identical to Case 4, but assumes a very high train speed ($u_z = 700$ km/h) in order to generate an entry wave with an amplitude which is expected to be greater than any current or near-future high speed train (i.e. $p_1/p_0 \approx 0.11$).
- Case 6 uses an unrealistically large cavity cross-section to generate a large value of κ (i.e. $\tilde{w}_1 = 0.15$, $\tilde{h}_1 = 0.1$ in Figure 3.2). The degree of wave

case	N_c	d_n	l_c	l_n	l_a	l_{ex}	ω_e	$\tilde{L}$	p_1
-	-	(m)	(m)	(m)	(m)	(m)	(rad s^{-1})	-	(kPa)
1	2	1.24	19.0	0.12	38.0	0.0	71.0	0.2	2.81
2	2	1.24	3.80	0.12	22.8	15.2	161.0	0.2	2.81
3	10	1.24	3.80	0.12	38.0	0.0	161.0	1.0	2.81
4	10	1.24	3.80	0.12	38.0	0.0	161.0	0.2	2.81
5	10	1.24	3.80	0.12	38.0	0.0	161.0	1.0	10.79
6	10	1.24	3.80	0.12	38.0	0.0	87.9	1.0	2.81

Table 4.2: Array configurations used for the comparative study. p_1 is calculated from Equation 2.7 with the parameters in Table 3.1 and $u_z = 400$ (Cases 1-4, 6), and 700 (Case 5) km/h. The array geometry is defined in § 5.2.2.

case	σ	ϖ	φ	κ	ϵ
1	0.73	0.73	0.5	0.04	0.04
2	0.73	0.15	0.5	0.04	0.04
3	0.13	0.13	0.4	0.04	0.04
4	0.13	0.13	0.5	0.04	0.04
5	0.13	0.13	0.5	0.04	0.13
6	0.13	0.13	0.5	0.13	0.04

Table 4.3: Dimensionless parameters for 1-D model assumptions (see § 3.2.2). Parameters σ, φ, and ϖ are based on the estimated characterstic frequency of the incident wavefront.

reflection and the interaction between neighbouring resonators is unlikely to be negligible.

4.3.5 Results

The predicted pressure waveforms at the end of the arrays are compared in Figure 4.9, considering the 1-D inviscid linear ($U = W = 0$ in Equation 3.23b) and non-linear resonator response. The 1-D viscous predictions with the non-linear resonator response are also plotted for comparison. 1-D inviscid predictions are found by setting the kinematic viscosity to a small non-zero number (e.g. $\nu \times 1.0\text{e}{-6}$).

The 1-D waveforms from the far-field system in Equation 3.23 are first changed to the near-field variables using Equations 3.21 and 3.22, and then time-shifted using Equation 4.1 to be consistent with the 3-D model. The 3-D waveforms are

obtained from the area-weighted average pressure across the downstream boundary at each time step using the `patchAverage` function from the Swak4Foam toolbox (Gschaider, 2013) for OpenFOAM. The area-weighted average pressure across a boundary is defined by (Gschaider, 2014):

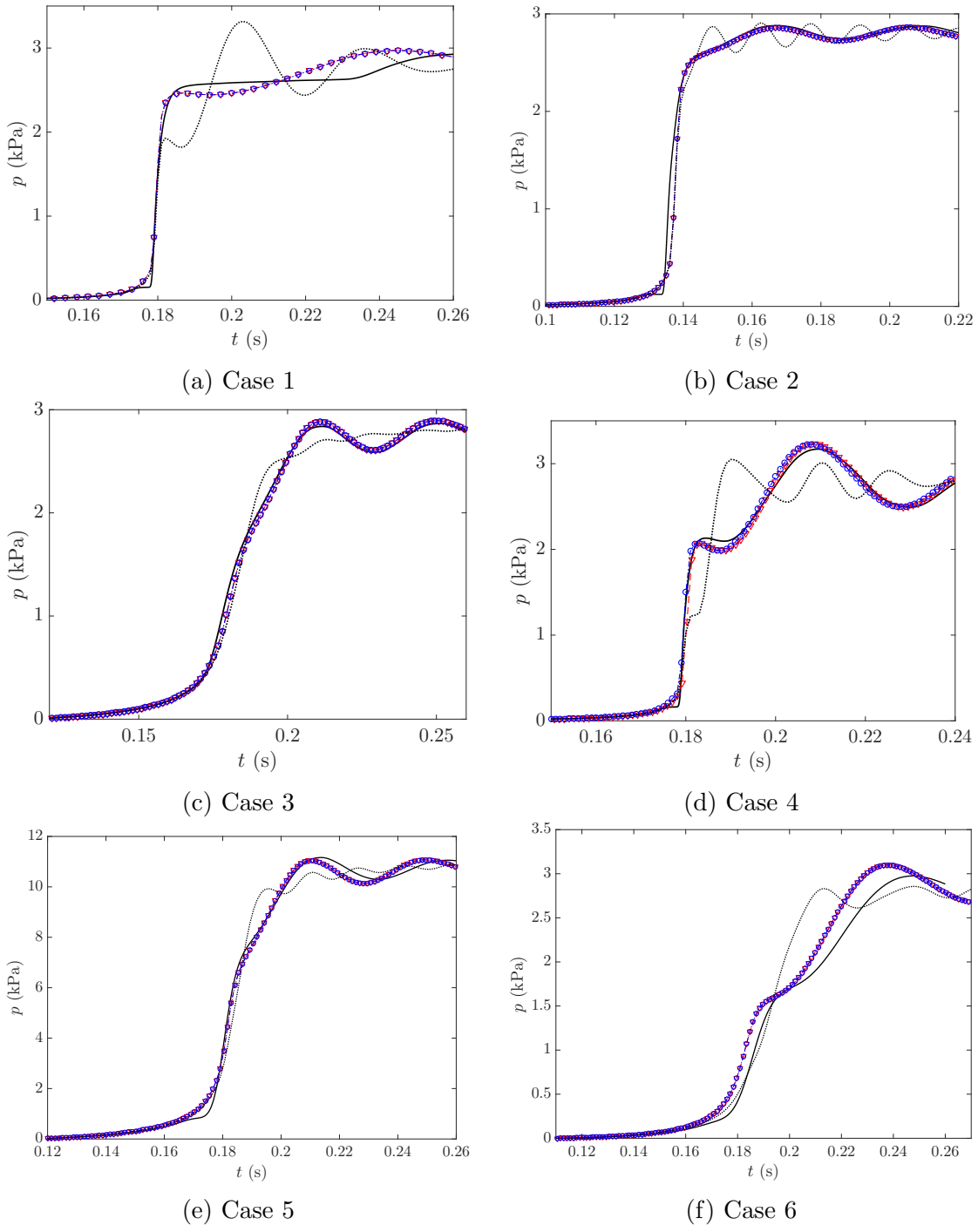
$$\overline{p}(t) = \frac{\sum_{i=1} p_i(t) S_i}{\sum_{i=1} S_i} \tag{4.4}$$

where S_i is the face area of cell i at the boundary, and p_i is the corresponding pressure at the cell face.

As anticipated, there is negligible difference between all of the 1-D viscous and inviscid waveforms in Figure 4.9, considering the relatively short length of the array. The 1-D linear resonator response produces spurious oscillations in all cases, indicating that non-linear dissipation associated with the flow field around resonator neck cannot be neglected. This result also supports experimental observations (Richoux et al., 2015; Sugimoto et al., 2004). An example of the flow field in the resonator is shown in Figure 4.10, for Case 6. There is a clear difference between the inflow and outflow patterns at the neck.

It was intended that the assumption of a continuum distribution of resonators would no longer hold for Cases 1 and 2 (see Figure 4.9), where $\sigma \approx 0.7$. However, there was still good agreement between the 1-D and 3-D predictions for Case 2. This result matches with observations in § 3.4.1.3, where good agreement was also obtained between the 1-D models accounting for a continuum and discrete treatment of the resonators, even for large values of $\sigma > 1$. In addition, it was suggested from the PSD plots in § 4.3.2.3 that the predicted value of σ may be overestimated.

On the other hand, there is poor agreement between the waveforms for Case 1 in Figure 4.9a. This case is intended to violate the lumped element approximation for the resonator response, which is apparent from the pressure contours for the 3-D model for Case 1 (see Figure 4.11). The wave propagation time in the cavity can no longer be assumed to be negligible (i.e. a non-uniform pressure field), resulting in an apparent delay in the resonator response. For example,



(a) Case 1

(b) Case 2

(c) Case 3

(d) Case 4

(e) Case 5

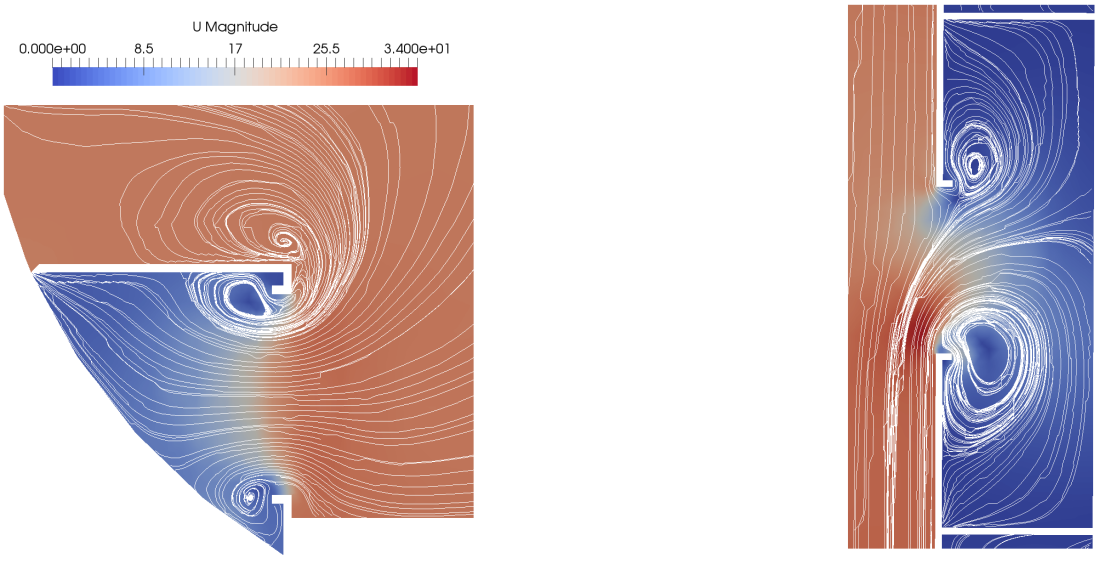
(f) Case 6

Figure 4.9: Comparison of waveforms for the array configurations in Table 4.2 for: 3-D inviscid (—); 1-D viscid (—○—); 1-D inviscid (—▽—); 1-D viscid with linear resonator response (····).

the pressure-distance profile in Figure 4.11e reveals a "blip" at $x \approx 60$ m, where the waves reflected from the far cavity walls have returned to the neck of the resonator. This delayed response occurs after the tunnel pressure wavefront has propagated approximately 23 m since passing the resonator neck, which is similar to the distance propagated by the reflected wave in the cavity (approximately 19 m). The delayed resonator response manifests as a phase lag between the 1-D and 3-D predictions in Figure 4.9a.

As expected, there is good agreement between the 1-D and 3-D predictions for Cases 3 and 4, which have relatively small values for all of the dimensionless parameters in Table 4.3. The amplitude of the upstream oscillations in Case 4 (Figure 4.9d) are comparable to the initial pressure rise. The use of irregular resonator geometry, and hence a variable natural frequency, could be used to break these large oscillations into several smaller ones, which is considered in § 5.7.2. Good agreement is obtained for Case 5 in Figure 4.9e, considering that the amplitude of the incident wavefront is larger than expected for modern and future high-speed rail operations in tunnels. There is a small but noticeable phase lag between the 1-D and 3-D predictions for the upstream oscillations.

There is a noticeable time delay between the 1-D and 3-D predictions in Case 6 (see Figure 4.9f), which most likely arises from the relatively large value of κ. Sugimoto et al. (1999) posit that the wave propagation speed of an acoustic soliton is bounded by $a_0/(1+\kappa/2) < u < a_0$. Therefore, larger values of κ will reduce the lower bound of the propagation speed in the tunnel. The assumption of negligible resonator interaction and reflection is no longer valid for sufficiently large values of κ. This is expected to result in a noticeable reduction in the amplitude of the downstream propagating wavefront as a small portion of acoustic energy is reflected by each resonator. For example, the maximum amplitude predicted by the 3-D model is approximately 120 Pa less than the 1-D model at the end of the array. Consequently, the rate of non-linear wave steepening (which is amplitude dependent) is reduced (as seen in the 3-D waveform), resulting in a reduction in the wavefront speed, and hence a time lag in the waveform predicted by the 3-D



(a) cut (d) (b) cut (e)

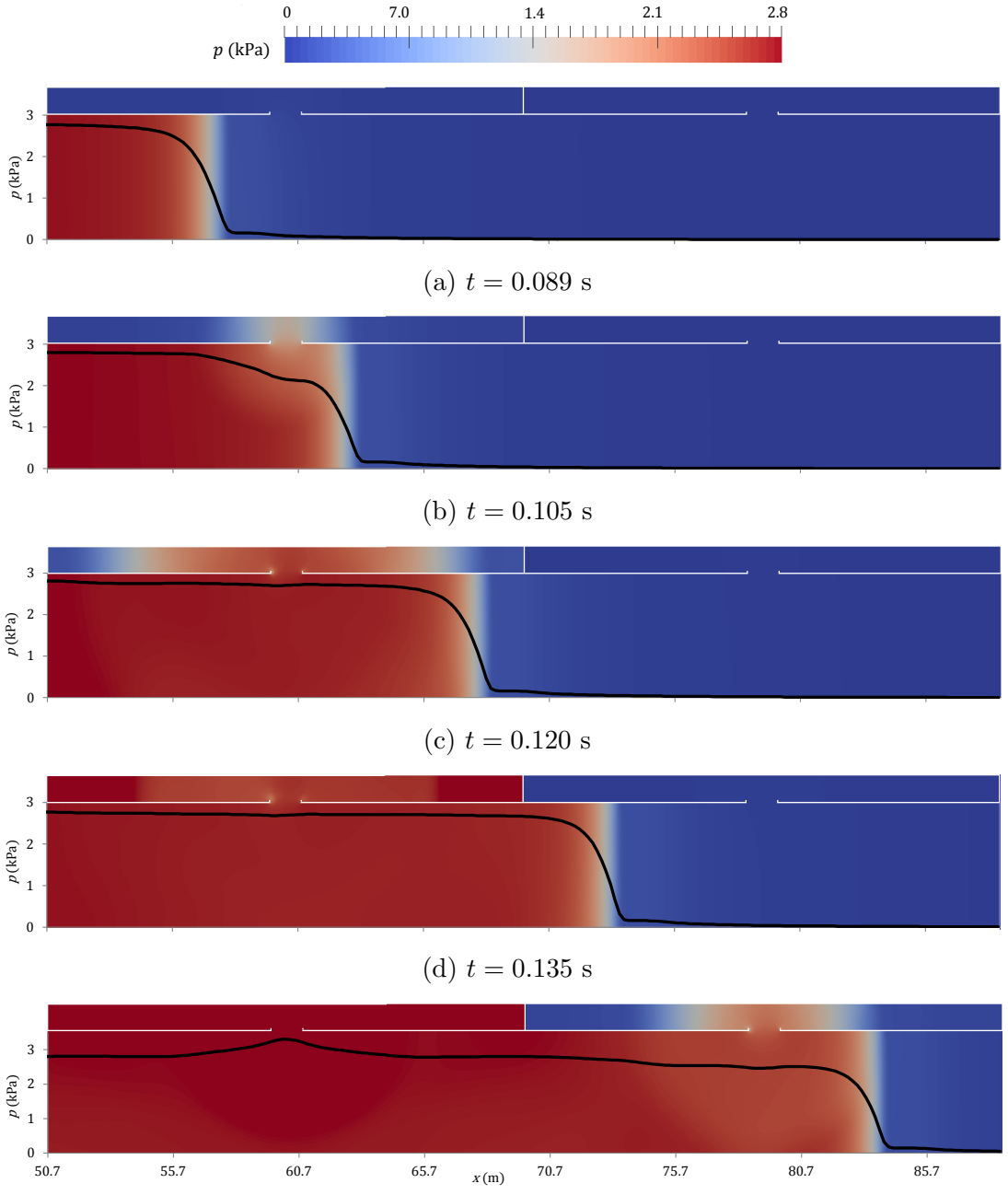
Figure 4.10: Velocity magnitude field ($\mathrm{m\,s^{-1}}$) and streamlines for one of the resonator cavities, with reference to Figure 4.4, at $t = 0.12$ s in Case 6.

model. Even with this apparent lag, the 1-D model still accurately resolves the features of the propagating wave.

4.3.6 Discussion

A 3-D benchmarking exercise has been used to identify the limitations of the 1-D model. The lumped element approximation is an important parameter to consider if long resonator cavities are desired. It can have a significant impact on the physical accuracy of the predictions, particularly on the upstream oscillations following the initial pressure rise of the wavefront. The results suggest that the assumption of negligible interaction between neighbouring resonators is unlikely to be an issue for an array embedded in the tunnel structure, due to the limited cross-sectional area of the cavities. For example, an impractically large value of $\kappa \approx S_\mathrm{c}/S_\mathrm{t} \approx 0.13$ was tested, resulting in a temporal delay between the 1-D and 3-D waveforms. Despite this, the shape of the transmitted waveform was accurately represented by the 1-D model.

A large value of $\sigma \approx 0.7$ for the continuum distribution parameter did not appear to have much effect on the physical accuracy of the model. However,



(a) $t = 0.089$ s

(b) $t = 0.105$ s

(c) $t = 0.120$ s

(d) $t = 0.135$ s

(e) $t = 0.165$ s

Figure 4.11: Pressure contours for cut (e) in Figure 4.4 for Case 1, overlayed with the pressure-distance plot at the point in Figure 4.4d over the length of the array.

it is suggested that the value of σ is overestimated for the incident waveform considered in the analysis. There was very little difference between the 1-D and 3-D predictions for a high amplitude incident wavefront which gives a value of ϵ that exceeds what is expected for modern and future high-speed rail operations in tunnels (see § 3.2.2).

It is noted that this benchmarking exercise has been performed for a relatively short array length ($\tilde{l_{\mathrm{a}}} < 5$), due to limited computational resources for 3-D CFD. Indiscernible physical differences between the predictions due to the underlying assumptions of the 1-D model may become more pronounced for longer array lengths (e.g. $\tilde{l_{\mathrm{a}}} \approx O(50)$).

Two approaches are proposed for resolving the issue of large cavities that violate the lumped element approximation in the 1-D model. The first is to consider the equation of motion along the longest dimension of the cavity (in this case the length, l_{c}), in addition to just continuity (p.61 Sugimoto, 1992). The response of each resonator would then be described by a PDE, rather than an ODE. This approach could significantly increase the computational overhead of the model (particularly if there are many cavities), but it would accurately capture the delayed response of the resonators. A simpler but more restrictive approach is to place an upper limit on the maximum length of each cavity, based on the characteristic wavelength, so that the lumped parameter approximation is always satisfied. The second approach can be implemented for optimisation using non-linear constraints (see § 5.5.3).

4.4 Conclusions

The numerical model developed in Chapter 3 has been validated against experimental data from a shock tube connected to a lattice of equidistant and identical resonators. Good agreement with experiments was obtained, particularly considering that the parameters used to quantify the assumptions of negligible wave reflection/interactions ($\kappa \ll 1$) and weak acoustic non-linearity ($\epsilon \ll 1$) (see § 3.2.2) were relatively large. Crucially, the predicted values of these parameters are much

larger than what is expected for high-speed rail operations in tunnels. Therefore, the 1-D model should remain valid (at least for parameters κ and ϵ) when scaled to a full-scale high-speed rail tunnel system.

Subsequently, the 1-D model was benchmarked against inviscid 3-D models in OpenFOAM, for a representative full-scale tunnel system with an array of Helmholtz resonators. Good agreement was obtained for a variety of cases which were designed to violate different assumptions of the 1-D model. The primary exception was where the cavity length was comparable to the characteristic wavelength of the incident compression wave, violating the lumped element approximation. The finite wave propagation speed in the cavity manifests as a phase lag in the response of the resonator when compared to the 1-D model. Two methods are suggested to overcome this issue:

- incorporate 1-D wave propagation in the cavity for the resonator response, as the current solution only considers conservation of mass for the cavity;
- apply non-linear constraints for the cavity length to ensure that the lumped parameter approximation is not violated.

The latter option is much simpler to implement but can be restrictive, as long cavities which may be effective cannot be considered by an optimisation algorithm. Non-linear constraints have been used to enforce the lumped element approximation in the next chapter.

It is noted that the average simulation times for a short demonstrative array using the low-order 1-D and high-order 3-D CFD models (which give nearly identical predictions) are of the order of 1 s and 5 hrs, respectively. Therefore, the 1-D model offers a speed-up in the order of 20,000-fold. This speed-up is crucial to being able to optimise the performance of the array, particularly for long arrays.

The satisfactory agreement with experimental data and full scale 3-D simulations indicate that the 1-D modelling framework developed in Chapter 3 is suitable for designing and optimising an array of Helmholtz resonators for use in high-speed train tunnels.

Chapter 5

1-D Model Application for a Demonstrative Array

5.1 Introduction

In this chapter the 1-D numerical model developed in Chapter 3 is used to: (i) develop an optimisation procedure for the array, subject to realistic tunnel and train operating constraints; (ii) demonstrate the effectiveness of an array of Helmholtz resonators in a real-world system, for future consideration by railway engineers.

An optimisation procedure for the geometry of an array of resonators which results in the greatest reduction in the amplitude of emitted micro-pressure waves from the tunnel exit is presented in § 5.5. An idealised initial condition representative of the compression wave generated by a high speed train entering a tunnel is specified in § 5.3. The incident wavefront is parametrised by the entry speed of the train and a characteristic length scale that is influenced by shape of the tunnel entrance and train nose. An order of magnitude analysis of the 1-D model PDE terms (§ 5.4) and a sensitivity analysis of the geometric optimisation variables (§ 5.6) are used to identify non-influential factors and reduce the computational cost and complexity of optimisation. The questions posed for the optimisation procedure are:

- How much of a reduction in the maximum rate of change of pressure of the in-

cident wavefront can be achieved by using an array of Helmholtz resonators, as the length of the array varies;

- How robust is an optimised array to variations in the operating conditions of the train, e.g. operating speed and the length of the incident wavefront, L;

- Is an array which uses irregular resonator geometry (variable cavity length and neck diameter) more robust to the operating conditions of the train than an array of an equivalent length which uses regular geometry (identical equispaced resonators);

- Does optimising the array based on the average of a range of operating points (different combinations of train velocity and wavefront length) lead to improvements in its robustness, compared to using just one operating point.

The array is also combined with an entrance hood (for example see Figure 2.3) in order to analyse their combined effect over a range of operating speeds. Finally, the robustness of the array to different incident wavefront shapes more representative of the type of compression waves seen in tunnels with entrance hoods or side branches (e.g. ventilation shafts) is studied. Will the array attenuate these compression waves as effectively as for an idealised incident compression wave?

5.2 Array Specification

5.2.1 Overview

In Chapter 2 it is mentioned that the cavities for an array of Helmholtz resonators would need to be relatively large in order to be effective against the low frequency pressure waves typically seen in high-speed train tunnels. Takayama et al. (1995) and Sasoh et al. (1998) propose to use a perforated liner on the wall of the tunnel. However, this would reduce the available cross-sectional area of the tunnel

without removing additional material in regions where the liner is installed. Alternatively, it is envisaged that redundant space in the tunnel could be used to house the resonators. For example, hollow pre-fabricated slab sections could be installed in the tunnel at certain intervals, or over a stretch of the total tunnel length. The cavities could be positioned underneath evacuation and maintenance access walkways and/or under the track, provided there is sufficient space. The demonstrative tunnel cross-section used for this analysis is shown in Figure 3.2, based loosely on the type of single-bore tunnel sections planned for stretches of the High Speed Two (HS2) route between London and Birmingham (High Speed Two Limited, 2015).

The length of the cavity and the neck diameter are the main variables which can be used to control the response of the array for this array design (see the sensitivity analysis in § 5.6), due to the restriction in the dimensions of the cavity through the cross-section of the tunnel. It is assumed that the incident pressure waves are of a sufficiently low characteristic frequency such that they will not be significantly influenced by the internal shape of the cavity (see § 3.2.2). This assumption provides greater flexibility in how the cavities could be incorporated into the tunnel structure. For example, long thin cavities could be used where there is insufficient space through the cross-section. The limitation of the lumped element approximation must be considered when the cavity dimensions (i.e. the cavity length) are similar to the characteristic wavelength, as was found in § 4.3.

The structural implications of using cavities embedded in the tunnel structure (which may be load bearing) are not investigated in this work. It is assumed that the cavities are hollow. A porous material, such as mineral wool could be installed in the cavities in order to provide additional viscous dissipation at higher frequencies.

5.2.2 Optimisation Variables

The optimisation variables selected for this study are all geometric properties of the array and are shown in Table 5.1, with reference to Figure 3.2. The tilde accent is

used to denote a dimensionless/normalised quantity. Normalised variables simplify the optimisation problem by allowing lower and upper bounds to be used in place of non-linear inequality constraints, which may be difficult to satisfy. For example, the length of the resonator neck is normalised by the depth of the cavity (see Equation 5.1), and so a value of $0 < \tilde{l_{\mathrm{n}}} < 1$ can be used. The dimensional values of the neck and cavity length, and the neck diameter are calculated with reference to Table 5.1 and Figure 3.2 by:

$$l_{\mathrm{n}} = \tilde{l_{\mathrm{n}}} \cdot w_{\mathrm{c}} \tag{5.1}$$

$$l_{\mathrm{c},i} = l_{\mathrm{c},0} + \left(\frac{l_{\mathrm{c},1} - l_{\mathrm{c},0}}{N_{\mathrm{c}} - 1} \right) (i-1)\,, \qquad l_{\mathrm{c},0} = \tilde{l_{\mathrm{c},0}} d_{\mathrm{t}}, \qquad l_{\mathrm{c},1} = \tilde{l_{\mathrm{c},1}} d_{\mathrm{t}} \tag{5.2}$$

$$d_{\mathrm{n},i} = \tilde{d_{\mathrm{n},i}} \min\left(h_{\mathrm{c}}/N_{\mathrm{n}}, l_{\mathrm{c},i}\right), \qquad \tilde{d_{\mathrm{n},i}} = \tilde{d_{\mathrm{n},0}} + \left(\frac{\tilde{d_{\mathrm{n},1}} - \tilde{d_{\mathrm{n},0}}}{N_{\mathrm{c}} - 1} \right) (i-1) \tag{5.3}$$

where $i = 1, N_{\mathrm{c}}$ is the resonator cavity index. The volume of the cavity is then $V_{\mathrm{c}} = S_{\mathrm{c}} l_{\mathrm{c}} - S_{\mathrm{n}} l_{\mathrm{n}}$, where S_{n} is scaled to account for the number of necks (N_{n}) for each cavity (intra-necks). The intra-necks are aligned perpendicularly to the 1-D flow direction in the tunnel (i.e. aligned vertically). Increasing the number of intra-necks reduces the neck diameter, which in turn increases viscous dissipation from the boundary layer in accordance with Equation 3.24.

The effect of multiple necks per cavity aligned along the length of the tunnel is not considered. It may be possible to treat a small group of axially aligned intra-necks as if they are at the same point, if the intra-neck distance is small compared to the characteristic wavelength. However, for a relatively large intra-neck spacing (and a large value of the lumped element parameter) the physical model must be modified to consider the finite wave propagation speed in the cavity and the unique axial position of each intra-cavity neck.

The total length of the resonator array is the sum of the cavity lengths, in-

Symbol	Definition	LB	UB
N_c	Number of resonator cavities	1	25
N_n	Number of necks per cavity (vertically aligned)	1	3
$\tilde{l_n}$	Normalised resonator neck length	0.01	0.80
$\tilde{d_{n,0}}$	Normalised first resonator neck diameter	0.05	0.95
$\tilde{d_{n,1}}$	Normalised final resonator neck diameter	0.05	0.95
$\tilde{l_{c,0}}$	Normalised first cavity length	0.01	1.0
$\tilde{l_{c,1}}$	Normalised final cavity length	0.01	1.0

Table 5.1: Summary of normalised optimisation variables and corresponding lower (LB) and upper (UB) bounds, with reference to Figure 3.2.

cluding additional spacing, l_{ex}, between the cavities. The parameters in Table 5.1 permit an irregular neck diameter and cavity length, based on simple linear scaling with the resonator index (see Equations 5.2 and 5.3). The linear function is described by two parameters, e.g. $\tilde{l_{c,0}}$ and $\tilde{l_{c,1}}$, for the normalised first and last cavity length, respectively. Alternative scaling factors could also be considered for an irregular neck diameter and cavity length. For example, a quadratic scaling factor would require three parameters, thereby increasing the complexity of optimisation, but possibly providing better attenuation of the wavefront. In the case of equispaced and identical resonators (i.e. $\tilde{l_{c,1}} = \tilde{l_{c,0}}$ and $\tilde{d_{n,0}} = \tilde{d_{n,1}}$), Equations 5.2 and 5.3 reduce to:

$$l_{c,i} = l_{c,0}, \qquad d_{n,i} = \tilde{d_{n,0}} \min\left(h_c/N_n, l_{c,i}\right) \tag{5.4}$$

The array geometry could also be parametrised by the natural frequency of the resonators and the total length of the array, replacing several parameters in Table 5.1 (i.e. N_c, $\tilde{l_{c,0}}$ and $\tilde{l_{c,1}}$). The requirement for integer constraints (at least due to N_c) would be then removed, increasing the scope of optimisation algorithms that can be used (as discussed in § 5.5). Alternatively, non-linear constraints can be used to set upper and lower bounds for the length of the array and the natural frequencies of the resonators (see § 5.5.3) when using the variables in Table 5.1.

5.3 Initial Condition

5.3.1 Characteristic Wavefront

The initial condition for this system should represent a typical wavefront generated by a high-speed train entering a tunnel. This qualitatively resembles the form shown in Figure 5.1, based on experimental measurements (Mashimo et al., 1997; Ozawa and Maeda, 1988). The pressure rise at any point x on the curve is assumed to satisfy (Aoki et al., 1999):

$$p\left(x,0\right)=p_1\left[\frac{1}{2}-\frac{1}{\pi}\arctan\left\{\frac{\pi x}{L}\right\}\right] \tag{5.5}$$

where p_1 is the difference between the asymptotic pressures at $x=\pm\infty$, and L is a length used to characterise the maximum steepness of the wavefront (not to be confused with the characteristic wavelength, λ). In order for the wavefront to be used numerically, its range is restricted to $-b<x<b$, where b is the half-range of the initial condition ($b=10\dot{d}_\mathrm{t}/3$). The IC is scaled so that $p(-b,0)=p_1$ and $p(b,0)=0$, in-line with previous work by Aoki et al. (1999). Therefore, the scaled initial condition is given by:

$$p(x,0)_\mathrm{sc}=\frac{p_1}{p(-b,0)}\left[p(x,0)-p(b,0)\right] \tag{5.6}$$

Considering linear wave propagation, the substitution $x\sim-a_0t$ is made in order to define Equations 5.5 and 5.6 on time. Assuming negligible distortion of the wavefront between the tunnel entrance and the start of the array, p_1 can be predicted using Equation 2.7 and L can be approximated by (Vardy, 2008):

$$L\approx\left(a_0/u_\mathrm{z}-1\right)\phi\dot{d}_\mathrm{t} \tag{5.7}$$

where ϕ is an empirical coefficient typically in the range $0.75 < \phi < 1.25$ that accounts for the nose and tunnel entrance shape. Increasing the value of ϕ reduces the slope of the generated wave. The value of ϕ can be much larger for modern trains with optimised nose profiles and entrance hoods. Equation 5.7 is not used for the purpose of optimisation in this work as: (1) the accuracy of this expression is unknown, due to the empirical nature of parameter ϕ; (2) the sensitivity of the countermeasure to the incident waveform can be tested as a function of the wave amplitude, $p_1 = f(u_z)$ and the value of L.

The assumptions made when using the idealised IC defined in Equations 5.5 and 5.7 are summarised below:

- **Generation**: The effect of the train nose shape and an entrance hood on the profile of the entry compression wave is not accurately captured. For example, Miyachi et al. (2016) show that these countermeasures tend to produce a double peak in the profile for the rate of change of pressure of the entry wave (see § 5.11), rather than a single peak described by the smooth idealised initial condition. Furthermore, the multiple-peak pressure waveforms exhibit different steepening characteristics over the course of propagation. More sophisticated analytical models can predict the entry waveform by accounting for the axial area variation of the entrance hood and the train nose (Howe et al., 2008). However, they are more complex to use for initial design purposes.

- **Propagation**: Negligible distortion of the entry compression wave between the tunnel entrance and start of the array/countermeasure is assumed (unless stated otherwise). For example, the wavefront will steepen due to nonlinearity over large propagation distances in slab track tunnels. On the other hand, viscous losses from the tunnel wall and reflections from branches and other obstacles will counteract steepening and distort the initial shape of the wave.

The energy spectra of the signal described by Equation 5.5 is distributed over a range of frequencies (see Figure 4.5) and so it is difficult to define a precise

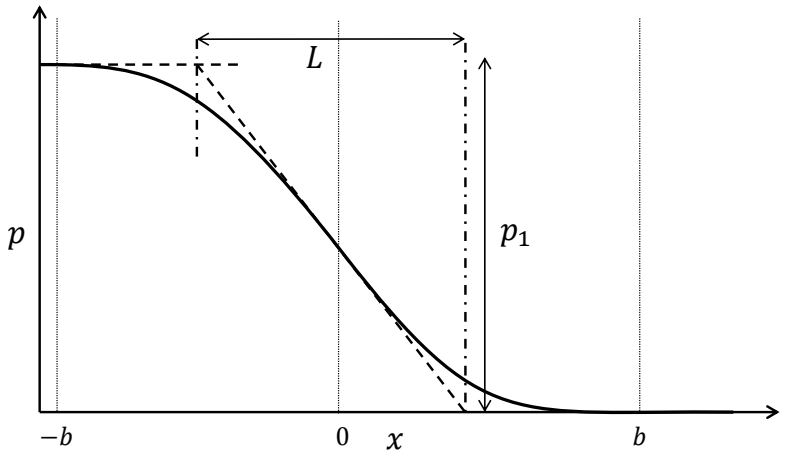


Figure 5.1: Characteristic pressure wave generated by train-nose entry into a tunnel (not to scale) using Equation 5.5. The signal at $x = \pm b$ is scaled to the asymptotic conditions at $x = \pm\infty$.

characteristic wavelength. For numerical modelling the characteristic wavelength is approximated by:

$$\lambda \approx \text{mean}(L, 2b) \tag{5.8}$$

This equation represents the average of the shortest and longest known length scales in the signal. As has been mentioned in previous chapters (see § 4.3.2.3), the characteristic wavelength becomes a less suitable metric for cases where the signal energy is distributed over a wide range of frequencies, as its value cannot be accurately defined. The characteristic frequency is then $\upsilon = c_0/\lambda$. The smallest grid resolution is selected as $\Delta t < 1/10\upsilon_L$, where $\upsilon_L = c_0/L$, in order to provide at least 10 points across the period of L.

5.3.2 Comparison with Other Initial Conditions

Equation 5.5 is equivalent to Equation 8 from Mashimo et al. (1997) with the substitution:

$$\left(\frac{\partial p}{\partial t}\right)_{\max} = \frac{p_1 a_0}{L} \tag{5.9}$$

in Equation 8. An expression for the idealised entry waveform is also given by (Yamamoto, 1977):

$$p(0,t) \approx p_1 \left[\frac{1}{2} + \frac{1}{\pi} \arctan\left(\frac{u_z t}{c d_t} \right) \right] \tag{5.10}$$

where $c \approx 0.33$ (Matsuo et al., 1997) is determined from experimental data for tunnel entry compression waves on the Sanyo-Shinkansen. Considering linear wave propagation with $t \sim -x/a_0$, Equation 5.10 becomes:

$$p(x,0) \approx p_1 \left[\frac{1}{2} - \frac{1}{\pi} \arctan\left(\frac{3.03 M_z x}{d_t} \right) \right] \tag{5.11}$$

On the other hand, substituting Equation 5.7 into Equation 5.5 gives:

$$\begin{aligned} p(x,0) &= p_1 \left[\frac{1}{2} - \frac{1}{\pi} \arctan\left(\frac{\pi M_z x}{(1 - M_z)\, \phi d_t} \right) \right] \\ &\approx p_1 \left[\frac{1}{2} - \frac{1}{\pi} \arctan\left(\frac{\pi M_z x}{d_t} \right) \right], \quad \text{with } \phi \sim 1,\ M_z \ll 1 \end{aligned} \tag{5.12}$$

which is nearly the same as Equation 5.11. From Equation 5.10, the maximum rate of change of pressure of the generated compression wave is:

$$\left(\frac{\partial p}{\partial t} \right)_{\max} = \frac{u_z p_1}{\pi c d_t} \tag{5.13}$$

Equating Equations 2.8 and 5.13 allows a relation between empirical parameters ϕ and c to be found:

$$\phi = \frac{\pi c}{1 - M_z} \tag{5.14}$$

For example, $\phi \approx 1.4$ when $u_z = 300$ km/h.

5.3.3 Non-Uniform Grid

A non-uniform sampling of Equation 5.5 can be used to refine the mesh at the centre of the domain when using the far-field frame of reference ($x = 0$ in Figure 5.1), where the wavefront is steepest. The following distribution of nodes is used:

$$\begin{aligned} \Delta x_1 &= k\Delta x_0 \\ \Delta x_2 &= k\Delta x_1 \\ \Delta x_3 &= k\Delta x_2 \\ &\vdots \\ \Delta x_i &= k^i \Delta x_0 \end{aligned} \tag{5.15}$$

where k is a linear scaling factor for the nodal spacing. It is also required that:

$$\sum_{i=1}^{A} \Delta x_i = b \quad \Longrightarrow \quad \Delta x_0 \sum_{i=1}^{A} k^i = b \tag{5.16}$$

where $A = N_x/2$. This summation can be expanded as a series, which along with the condition $\Delta x_A = k^A \Delta x_0$ (from Equation 5.15 with $i = A$), results in the following equation:

$$\frac{1 - r^{\frac{A+1}{A}}}{1 - r^{\frac{1}{A}}} = \frac{b}{\Delta x_0} \tag{5.17}$$

where $r = \Delta x_N / \Delta x_0$. This equation must be solved numerically to find A and k. It can be solved by any non-linear root finding approach, but the `fzero` function (MathWorks, 2017a) is used in this work. Therefore, given a minimum and maximum sample frequency, a distribution of nodes can be generated that is biased towards the centre of the far-field domain where the wavefront is steepest. Fewer grid points can then be used, compared to a uniform grid across the entire domain with the maximum sample frequency. The position of the steepest part of the

Symbol	Definition	LB	UB	unit/normalisation
υ_c	incident wave frequency	5	50	Hz
T_0	ambient temperature	283	308	K
d_t	bore diameter	7	14	m
u_z	train velocity	150	500	km/h
β	train-tunnel blockage	0.1	0.30	-
$\tilde{l_{ex}}$	inter-cavity spacing	0.0	5.0	d_t
$\tilde{x}$	derivative length scale	1	10	d_t
$\tilde{w_1}$	see Figure 3.2	0.2	0.8	d_t
$\tilde{h_1}$	”	0.1	0.5	d_t
$\tilde{h_2}$	”	0.8	0.95	d_t
h_{wall}	roughness height	0.1	5.0	mm

Table 5.2: Summary of normalised geometric variables and corresponding lower (LB) and upper (UB) bounds for the order of magnitude analysis.

wavefront will change over the course of propagation, which should be considered when choosing the values of the minimum and maximum sample frequencies.

5.4 Scale Analysis

A scale (also referred to as order-of-magnitude) analysis has been carried out for the far-field system with the continuum approximation, in order to determine the significance of the different equation terms on the numerical solution and to identify if any terms can be neglected from the simulation. The physical constants and tunnel geometric bounds used for the analysis are specified in Tables 3.1 and 5.2, while the geometric bounds for the resonators are specified in Table 5.1.

The equation terms have been calculated for 1 million samples, representing different combinations of tunnel geometry and operating conditions. The Quasi-random low discrepancy Sobol sequence (Sobol, 1967) was used to generate the samples using the `sobolset` MATLAB function (MathWorks, 2017a). Quasi-random sequences posses better convergence properties for the same number of samples as random sequences by providing a more even coverage of the search space.

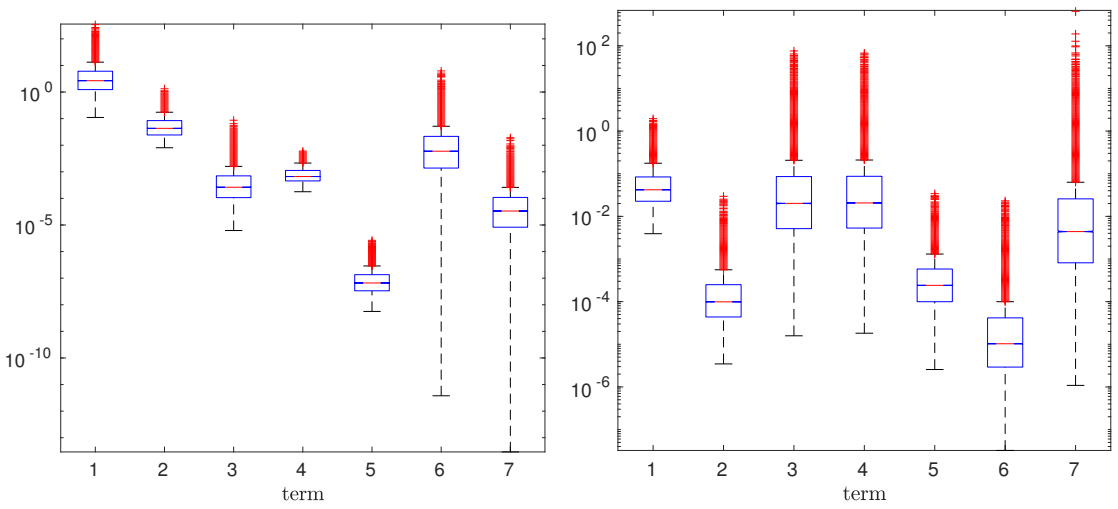
The results of the scale analysis are illustrated using a box plot in Figure 5.2.

The PDE terms (on the x-axis of Figure 5.2a) for the propagation of pressure waves in the tunnel are identified with reference to § 3.2.4 as: (1) space marching; (2) Burgers' advective flux; (3) unsteady friction from the laminar boundary layer; (4) quasi-steady skin friction; (5) diffusivity of sound; (6) linear source term component; (7) non-linear source term component.

The ODE terms (Figure 5.2b) for the non-linear response of the resonator are: (1) 2nd derivative in time; (2) boundary layer in the resonator neck; (3) "stiffness" of cavity, Ωg; (4) resonator forcing term, Ωf; (5-6) adiabatic losses in the cavity; (7) dissipation of the vortex jet.

The top and bottom of each box are the 25th and 75th percentiles, respectively, and the distance between the top and bottom is the interquartile range. The central horizontal lines are the median values, while the top and bottom "whiskers" are the maximum and minimum observations. Outliers are identified by red crosses, which are more than 1.5 times the interquartile range from the top or bottom of the box.

Firstly, there appears to be a high degree of variability in the order of magnitude of the terms, due to the large range in the variable bounds used. It can be seen that the effect of the diffusivity of sound is negligible. Despite this, it should be noted that this term only has a noticeable effect over very small lengths scales, such as a shock. The laminar boundary layer terms for both the tunnel and resonator necks are relatively small. Therefore, there may be a case for dropping these terms from the numerical analysis, particularly for the purpose of optimisation. The evaluation of the fractional derivatives in these terms is the most computationally expensive part of the entire calculation, due to the significant increase in the size of the Jacobian matrix incurred by using the diffusive representation (see § 3.3.1.2). The terms representing adiabatic losses in the resonator cavities are insignificant compared to non-linear jet losses from the neck ends and can be neglected.



(a) Wave propagation in tunnel (b) Non-linear resonator response

Figure 5.2: Box plot for an order-of-magnitude analysis of the continuum far-field equations.

5.5 Optimisation Strategy

5.5.1 Objective Function

One strategy to attenuate the propagation of pressure waves would be to match the natural frequency of an array of resonators to the expected characteristic frequency of the incident wavefront. This approach is suitable if the specific shape of the incident waveform is unknown (or highly variable), or a characteristic frequency can be clearly identified (i.e. a narrow frequency band around the characteristic frequency). The entry compression wave is idealised in § 5.3.1, where it is difficult to identify a specific characteristic frequency (see Figure 4.5). Therefore, an optimisation procedure is proposed to overcome this issue.

The main objective of the array is to reduce the amplitude of MPWs generated at the tunnel exit, which according to Equation 2.9 is proportional to the maximum rate of change of pressure of the pressure waves reaching the exit. Consequently, the objective is chosen as the ratio between the maximum absolute rate of change of pressure of the wavefront for an identical waveguide: (i) with the array and (ii) without an array, at a distance corresponding to the end of the array. This objective is equivalent to the following expression using the far-field variables (see

§ 3.2.4):

$$\alpha_{\mathrm{a}} = \max\left|\frac{\partial p}{\partial t}\right|_{\mathrm{a}} \Big/ \max\left|\frac{\partial p}{\partial t}\right|_{\mathrm{na}} \equiv \max\left|\frac{\partial f}{\partial \mathcal{T}}\right|_{\mathrm{a}} \Big/ \max\left|\frac{\partial f}{\partial \mathcal{T}}\right|_{\mathrm{na}} \tag{5.18}$$

where the subscripts a and na denote with and without an array, respectively. This objective is easy to interpret as a value of $\alpha_{\mathrm{a}} < 1$ indicates that the array is effective. It is also a useful metric to compare against the performance of other MPW countermeasures.

This approach does have drawbacks: (1) numerical errors in the value of α become more pronounced for steep wavefronts in the denominator term; (2) it is less informative if a shock wave emerges in the solution without an array, as $\alpha_{\mathrm{a}} \to 0$; (3) it requires the calculation of two numerical solutions (although the solution without an array is very fast to evaluate); (4) it is a relative measure and provides no information about the true values of the pressure gradient. Increasing the mesh refinement around steep wavefronts and using high-order numerical schemes can help with points (1) and (2) by reducing numerical error. Alternatives to this objective function could include $\alpha = p'(t)_{\mathrm{a}} - p'(t)_{\mathrm{na}} < 0$, or a percentage difference, although these would still be impractical in the event of a shock.

The reduction in sound pressure level (SPL) of MPWs due to the presence of the array can be estimated from Equation 2.9 and assuming no further distortion of the wavefront occurs between the end of the array and the tunnel exit:

$$\Delta\mathrm{SPL} = \mathrm{SPL}_{\mathrm{a}} - \mathrm{SPL}_{\mathrm{na}} = 20\log_{10}\left(\alpha_{\mathrm{a}}\right) \tag{5.19}$$

For example, a 50% reduction in the maximum rate of change of pressure ($\alpha_{\mathrm{a}} = 0.5$) approximately corresponds to a 6 dB reduction in SPL of the MPW in the low frequency and far-field approximations. Note that Equation 5.19 does not account for the relative loudness perceived by the human ear, depending on the frequency of the noise.

Equation 5.18 can be used for single-objective optimisation if the number of resonator cavities is fixed, as the most effective array will also generally be the one with the most cavities. However, it is useful to optimise the performance of

the array over different propagation distances. Therefore, the total length of the array is introduced as a second objective:

$$l_{\mathrm{a}} = N_{\mathrm{c}} \cdot l_{\mathrm{ex}} + \sum_{i=1}^{N_{\mathrm{c}}} l_{\mathrm{c},i} \tag{5.20}$$

The array length is usually normalised by the diameter of the tunnel bore, $\tilde{l_{\mathrm{a}}} = l_{\mathrm{a}}/\dot{d_{\mathrm{t}}}$. The optimal performance of the array can then be compared against its length, which becomes a multi-objective optimisation problem. Railway engineers may benefit from the objective functions described in this section, as they can be used as a comparative metric against other MPW countermeasures and as the basis of an optimisation procedure.

5.5.2 Optimisation Procedure

A multi-objective optimisation problem was defined at the end of the previous section. The objective is non-linear and discontinuous (i.e. non-differentiable), due to the use of mixed-integer constraints (i.e. N_{c} and N_{n} are integers) and functions such as `min`, `max` and conditional `if` statements. Consequently, gradient based optimisation algorithms cannot be used. Furthermore, a good starting point (i.e. the initial geometry of the array) for optimisation is not necessarily known, and so global optimisation should be used.

In light of the points above, a multi-objective Genetic Algorithm (MOGA) based on the non-dominated Sorting Genetic Algorithm-II (NSGA-II) (Deb et al., 2002) has been chosen from the MATLAB Optimisation Toolbox (`gamultiobj` function). The MOGA has been adapted to support mixed-integer constraints (see MathWorks, 2013), by using custom creation, mutation and crossover functions. The genetic algorithm (GA) is a stochastic, derivative-free and population based global optimisation approach that is well suited to discontinuous and non-linear objective functions where there may be multiple local minima. A good initial guess to the solution does not necessarily need to be provided.

The GA mimics the process described by the theory of evolution, whereby the

"fittest" individuals (configuration of variables) in a population (a group of variable configurations) pass their characteristics onto the next generation. A randomly generated initial population (within the variable bounds specified by the user) evolves towards better regions of the search space via randomised processes of selection (e.g. mutation, cross-over and recombination), leading to an optimal configuration over successive generations.

Although the GA is fairly robust and easy to implement as a black box solver, it tends to converge more slowly than deterministic algorithms, or ones where more information is available to the solver (e.g. the Jacobian of the objective function). It does not guarantee convergence to a global optimum. Instead, a solution obtained using a GA is selected to be sufficient for the users needs, for example based on a convergence criterion. Furthermore, the quality of the result and the convergence rate is influenced by the quality of the initial population. The search space should be seeded evenly, or concentrated in the region of the global optimum (if known), and with a sufficient population size in order to avoid becoming stuck in local minima.

Several methods are suggested to improve the convergence rate and quality of the optimised arrays. These can be used together and have not been implemented in this work due to time constraints. For example, an approximate surrogate model (see Bandler et al., 2004; Jin, 2011) can be used in place of the numerical model, if the objective is expensive to evaluate (e.g. complex 3-D models). Adaptive GAs are proposed as a way to accelerate convergence by dynamically adjusting the probabilities of crossover and mutation, depending on the diversity of the current population (see Jakobović and Golub, 1999; Srinivas and Patnaik, 1994).

Hybrid optimisation can be used, where the approximate location of the global optimum is first found by the GA. The approximate optimum location is then used as the starting point for a more efficient algorithm for local search (e.g. Pattern search Hooke and Jeeves, 1961). However, hybrid algorithms cannot be used for this particular case, due to the limitation of only the GA and MOGA supporting

mixed-integer constraints in the MATLAB Optimisation Toolbox (as of 2017). Hybrid optimisation may be a useful method to consider if the integer parameters are fixed.

The MOGA allows a global Pareto optimal set of optimal array configurations to be obtained for two or more objective functions. The Pareto optimal represents the best known solution with respect to all objectives and cannot be improved in one objective without worsening another. Each point on the Pareto front represents an optimal configuration with respect to the objectives. Upper and lower bounds have been prescribed for the input variables, based on realistic tunnel geometry constraints (see Table 5.1).

5.5.2.1 Modified Optimisation Procedure

A two-stage optimisation approach was proposed in order to improve the quality of the optimised resonator geometry, for fewer evaluations of the objective function in Equation 5.18. The first optimisation procedure attempts to generate an initial population that is closer to the global optimum, rather than using default initial population creation settings for evaluating Equation 5.18 (i.e. essentially a random distribution that satisfies the constraints). Two choices for the objective function are proposed below for generating this initial population.

1. Minimise $\alpha_{\mathrm{a1}} = -\Omega$ (see Equation 3.23), so that $\Omega \gg 1$. This gives the Korteweg-de Vries equation, resulting in acoustic solitons (see § 3.2.4), and so a shock wave cannot emerge.

2. Minimise $\alpha_{\mathrm{a2}} = |1 - \Omega|$, so that $\Omega \to 1$. $\Omega = 1$ matches the natural and characteristic frequency so that attenuation is maximised.

These two objectives do not provide any insight into the shape of the transmitted wavefront due to the array. Despite this, they are much faster to evaluate compared to Equation 5.18, as the numerical solution of the PDE system is not required. The points on the Pareto front are then used as the initial population for a second optimisation based on Equation 5.18.

This two-stage optimisation procedure was found to provide no noticeable reduction in the value of α, compared to using the default population creation settings. Reasons for why the modified procedure did not improve the quality of the optimised arrays are suggested below.

- Minimising α_{a1}, or α_{a2} does not mean that α_{a} will also be minimised.
- The population generated by the initial optimisation procedure is insufficiently diverse. As a result, it may be more likely to converge to local minima in the subsequent optimisation using Equation 5.18. Combining the optimised initial population with a population generated using the default population creation settings may help to improve diversity.
- The calculation of Ω requires the characteristic frequency of the pressure wave. This may not be easy to accurately define and changes as the wavefront propagates through the array.

5.5.3 Non-linear Constraints

Non-linear inequality constraints of the form $c(x) \leq 0$, where x is the optimisation variable, occur when the constraint is a non-linear function of the optimisation variables. For example, the constraint may be quadratic, or discontinuous. Iteration is required in order for the objective function to satisfy non-linear constraints. Therefore, it is often useful to remove them, if possible. In § 5.2.2 the optimisation variables are normalised so that upper and lower bounds are used instead. However, non-linear inequality constraints are still required for the following conditions:

1. negligible interaction between neighbouring resonators ($\kappa < 0.15$ - see Appendix C);
2. a lumped element approximation for the resonator response ($\varpi < 0.25$);
3. a maximum and minimum array length, i.e. $l_{\mathrm{a,min}} < l_{\mathrm{a}} < l_{\mathrm{a,max}}$;

4. a maximum and minimum natural frequency, i.e. $\omega_{\mathrm{a,min}} < \omega < \omega_{\mathrm{a,max}}$.

For Constraint 2, the cavity length is limited to a quarter of the characteristic wavelength, in order to reduce the likelihood of standing waves in the cavity. The last two constraints are usually set to $0 < l_{\mathrm{a}} < \infty$ and $0 < \omega < \infty$, i.e. they are unbounded. The optimisation procedure may avoid effective geometric configurations that do not satisfy these constraints. Non-linear constraints are implemented for the mixed-integer GA in MATLAB by minimising a penalty function, instead of the objective function (see Mathworks, 2017).

The numerical model features the capability of switching from a continuum (§ 3.2.4) to a discrete (§ 3.4.1) treatment of the array of resonators, if the continuum distribution parameter exceeds a threshold value. The continuum model is more efficient in terms of simulation time. However, it can fail to converge when using variable resonator geometry, due to the increased numerical stiffness of the PDE system (see § 3.4.1). The discrete model is more robust to irregular geometry at the expense of increased simulation time.

5.6 Objective Function Sensitivity Analysis

5.6.1 Overview

Sensitivity analysis can be used to provide a qualitative indication about the importance of each input on the value of the objective function. It is a useful tool for identifying non-influential inputs which can be removed as variables for the purpose of optimisation. Elementary effects (EE) is a popular screening method that is relatively easy to understand and does not depend on modelling assumptions, e.g. monotonicity.

EE is a one-factor-at-a-time method; one input is varied while the others are held constant. This process is repeated for each input in order to characterise the sensitivity of the objective function. Elementary effects are approximations of the first order partial derivative and are estimated at random sampling points. The method provides two measures for the distribution of absolute values of the

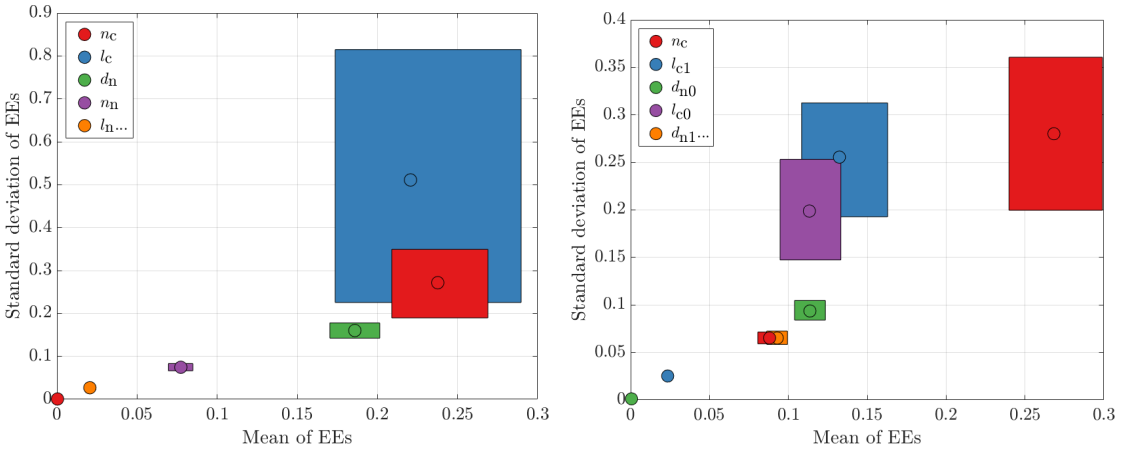
elementary effects for each input: (i) the mean value (μ_i^*), and (ii) the standard deviation (σ_i). The mean signifies the importance of each input on the objective, while the standard deviation indicates the degree of higher order effects (i.e. non-linearity and/or interactions with other inputs). Low values for both would signify a non-influential input. EE is a global method as the final measure is obtained by averaging a number of elementary effects. The sensitivity analysis is performed using the SAFE Toolbox (Pianosi et al., 2015). The use of finite differences for evaluating the partial derivatives means that the accuracy of the EE method depends on the smoothness of the sampled objective over the domain, and hence the total numbers of samples.

5.6.2 Results and Discussion

Upper and lower bounds for the inputs are defined in Table 3.1 and are identical to those used for the optimisation procedure. The sensitivity of the objective function in Equation 5.18 is solved under an extreme operating envelope with two optimisation points (see Table 5.3) to provide robust results over a range of train operating regimes. The sensitivity analysis is repeated for four cases:

- with a variable number of resonator cavities ($1 \leq N_\mathrm{c} \leq 20$), with:
  - regular resonator geometry (equispaced identical resonators);
  - irregular resonator geometry (variable neck diameter and cavity length);
- a constant number of cavities ($N_\mathrm{c} = 20$), with
  - regular resonator geometry;
  - irregular resonator geometry;

The sensitivity analysis is also performed with a constant number of cavities in order to isolate the effect of the resonator geometry on the objective, without being influenced too much by the length of the array. Figure 5.3 shows that the number of cavities has the largest influence, as indicated by the mean value of



(a) Regular geometry (b) Irregular geometry

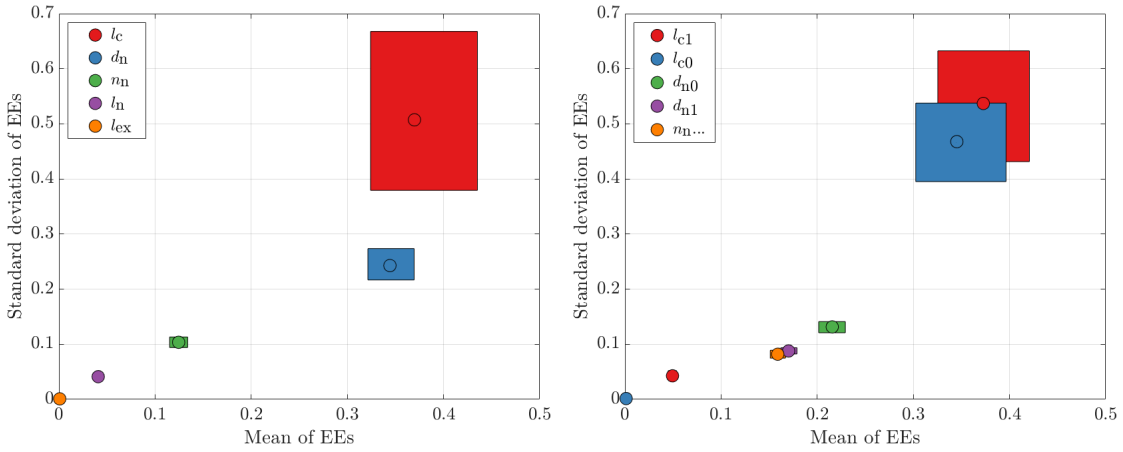
Figure 5.3: EE sensitivity analysis for $1 \leq N_c \leq 20$.

its elementary effects. This variable also has a relatively high standard deviation with large bounds on both its mean and standard deviation of the elementary effects. Therefore, it is affected strongly by non-linear effects or interactions with the other variables.

The next best parameters to adjust the performance of the array are the length of the cavities, which also has large bounds on its standard deviation and mean value, and the diameter of the neck. The effect of the remaining variables is much smaller in comparison. It is noted that the mean of the EEs are very similar for the first and last cavity length, and neck diameter, when considering irregular geometry. When the number of cavities is fixed (as in Figure 5.4) the length of the cavities and the neck diameter remain the most influential variables. These results are expected as the number of cavities, neck diameter, and cavity length have the greatest range in their values for the tunnel geometry considered.

5.7 Optimisation Results

The array is optimised for both regular and irregular resonator geometry (i.e. variable cavity length and neck diameter). The optimised arrays are then compared in order to see if using irregular resonator geometry can: (i) provide greater reductions in the normalised maximum rate of change of pressure over an equiva-



(a) Regular geometry (b) Irregular geometry

Figure 5.4: EE sensitivity analysis for $N_c = 20$.

lent distance; (ii) increase the robustness of the array to different train operating conditions.

The geometric configuration of the array has been optimised for three cases, as shown in Table 5.3. Case 1 uses an incident wavefront representative of demonstrative typical operating conditions. It is likely that a real array will be exposed to a range of incident wavefronts. For example, train operating speeds may increase after the array is constructed. Alternatively, new rolling stock may be introduced with different nose profiles, which would affect the wavefront shape. Therefore, the array has also been optimised for a range of incident wavefronts (optimisation points), representing an extreme envelope of operating conditions with two and five optimisation points. An arbitrary number of optimisation points can be chosen. However, the evaluation time of the objective function increases with the number of optimisation points. As a result, the number of optimisation points required to provide sufficiently robust performance (i.e. convergence in the objective value with an increasing number of optimisation points) should be minimised.

The objective function is calculated as the average of Equation 5.18 for the extreme operating envelopes, based on various combinations of $\tilde{L}$ and u_z for the incident wavefront. A margin of $\mp 25\%$ on u_z and $\pm 50\%$ on $\tilde{L}$ is used for the extreme operating envelope. The genetic algorithm is terminated after 200 generations, or if the average relative change in the best fitness function value over

Optimisation Regime	Typical	Extreme		Extended Extreme				
Point no.	1	1	2	1	2	3	4	5
$\tilde{L}$	2.0	3.0	1.0	1.0	2.0	3.0	1.0	3.0
u_z (km/h)	400	300	500	300	400	300	500	500

Table 5.3: Optimisation points for evaluation of the objective function for reference $\tilde{L} = 2 \pm 50\%$.

$\tilde{l_a}$	N_c	N_n	l_n	d_n	l_c
5	31	2	0.04	0.56	1.26
10	40	2	0.06	0.57	1.98
15	44	2	0.07	0.56	2.61
20	47	2	0.07	0.56	3.24

(a) Typical regime

$\tilde{l_a}$	N_c	N_n	l_n	d_n	l_c
5	35	2	0.07	0.57	1.13
10	38	1	0.04	1.06	2.05
15	46	3	0.07	0.38	2.49
20	44	1	0.06	0.88	3.45

(b) Extreme operating envelope

Table 5.4: Variation of optimised resonator dimensions (in metres) with non-dimensional array length, based on the Pareto front in Figure 5.5, for regular resonator geometry.

the maximum number of stall generations (i.e. no change in the objective value) is less than a tolerance of 1e−4.

5.7.1 Regular Geometry

This section considers regular array geometry, i.e. equispaced and identical resonators. An example of what the array could look like is provided in Figure 4.4a. The Pareto optimal sets of array configurations for the different operating regimes are plotted in Figure 5.5. The corresponding resonator dimensions for a selection of Pareto points are provided in Table 5.4.

The Pareto front exhibits a near-linear reduction in the objective value with propagation distance, where the dispersive effect of the array is greater than nonlinear steepening. However, the Pareto fronts diverge after $\tilde{l_a} \approx 8$. At this point the arrays optimised under the extreme operating envelopes can no longer match the performance of the typical regime. This divergence is expected as the extreme envelope attempts to provide greater robustness to different incident wavefront shapes.

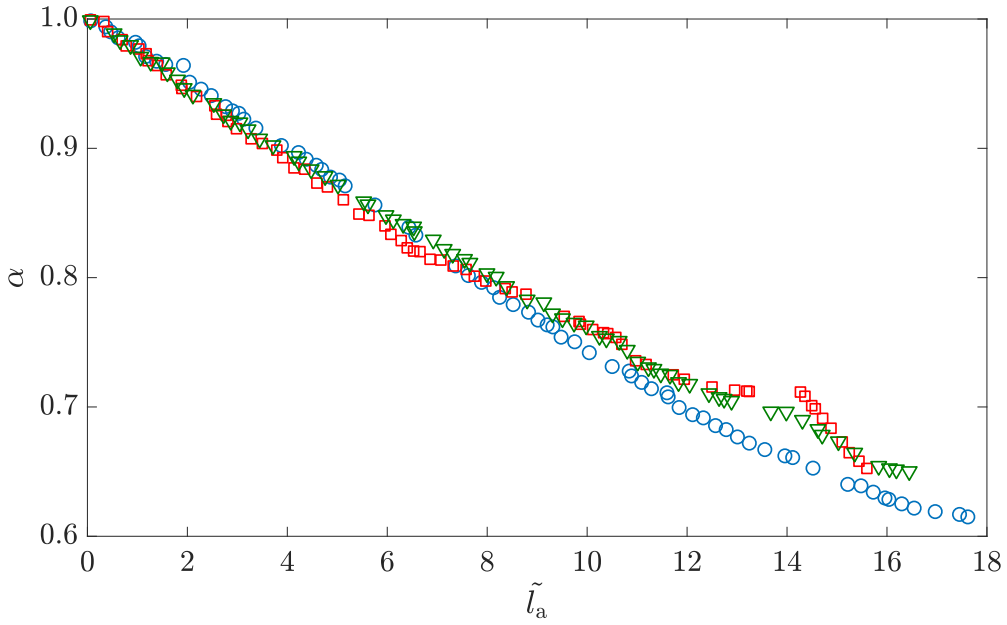
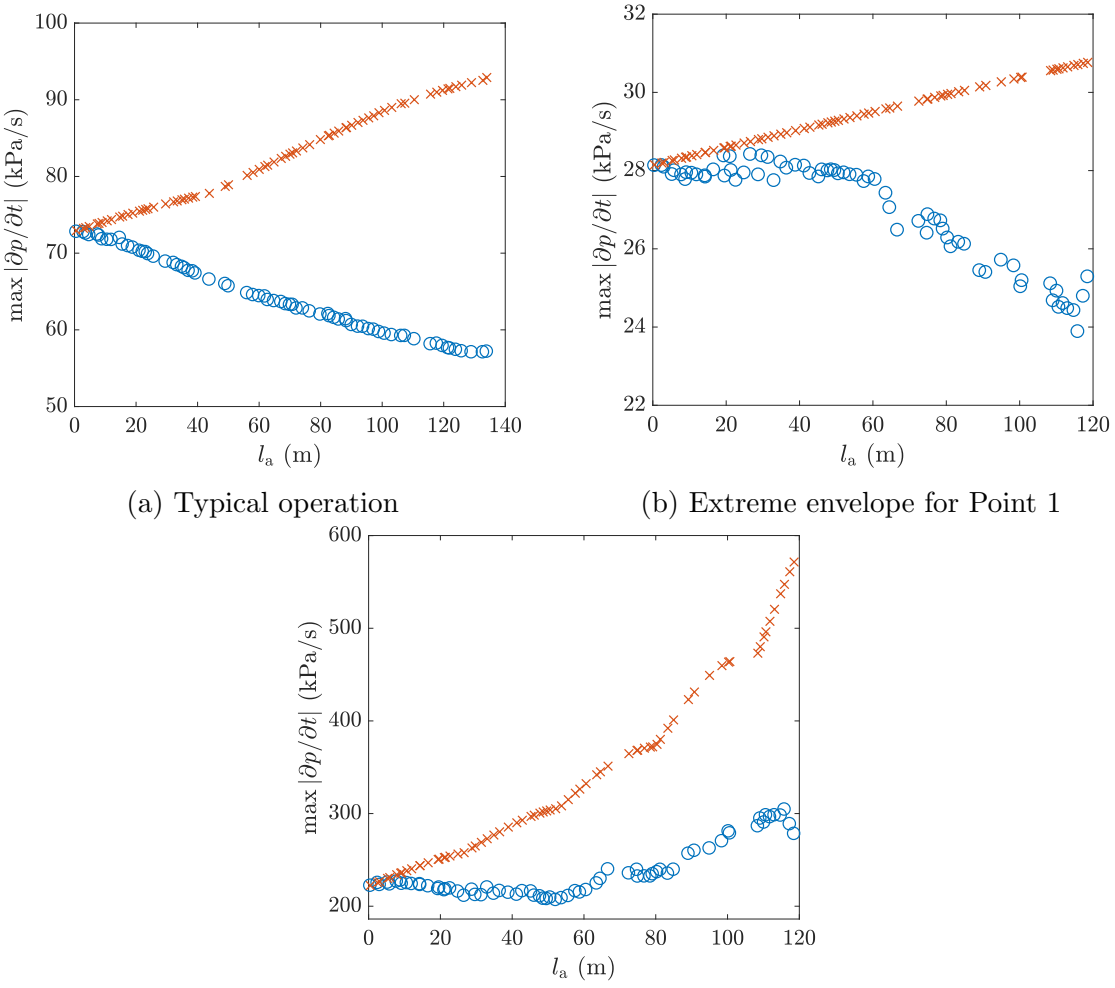


Figure 5.5: Pareto set under the: typical regime (○); extreme envelope (□); and extended extreme envelope (▽), for regular resonator geometry.

The poorer specific performance of the extreme envelop is also seen in Figure 5.6, where there is greater variability in the pressure gradient for the longer Pareto array configurations under the extreme operating envelope, compared to the typical regime. The effect of non-linear steepening without the array is significant, particularly in Figure 5.6c for the extreme envelope. In this case, the maximum pressure gradient has tripled over 120 m. The dispersive effect of the array significantly reduces the maximum pressure gradient, but cannot compete with non-linear steepening for longer array configurations, i.e. $l_a > 60$ m. The wavy behaviour seen without the array in Figure 5.6c is associated with the numerical error in the calculation of steep gradients, as the line becomes smoother by refining the grid.

Examples of waveforms corresponding to the smallest objective values from the Pareto fronts are shown in Figure 5.7 under typical operating conditions and Figure 5.8 under the extreme envelope (with two optimisation points). The transmitted waveforms are compared both with and without (na in the legend) an array, over the same propagation distance. The incident waveform (at $\mathcal{X} = 0$) is also provided for reference. It is noted that the non-dimensional time and space



(a) Typical operation

(b) Extreme envelope for Point 1

(c) Extreme envelope for Point 2

Figure 5.6: Maximum rate of change of pressure versus equivalent array length for the Pareto optimal configurations with (○), and without (×) an array, with reference to Table 5.3.

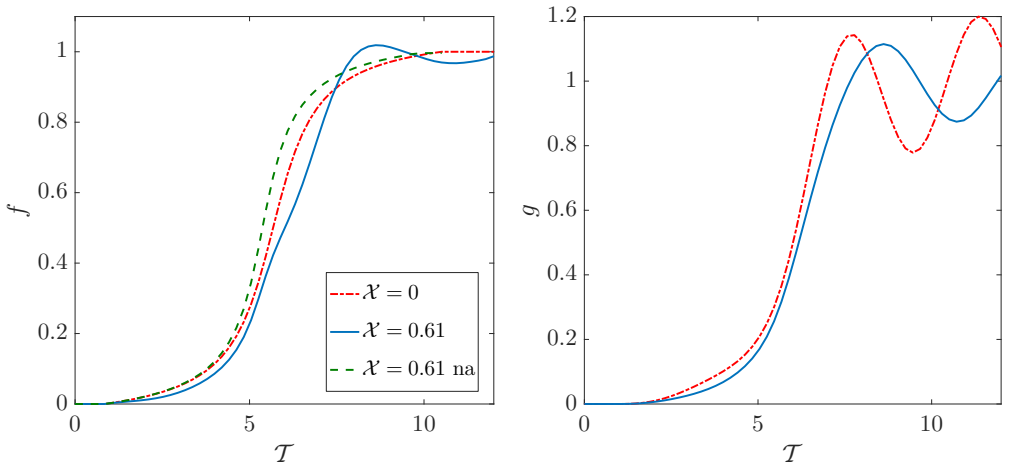


Figure 5.7: Wavefront (left), and resonator response (right) for $\alpha_a = 0.61$ in Figure 5.5, under typical operation for regular geometry. $\upsilon_0 = 17.4$ Hz.

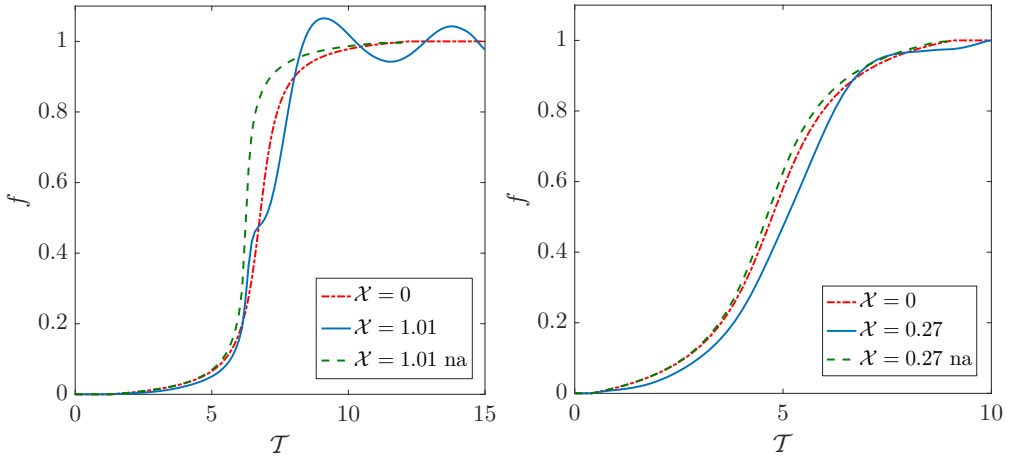


Figure 5.8: Wavefront for $\alpha_a = 0.65$ in Figure 5.5 for lower (left), and upper (right) bounds of the extreme operating envelope for regular geometry. $\upsilon_0 = 20.5$ Hz.

scales differ in Figure 5.8, due to the different values of L and u_z. Non-linear steepening is clearly evident in the waveforms without the array present. Visco-thermal effects do not appear to be sufficient to prevent the emergence of a shock further along the tunnel. In contrast, the resonator array strongly disperses the wavefront and introduces oscillatory behaviour in its wake, corresponding to the natural frequency of the resonators. However, the amplitude of the oscillations is less than that of the initial pressure rise.

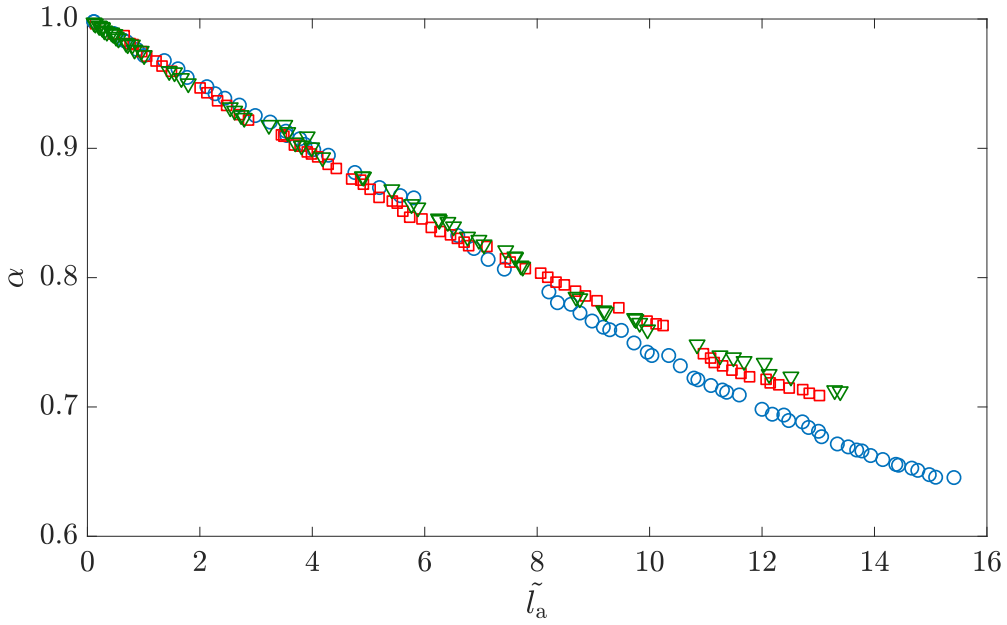


Figure 5.9: Pareto set under the: typical regime (○); extreme envelope (□); and extended extreme envelope (▽), for irregular resonator geometry.

5.7.2 Irregular Geometry

This section considers irregular array geometry, i.e. a variable cavity length and neck diameter. The Pareto optimal sets of array configurations for irregular resonator geometry are plotted in Figure 5.9. The Pareto fronts diverge after $\tilde{l}_a \approx 8$, which is similar to the regular geometry.

Using irregular resonator geometry provides no discernible reduction in the objective function across the Pareto front for the incident wavefront considered. However, the extreme and extended extreme envelopes exhibit smoother Pareto fronts in comparison to Figure 5.5. It is noted that the optimisation search space increases by two dimensions (i.e. by $\tilde{l_{c,1}}$ and $\tilde{d_{n,1}}$) when using irregular geometry, thereby increasing the difficulty of finding the global optimum. Consequently, the GA needs to be solved for more generations, and with a greater initial population size in order to converge successfully. For example, the points are less evenly distributed along the Pareto fronts for the irregular geometry and appear to be more concentrated towards shorter array lengths.

Examples of waveforms corresponding to the smallest objective values from the Pareto fronts are shown in Figure 5.10 under typical operating conditions,

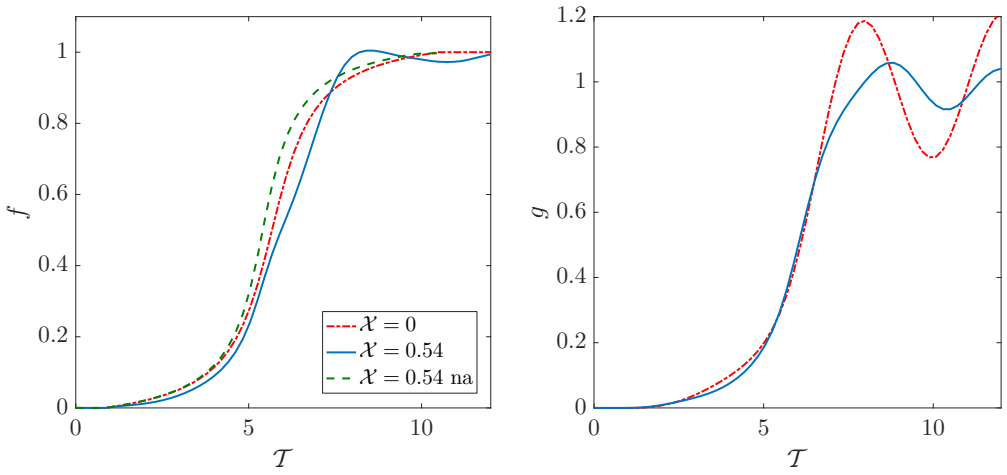


Figure 5.10: Wavefront shape (left), and resonator response (right) for $\alpha_a = 0.65$ for the Pareto plot in Figure 5.9, under typical operation for irregular geometry. $15.5 < v_0 < 22.0$ Hz.

and Figure 5.11 under the extreme envelope. They are similar to the waveforms obtained with regular resonator geometry (see Figs. 5.7 and 5.8). The amplitude of the upstream oscillations after the initial pressure rise has been slightly reduced, due to the non-uniform natural frequency of the irregular geometry. In addition, the initial pressure rise appears to be slightly smoother in Figure 5.11, compared to Figure 5.8.

The effectiveness of irregular resonator geometry appears to be more pronounced for steeper incident wavefronts, as is demonstrated in Figure 5.12. Nonlinear steepening in the region $\mathcal{T} = 6 - 7$ is unaffected by the array. This profile is qualitatively similar to the waveforms obtained from scale model experiments and 2-D numerical models by Sasoh et al. (1998), for a shock wave propagating in a duct lined with cavities. The wavefront is characterised by three sections (with reference to Figure 5.12), in order of increasing $\mathcal{T}$: (1) an initial shock front whose overpressure (defined by the initial sharp peak) decreases monotonically with propagation distance ($6 < \mathcal{T} < 8$); (2) a compression wave for which the overpressure is locally higher than that of the undisturbed waveform ($8 < \mathcal{T} < 12$); (3) damped oscillations upstream of the wavefront ($\mathcal{T} > 12$).

It may be possible to reduce the oscillatory behaviour of the transmitted waveforms by increasing the damping. For example, increase the surface roughness of

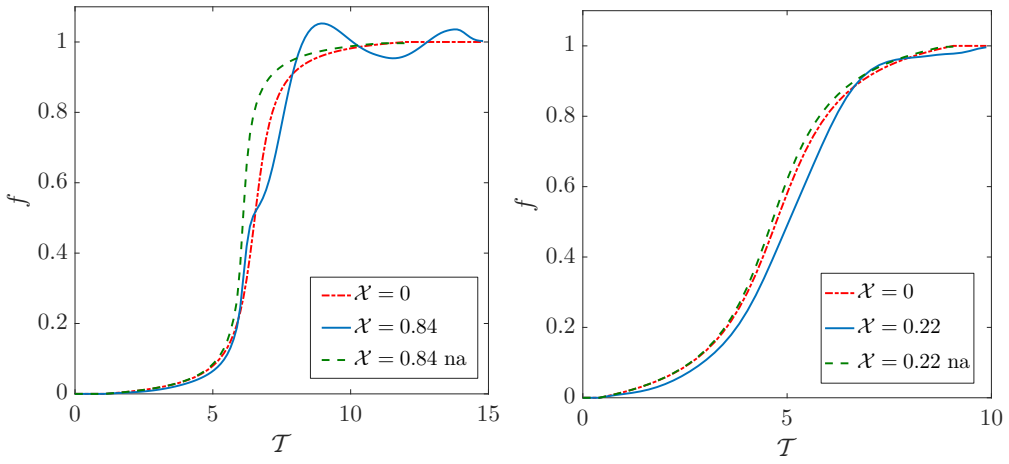


Figure 5.11: Wavefront shape for $\alpha_a = 0.71$ in Figure 5.9 for lower (left), and upper (right) bounds of the extreme operating envelope for irregular geometry. $18.0 < v_0 < 23.0$ Hz.

no. opt	1	2	5
min	0.581	0.571	0.585
max	0.836	0.844	0.834
mean	0.691	0.694	0.692
stdev	0.067	0.074	0.065

(a) Figure 5.13

no. opt	1	2	5
min	0.600	0.601	0.641
max	0.820	0.810	0.786
mean	0.691	0.691	0.697
stdev	0.056	0.054	0.038

(b) Figure 5.14

Table 5.5: Statistics for the sensitivity of the different operating regimes as a function of the number of optimisation points.

the tunnel and necks, or use porous media in the cavities.

5.8 Sensitivity to Operating Conditions

The sensitivity of the longest Pareto optimal array configurations (for $\tilde{l}_a \approx 13$) in Figure 5.5 and 5.9 to the shape of the incident pressure wavefront has been tested for the different operating envelopes in Table 5.3. The objective function has been evaluated over a range of train speeds (which controls the acoustic pressure) and characteristic wavefront lengths, for the optimal array configurations. This is plotted in Figures 5.13 and 5.14 for the regular and irregular resonator geometry, respectively. The corresponding minimum, maximum, mean and standard deviation for these contour plots are included in Table 5.5.

Using multiple optimisation points covering a range of operating conditions for

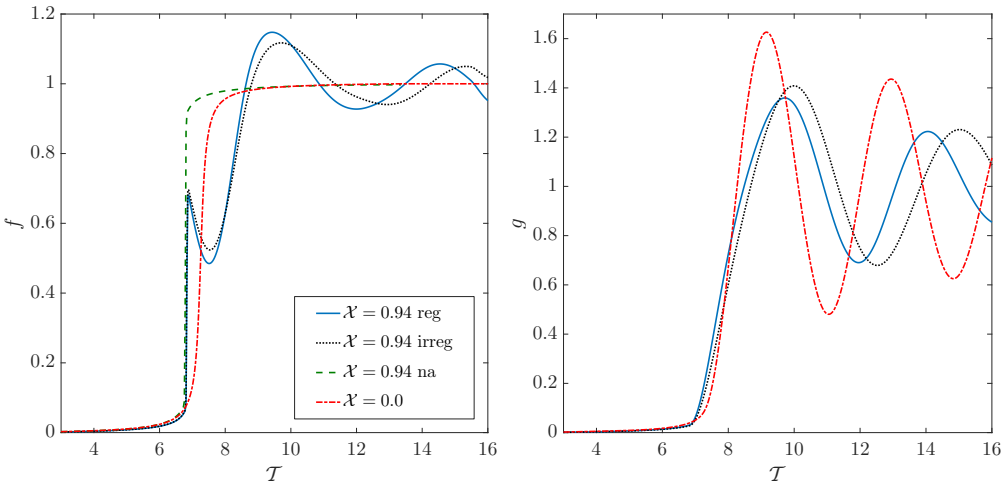


Figure 5.12: Comparison of the wavefront shape (left), and resonator response (right) for $\tilde{l}_a \approx 13$ on the Pareto fronts for the extreme envelope (with 2 optimisation points) with regular and irregular resonator geometry. $\tilde{L} = 0.2$ with $u_z = 500$ km/h.

the regular resonator does not appear to make much difference to the robustness of the array. On the other hand, the arrays with irregular geometry exhibit a smaller standard deviation from the mean, even though the minimum values are not quite as low as that with regular geometry. These results suggest that using five optimisation points does not offer much advantage in robustness over two points, particularly considering that the use of five points increases the cost of each fitness function evaluation at least two-fold.

It is difficult to see much improvement when using irregular resonator geometry, at least for the idealised entry wave considered in this section. It is expected that the use of irregular resonator geometry would improve the robustness of the array to different operating conditions, as the array would feature a range of natural frequencies across the frequency bandwidth of the incident waveform. In comparison, a greater improvement in the robustness of the optimised arrays is seen for the more severe case of $\tilde{L} = 1 \pm 50\%$ when using both irregular geometry and multiple optimisation points (see Appendix E). It may be more difficult to optimise the array geometry for incident waves with lower characteristic frequencies, due to the constraints imposed on the maximum size of the array geometry (see § 5.2.2 and 5.5.3).

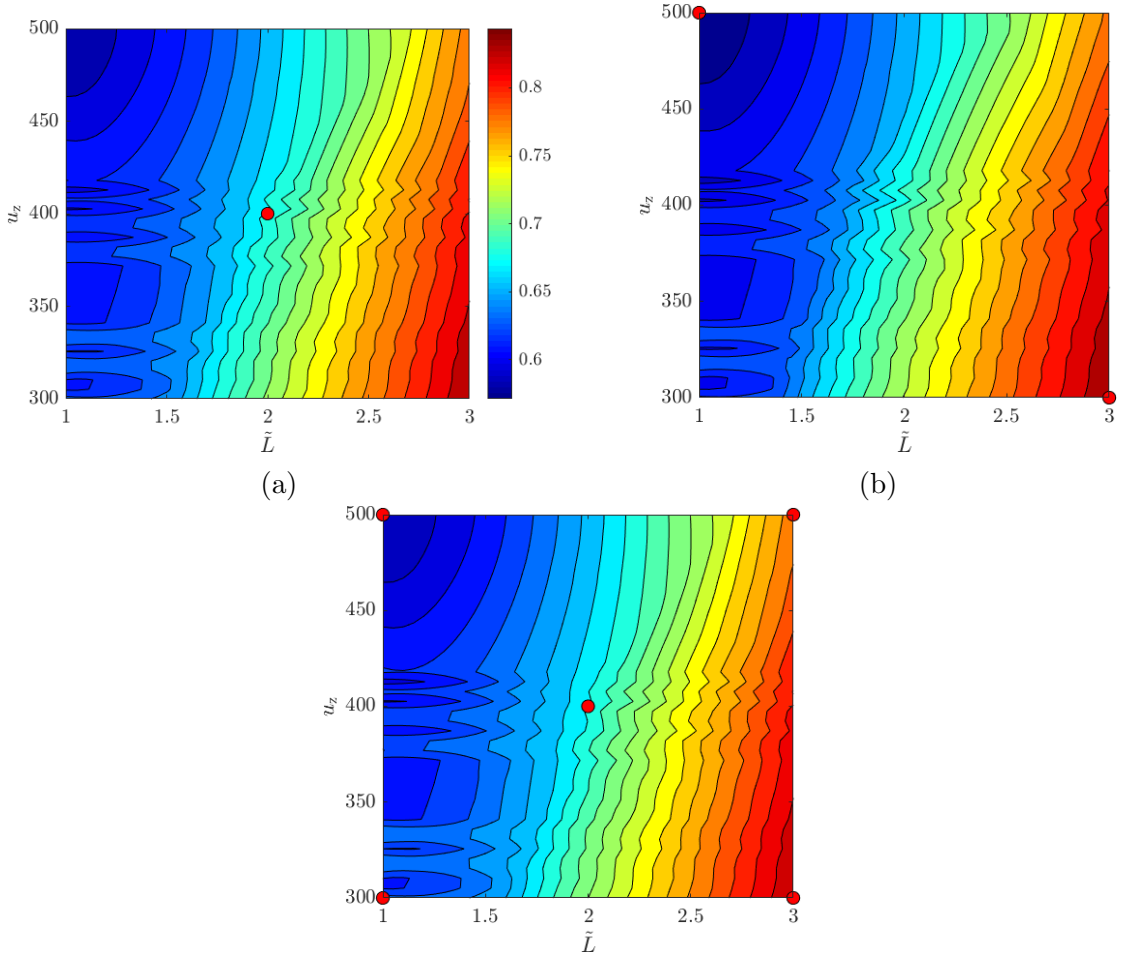


Figure 5.13: Sensitivity of the objective function to $\tilde{L}$ and u_z, for $\tilde{l_a} \approx 13$ and $\tilde{L} = 2 \pm 50\%$, optimised with: (a) one; (b) two and (c) five optimisation points (see Table. 5.3), with regular resonator geometry.

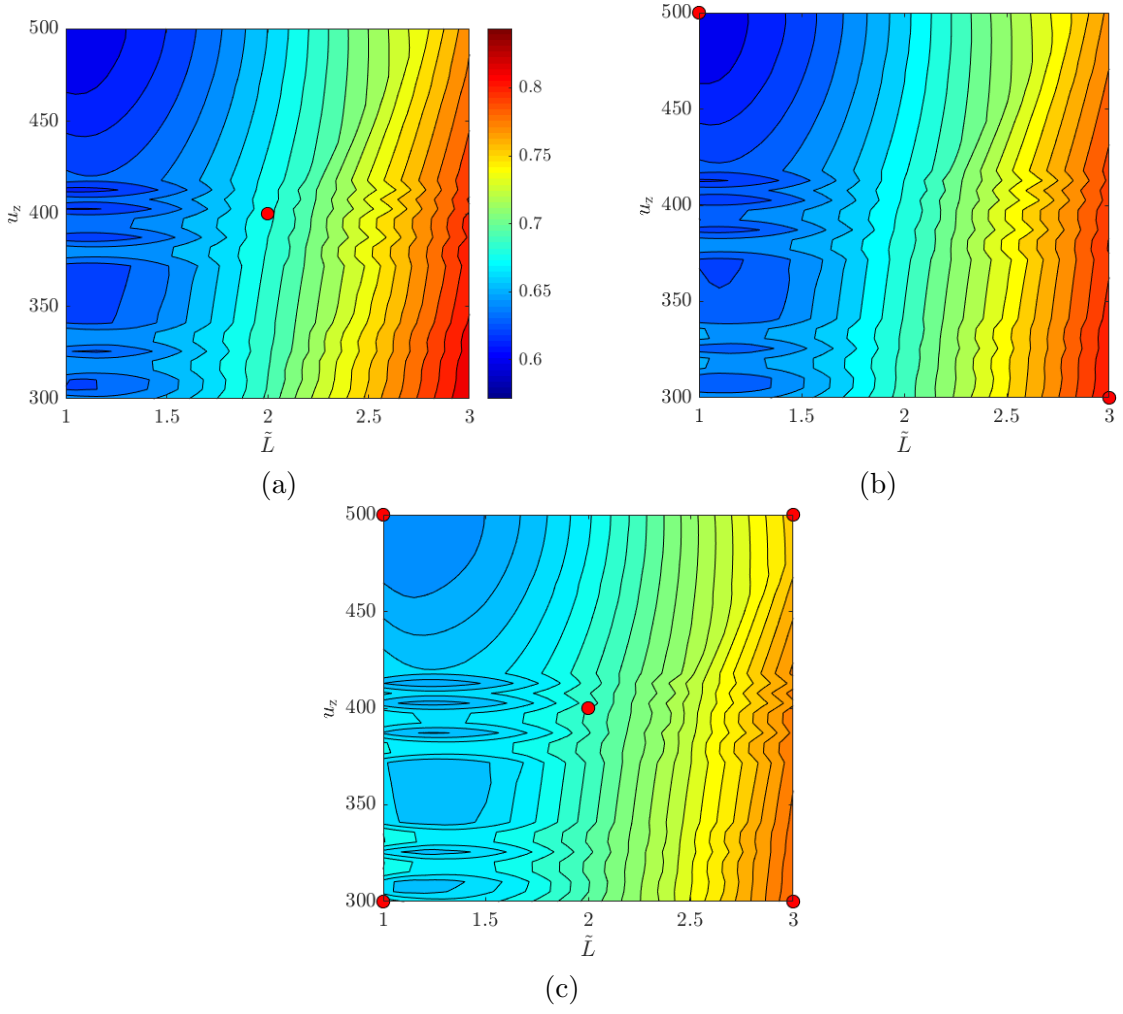


Figure 5.14: Sensitivity of the objective function to $\tilde{L}$ and u_z, for $\tilde{l_a} \approx 13$ and $\tilde{L} = 2 \pm 50\%$, optimised with: (a) one; (b) two and (c) five optimisation points (see Table. 5.3), with irregular resonator geometry.

These results suggest that using irregular resonator geometry or multiple optimisation points does not produce a significant increase in the robustness of the array to different train operating regimes, at least for $\tilde{L} = 2 \pm 50\%$. It is noted that using irregular resonator geometry increases the optimisation search space by up to two dimensions. As a result, the GA would likely need to run for more generations and with a larger population size to produce results which are at least comparable to the regular geometry.

Suggestions for how the results for irregular geometry could be improved include: (1) increasing the upper limit on the number of generations for the GA; (2) increasing the population size, in order to reduce the likelihood of convergence to local minima; (3) reducing the tolerance on the convergence of the objective function. The effect of using irregular resonator geometry for more complex incident wavefronts, due to a series of side-branches upstream of the array, is investigated in § 5.11.

The GA was also compared against the pattern search algorithm in MATLAB (MathWorks, 2017b) for fixed values of the integer parameters N_c and N_n. The pattern search algorithm converges more quickly, although the GA generally obtained smaller values of the objective function. It may be possible to increase the likelihood of the pattern search algorithm converging towards the global minimum with additional consideration of the algorithm settings.

5.9 Effect of Train Entry Speed on MPWs

One of the simplest approaches to reduce the amplitude of MPWs at the tunnel exit as a result of the entry compression wave (primary wave) is to temporarily reduce the speed of the train as it enters the tunnel. No modification to the tunnel or train is required and so there are no associated fixed costs. However, the journey time and maintenance requirements will be affected, due to additional braking/acceleration.

The effect of modifying the train speed on the strength of the primary MPW is studied in this section, incorporating the effect of non-linear steepening in long

tunnels. The associated time penalty is also estimated. The analytical model developed in this section can be used to predict the effect of non-linear steepening of a characteristic wavefront over large propagation distances.

5.9.1 Analytical Model

The entry compression wave is characterised by its maximum amplitude at the point of generation, p_1, and the characteristic length of the steepest part of the wave, L (see Figure 5.1). The amplitude can be accurately predicted using Equation 2.7, while the characteristic length can be approximated using Equation 5.7.

The subsequent propagation of the pressure wave in a slab track tunnel is predicted using the dimensional form of the far-field system in Equation 3.41 (excluding the source term for the resonator array), which is given by:

$$\frac{\partial p}{\partial X} - \alpha p \frac{\partial p}{\partial T} - \beta \frac{\partial^2 p}{\partial T^2} - C \frac{\partial^{1/2} p}{\partial T^{1/2}} = 0 \tag{5.21}$$

where $\alpha = (\gamma + 1)/(2\gamma a_0 p_0)$, $\beta = \mathcal{C}\sqrt{\nu}/r_\mathrm{t}$, and $C = \nu_\mathrm{d}/(2a_0^3)$. X and T are the dimensional far-field variables:

$$T = \left(t - \frac{x}{a_0} \right), \qquad X = x \tag{5.22}$$

These should not be confused with the non-dimensional far-field variables, $\mathcal{T}$ and $\mathcal{X}$, introduced in § 3.2.4. The terms with coefficients β and C represent the diffusivity of sound and the laminar boundary layer of the waveguide, respectively. They are assumed to be negligible in the absence of strong changes in gradients and in smooth walled concrete slab track tunnels. Therefore, Equation 5.21 reduces to the inviscid Burgers' equation, for which the general solution can be found using the method of characteristics:

$$p(X,T) = c\left(T + \alpha p X\right) \tag{5.23}$$

where c is a temporary constant of integration. The general solution to the Burgers' equation must satisfy the initial condition in Equation 5.5 with $x \sim -a_0 t$, i.e. the characteristic profile of the entry compression wave defined on time:

$$p(0,T) = c\left(T\right) = p_1\left[\frac{1}{2} + \frac{1}{\pi}\arctan\left\{\frac{\pi a_0}{L}T\right\}\right] \tag{5.24}$$

Therefore, the solution to the inviscid Burgers' equation for this initial condition is:

$$p = p_1\left[\frac{1}{2} + \frac{1}{\pi}\arctan\left\{\frac{\zeta}{L}\right\}\right] \tag{5.25}$$

where $p = p(X,T)$ and $\zeta = \zeta(X,T) = \pi a_0\left(T + \alpha p X\right)$. An explicit solution is not available for this equation in terms of p. However, this work is only concerned with the maximum rate of change of pressure for the purpose of estimating the maximum MPW amplitude in the low frequency and far-field approximations. The explicit solution is found through differentiation of Equation 5.25:

$$\frac{\partial p}{\partial T} = \frac{a_0 p_1}{L\left(\frac{\zeta^2}{L^2} + 1\right) - X\alpha a_0 p_1} \tag{5.26}$$

The maximum rate of change of pressure occurs at the inflexion point $\partial^2 p/\partial T^2 = 0$, which is given by:

$$\frac{\partial^2 p}{\partial T^2} = -\frac{2\zeta a_0 p_1}{L^3\left(\frac{\zeta^2}{L^2} + 1\right)^2 - L^2 X\alpha a_0 p_1\left(\frac{\zeta^2}{L^2} + 1\right)} \tag{5.27}$$

Solving this equation for T gives $T_{\mathrm{p'},\max} = -X\alpha p\,(X, T_{\mathrm{p'},\max})$, which is valid under the conditions $L \neq 0$ and $L \neq X a_0 \alpha p$. Substituting $T_{\mathrm{p'},\max}$ into Equation 5.25 gives $p\,(X, T_{\mathrm{p'},\max}) = p_1/2$, and so $T_{\mathrm{p'},\max} = -(X\alpha p_1)/2$. Therefore, the maximum rate of change of pressure is given by substituting $T_{\mathrm{p'},\max}$ into Equation 5.26:

$$\left(\frac{\partial p}{\partial T}\right)_{\max} = \frac{a_0 p_1}{L - X\alpha a_0 p_1} \tag{5.28}$$

In § 5.3 the initial condition is scaled so that $p|_{x=-b} = p_1$ and $p|_{x=b} = 0$, in order for it to be used numerically. Applying the procedure used above to the scaled form of the initial condition in Equation 5.6 gives the maximum rate of change of pressure as:

$$\left(\frac{\partial p}{\partial T}\right)_{\max} = \frac{2\,\pi\,a_0\,p_1}{2\,L\,\arctan\!\left(\frac{\pi\,b}{L}\right) + L\,\pi - 2\,\pi\,X\,a_0\,\alpha\,p_1} \tag{5.29}$$

This equation is useful for comparisons against numerical predictions and is equivalent to Equation 5.28 as $b \to \infty$. Ozawa et al. (1993) proposed an empirical formula for the maximum pressure gradient as a function of propagation distance for ballast track tunnels:

$$\left(\frac{\partial p}{\partial T}\right)_{\max,\mathrm{Ozawa}} = \left(\frac{\partial p}{\partial T}\right)_{\max,0} \exp(-\zeta X) \approx \left(\frac{a_0 p_1}{L}\right) \exp(-\zeta X) \tag{5.30}$$

where ζ is the attenuation coefficient, which is calculated from experimental data ($\zeta \approx 1.8 \times 10^{-4}$ [1/m] for ballast track tunnels in Japan). Clearly, the dispersion from the ballast overcomes non-linear steepening.

A discontinuity (shock wave) emerges at the distance where the maximum rate of change of pressure tends to infinity (not to be confused with where $L \to 0$), which from Equation 5.28 gives:

$$X_{\mathrm{s}} = \lim_{\left[\left(\frac{\partial p}{\partial T}\right)_{\max} \to \infty\right]} \frac{L}{\alpha a_0 p_1} - \frac{1}{\alpha \left(\frac{\partial p}{\partial T}\right)_{\max}} = \frac{L}{\alpha a_0 p_1} \tag{5.31}$$

Equation 5.31 is equivalent to Equation 4.26 by Rienstra and Hirschberg (2004), with $(\partial p/\partial t)_{x=0} = (a_0 p_1)/L$. Similarly, from Equation 5.29, the distance where a shock emerges for the bounded form of the initial condition is given by:

$$X_{\mathrm{s}} = \frac{L\,\left[\pi + 2\,\arctan\left(\frac{\pi\, b}{L}\right)\right]}{2\,\pi\, a_0\, \alpha\, p_1} \tag{5.32}$$

The length of the tunnel, l_{t}, is used for the value of X in Equation 5.28 and 5.29 in order to estimate the MPW amplitude at the exit portal. Using $X = 0$ implies no distortion of the wavefront between the entrance and exit of the tunnel.

The model is conservative, as it will overestimate the maximum rate of change of pressure, particularly for steep wavefronts (e.g. high train speeds and large propagation distances). Heat conduction and friction are no longer negligible for strong changes in gradient, which in turn limits the wave steepening process. Ignoring these mechanisms may be acceptable for smooth concrete slab track tunnels, but not for ballast track, which is strongly dispersive (see § 3.2.4.1). The numerical method described in § 3.3.2 must be used to predict the transmitted wave including these effects.

Equation 5.28 has been validated against experimental data gathered at RTRI (see Figure A.4). The value of L is estimated using Equation 5.7. Good agreement is obtained between experiments and predictions, although the analytical model tends to over-predict the maximum rate of change of pressure with increasing train speed and measurement distance from the tunnel entrance. Visco-thermal losses can no longer be neglected for steep wavefronts, as they counteract the steepening process.

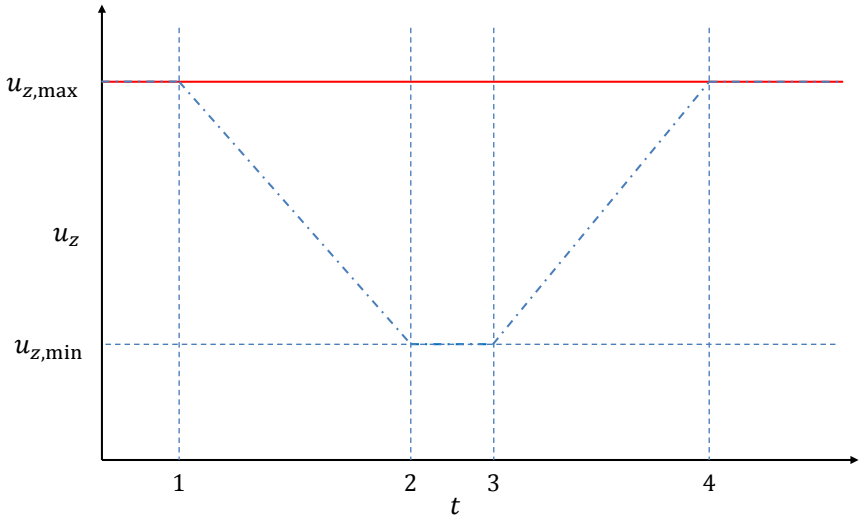


Figure 5.15: Train time-speed profile for tunnel passage for a train with a speed reduction on tunnel entry (----), and a constant speed (—).

5.9.2 Demonstrative Case

The train time-speed profile for tunnel entry is shown in Figure 5.15. The train reduces its velocity linearly from its nominal operating speed (t_1) to where the train enters the tunnel (t_2), in order to minimise passenger discomfort. An acceleration of $\pm 0.05g$ is used ($g = 9.81\ \mathrm{m\,s^{-2}}$), where $0.1g$ is the approximate limit that can be sustained without discomfort for standing passengers (Powell and Palacín, 2015). The train is then held at a constant velocity until the tail has passed the tunnel entrance (t_3), in order to avoid the generation of strong expansion waves. The train then applies a constant acceleration (the same as for the speed reduction) until it has reached its nominal operating speed at t_4.

The effectiveness of reducing the train speed is measured by the reduction in the maximum SPL, relative to an equivalent train that does not reduce its speed on tunnel entry (see Equation 5.19). The tunnel and train geometry as well as the physical parameters considered for this study are provided in Table 3.1. The change in SPL (based on Equation 5.28) and the associated time penalty as a function of train speed (with a nominal operating speed of 380 km/h) is plotted in Figure 5.16.

Large reductions in the SPL of the MPW can be achieved simply by reducing

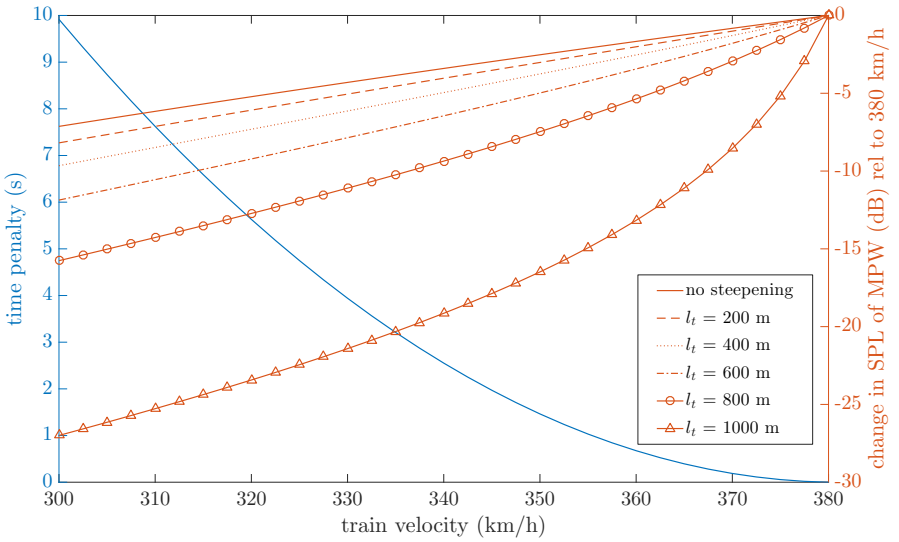


Figure 5.16: The effect of reducing the train speed (from 380 km/h) on the added journey time (for one tunnel) and the change in the analytical maximum MPW SPL.

the speed of the train at tunnel entry, with a small penalty in terms of added journey time. Although the time penalty may be fairly insignificant for one tunnel (an addition of $\sim 0.1\%$ on a 2-hour journey based on a speed reduction from 380 to 300 km/h), it could become significant for journeys involving many tunnels. The reduction in SPL increases with tunnel length as the rate of non-linear steepening increases with the amplitude of the entry compression wave, as shown in Equation 5.28. Tunnels with lengths greater than 1 km are not considered, as a discontinuity would emerge in the analytical solution for train speeds above 380 km/h.

The reduction in SPL has also been predicted using the numerical solution of Equation 5.21, and is plotted in Figure 5.17 for $l_\mathrm{t} = 1$ km. There is relatively little difference between the numerical predictions with and without the inclusion of viscous terms. In addition, the change in the rate of steepening is caused almost entirely by the boundary layer of the tunnel. Note that the term for quasi-steady skin friction is not included in this formulation (see § 3.2.3). This term will generally have a greater effect compared to the laminar boundary layer for a rough tunnel wall. The reduction in SPL is under-predicted by the inviscid numerical solution, compared to the analytical one for two main reasons: (i) the bounded

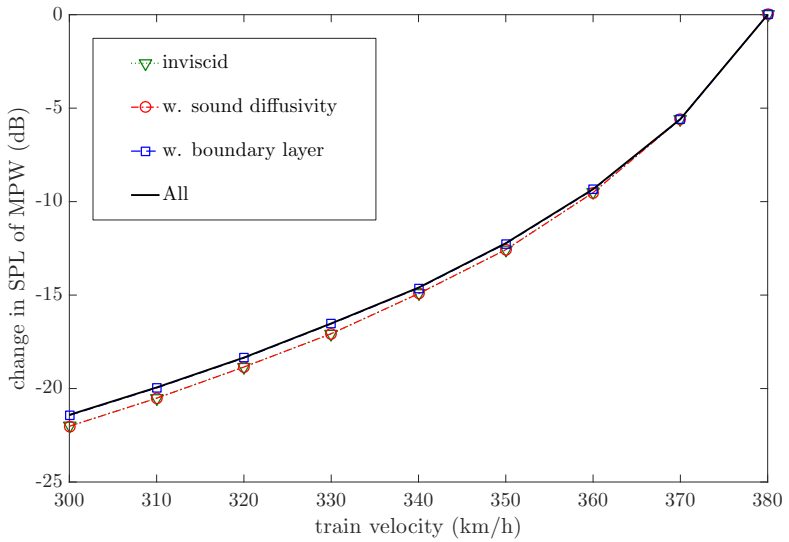


Figure 5.17: The effect of reducing the train speed (from 380 km/h) on the maximum MPW SPL for $l_t = 1$ km, based on numerical modelling of wave steepening.

form of the IC (Equation 5.6), which is used for the numerical solution, is steeper than the unbounded form used in Figure 5.16; (ii) numerical diffusion, particularly around high gradients.

5.10 Comparison of MPW Countermeasures

In this section the effectiveness of an array of Helmholtz resonators is compared to existing countermeasures, in particular the entrance hood. The tunnel entrance hood is one of the most effective methods for reducing the gradient of the entry compression wave and the amplitude of MPWs, even in long tunnels. However, Takayama et al. (1995) found that a hood becomes less effective at higher operating speeds, while an array is less effective at lower speeds. Therefore, combining the two countermeasures was found to provide better performance over a wide range of piston speeds, i.e. up to an 80% reduction in the maximum rate of change of pressure compared to without any countermeasures.

Ozawa and Maeda (1988) produced an empirical formula for the relative reduction in the maximum rate of change of pressure of the entry compression wave

with and without an optimal unventilated entrance hood:

$$\alpha_{\mathrm{h}} = \max\left|\frac{\partial p}{\partial t}\right|_{\mathrm{h}} \Big/ \max\left|\frac{\partial p}{\partial t}\right|_{\mathrm{nh}} \approx \frac{1}{1 + l_{\mathrm{h}}/L} \tag{5.33}$$

where l_{h} is the length of the hood, L is the characteristic length (accounting for the entry speed and the shape of the train nose and tunnel entrance), and subscripts h and nh refer to with and without the hood, respectively. The value of L is approximated using Equation 5.7, where empirical coefficient ϕ is also a function of the geometry of the train nose and tunnel entrance, including the length of the hood. This implicit dependency cannot be considered in this simple model. A typical value of L is 30-40 m for modern Shinkansen trains with long noses.

A more accurate prediction of the reduction in the pressure gradient can be made by using the analytical model developed by Howe et al. (2008). This model accounts for the cross-sectional area profile of the train nose, $S_{\mathrm{n}}(x)$, and tunnel entrance, $S_{\mathrm{h}}(x)$. However, the model is more complex to implement for design purposes. Using Equation 5.33 with 5.9, the value of L with an entrance hood is approximately given by

$$L_{\mathrm{h}} = \left(\frac{p_{\mathrm{h}}}{p_{\mathrm{nh}}}\right)\frac{L_{\mathrm{nh}}}{\alpha_{\mathrm{h}}} \approx \frac{L_{\mathrm{nh}}}{\alpha_{\mathrm{h}}} \approx L_{\mathrm{nh}} + l_{\mathrm{h}} \tag{5.34}$$

where L_{nh} is the characteristic length without a hood and it is assumed that $p_{\mathrm{h}} = p_{\mathrm{nh}}$. Equation 5.33 does not account for the effect of non-linear steepening between the entrance and exit of the tunnel. A modified form of Equation 5.33 accounting for non-linear steepening of the wavefront after a specific distance from the tunnel entrance is given by:

$$\alpha_{\mathrm{h}} = \frac{p'(t)_{\mathrm{h,na}}}{p'(t)_{\mathrm{nh,na}}} \tag{5.35}$$

where $p'(t)_{\mathrm{h,na}}$ and $p'(t)_{\mathrm{nh,na}}$ are the maximum rate of change of pressures, which can be approximated using the analytical expression in Equation 5.28 or 5.29 with $L = L_{\mathrm{h}}$ and $L = L_{\mathrm{nh}}$, respectively. Therefore, using Equation 5.35 with

Equation 5.28 gives:

$$\alpha_{\mathrm{h}} = \frac{L_{\mathrm{nh}} - X a_0 p_{\mathrm{nh}}}{L_{\mathrm{nh}} + l_{\mathrm{h}} - X a_0 p_{\mathrm{nh}}} \tag{5.36}$$

5.10.1 Array Versus a Hood

The performance of an optimal entrance hood is compared to the Pareto front of an optimised array of identical Helmholtz resonators in Figure 5.18, for a train operating at 300, 400 and 500 km/h. The array is optimised under typical operating conditions (see § 5.7.1) and does not account for the effect of an entrance hood on the incident wavefront. On the other hand, the value of α_{h} is calculated using Equation 5.33 and does not consider the effect of non-linear steepening. The value of L is identical for both countermeasures (i.e. identical initial conditions) and is calculated using Equation 5.7 with $\phi = 1.0$, for a short nosed train.

The optimal hood provides a significant reduction in the maximum pressure gradient compared to an array of Helmholtz resonators of the same length. However, it is expected that the hood will be relatively short ($\tilde{l_{\mathrm{h}}} < 5$), while the array will be significantly longer ($\tilde{l_{\mathrm{a}}} \gg 5$) in most real tunnel systems. Furthermore, the value of α_{h} will increase significantly (i.e. it becomes less effective) if non-linear steepening is included over a distance corresponding to the length of the array.

5.10.2 Array Combined with a Hood

The effectiveness of combining an entrance hood with an array of Helmholtz resonators is now considered. The geometry used for the array is based on the Pareto front in Figure 5.18, with $u_{\mathrm{z}} = 400$ km/h and $\tilde{l_{\mathrm{a}}} \approx 20$ (see Table 5.4). A realistic hood length of $\tilde{l_{\mathrm{h}}} = l_{\mathrm{h}}/d_{\mathrm{t}} = 3$ is used throughout the analysis.

The total combined effect of the hood and an array (α_{tot}) is calculated for two cases. The first is representative of the real system, where the incident pressure wave for the array also accounts for the effect of the hood, i.e. $\alpha_{\mathrm{a}} = f(L_{\mathrm{h}})$. This

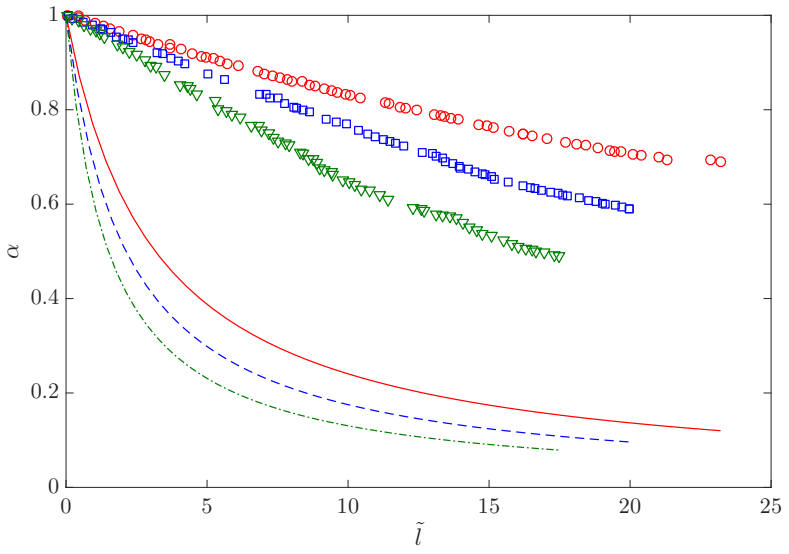


Figure 5.18: Variation of α with non-dimensional countermeasure length for the array (α_a) Pareto front with an entry speed of 300 km/h (○); 400 km/h (□); 500 km/h (▽), and for the optimal entrance hood (α_h) with an entry speed of: 300 km/h (—); 400 km/h (– – –); 500 km/h (– · – ·), with $\phi = 1$.

is given by:

$$\alpha_{tot,1} = \alpha_h \cdot \alpha_a(L_h) = \frac{p'(t)_{h,na}}{p'(t)_{nh,na}} \cdot \frac{p'(t)_{h,a}}{p'(t)_{h,na}} = \frac{p'(t)_{h,a}}{p'(t)_{nh,na}} \tag{5.37}$$

In the second case, identical incident wavefronts are assumed for the hood and array, i.e. $\alpha_a = f(L_{nh})$. This assumption conveniently allows the value of α_a to be calculated without needing to account for the effect of an entrance hood on the incident wavefront for the array. This gives:

$$\alpha_{tot,2} = \alpha_h \cdot \alpha_a(L_{nh}) = \frac{p'(t)_{h,na}}{p'(t)_{nh,na}} \cdot \frac{p'(t)_{nh,a}}{p'(t)_{nh,na}} \tag{5.38}$$

The variation of the maximum rate of change of pressure with train velocity is plotted in Figure 5.19 for four cases: (1) no hood & no array; (2) no hood & with an array; (3) with a hood & no array; (4) with a hood & an array. Propagation distances of 20 and 70 times the tunnel diameter are considered. Identical resonator geometries are used for both distances, where the number of cavities, N_c, is scaled-up for the array with $\tilde{l}_a \approx 70$.

Non-linear steepening of the wavefront is considered for a distance equivalent

to the length of the array in the cases where there is no array present (1 & 3). Clearly, combining an entrance hood with an array is more effective than using them separately, particularly for longer tunnels. The effectiveness of the array (Case 2) is nearly identical to the hood (Case 3) for $\tilde{l_a} \approx 70$, across the full range of train speeds considered (see Figure 5.19b). Therefore, the hood is efficiently augmented by the array in the case of very long tunnels.

Figure 5.20 shows that the two methods used to calculate α_{tot} give very different predictions. Equation 5.38 over-predicts the combined performance of the hood and array compared to Equation 5.37. Therefore, the simplified approximation in Equation 5.38 should not be used.

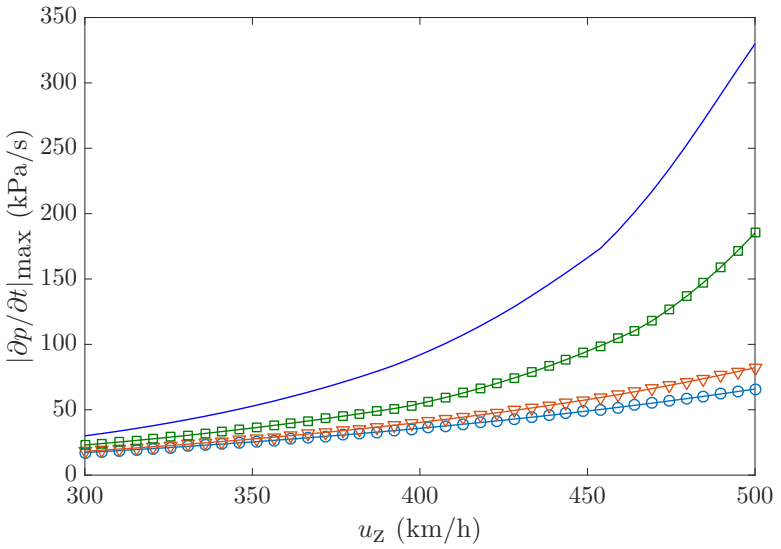
5.11 Multi-Peak Waveforms

5.11.1 Overview

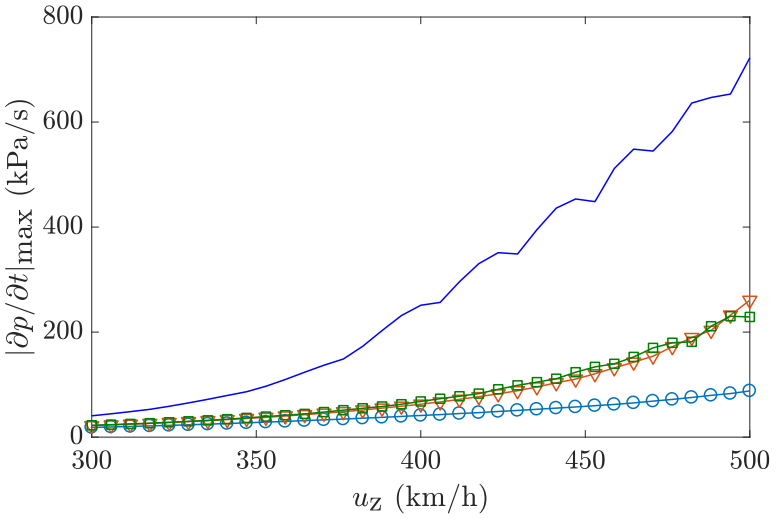
Up to this point it has been assumed that the incident pressure wave for an array of Helmholtz resonators is identical to the idealised compression wave generated as the train enters the tunnel (see § 5.3.1). In reality, the effect of an entrance hood and the partial reflection of the wavefront as it propagates (from side branches, etc.) distorts the shape of the entry wave. Miyachi et al. (2016) showed that the effect of this distortion can result in a pressure-time derivative profile with multiple peaks with different steepening characteristics. This section investigates the effectiveness of an array of Helmholtz resonators on more complex incident wavefronts due to the distortion from side branches.

5.11.2 Modelling of Branch Waves

A series of closed side branches is positioned upstream of the array, in order to simulate an incident waveform with multiple peaks in the profile for the rate of change of pressure. Ozawa et al. (1993) derived an analytical expression for the transmitted planar waveform due to a simple closed side branch:



(a) $\tilde{l}_a \approx 20$



(b) $\tilde{l}_a \approx 70$

Figure 5.19: Maximum rate of change of pressure versus train velocity for an optimised entrance hood ($\tilde{l}_h = 3$) and array for: Case 1 (—); Case 2 (—□—); Case 3 (—▽—); Case 4 (—○—).

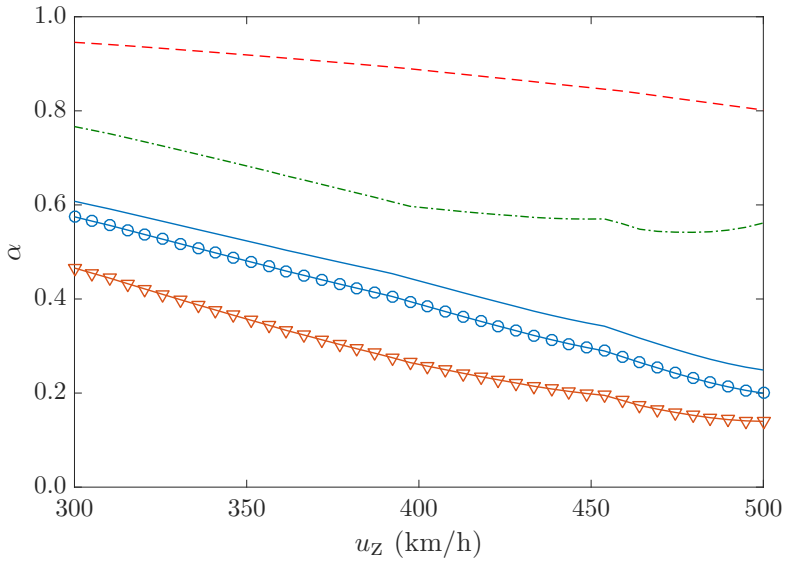
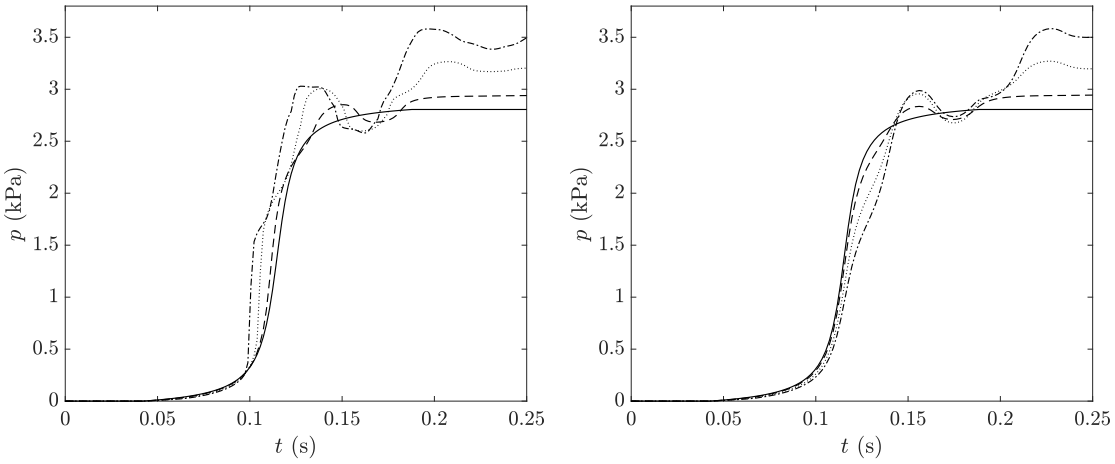


Figure 5.20: Normalised maximum rate of change of pressure as a function of train velocity for an optimised entrance hood and array ($\tilde{l_h} = 3$, $\tilde{l_a} \approx 20$) with: $\alpha_{tot,1}$ (⊖); $\alpha_{tot,2}$ (▽); $\alpha_a(L_h)$ (– – –); $\alpha_a(L_{hn})$ (– · – · –); α_h (——).

$$p_t(t) = \frac{2}{2+\theta}p_i(t) + \frac{4\theta}{(2+\theta)^2}p_i(t-2t_b) - \frac{4\theta}{(2+\theta)^2}\left(\frac{2-\theta}{2+\theta}\right)p_i(t-4t_b) + \frac{4\theta}{(2+\theta)^2}\left(\frac{2-\theta}{2+\theta}\right)^2 p_i(t-6t_b) + \cdots \tag{5.39}$$

where $\theta = S_b/S_t < 1$ is the ratio of cross-sectional areas between the branch and tunnel, $p_i(t)$ is the incident pressure waveform and $t_b = l_{b,eff}/a_0$. The effective branch length, $l_{b,eff} = l_b + \delta_{nt}$, includes a length correction, which is calculated using Equation 3.8. Equation 5.39 can be used when the spacing interval of the side branches is large enough to neglect interactions with neighbouring branches. Furthermore, this equation neglects the effect of wave-steepening in the branch (negligible for short branches).

Equation 5.39 is recursively applied to the characteristic entry compression waveform in Equation 5.6 with $x = a_0 t$, in order to predict the transmitted pressure waveform after n_b side branches along the length of the tunnel. The effects of non-linear steepening and friction from the tunnel wall on the shape of the compression wave as it propagates between the branches can be predicted using Equation 3.23



(a) With non-linear advection (b) Without non-linear advection

Figure 5.21: Example of the recursive application of Equation 5.39 on an idealised entry compression wave, for $n_\mathrm{b} = 0$ (—); $n_\mathrm{b} = 1$ (– – –); $n_\mathrm{b} = 3$ (····); $n_\mathrm{b} = 5$ (–·–·–). $\tilde{L} = 1$, $u_\mathrm{z} = 400$ km/h, $\theta = 0.2$, $l_\mathrm{b} = 3$ m, with a branch spacing of 100 m.

with $\bar{K} = 0$.

An example of the transmitted waveform is plotted in Figure 5.21, with and without the inclusion of non-linear steepening, for different values of n_b. The presence of the branches strongly distorts the wavefront, but is insufficient to counteract non-linear steepening for this case. The transmitted waveform is then used as the initial condition for an array of Helmholtz resonators.

5.11.3 Initial Comparison of Waveforms

Three cases are considered for the geometry of the array, all of which have the same total length: (1) equispaced and identical resonators; (2) equispaced resonators but with a variable neck diameter, based on Equation 5.3; (3) irregularly spaced resonators with a variable neck diameter and cavity length, based on Equation 5.2.

The dimensions and physical parameters chosen for the arrays are given in Tables 5.6 and 3.1, with reference to Figure 3.2. It is assumed that there are $n_\mathrm{b} = 5$ closed side branches preceding the array, with $\theta = 0.2$ and $l_\mathrm{b} = 5.0$ m. Distortion of the wavefront between the side-branches is neglected, i.e. a short distance between them. The range of cavity lengths and neck diameters used for the irregular resonator geometry are selected in order to span a range of natural

Case	N_c	N_n	$\tilde{l_{ex}}$	$\tilde{l_n}$	$\tilde{d_{n,0}}$	$\tilde{d_{n,1}}$	$\tilde{l_{c,0}}$	$\tilde{l_{c,1}}$	ω_e (rad s^{-1})
1	50	1	0.0	0.3	0.50	0.50	0.50	0.50	129.0
2	50	1	0.0	0.3	0.80	0.20	0.50	0.50	60 - 190
3	50	1	0.0	0.3	0.80	0.20	0.20	0.80	48 - 253

Table 5.6: Normalised dimensions for the array test cases, with reference to § 5.2 and with $l_a = 190$ m for all cases.

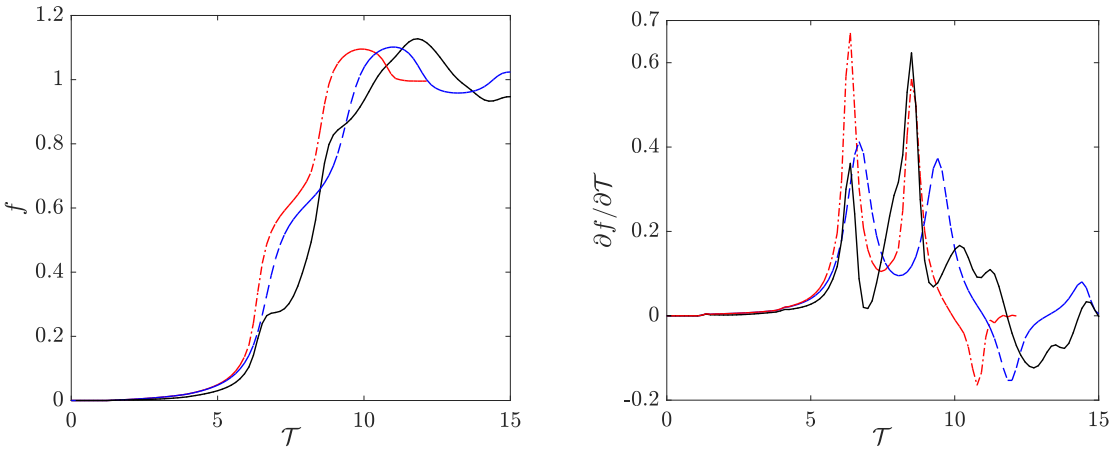
frequencies, while the regular array uses the average of the ranges. For the initial condition, the entry speed of the train is $u_z = 400$ km/h with $\tilde{L} = 1$.

The pressure waveforms and corresponding time-derivatives are plotted in Figure 5.22. The maximum rate of change of pressure without the array has more than doubled over 190 m. On the other hand, the maximum rate of change of pressure after 190 m with the array is comparable to the incident pressure wave. The use of irregular resonator geometry provides additional smoothing of the wavefront. The performance of the irregular array geometry may be improved by optimisation, subject to the incident waveform profile (including the effects of the side branches).

5.11.4 Optimisation

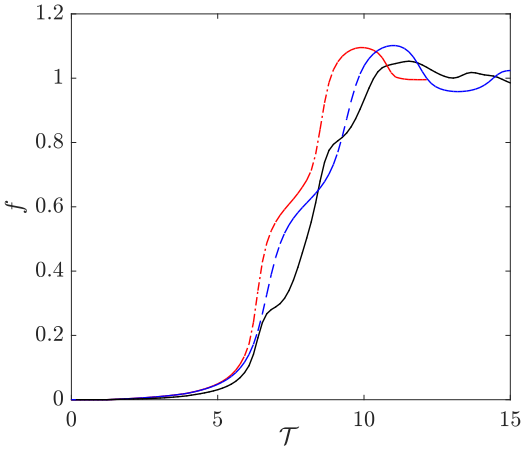
The array of resonators has been optimised using a single objective GA with regular and irregular geometry to see if optimisation can provide a greater reduction in the maximum rate of change of pressure, compared to the transmitted waveforms in Figure 5.22. The objective function is defined by Equation 5.18. The initial condition is identical to the one used in § 5.11.3 (i.e. $u_z = 400$ km/h with $\tilde{L} = 1$). The geometric variable bounds are specified in Table 5.1, except for the number of cavities, which is fixed (i.e. $N_c = 50$). Non-linear inequality constraints are used to ensure that $l_a = 190 \pm 2$ m (see § 5.5.3), in order to be consistent with the array configurations in Table 5.6.

The waveforms for the arrays optimised with regular and irregular geometry (see Table 5.7) are compared in Figure 5.23. The optimised arrays provide a greater reduction in the maximum rate of change of pressure compared to the

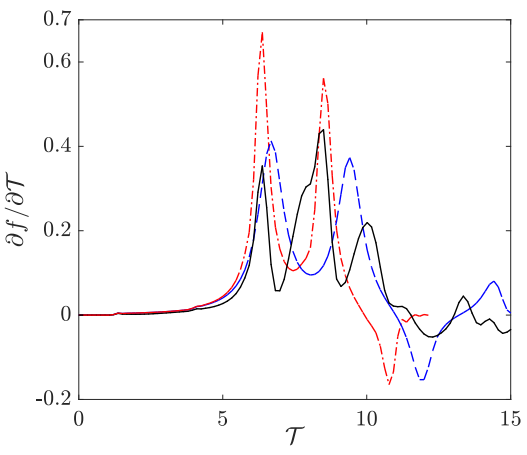


(a) Regular geometry

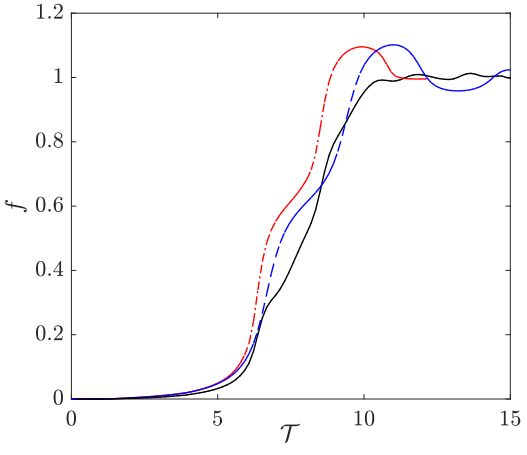
(b) Regular geometry



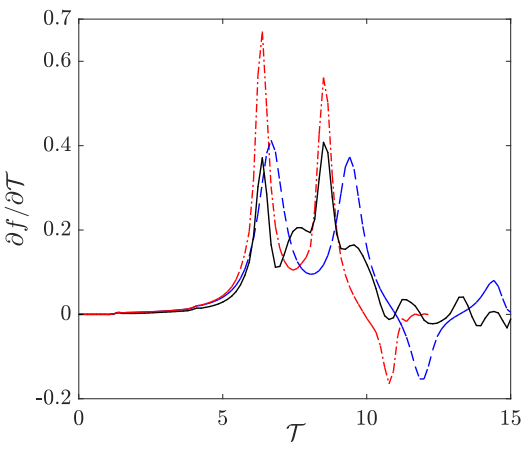
(c) Irregular geometry (variable d_{n})



(d) Irregular geometry (variable d_{n})



(e) Irregular geometry (d_{n} & l_{c})



(f) Irregular geometry (d_{n} & l_{c})

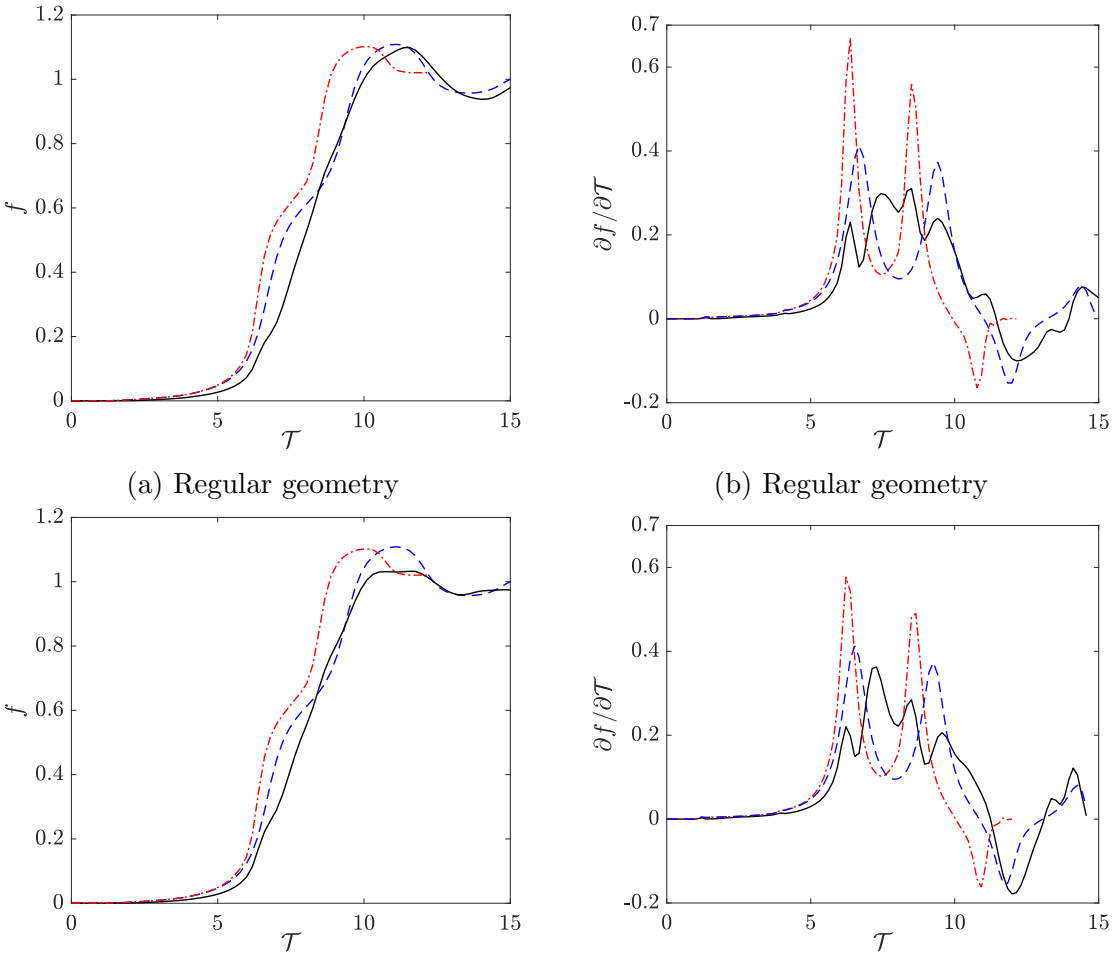
Figure 5.22: Dimensionless tunnel pressure waveforms (left) and corresponding time-derivatives (right), for an incident pressure wave preceded by side branches (– – –); and after 190 m with (——); and without (- - - -) an array.

Case	N_c	N_n	$\tilde{l_{ex}}$	$\tilde{l_n}$	$\tilde{d_{n,0}}$	$\tilde{d_{n,1}}$	$\tilde{l_{c,0}}$	$\tilde{l_{c,1}}$	ω_e (rad s^{-1})
reg	50	3	0.0	0.01	0.95	0.95	0.50	0.50	169
irreg	50	2	0.0	0.01	0.95	0.27	0.38	0.63	77 - 196

Table 5.7: Normalised dimensions for the optimised arrays, with reference to § 5.2, and with $l_a \approx 190$ m.

unoptimised waveforms in Figure 5.22. The use of irregular resonator geometry provides a noticeable improvement over regular geometry, compared to the results of the optimisation study in § 5.7, which only considers the undistorted idealised train entry compression wave.

Distortion from the side-branches increases the frequency content of the incident wavefront. Therefore, this type of waveform is better suited to irregular resonator geometry. These results suggest that the use of irregular geometry can increase the effectiveness of the array, particularly for a compression wave which has been distorted due to the presence of side branches.



(a) Regular geometry

(b) Regular geometry

(c) Irregular geometry (d_n & l_c)

(d) Irregular geometry (d_n & l_c)

Figure 5.23: Optimised dimensionless tunnel pressure waveforms (left) and corresponding gradients (right), for an incident pressure wave preceded by side branches (– – –); and after $\sim$ 190 m with (——); and without (- - - -) an array.

5.12 Conclusions

This chapter presents a demonstrative design for how an array of Helmholtz resonators could be integrated into redundant space in the tunnel, by using space under the track or under maintenance/emergency access walkways. A small availability of space through the tunnel cross-section could potentially be compensated for by using longer cavities in order to make up the required volume. A representative initial condition is introduced and is parametrised by the entry speed of the train and the shape of the train nose and tunnel entrance.

An objective function is specified for the purpose of optimisation, which tries to minimise the maximum rate of change of pressure of the wavefront, relative to an equivalent distance without an array. This is the most critical parameter in predicting the amplitude of MPWs. A sensitivity analysis indicated that the length of the cavities and diameter of the neck were the two most influential parameters affecting the objective function. The array was then optimised using a multi-objective genetic algorithm, producing a pareto front which represents a trade-off between the effectiveness and the total length of the array. For example, a 100 m long array could provide up to a 30% reduction in the maximum rate of change of pressure versus an equivalent distance without the array, for conditions approximately representative of high speed rail operations in tunnels, i.e. $\tilde{L} \sim 2$. It is noted that the array becomes more effective for steeper incident wavefronts when using this objective function, as the steepening rate is higher.

The effectiveness of irregular resonator geometry was also studied by performing a sensitivity analysis of approximately equal length optimal array configurations with regular and irregular geometry. Different train operating envelopes as a function of the train speed and characteristic length of the wavefront, L, were considered. The use of irregular resonator geometry and optimising for an extreme operating envelope provided a marginal improvement over regular geometry in terms of robustness to the incident wavefront. However, further numerical experiments are required. For example, it may be useful to improve the optimisation procedure so that it converges faster (see § 5.5.2), and to investigate the

performance of the array for a greater range on incident wavefront shapes.

The effectiveness of an array of resonators is compared and combined with a tunnel entrance hood. The performance of an optimised array cannot compete with an entrance hood of an equivalent length. However, the effectiveness of an array in reducing the maximum pressure gradient becomes comparable to a fixed length entrance hood over a sufficiently large propagation distance. Therefore, the array is intended to augment the entrance hood in cases where very high train speeds are combined with tunnels that are sufficiently long such that significant wave steepening could occur before the wavefront reaches the exit portal.

Finally, the effect of the shape of the incident compression wave on the performance of the array is investigated by considering a series of side branches just upstream of the array. It was found that the use of irregular resonator geometry was more effective in this case, compared to the idealised entry wave used for the main optimisation study.

Chapter 6

Branch Micro-Pressure Waves

6.1 Introduction

In § 2.4 it was suggested that unacceptable MPWs could be generated from tunnel side branches with increasing train speeds (e.g. from ventilation shafts and pressure relief ducts). Existing countermeasures (see § 2.5) and an array of Helmholtz resonators (see Chapter 3) will be effective for attenuating the compression wave generated as the train enters the tunnel before it splits at the branch junction. However, these countermeasures are ineffective for the pressure waves generated by a train passing a branch, except for the train nose shape. A preliminary parametric study is conducted in this chapter on the effect of modifying the tunnel-branch junction geometry on the amplitude of MPWs emitted from the branch portal.

An overview of the main types of branch MPWs is provided in § 6.2. Predictions are made about an increase in the amplitude of branch MPWs with increasing train operating speeds, based on representative tunnel and train geometry. A parametric study of the branch geometry is defined in § 6.3 and is carried out using 2-D CFD in order to provide a compromise between physical accuracy and acceptable simulation times. The models are intended to provide a qualitative indication of the effectiveness of modifying the branch geometry and whether further investigation is warranted.

6.2 Overview of Branch MPWs

Miyachi et al. (2014) derived an analytical model to approximate the maximum amplitude of the two main types of branch MPWs, as illustrated in Figure 6.1:

- **Primary branch** waves are due to the Primary compression wave generated as the train nose enters the tunnel (and to a lesser extent the expansion wave as the train tail enters). The compression wave splits at the junction with a portion of the acoustic energy going into the branch, depending on the ratio between the branch and tunnel areas. A portion of the signal energy is reflected upstream as an expansion wave from the branch junction.

- **Secondary branch** waves occur as the train passes the branch. Expansion and compression waves are generated in the branch as the train nose and tail passes, respectively. The amplitude of the branch waves are dependent on the train velocity and the ratio of the branch and tunnel areas, while the waveform of the branch wave is also affected on the geometry of the train nose and branch junction. A compression wave is also generated in the tunnel as the nose passes the branch.

Part of the branch wave acoustic energy is reflected from the branch outlet. This is not shown in Figure 6.1.

The analytical model of Miyachi et al. (2014) is used to demonstrate how increasing train speeds could affect the maximum amplitude of branch MPWs (as plotted in Figure 6.2a), for example with the introduction of magnetically levitating trains. The model assumes that the tunnel and branch are sufficiently long such that no wave reflection occurs from the ends. Furthermore, the geometry of the branch junction has no effect on the transmitted pressure waves, as the characteristic wavelength of is much greater than the effective size of the branch geometry. A blockage ratio (β) and nose length (l_{zn}) roughly consistent with modern Shinkansen rolling stock is assumed ($\beta \sim 0.16$ & $l_{\mathrm{zn}} \sim 15$ m). The branch area is conservatively assumed to be only 10% of the cross-sectional area of the

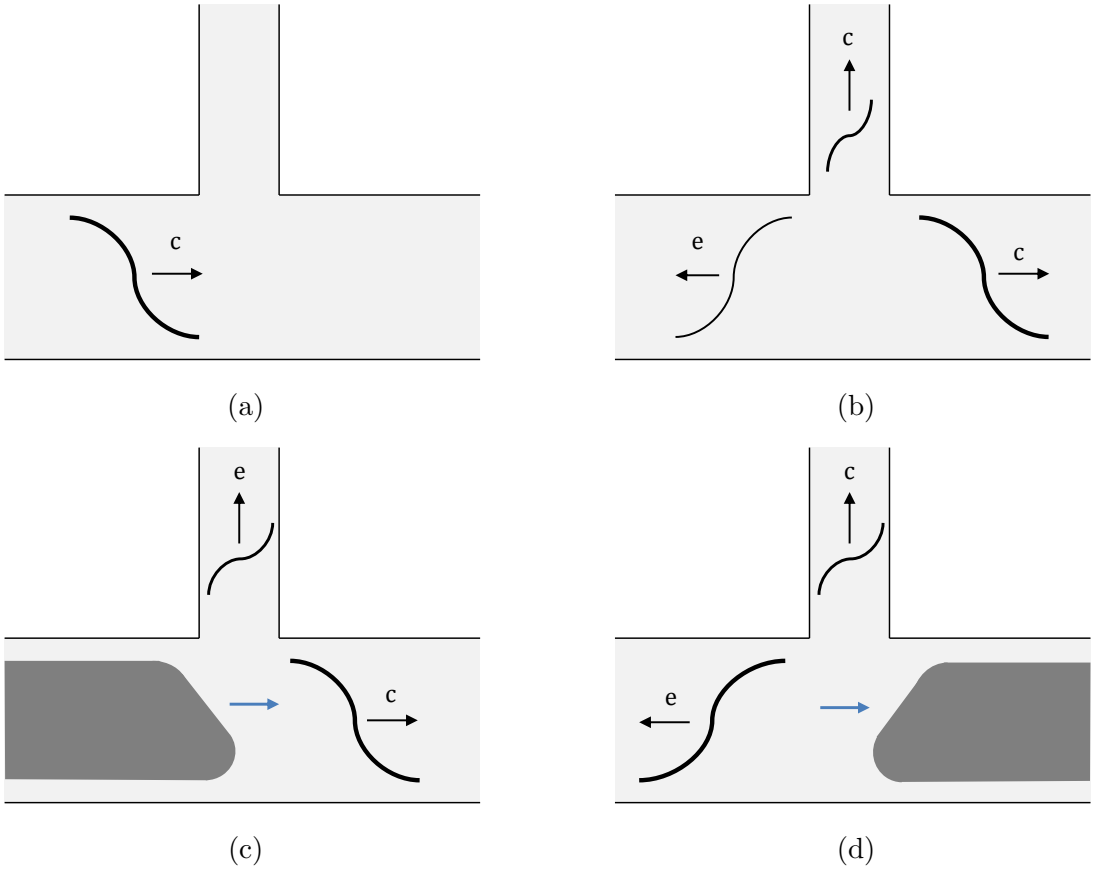


Figure 6.1: Illustration of the generation of the Primary branch wave (a) before and (b) after the entry wave has reached the branch, and the Secondary branch wave (c) before and (d) after the train nose and tail have passed the branch, respectively. Symbols **c** & **e** denote compression and expansion waves, respectively.

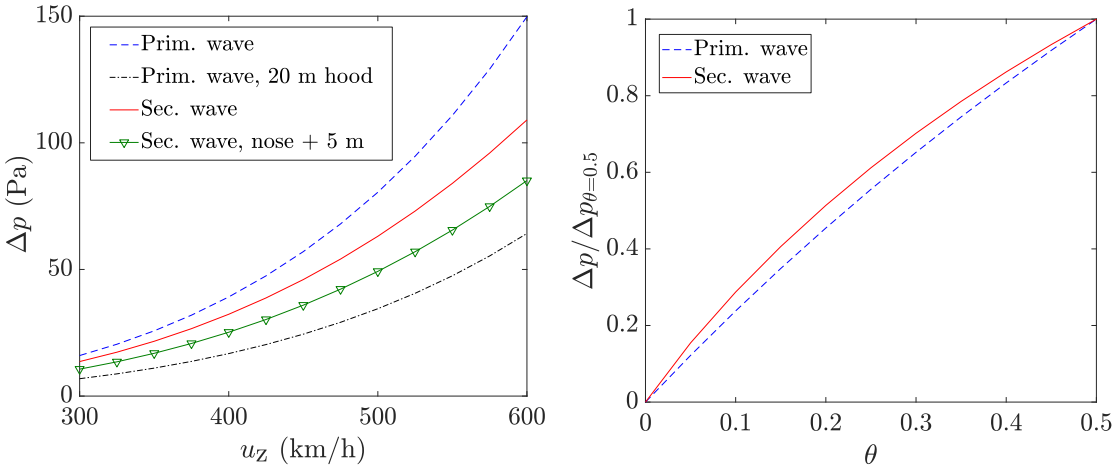


Figure 6.2: The effect of: (a) train speed on the maximum MPW amplitude with $\theta = 0.1$; (b) θ on the maximum branch MPW amplitude (normalised by the maximum branch MPW amplitude for $\theta = 0.5$).

tunnel (i.e. $\theta = S_b/S_t = 0.1$). Therefore, most of the acoustic power is transmitted in the tunnel, rather than into the branch.

At speeds approaching 400 km/h the predicted maximum MPW amplitude at $1d_t$ outside of the branch portal is estimated to be 20-40 Pa. This is in the upper limit for human comfort, according to Vardy (2008). The amplitude of the Primary branch wave is greater than the Secondary branch wave. Equation 5.39 can be used to estimate the transmitted pressure waveform for an infinitely long side branch. The formula accounts for the tunnel and branch areas, but assumes that the branch is acoustically compact (He $\ll 1$ in § 2.2.1). Therefore, it cannot account for the effect of the branch geometry.

Currently employed MPW countermeasures, such as tunnel entrance hoods and nose shape optimisation (see § 2.5), will be effective for Primary branch waves. However, only nose shape optimisation will be effective for Secondary branch waves. Therefore, additional countermeasures will need to be developed for Secondary branch waves. For example, Saito et al. (2010, 2013) propose the use of a branch exit hood, which yields up to a 30% reduction in the amplitude of the branch MPW. Despite this, the hood may interfere with ventilation or pressure relief requirements as it partially obstructs the branch outlet.

Figure 6.2b shows that reducing the cross-section of the branch can be effective in reducing the amplitude of both Secondary and Primary branch MPWs. However, reducing this area may conflict with ventilation or pressure relief requirements, without installing more branches to compensate. A possible workaround is to install a reactive silencer (acoustic muffler) at the exit of the branch (see § 2.6.2). The silencer would need to be large in order to be effective against the low-frequency waves typically seen in train tunnels. Alternatively, it may be possible to mimic the functionality of a tunnel entrance hood by modifying the shape of the tunnel-branch junction in order to provide a gradual transition between the tunnel and the branch.

6.3 Branch Geometry Parametric Study

A preliminary analysis on the effect of modifying the branch-tunnel junction geometry on the branch MPW is described in this section, in order to identify whether further investigation of this type of countermeasure is warranted. Gas flow dynamics in a tunnel system can be accurately modelled in 1-D under the plane wave approximation (see Equation 3.9 and Chapter 3), except in regions dominated by 3-D flows, including branch junctions (i.e. Secondary branch waves). However, 3-D CFD can be computationally expensive, particularly for the purpose of a parametric study where many simulations are required.

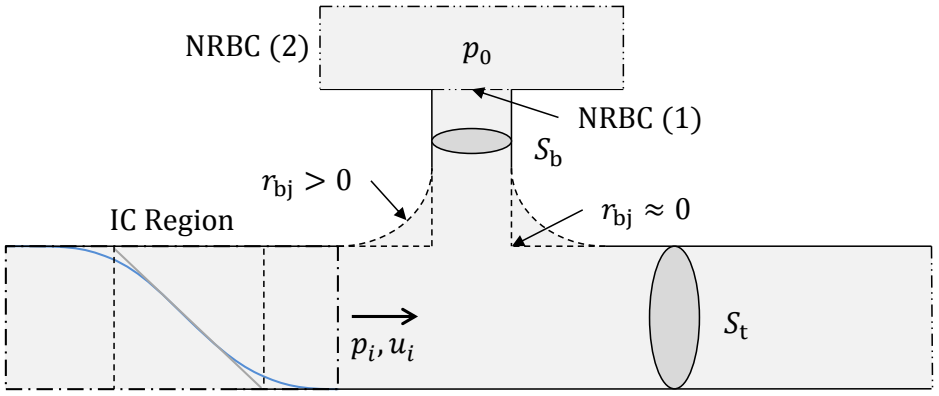
Modelling the Secondary branch wave requires mesh motion, i.e. a mesh containing the train sliding past a static mesh of the branch. Information is transferred between the two meshes via interpolation (see § 6.4). Mesh motion increases the modelling complexity and computational overhead, particularly in three-dimensions. The number of cell faces on the sliding mesh boundaries in 3-D (represented by a 2-D face) is significantly higher than in two-dimensions (a 1-D line). Therefore, a compromise is made between physical accuracy and modelling complexity (and simulation time) by adopting a 2-D CFD strategy. This approach should provide a qualitative indication about the effectiveness of modifying the branch geometry.

A 2-D representation can be considered when physical phenomena (e.g. velocity and gradients of the physical fields) in the out-of-plane dimension, z, are much less than the in-plane dimensions, x and y (see Figure 3.2). This condition may be met if the geometry can be considered as 2-D (i.e. $\partial y/\partial x \gg \partial y/\partial z, \partial x/\partial z$) and the motion of the object is confined to one of the in-plane dimensions. It is noted that physically representative predictions accounting for the effects of turbulence require fully 3-D models (e.g. large or detached eddy simulation). The geometric variation of the train nose and branch junction in the z-plane is similar to the x and y planes, while the annulus formed between the train and tunnel is restricted to above and below the train in 2-D. Consequently, low order 2-D CFD is expected to provide conservative predictions (of amplitudes and gradients) of the pressure transients, compared to a 3-D model.

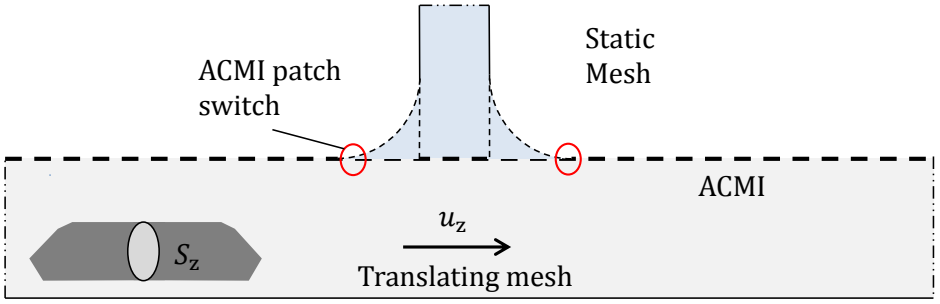
In this preliminary study, the branch junction is modelled as an arc with internal radius r_{bj} (see Figure 6.3a). The arc provides a smooth transition between the tunnel and the branch. It is envisaged that more effective branch geometries could be considered in future work. For example, the branch geometry could be parametrised so that optimisation can be used to minimise the maximum rate of change of pressure of generated branch waves. However, an analytical model is better suited to optimisation due to its speed, as discussed in § 6.8.

6.4 Boundary Conditions

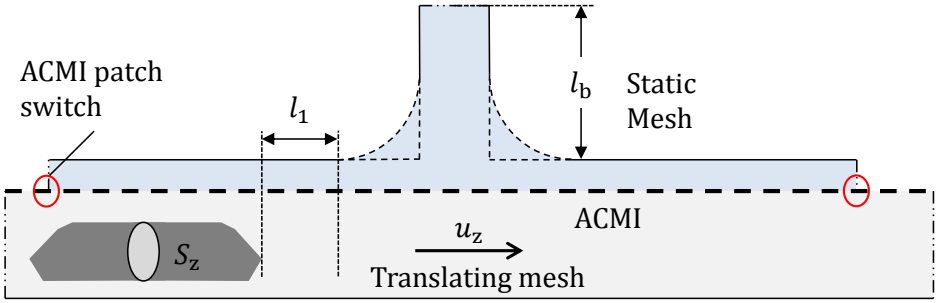
The boundary conditions used for the two cases are illustrated in Figure 6.3. This section mostly focuses on the Secondary branch wave, as it requires a more complicated modelling strategy. The first part of this section is related to issues encountered with mesh motion for the Secondary wave model. The reader is directed to § 4.3.1 for the boundary and initial conditions for a 3-D model of an array of Helmholtz resonators, as this is nearly identical to the Primary branch wave configuration. The Primary branch wave model is relatively simple to implement as there is no requirement for mesh motion.



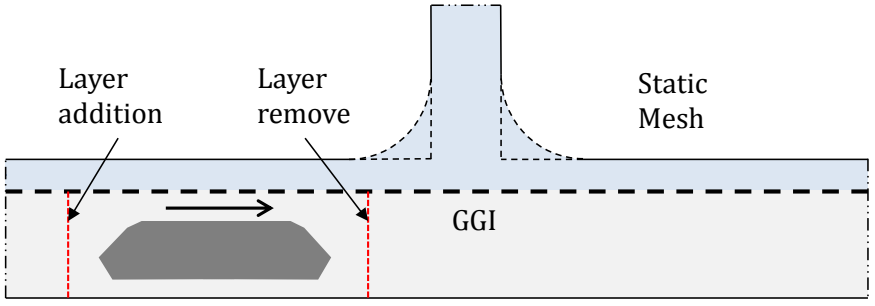
(a) Primary branch wave model



(b) Original Secondary branch wave model



(c) Current Secondary branch wave model



(d) Secondary branch wave model with layer addition/removal

Figure 6.3: Overview of the branch wave model boundary conditions (not to scale).

6.4.1 Mesh Motion

6.4.1.1 Methods for Mesh Motion

Three methods for mesh motion are proposed below to model the train passing the branch, in order to generate the Secondary branch wave.

The first option is a sliding mesh interface between a static and translating mesh. The Arbitrarily Coupled Mesh Interface (ACMI) boundary condition (`cyclicACMI`), introduced in OpenFOAM 2.3, uses local Galerkin projection to provide conservative interpolation between two non-conformal meshes (Farrell and Maddison, 2011). ACMI allows two boundary conditions to be blended (coupled) for translational mesh motion when part of the translating mesh is not in contact with the static mesh (i.e. overlapping faces). For example, see the ACMI BC switching points highlighted by the circles in Figures 6.3b and 6.3c.

A modification to the first option is to use cyclic symmetric boundary conditions at the ends of the tunnel and the Arbitrary Mesh Interface (`cyclicAMI`), instead of ACMI. As a result, the need for a patch coupling method is removed. However, the modelling domain would need to be slightly rounded and with a very large rotational radius in order to represent translational motion.

The third option is layer addition and removal. A layer of cells is automatically added behind and removed ahead of the mesh region containing the moving object. This is available in the FOAM-extend fork of OpenFOAM by using the `multiTopoBodyFvMesh` class. Non-conformal matching between the mesh undergoing layer addition/removal and the static mesh containing the branch is achieved by using the General Grid Interface (GGI) (Beaudoin and Jasak, 2008) (see Figure 6.3d). Unlike ACMI, this approach does not require the mesh region containing the train to be extended beyond the ends of the static mesh. Consequently, the mesh size can be smaller than the first two options with ACMI and AMI.

6.4.1.2 Implementation

The first option with ACMI was chosen for mesh motion, as it presented the fewest obstacles at the time to getting a working model. For example, attempts

to use layer addition and removal in FOAM-extend 3.1 were unsuccessful, due to the generation of non-physical pressure spikes in the cell layers being added or removed. However, it may be worth reconsidering layer addition and removal for future work if this issue can be resolved.

It was originally intended that the translating mesh region would encompass the tunnel and the branch would be static (see Figure 6.3b), minimising the number of ACMI cell faces to just the tunnel-branch junction. Two issues were identified with this configuration. Firstly, highly skewed and non-orthogonal cells are generated in the static mesh at the ACMI patch switching points (see the circles in Figure 6.3b), depending on the radius of the branch junction. The mesh distortions can lead to erroneous predictions, even if a high degree of non-orthogonal correction is applied and least-squares discretisation is used for gradient terms (see § 4.3.2.5). These meshing issues can be resolved by using an unstructured grid, at least in the region of the branch junction.

More importantly, a bug was identified in the ACMI BC (as of September 2015) that affects compressible flows. The bug manifests as non-physical and high amplitude pressure oscillations at the BCs undergoing a switch in boundary conditions, e.g. from a wall or zero-gradient (Neumann type) BC to a mesh interface (see the red circles in Figure 6.3b). These oscillations were apparent for all mesh motion speeds considered and can severely distort the results if they reach the branch outlet in the simulation timespan.

A work-around to the ACMI bug was achieved by modifying the mesh so that the patch switching cells are a sufficient distance from the branch junction. Consequently, erroneous pressure oscillations cannot reach and affect the pressure waves in the branch in the simulation timespan (see Figure 6.3c). This distance can be predicted given the velocity profile of the train in Equation 6.1, the propagation speed of the non-physical pressure waves (estimated as the local speed of sound, a_0), the geometry of the branch, and the required simulation timespan. This workaround also removes the issue of highly skewed and non-orthogonal cells at the corners of the branch junction when using a structured mesh. However, the

tunnel must now be made significantly longer in both directions to account for the propagation of the erroneous pressure waves from the switching patches, resulting in a significantly higher number of cells than would otherwise be required.

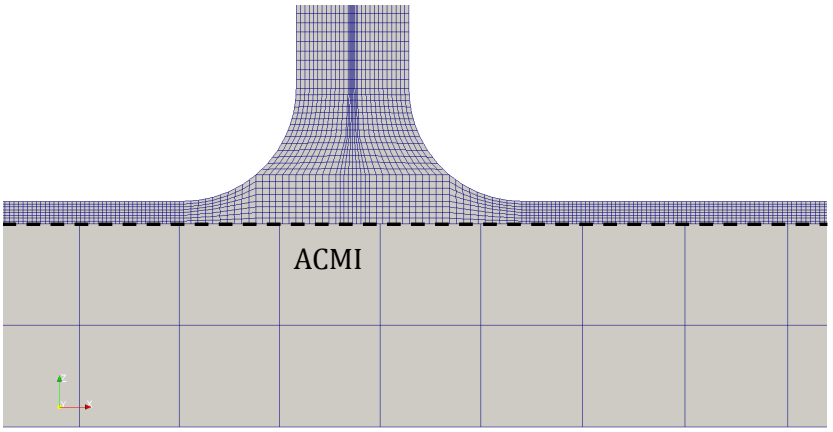
The high cell count can be reduced by gradually coarsening the mesh away from the branch junction and the region around the train, as is demonstrated in Figure 6.4. The moving mesh (bottom mesh) is significantly coarser than the static mesh (top mesh) for the time point and region shown in Figure 6.4a (i.e. the cells are $15 - 20$ times larger in the moving mesh) as the idealised train (see Figure 6.4b) is far upstream from the branch junction. A cell expansion ratio of $\Delta x_i/\Delta x_{i+1} \approx 30$ is used when moving away from the branch and train regions. It is noted that the quality of interpolation across the sliding mesh interface for this region and time point will be poor. However, this work is primarily concerned with the pressure field around the train when it is close to the branch junction, at which point the cell sizes at the interface of the two meshes are closely matched.

6.4.2 Other Boundary Conditions

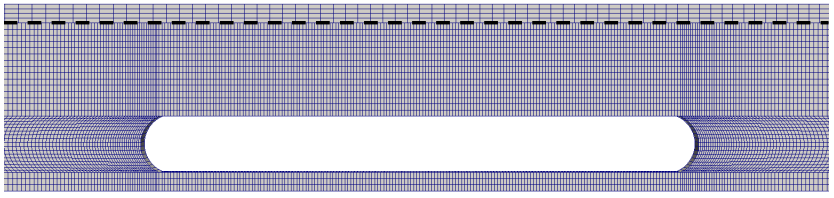
1-D non-reflective boundary conditions (NRBCs)(see § 4.3.2.4) are prescribed at both ends of the tunnel for all fields. This is intended to be representative of an infinitely long tunnel. The branch outlet can be treated in three ways:

1. It is assumed that the branch is sufficiently long so that the branch wave is not affected by reflections from the branch portal in the time span of interest. A NRBC is used at the branch outlet, which is placed sufficiently far from the branch-tunnel junction so that a planar wave has formed, i.e. $l_\mathrm{b} \sim 5d_\mathrm{t}$ (see NRBC (1) in Figure 6.3a). This boundary condition isolates the effect of the branch on the pressure waves. In this case, the area-weighted average pressure is measured across the branch outlet using the `patchAverage` (Gschaider, 2013) function.

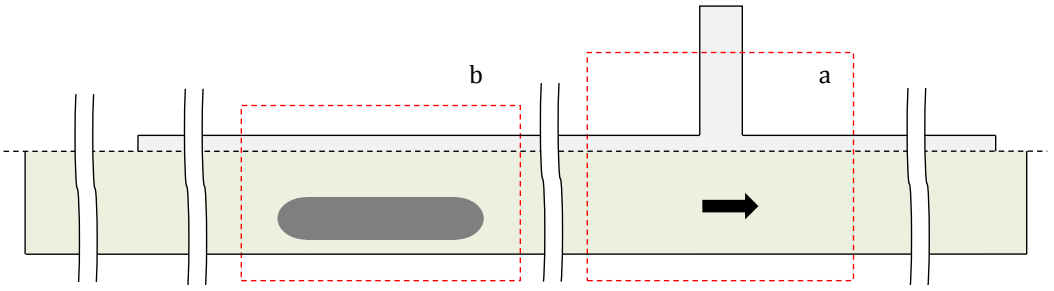
2. The branch opening to atmosphere is modelled as a quasi-infinite 2-D baffle. NRBCs are placed at approximately $10d_\mathrm{t}$ from the branch outlet (see NRBC



(a) Branch junction, with $\tilde{r_{\text{bj}}} = 0.5$ and $\theta = 0.5$.



(b) Train region



(c) Overview. Vertical cuts are used are due to the length of the tunnel

Figure 6.4: Example of the mesh for the Secondary branch wave model.

(2) in Figure 6.3a). This is more physically representative than the first option. The mesh in the open region is coarsened away from the branch portal, in order to reduce the total number of cells. In this case, the `probes` function is used to measure the pressure-time history at a distance of $1d_t$ directly above the branch outlet.

3. A modification of Option 1 would be to prescribe a pressure release BC ($p = p_0$) at the branch outlet instead of a NRBC, assuming that an expansion wave is reflected from the outlet (i.e. an infinite baffle). This BC is an idealised version of Option 2.

The first option above is used for the parametric study, as the resultant mesh has fewer cells and the effect of the branch on the transmitted pressure wave is isolated without interference from reflections from the branch outlet. The tunnel walls are treated using the no-slip condition with $u_x = u_y = u_z = 0$, and zero-gradient (Neumann) conditions for pressure for both the Primary and Secondary branch wave models. The `movingWallVelocity` BC is prescribed for velocity at the boundary of the train in the Secondary wave model, which corrects the flux due to mesh motion and provides a no-slip condition.

6.5 Initial Conditions

The idealised initial condition described in § 4.3.2.3 is used to represent the compression wave generated by a train entering the tunnel for the Primary branch wave. This IC is prescribed as a pressure and velocity field at $t = 0$, in a region just upstream from the start of the branch junction (see Figure 6.3a). For more information, the reader is directed to § 4.3.2.3 for the incident wavefront to an array of Helmholtz resonators.

For the Secondary branch wave, the model is initialised by accelerating a stationary train in the tunnel to its nominal operating speed (see Figure 6.3c). The train reaches its maximum speed at a distance of l_1 m between the nose and the start of the branch junction (i.e. $l_1 \approx 6d_t$). This is to minimise the effect of

the acceleration phase on the generated branch wave. A smooth acceleration profile (Kwon et al., 2001) is used, where the corresponding displacement-time profile for the train (i.e. the moving mesh region) is derived as:

$$x(t) = \frac{1}{60} t_{\mathrm{a}}^4 \left[2t_{\mathrm{a}} \left(5c_1 t_{\mathrm{a}} - 6c_2 \right) + 15c_3 \right] \tag{6.1}$$

where $a = 120u_{\mathrm{z}}/t_{\mathrm{a}}^5$, $c_1 = a/20$, $c_2 = at_{\mathrm{a}}/8$, $c_3 = at_{\mathrm{a}}^2/12$ and t_{a} is the acceleration time period from $u_{\mathrm{z}} = 0$ to $u_{\mathrm{z}} = u_{\mathrm{z,max}}$. This equation is used to minimise the gradient of the compression wave generated ahead of the accelerating train when compared to a step, or linear change in the velocity of the train. A smooth acceleration profile also reduces the number of solver iterations required for convergence in the first few time-steps.

The value of t_{a} was chosen through trial and error to be sufficiently large such that the maximum rate of change of pressure of the compression wave generated by the accelerating train was negligible when compared to the Secondary branch wave. A value of $t_{\mathrm{a}} \approx 10$ s was settled-on, giving an approximate maximum rate of change of pressure for the acceleration compression wave of $\partial p/\partial t \approx p_1/t_{\mathrm{a}} \approx 0.3$ kPa/s. The value of p_1 is calculated using Equation 2.7 with $\beta = 0.15$ and $u_{\mathrm{z}} = 400$ km/h. The acceleration period typically constitutes around 80% of the virtual model time.

A more physically representative approach compared to smoothly accelerating the train in the tunnel would be to combine the Primary and Secondary branch wave models by modelling the train entering the tunnel (in order to generate the Primary compression wave) and subsequently passing the branch junction (for the Secondary branch wave). This strategy might also generate a more accurate representation of the Primary compression wave, compared to using an idealised incident wavefront. However, the main advantage of using separate Primary and Secondary wave models is that the effects of the different branch waves can be isolated. In contrast, branch MPW measurements in the combined model for the Secondary branch wave will be affected and obscured by the partial reflection of the Primary wave from the branch junction and outlet before the train has reached

the branch.

Equation 6.1 may still be required to smoothly accelerate the train up to its operating speed in the open environment before it enters the tunnel for the combined modelling approach. Alternatively, the initial pressure and velocity fields (and other required fields) at $t = 0$ could be interpolated from a steady state model of the train at cruising speed in an open environment. In the steady-state (i.e. wind tunnel) model the train is static and an inlet velocity of $-u_z$ is prescribed. Dynamic mesh motion is not required for the steady-state model, and a solver based on the SIMPLE algorithm (see Ferziger and Peric, 2012) can be used to quickly converge to a steady state solution (not accounting for the unsteady wake behind the train). Consequently, the simulation time could be significantly reduced without the need for a long initial acceleration period in the dynamic mesh model. It is non-physical to use a steady state model to generate the initial fields for the train once it is in the tunnel (i.e. the Secondary wave model), due to the presence of the branch.

6.6 Solver Settings

The Primary wave model is solved using the inviscid Euler equations with the density-based solver `rhoCentralFoam` (Greenshields et al., 2010), which uses the central-upwind scheme of Kurganov and Tadmor (2000). The van Leer flux limiter (van Leer, 1974) is used for convective terms to fulfil the TVD criterion. `rhoPimpleDyMFoam` (Aguerre et al., 2013) is used for the Secondary wave case. This is a transient compressible solver for the Navier-Stokes equations, based on the PIMPLE (merged PISO-SIMPLE) algorithm (see Ferziger and Peric, 2012). It also supports dynamic mesh motion.

The $k-\omega$ SST Reynolds-averaged Navier-Stokes (RANS) turbulence model (see Ferziger and Peric, 2012; Moukalled et al., 2015) has been used in order to improve the stability of the Secondary wave model by adding viscous dissipation. The instability arises from vortex shedding from the blunt tail of the idealised train. The Reynolds number is sufficiently high such that the flow regime can be treated

as inviscid, except in the vicinity of the train (in particular the tail), the "wake" of the train, and possibly localised separation at the branch junction (depending on the smoothness of the tunnel-branch transition).

The thermophysical properties for air are provided in Table 3.1. Adaptive time-stepping based on a maximum Courant number of 0.5 is used for both cases, where an acoustic Courant number smaller than one is required in order to resolve acoustic waves. Various solver controls and discretisation schemes have been experimented with in order to reduce the simulation time and improve stability and accuracy for the Secondary wave case. More information about the modelling methodology used is provided in § 4.3.2.

The main solver configurations found to be effective considering the difficulties encountered with ACMI are listed below:

- Flux limiters have been used for the convective terms, namely `limitedLinear`, which is based on the Sweby limiter (Sweby, 1984). Multi-Dimensional gradient limiters (`cellMDLimited 1`) are used to ensure gradients are physically bounded (see Nozaki, 2014).

- Explicit under-relaxation is used for the velocity and turbulence equations, and the pressure field. Under-relaxation is removed on the final PIMPLE iteration in order to preserve continuity.

- An automatic number of outer-corrector iterations on the PIMPLE loop for pressure-velocity coupling (Aguerre et al., 2013), based on user defined residual tolerances for the fields.

- A small degree of non-orthogonal correction on the pressure correction equation (typically 1-2 correction loops), due to the mesh around the branch junction and train.

- First order temporal discretisation in order to aid stability. The solver would occasionally fail to converge and produce non-physical solutions with second order temporal schemes. It is noted that second order temporal discretisation

is generally desired for transient simulations, unless the maximum step size is reduced to compensate when using a first order scheme. A blended 1st-2nd order accurate time marching scheme may help to maintain physical boundedness (see § 4.3.2.1).

The quality and numerical stability of the predictions may be improved by using the `pisoCentralDyMFoam` (Kraposhin et al., 2015) dynamic mesh solver, which blends the pressure based PISO algorithm with the density based central-upwind scheme of Kurganov and Tadmor (2000). The static mesh version of this solver was successfully used in § 4.3. This solver was published after the work on branch waves had been finished.

It is proposed that the simulation time and numerical accuracy of the Secondary branch wave model could be improved by modifying the solver settings with the following steps, during the simulation:

1. Specify a large maximum Courant number (the PIMPLE algorithm can stably support $c_{\max} \gg 1$ with explicit under-relaxation) and loose tolerances on the equation solvers (e.g. `relTol`$\approx$ 1e$-$1 & `absTol`$\approx$ 1e$-$3) for the initial train acceleration period (see § 6.5), where numerical accuracy is less important. First order accurate implicit Euler time marching can be used to maintain physical boundedness and minimise the computational demands of time marching in this period. It is anticipated that these modifications will increase the degree of artificial diffusion and smooth the compression wave generated by the accelerating train.

2. Switch to a much smaller maximum Courant number ($c_{\max} \ll 1$) and tighten the tolerances on the equation solvers (e.g. `relTol`$\approx$ 1e$-$4 & `absTol`$\approx$ 1e$-$6) in the time period where the train is passing the branch junction. This is to accurately resolve the generation of the branch waves. A 2nd order accurate temporal scheme, such as Crank-Nicolson or second order upwind differencing (see Jasak, 1996; Moukalled et al., 2015) is used over this time-span to minimise numerical diffusion.

Symbol	Value	Comments
β	0.3	$= S_z/S_t$. Approximated as rectangular sections in 2-D
d_t	7.6	height of tunnel in 2-D
θ	0.5	$= S_b/S_t$. Approximated as rectangular sections
Δx	30-45	$= d_t/\Delta x$. Approx. minimum cell size
$\tilde{l_{zn}}$	0.1	arc radius/ nose length, w.r.t. d_t
$\tilde{l_z}$	3.0	train length w.r.t. d_t
$\tilde{h_z}$	0.3	train height, w.r.t. d_t
t_a	10.0 s	see Equation 6.1

Table 6.1: Fixed side-branch and tunnel geometric parameters for parametric study.

6.7 Results and Validation

6.7.1 Overview

A shell batch script was created to automate the parametric study for various combinations of branch radii and train velocity (see Appendix D.2). The script was executed on the Imperial College high-performance cluster (HPC-CX1), for both the Primary and Secondary branch waves. Up to 32 models were solved simultaneously, each on a single processor core. Attempts to run the Secondary wave model in parallel using Message Passing Interface (MPI) were unsuccessful, due to errors related to the ACMI boundary condition.

A wide range of branch junction radii were considered, from $\tilde{r_{bj}} = 0 - 2$, i.e. a right-angle to a very large arc. Similarly, the train velocity was varied from u_z = 300 - 500 km/h, which covers the current high speed regime, up to future very high-speed trains (e.g. Maglev vehicles). Both the Primary and Secondary branch wave models were solved without the simulation of the branch exit portal, in order to avoid reflections (see § 6.4). The model parameters are provided in Table 6.1, and the area-weighted average pressure waveforms are measured at the branch outlet for all cases in this section.

6.7.2 Validation

Good agreement is obtained between predictions from the 2-D model and a semi-analytical model for the Primary branch waveform at the branch outlet (see Figure 6.5), with $r_{\tilde{\mathrm{bj}}} \approx 0$ (i.e. a right-angled branch junction), $u_{\mathrm{z}} = 400$ km/h, $\tilde{L} = 1$ and $0.1 \leq \theta \leq 0.5$. The semi-analytical prediction accounts for:

1. non-linear wave steepening between the initial pressure wave position (assumed as $x = 0$ in Figure 5.1) and the branch junction (i.e. a distance of approximately $b + r_{\mathrm{b}} + r_{\mathrm{bj}}$ m);

2. the transmitted branch wave, using Equation 5.39;

3. non-linear steepening of the transmitted branch wave between the junction and the branch outlet ($l_{\mathrm{b}} \approx 8d_{\mathrm{t}}$ m).

Non-linear wave steepening is predicted numerically using Equation 3.23a with $K = 0$ (i.e. no array of Helmholtz resonators). There are small pressure fluctuations in the 2-D predictions after the initial pressure rise, which are most likely due to secondary reflections from the branch junction.

The 2-D models are also compared against the analytical model of Miyachi et al. (2014) in Figure 6.6, for both the Primary and Secondary branch waves with $r_{\tilde{\mathrm{bj}}} \approx 0$. The Secondary branch wave predictions exhibit a greater degree of variation from the analytical model compared to the Primary branch wave, which may be due to one or several of the following reasons:

1. Numerical errors associated with interpolation using the ACMI boundary condition.

2. The compression wave and associated interference pattern generated by the initial acceleration of the train (for example see Figure 6.7) has a non-negligible effect on the Secondary branch wave.

3. Miyachi's analytical model assumes that the tail of the train does not reach the branch junction and affect the pressure wave generated by the nose

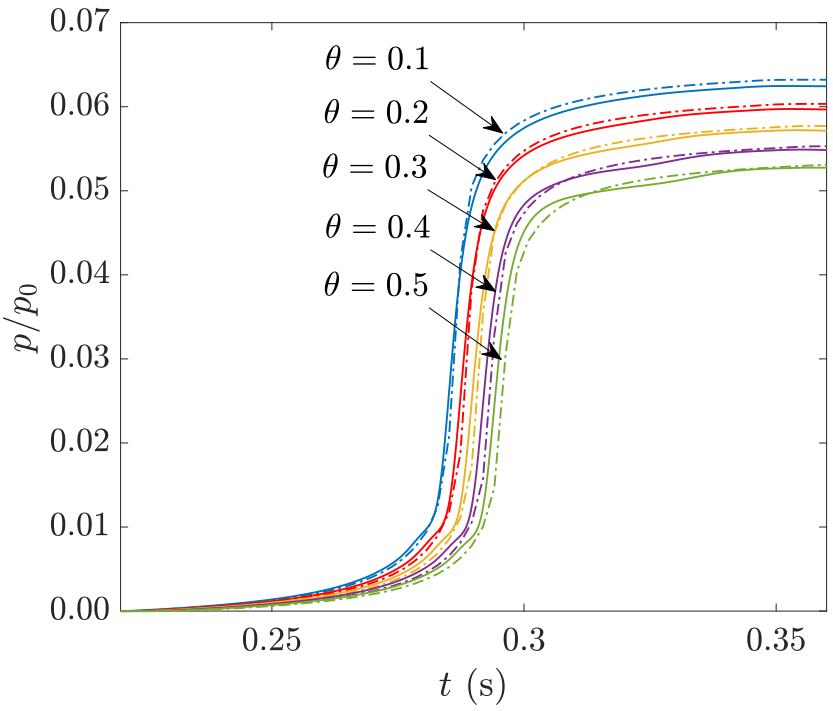


Figure 6.5: Dimensionless Primary branch waveforms predicted using the 2-D (—); and semi-analytical (----) models, with $\tilde{r_{\text{bj}}} \approx 0$.

passing the branch, i.e. $l_{\text{z}} \gg \min(d_{\text{t}}, l_{\text{zn}})$. However, $l_{\text{z}} = 3d_{\text{t}}$ and $l_{\text{z}} = 30l_{\text{zn}}$ in the 2-D model. Therefore, the branch waveform generated by the nose may also be affected by the tail.

For the second point above it is noted that the pressure variation downstream of the train is also likely to be non-uniform along the length of a real tunnel system due to the partial reflection of the tunnel entry compression wave from branches and the exit portal (at least in slab track tunnels with no dissipation from ballast or an array of Helmholtz resonators).

Experimental data or analytical models were not available for the Secondary or Primary branch waves when considering variable branch geometry.

6.7.3 Main Results

An example of the pressure and velocity fields for the Secondary branch wave model when the train is far from the branch region are shown in Figures 6.7 and 6.8. The interference pattern downstream of the train (in Figure 6.7) is

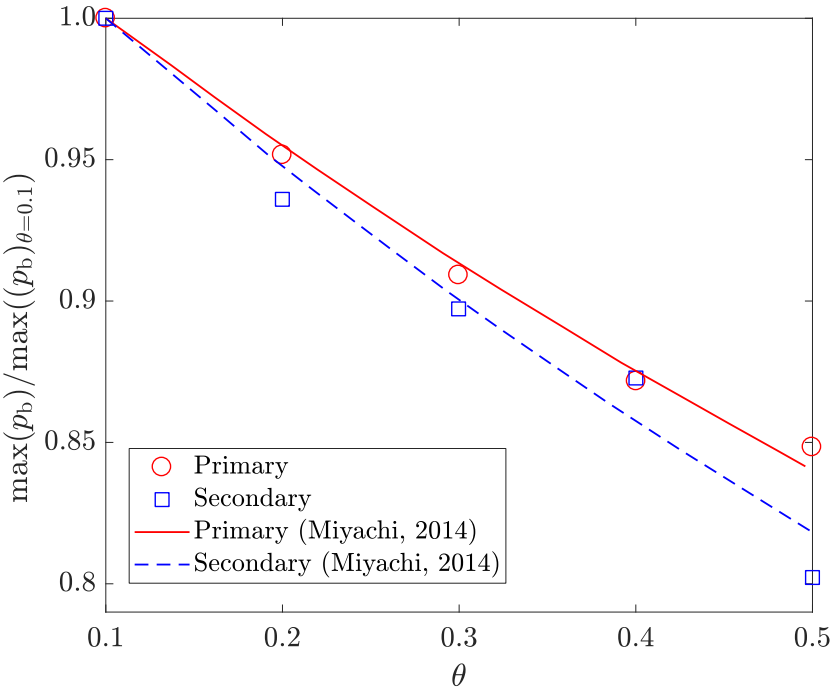


Figure 6.6: Normalised maximum overpressure in the branch (w.r.t. branch with $\theta = 0.1$) versus θ, for comparison of the analytical model (Miyachi et al., 2014) with 2-D predictions. $M_z \approx 0.32$ and $\tilde{r_{bj}} \approx 0$ (0.01).

due to the reflection of the compression wave generated during the initial train acceleration period by the branch junction. The gradients of these reflected waves can be reduced by increasing the train acceleration period, and are deemed to be acceptable provided that they are much less than the gradient of the Secondary branch wave (see Equation 6.1).

The Primary and Secondary branch waveforms at the branch outlet, as a function of r_{bj}, are plotted in Figure 6.9. The amplitude of the small pressure fluctuations after the initial pressure rise ($t > 0.3$ s) increases with branch junction radius and effective train velocity for the Primary branch wave (Figures 6.9a to 6.9c). These fluctuations are associated with secondary reflections from the branch junction, after the Primary compression wave has entered the branch. It is noted that the semi-analytical model used in Figure 6.5 becomes less accurate as the branch junction radius increases.

The waveforms for the Secondary branch wave are plotted in Figures 6.9d to 6.9f. The smooth initial pressure rise ($t < 4$ s) is due to the compression wave

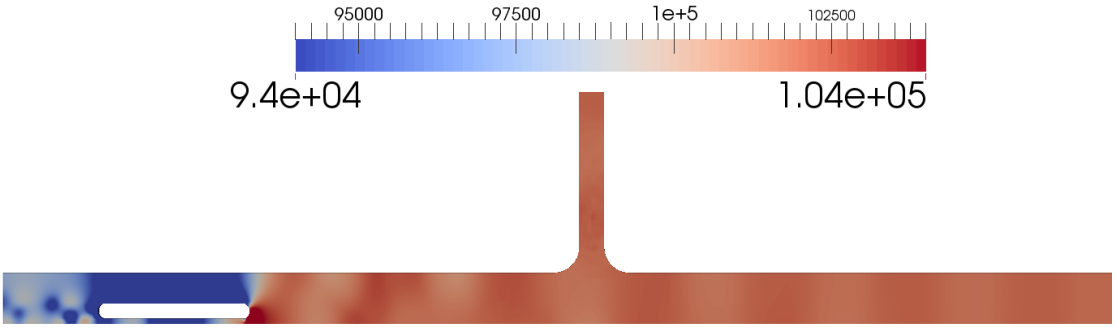
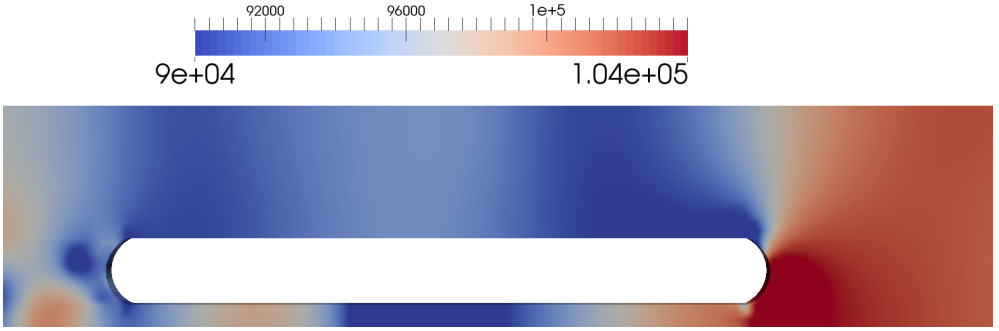
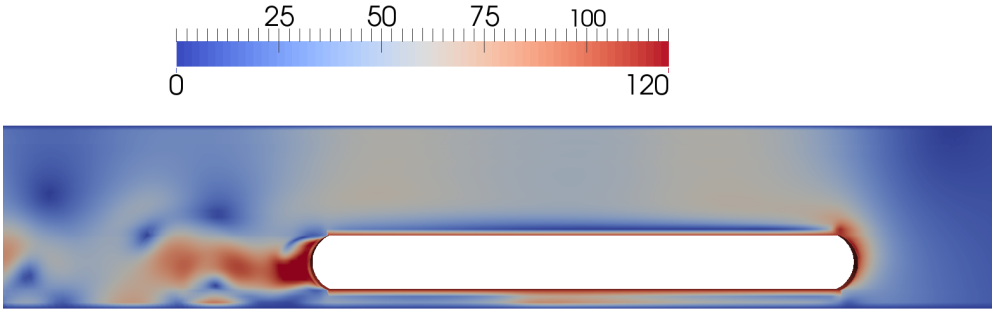


Figure 6.7: Example of the static pressure field in the branch region for $u_z = 400$ km/h, $\tilde{r_{bj}} = 0.5$ and $\theta = 0.5$. The tunnel has been cut after $\sim 12d_t$ from the branch junction for illustrative purposes.

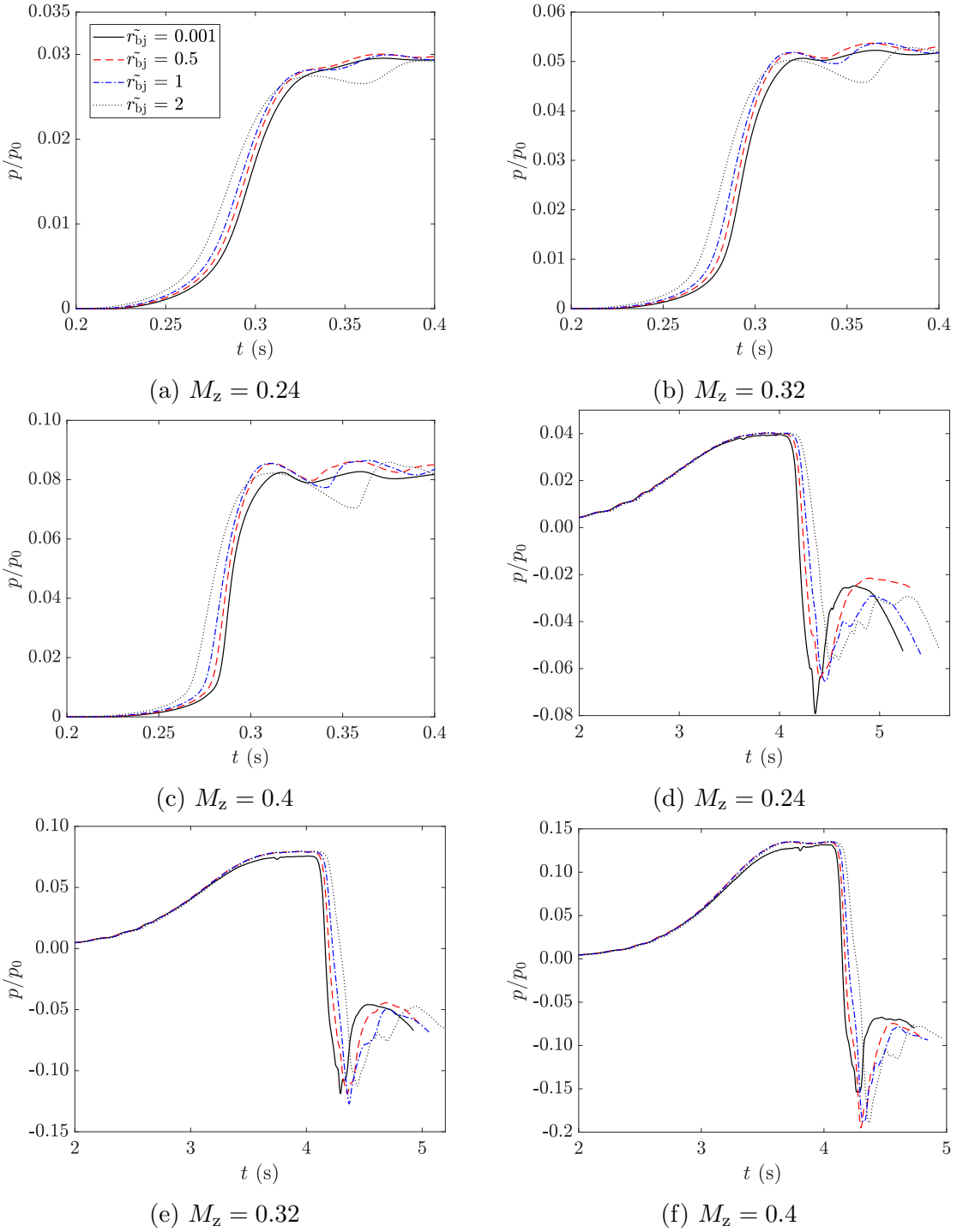


(a) Static pressure field



(b) Velocity magnitude field

Figure 6.8: Example of predicted fields in the region around the idealised train, with reference to Figure 6.7.

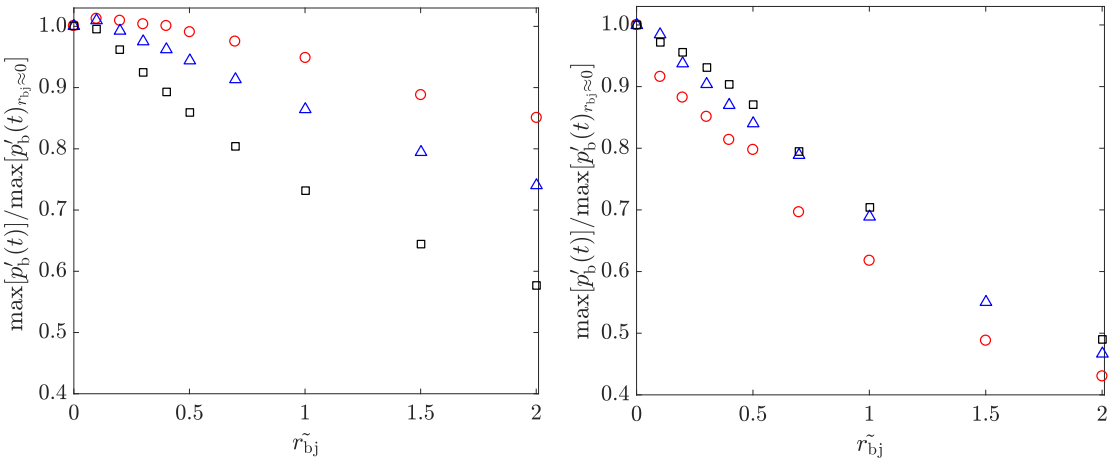


(a) $M_z = 0.24$ (b) $M_z = 0.32$

(c) $M_z = 0.4$ (d) $M_z = 0.24$

(e) $M_z = 0.32$ (f) $M_z = 0.4$

Figure 6.9: Dimensionless pressure waveforms for the Primary (a-c) and Secondary (d-f) branch waves for a selection of the branch radii.



(a) Primary branch wave

(b) Secondary branch wave

Figure 6.10: Maximum rate of change of pressure (normalised by a branch with $\tilde{r_{bj}} \approx 0$) versus branch junction radius, for $M_z =:$ 0.24 (◯); 0.32 (△); 0.4 (□).

generated by the accelerating train. It is noted that a significant amount of the simulation time is spent in the train acceleration phase ($\sim$ 4 s), compared to the duration of the pulse generated as the train passes the branch ($<$ 0.5 s). A sudden drop in pressure occurs at $t \approx 4$ s as the expansion wave generated by the train nose passing the branch reaches the branch outlet. The pressure will then recover as the tail passes the branch junction. The maximum rate of change of pressure of the initial pressure rise is significantly less than the pressure drop due the train nose passing the branch, as is intended by using the smooth acceleration profile in Equation 6.1.

Figure 6.10a indicates that the effect of the junction radius on the Primary branch MPW amplitude becomes more pronounced as the train speed increases. Reductions of up to $\sim$ 20% in the branch MPW amplitude are predicted for very high speed trains and for physically plausible branch radii (i.e. $\tilde{r_{bj}} < 1.0$). However, modifying the branch-junction radius offers only marginal improvements for current high speed trains ($u_z \sim 300$ km/h).

The characteristic size of the branch junction (assumed as the axial length of the branch junction, $l_{ch} \approx 2[r_{bj} + r_b]$) should be comparable to, or greater than, the characteristic wavelength of the incident compression wave, in order to have a significant effect on the branch pressure transients, i.e. He $= l_{ch}/\lambda \sim 1$ (see

§ 2.2.1). Equations 5.7 and 5.8 show that the characteristic wavelength decreases with increasing train velocity. Additionally, Figure 6.10a indicates that the branch geometry would need to be impractically large to be effective against the low frequency pressure waves in tunnels. These results suggest that for relatively low entry speeds and short slab track tunnels (where non-linear steepening is minimal) existing countermeasures such as tunnel entrance hoods and nose shape optimisation are likely to be more effective for suppressing Primary branch MPWs, compared to modifying the branch geometry.

In contrast, greater reductions in the maximum rate of change of pressure are predicted for the Secondary branch wave for all of the train speeds considered, as is seen in Figure 6.10b. The relationship between branch radius and the relative reduction in the maximum rate of change of pressure in the branch appears to be largely independent of train velocity compared to the Primary branch wave, at least for the speeds and branch radii considered. Figure 6.10b suggests that modifying the branch geometry is slightly more effective for lower train speeds, which is the opposite of the predictions for the Primary branch waves. This unexpected result could be due to numerical errors, but may warrant further investigation. For example, additional train speeds, or different values of θ could be modelled.

There is a greater degree of variability in the Secondary branch wave predictions, compared to the Primary branch wave, which may be due to numerical artefacts. For example, errors associated with the interpolation of fluxes across the ACMI boundary, particularly where high gradients are present may affect the results in the branch. Further consideration of numerical schemes and mesh motion controls is required for future work.

6.8 Conclusions and Future Work

Branch MPWs are likely to become an environmental noise problem with increasing train operating speeds. The results of a preliminary parametric numerical study indicate that modifying the tunnel-branch geometry can reduce the ampli-

tude of both Primary and Secondary branch micro-pressure waves (as measured by the maximum rate of change of pressure in the branch) with increasing train speeds.

Large reductions in the branch-MPW amplitude are predicted with an increase in branch radius for the Secondary wave case, while the trend is largely independent of the train velocity (for $u_z = 300 - 500$ km/h). This is a useful result, as existing countermeasures for MPWs, such as tunnel entrance hoods are ineffective for Secondary branch waves. For the Primary branch MPW, modifying the branch geometry only becomes effective at very high train speeds (e.g. $u_z \sim 500$ km/h for the case considered), or when the effective size of the branch junction becomes comparable to the characteristic wavelength of the incident compression wave.

Modifying the branch geometry can reduce the amplitude of branch-MPWs without needing to reduce the cross-sectional area of the branch, thereby minimising issues associated with ventilation requirements. It is now recommended that experiments are used to validate the numerical predictions in this chapter for varying branch geometries, and to test the effectiveness of more complicated branch geometries.

The Primary branch wave can be represented experimentally by using a shock or impedance tube with a modifiable section for the branch junction for different branch geometries. The tube and branch must use anechoic termination at the ends, or be sufficiently long to avoid unwanted wave reflections. For the Secondary branch wave, a moving object representative of a train passing a side branch is required, for example by using a scale moving model rig. Facilities of this type exist at the University of Birmingham Centre for Railway Research and the Railway Technical Research Institute in Tokyo, Japan. Alternatively, the same effect could be achieved by using a projectile fired by a gas gun. The tunnel-branch junction would again utilise a modular design, so that different branch geometries can be tested with relative ease.

It may be possible to derive an analytical model for the Secondary wave case, based on potential flow theory (irrotational and inviscid flow) and the methodology

used in (Howe, 1998; Howe et al., 2003a,b) for the effect of a tunnel entrance hood. The branch geometry could then be parametrised so that a multi-objective algorithm is used to find a branch geometry which minimises both the branch MPW amplitude and the volume of material removed (which is related to the cost of modifying the branch geometry). Alternatively, a solver could be developed for OpenFOAM based on the wave equation, with dynamic mesh motion support. This could be much faster to evaluate compared to the Euler equations, thereby facilitating a fully 3-D parametric study.

Chapter 7

Conclusions and Future Direction

Increasing train speeds will require new countermeasures in long tunnels in order to reduce environmental noise primarily from the tunnel exit, but also from other connections to atmosphere, e.g. ventilation shafts. The implementation of two new countermeasures for micro-pressure waves was numerically investigated in this work:

- an array of Helmholtz resonators embedded in the tunnel structure (see Chapter 3);
- modifying the geometry of the junction formed between the tunnel and a side-branch connected to atmosphere (see Chapter 6).

A reactive muffler/silencer installed at the end of the tunnel or branch portals was also suggested as a MPW countermeasure for steep incident wavefronts over large propagation distances (see Appendix B). The issue of non-linear wave steepening in long tunnels was of particular interest, as the steepening rate increases with the initial wavefront amplitude. Steeper wavefronts increase the severity of environmental noise due to micro-pressure waves.

7.1 An Array of Helmholtz Resonators

A 1-D numerical framework has been developed to rapidly predict the transmitted pressure wave due to an array of Helmholtz resonators (see Chapter 3). The

framework has been validated against experimental data and benchmarked against 3-D CFD models of a demonstrative array (see § 4.3). The assumptions of the 1-D model are valid for a range of operating conditions expected for high speed train operations in tunnels.

The framework was applied to a demonstrative array by integrating the cavities into redundant tunnel space, in order to prove the feasibility of using this concept in future tunnel projects for high-speed trains. The numerical application and optimisation of an array of Helmholtz resonators in a representative tunnel system had not been considered before. A Pareto front was generated, which can be used by railway engineers to provide a trade-off between the effectiveness of the array and its length (see § 5.7). For example, an optimised array could provide around a 30% reduction in the maximum rate of change of pressure over a length of around 12 times the tunnel diameter (equivalent to a reduction in SPL of $\sim$ 3 dB). This was for standard operating conditions approximately representative of modern and future high speed trains (see § 5.12).

The array was also optimised for irregular resonator geometry by using a variable cavity length and resonator neck diameter. A sensitivity analysis of the optimised array configurations to various combinations of the train entry speed and characteristic wavelength of the incident wavefront indicated that using irregular resonator geometry provides a marginal improvement in the robustness of the array to the incident wavefront shape. For example, the incident wavefront shape will change with increasing train speeds, or with the introduction of new rolling stock, after the array has been installed.

Numerical experiments revealed that irregular geometry was more effective when there was a greater range of frequency content in the incident waveform. For example, an array with irregular geometry provided a greater reduction in the maximum pressure gradient of steeper incident wavefronts (e.g. due to higher entry speeds, or longer propagation distances), and of wavefronts which had passed multiple closed side branches upstream of the array (see § 5.11), compared to regular geometry. It was demonstrated that combining an entrance hood with an

array of resonators is more effective than using these countermeasures separately, particularly for long tunnels with high operating speeds.

7.2 Branch Micro-Pressure Waves

A preliminary investigation was carried out in Chapter 6 on the effect of micro-pressure waves emitted from side branches (e.g. pressure relief ducts and ventilation shafts), due to the compression wave generated at the tunnel entrance splitting at the branch (Primary branch wave) and as the train passes the branch (Secondary branch wave). Unacceptable branch MPWs are likely to occur with increasing operating speeds, even though branch micro-pressure waves are smaller than those from the tunnel exit. For example, a peak branch MPW amplitude of ~ 40 Pa, or ~ 130 dB, is predicted for a train operating at 400 km/h.

Existing and proposed countermeasures for the tunnel exit MPW, such as an entrance hood or an array of Helmholtz resonators, are ineffective against Secondary branch waves. A parametric numerical study was carried out, which indicates that modifying the tunnel-branch junction geometry can reduce the amplitude of both Primary and Secondary branch micro-pressure waves with increasing train speeds.

2-D CFD is used to provide a qualitative indication of the effectiveness of modifying the branch geometry. Large reductions in the peak Secondary branch wave pressure gradient are predicted by increasing the radius of the tunnel-branch junction, while the trend appears to be largely independent of the train velocity. For example, a $\sim 20\%$ reduction is predicted for a branch junction with a radius of half the tunnel diameter (compared to a right-angled branch).

On the other hand, modifying the branch geometry has a much smaller effect on the Primary branch wave and its effect is strongly dependent on train velocity. For example, only a $\sim 10\%$ reduction in peak branch pressure gradient is predicted for a radius of half the tunnel diameter and for an entry speed of ~ 500 km/h. The modified branch geometry must be of a comparable size to the characteristic wavelength of the incident compression wave in order to be effective for the Primary

branch wave. Therefore, it is proposed that the use of countermeasures for the tunnel exit MPW (e.g. train nose shape optimisation, a tunnel entrance hood, or an array of Helmholtz resonators) will be more efficient for reducing Primary branch MPWs.

7.3 Future Work

Improvements are proposed for the numerical framework developed in this work for an array of Helmholtz resonators. The physical model can be expanded to account for wave propagation in the cavities. This modification will allow the optimisation procedure to consider longer cavities, or even cavities with multiple necks along its length. Visco-thermal losses could be increased by incorporating a model for porous media in the cavities. A speed-up in the simulation and optimisation times may be seen by porting the code base to a more efficient and non-proprietary programming language, such as C++.

This work has demonstrated the effectiveness of installing cavities underneath the side/emergency access walkway in a demonstrative tunnel system. 3-D CFD could be used to investigate the effect of the orientation of the resonator necks on the transmitted wavefront. For example, could facing the necks upstream (compared to perpendicular to the bulk flow) increase reflection, and hence reduce the gradient of the transmitted wavefront? Additionally, it is proposed that using asymmetric resonators could further reduce the gradient of the transmitted wavefront by creating a series of small reflections, rather than one large reflection.

It may be useful to investigate how an array impacts the pressure transients experienced by the body of the train (structural fatigue) and passengers (aural discomfort), and also the stability of the train as it passes the array.

It is now recommended that experiments are used to validate the CFD predictions for branch MPWs in § 6.7.3. The Primary branch wave can be represented experimentally by using a shock or impedance tube with a modifiable section for the branch junction. A scale moving-model rig is required for the Secondary branch wave. An analytical model for the Secondary branch wave can be derived

based on potential flow theory. Alternatively, the 2-D models could be accelerated by solving the wave equation, instead of the inviscid Euler or Navier-Stokes equations. This could facilitate the rapid optimisation of the branch geometry in order to simultaneously minimise emitted branch MPWs and the amount of tunnel material removed by the countermeasure.

Preliminary work has been carried out on the numerical investigation of a reactive muffler/silencer installed at the tunnel exit, or at the openings of side branches (see Appendix B). The geometry of the silencer could be optimised using the same methodology as an array of Helmholtz resonators. This countermeasure could be used in conjunction with an array of Helmholtz resonators, particularly in long slab track tunnels with steep compression wavefronts. It could also be used at branch portals, instead of modifying the branch junction geometry to counteract the emission of branch MPWs.

The costing of these countermeasures should be considered in greater detail as part of future work. The installation cost is difficult to predict as these countermeasures have not been implemented in a real tunnel system. It is envisioned that the Helmholtz resonator array could be integrated as pre-cast slabs, which may help to reduce costs. Closer links with the civil engineering sector may be necessary in order to develop a costing model, which could then be integrated into the optimisation framework.

Bibliography

Pathways to Deep Decarbonization: Intermin 2014 report. Technical report, Sustainable Development Solutions Network, 2014. 33

F. Acker, R. B. de R. Borges, and B. Costa. An improved WENO-Z scheme. *Journal of Computational Physics*, 313:726–753, 2016. 97

H. J. Aguerre, S. Marquez Damian, J. M. Gimenez, and N. M. Nigro. Modeling of Compressible Fluid Problems With Openfoam Using Dynamic Mesh Technology. *Mecánica Computacional*, 32:995–1011, 2013. 206, 207

T. Aoki, A. Vardy, and J. Brown. Passive Alleviation of Micro-Pressure Waves from Tunnel Portals. *Journal of Sound and Vibration*, 220(5):921–940, 1999. 34, 49, 56, 122, 144, 252

U. M. Ascher and L. R. Petzold. *Computer Methods for Ordinary Differential Equations and Differential-Algebraic Equations*. Society for Industrial and Applied Mathematics, 1998. 58, 62, 99

C. Baker. The flow around high speed trains. *Journal of Wind Engineering and Industrial Aerodynamics*, 98:277–298, 2010. 54

C. Baker. A review of train aerodynamics Part 1 Fundamentals. *The Aeronautical Journal*, 118(1201), 2014. 48

J. W. Bandler, Q. S. Cheng, S. A. Dakroury, A. S. Mohamed, M. H. Bakr, and K. Madsen. Space mapping: The state of the art. *IEEE Transactions on Microwave Theory and Techniques*, 52(1):337–361, 2004. 154

A. Baron, M. Mossi, and S. Sibilla. The alleviation of the aerodynamic drag and wave effects of high-speed trains in very long tunnels. *Journal of Wind Engineering and Industrial Aerodynamics*, 89(5):365–401, 2001. 51

T. J. Barth, D. E. Keyes, and D. Roose. *The Finite Element Method: Theory, Implementation, and Applications*, volume 6. Springer Science & Business Media, 2003. 60

BBC. Japan maglev train breaks world speed record again, 2015. URL `http://www.bbc.co.uk/news/world-asia-32391020`. 73

M. Beaudoin and H. Jasak. Development of a Generalized Grid Interface for Turbomachinery simulations with OpenFOAM. *Open Source CFD International Conference*, (December 2008), 2008. 200

M. Bellenoue. Experimental 3-D Simulation of the Compression Wave, Due To TrainTunnel Entry. *Journal Of Fluids And Structures*, 16(5):581–595, 2002. 44, 46

M. Berger, M. J. Aftosmis, and S. M. Murman. Analysis of Slope Limiters on Irregular Grids. In *43rd AIAA Aerospace Sciences Meeting and Exhibit*, pages 1–22, 2005. 128

C. Birk and C. Song. An improved non-classical method for the solution of fractional differential equations. *Computational Mechanics*, 46(5):721–734, 2010. 89

W. K. Blake. *Mechanics of Flow-Induced Sound and Vibration*. Elsevier, 2012. 47

P. T. Boggs. *Sequential quadratic programming*, volume 4. Springer, New York, 1996. 88

C. Casenave and G. Montseny. Introduction to diffusive representation. *IFAC Proceedings Volumes*, 43(21):370–377, 2010. 84

C. Chevalier and F. Pellegrini. PT-Scotch: A tool for efficient parallel graph ordering. *Parallel Computing*, 34(6):318–331, 2008. 126

E. K. Chong and S. H. Zak. *An introduction to Optimisation*. John Wiley & Sons, 2013. 65

C. F. Colebrook and C. M. White. Experiments with Fluid Friction in Roughened Pipes. *Proceedings of the Royal Society of London*, 161(906):367–381, 1937. 80

J. W. Cooley and J. W. Tukey. An Algorithm for Machine Calculation of Complex Fourier Series. *Mathematics of Computation*, 19(90):297–&, 1965. 61

Dassault Systèmes. ABAQUS v. 6.11, 2011. 72

Dassault Systèmes. SolidWorks 2013, 2013. 122

K. Deb, A. Pratap, S. Agarwal, and T. Meyarivan. A fast and elitist multiobjective genetic algorithm: NSGA-II. *IEEE Transactions on Evolutionary Computation*, 6(2):182–197, 2002. 153

K. G. Degen, C. Gerbig, and H. Onnich. *Acoustic Assessment of Micro-pressure Waves Radiating from Tunnel Exits of DB High-Speed Lines*, pages 48–55. Springer Berlin Heidelberg, Berlin, Heidelberg, 2008. 49

K. Diethelm. An investigation of some nonclassical methods for the numerical approximation of Caputo-type fractional derivatives. *Numerical Algorithms*, 47 (4):361–390, 2008. 84, 85, 86, 89

P. E. Farrell and J. R. Maddison. Conservative interpolation between volume meshes by local Galerkin projection. *Computer Methods in Applied Mechanics and Engineering*, 200:89–100, 2011. 200

J. H. Ferziger and M. Peric. *Computational methods for fluid dynamics*. Springer Science & Business Media, 2012. 40, 59, 62, 120, 121, 126, 206

B. Fornberg. Generation of finite difference formulas on arbitrarily spaced grids. *Mathematics of Computation*, 51(184):699–706, 1988. 98

B. Fornberg. *A Practical Guide to Pseudospectral Methods*. Cambridge university press, 1998. 61

F. N. Fritsch and R. E. Carlson. Monotone Piecewise Cubic Interpolation. *SIAM Journal on Numerical Analysis*, 17(2):238–246, 1980. 104

E. Gabriel, G. E. Fagg, G. Bosilca, T. Angskun, J. J. Dongarra, J. M. Squyres, V. Sahay, P. Kambadur, B. Barrett, A. Lumsdaine, R. H. Castain, D. J. Daniel, R. L. Graham, and T. S. Woodall. Open MPI: Goals, concept, and design of a next generation MPI implementation. *11th European PVM/MPI Users' Group Meeting*, pages 97–104, 2004. 126

C. W. Gear. The Automatic Integration of Ordinary Differential Equations. *Communications of the ACM*, 14(3):176–179, 1971. 62

H. Glöcke and P. Pfretzschner. High speed tests with ICE V passing through tunnels and the effect of sealed coaches on passenger comfort. In *International Symposium on the Aerodynamics and Ventilation of Vehicle Tunnels*, pages 23–44, 1988. 49

S. Godunov. *Different methods for shock waves.* PhD thesis, Moscow State University, 1954. 61, 93

C. Greenshields. OpenFOAM User Guide: 3.1 Programming language, OpenFOAM, 2015. URL `http://cfd.direct/openfoam/user-guide/programming-language-openfoam/`. 64

C. J. Greenshields, H. G. Weller, L. Gasparini, and J. M. Reese. Implementation of semi-discrete, non-staggered central schemes in a colocated, polyhedral, finite volume framework, for high-speed viscous flows. *International Journal for Numerical Methods in Fluids*, 63(1):1–21, 2010. 121, 206

A. Griewank and A. Walther. *Evaluating derivatives: principles and techniques of algorithmic differentiation.* Society for Industrial and Applied Mathematics, 2008. 99

B. Gschaider. simpleFunctionObjects, 2014. URL `https://openfoamwiki.net/index.php/Contrib/simpleFunctionObjects`. 131

B. F. W. Gschaider. The incomplete swak4Foam reference. Technical report, 2013. 131, 202

T. Hara. Aerodynamic Force Acting on High Speed Train at Tunnel Entrance. *Transactions of the Japan Society of Mechanical Engineers*, 4:547–553, 1961. 45

A. Harten. High Resolution Schemes for Hyperbolic Conservation Laws. *Journal of Computational Physics*, 49(3):357–393, 1983. 93

High Speed Two Limited. D7: Tunnel Construction and Methodology. Technical report, London, 2015. 141

Hitachi. Fatigue testing machine for the load caused by the air-pressure fluctuations, 2013. URL `http://www.hitachi-rail.com/products/rolling{_}stock/shinkansen/feature08.html`. 51

R. Hooke and T. A. Jeeves. "Direct" Search Solution of Numerical and Statistical Problems. *Journal of the ACM*, 8(2):212–229, 1961. 154

M. S. Howe. The compression wave generated by a high-speed train at a vented tunnel entrance. *The journal of the Acoustical Society of America*, 104(3):1158–1164, 1998. 218

M. S. Howe, M. Iida, T. Fukuda, and T. Maeda. Theoretical and experimental investigation of the compression wave generated by a train entering a tunnel with a flared portal. *Journal of Fluid Mechanics*, 425(2000):111–132, 2000. 53

M. S. Howe, M. Iida, and T. Fukuda. Influence of an unvented tunnel entrance hood on the compression wave generated by a high-speed train. *Journal of Fluids and Structures*, 17:833–853, 2003a. 51, 218

M. S. Howe, M. Iida, T. Fukuda, and T. Maeda. Aeroacoustics of a tunnel-entrance hood with a rectangular window. *Journal of Fluid Mechanics*, 487: 211–243, 2003b. 51, 218

M. S. Howe, A. Winslow, M. Iida, and T. Fukuda. Rapid calculation of the compression wave generated by a train entering a tunnel with a vented hood: Short hoods. *Journal of Sound and Vibration*, 311(1):254–268, 2008. 53, 145, 179

M. Iida, T. Matsumura, T. Fukuda, K. Nakatani, and T. Maeda. Optimization of Train Nose Shape for Reducing Impulsive Pressure Wave from Tunnel Exit. *Transactions of the Japan Society of Mechanical Engineers Series B*, 62(596): 1428–1435, 1996a. 51

M. Iida, T. Matsumura, K. Nakatani, T. Fukuda, and T. Maeda. Optimum nose shape for reducing tunnel sonic boom. In *IMechE conference transactions*, volume 8, pages 271–282. Mechanical engineering Publications Limited, 1996b. 51

R. I. Issa. Solution of the implicitly discretised fluid flow equations by operator-splitting. *Journal of Computational Physics*, 62(1):40–65, 1986. 120

D. Jakobović and M. Golub. Adaptive Genetic Algorithm. *Journal of Computing and Information Technology*, 7(3):229–235, 1999. 154

H. Jasak. *Error Analysis and Estimation for the Finite Volume Method with Applications to Fluid Flows*. PhD thesis, 1996. 59, 64, 121, 126, 208

Z. L. Ji. Acoustic length correction of closed cylindrical side-branched tube. *Journal of Sound and Vibration*, 283:1180–1186, 2005. 70

Y. Jin. Surrogate-assisted evolutionary computation: Recent advances and future challenges. *Swarm and Evolutionary Computation*, 1:61–70, 2011. 154

JR-EAST. R&D Themes, 2016. URL `https://www.jreast.co.jp/e/development/theme/market/market02.html`. 52

F. Kappel and A. V. Kuntsevich. Implementation of Shor's r-algorithm. *Computational Optimization and Applications*, 15:193–205, 2000. 89

F. Kemm. A comparative study of TVD limiters, well known limiters and an introduction of new ones. *International Journal for Numerical Methods in Fluids*, 67(4):404–440, 2011. 128

M. Kermani, A. Gerber, and J. Stockie. Thermodynamically based moisture prediction using Roe's scheme. In *4th Conference of Iranian Aerospace Society*, Amir Kabir University of Technology, Tehran, 2003. 93

H. Kim, T. Setoguchi, and K. Matsuo. Reduction of impulsive noise caused by unsteady compression wave. *JSME international journal. Series B, fluids and thermal engineering*, 40(2):223–229, 1997. 252

H. D. Kim, Y. H. Kweon, T. Aoki, and T. Setoguchi. A new technique for the control of a weak shock discharged from a tube. *Proceedings of the Institution of Mechanical Engineers, Part C: Journal of Mechanical Engineering Science*, 218(4):377–387, 2004. 252

M. Kraposhin. All Mach number implicit solver with Kurganov-Tadmore scheme - pisoCentralFoam, 2016. URL `https://www.cfd-online.com/Forums/openfoam-programming-development/158077-all-mach-number-implicit-solver-kurganov-tadmore-scheme-pisocentralfoam-5.html`. 121

M. Kraposhin, A. Bovtrikova, and S. Strijhak. Adaptation of Kurganov-Tadmor Numerical Scheme for Applying in Combination with the PISO Method in Numerical Simulation of Flows in a Wide Range of Mach Numbers. *Procedia Computer Science*, 66:43–52, 2015. 120, 208

A. Kurganov and E. Tadmor. New High-Resolution Central Schemes for Nonlinear Conservation Laws and ConvectionDiffusion Equations. *Journal of Computational Physics*, 160(1):241–282, 2000. 92, 120, 206, 208

H. Kwon, K. Jang, Y. Kim, K. Yee, and D. Lee. Nose shape optimization of high-speed train for minimization of tunnel sonic boom. *JSME International Series C*, 44(3):890–899, 2001. 51, 205

H. B. Kwon and C. S. Park. An Experimental Study on the Relationship between Ballast-flying Phenomenon and Strong Wind under High-speed Train. *Proceedings of the World Congress on Rail Research*, 2006. 54

T. A. M. Langlands and B. I. Henry. The accuracy and stability of an implicit solution method for the fractional diffusion equation. *Journal of Computational Physics*, 205(2):719–736, 2005. 83

S.-R. Lee, J.-Y. Kang, and K.-S. Rho. Fatigue Analysis of High Speed Passenger Train under Extreme Operating Conditions. In *Stress 20*, 2002. 33, 50

R. J. LeVeque. *Finite Difference Methods for Ordinary and Partial Differential Equations*. Society for Industrial and Applied Mathematics, Seattle, 2007. 59, 98, 99

H. Levine and J. Schwinger. On the Radiation of Sound from an Unflanged Circular Pipe. *Physical Review*, 73(4):383–406, 1948. 70

F. Linares and G. Ponce. *Introduction to Nonlinear Dispersive Equations*. Springer, 2014. 82

X.-D. Liu, S. Osher, and T. Chan. Weighted essentially non-oscillatory schemes. *Journal of computational physics*, 115:200–212, 1994. 92, 95

B. Lombard and J.-F. Mercier. Numerical modeling of nonlinear acoustic waves in a tube connected with Helmholtz resonators. *Journal of Computational Physics*, 259:421–443, 2014. 71, 77, 82, 84, 86, 87, 88, 89

B. Lombard, J.-F. Mercier, and O. Richoux. Numerical investigation of acoustic solitons. pages 1–7, 2014. 82

T. Maeda. Protecting the trackside environment. *Japan Railway & Transport Review*, 22:48–57, 1999. 34

T. Maeda, T. Matsumura, M. Iida, K. Nakatani, and K. Uchida. Effect of shape of train nose on compression wave generated by train entering tunnel. In *The In-*

ternational Conference on Speedup Technology for Railway and Maglev Vehicles, Yokohama, Japan, 1993. 51

T. M. Marinov, N. Ramirez, and F. Santamaria. Fractional Integration Toolbox. *Fractional calculus & applied analysis*, 16(3):670–681, 2013. 83, 84

S. Mashimo, E. Nakatsu, T. Aoki, and K. Matsuo. Attenuation and Distortion of a Compression Wave Propagating in a High-Speed Railway Tunnel. *JSME International Journal Series B*, 40(1):51–57, 1997. 144, 146

MathWorks. Is it possible to solve a mixed-integer multi-objective optimization problem using Global Optimization Toolbox, 2013. URL `https://uk.mathworks.com/matlabcentral/answers/103369-is-it-possible-to-solve-a-mixed-integer-multi-objective-optimization-problem-using-global-optimizati`. 153

MathWorks. MATLAB Function Reference R2017a. Technical report, Natick, Massachusetts, 2017a. 88, 101, 108, 148, 149, 255

MathWorks. Global Optimisation Toolbox R2017a. Technical report, Natick, Massachusetts, 2017b. 171

Mathworks. Mixed Integer Optimisation, 2017. URL `https://uk.mathworks.com/help/gads/mixed-integer-optimization.html{#}bs1cihn`. 157

MATLAB. *version 9.2.0.538062 (R2017a)*. The MathWorks Inc., Natick, Massachusetts, United States, 2017. 83

K. Matsuo, T. Aoki, S. Mashimo, and E. Nakatsu. Entry compression wave generated by a high-speed train entering a tunnel. In *BHR Group Conference Series Publication*, volume 27, pages 925–934. Mechanical engineering Publications Limited, 1997. 147

J.-F. Mercier and B. Lombard. A new model for nonlinear acoustic waves in a non-uniform lattice of Helmholtz resonators. *Preprint submitted to Wave Motion*, 2016. 79, 105, 106

S. Miura, H. Takai, M. Uchida, and Y. Fukada. The Mechanism of Railway Tracks. *Japan Railway & Transport Review*, 3:38–45, 1998. 54

T. Miyachi. Theoretical Model for Micro-pressure Wave Emission Considering the Effect of Wave Topography around the Tunnel Portal. *Quarterly Report of RTRI*, 52(2), 2011. 47

T. Miyachi. Acoustic model of micro-pressure wave emission from a high-speed train tunnel. *Journal of Sound and Vibration*, 391:127–152, 2017. 47, 248

T. Miyachi, T. Fukuda, and S. Saito. Model experiment and analysis of pressure waves emitted from portals of a tunnel with a branch. *Journal of Sound and Vibration*, 333(23):6156–6169, 2014. 33, 51, 194, 210, 212

T. Miyachi, S. Saito, T. Fukuda, Y. Sakuma, S. Ozawa, T. Arai, S. Sakaue, and S. Nakamura. Propagation characteristics of tunnel compression waves with multiple peaks in the waveform of the pressure gradient: Part 1: Field measurements and mathematical model. *Proceedings of the Institution of Mechanical Engineers, Part F: Journal of Rail and Rapid Transit*, 230(4):1297–1308, 2016. 80, 84, 145, 182

N. Montenegro Palmero and A. Vardy. Tunnel gradients and aural health criterion for train passengers. *Proceedings of the Institution of Mechanical Engineers Part F-Journal of Rail and Rapid Transit*, 228(7):821–832, 2014. 33, 49

F. Moukalled, L. Mangani, and M. Darwish. *The Finite Volume Method in Computational Fluid Dynamics: An Advanced Introduction with OpenFOAM and MATLAB*, volume 113. Springer, 2015. 40, 59, 64, 120, 126, 127, 206, 208

M. L. Munjal. *Acoustics of Ducts and Mufflers with application to exhaust and ventilation system design*. John Wiley & Sons, New York, 2014. 72, 253

J. Muñoz-Paniagua, J. García, and A. Crespo. Genetically aerodynamic optimization of the nose shape of a high-speed train entering a tunnel. *Journal of Wind Engineering and Industrial Aerodynamics*, 130:48–61, 2014. 51

F. Nozaki. Limited Gradient Schemes in OpenFOAM, 2014. URL `https://www.slideshare.net/fumiyanozaki96/limited-gradient-schemes-in-openfoam`. 126, 207

T. Ogawa and K. Fujii. Prediction and alleviation of a booming noise created by a high-speed train moving into a tunnel. In *ECCOMAS computational fluid dynamics conference*, pages 808–814, 1996. 34, 49

K. B. Oldham and J. Spanier. *The Fractional Calculus: Theory and Applications of Differentiation and Integration to Arbitrary Order*, volume 111. Dover, New York, 1974. 60, 83

S. Ozawa and T. Maeda. Tunnel entrance hoods for reduction of micro-pressure wave. *Railway Technical Research Institute, Quarterly Reports*, 29(3), 1988. 144, 178

S. Ozawa, T. Maeda, T. Matsumura, and K. Uchida. Effect of ballast on pressure wave propagating through tunnel. *Proceedings of the International Conference on Speedup Technology for Railway and Maglev Vehicles*, 2:299–304, 1993. 54, 78, 82, 174, 182, 254

F. Pianosi, F. Sarrazin, and T. Wagener. Environmental Modelling & Software Short communication A Matlab toolbox for Global Sensitivity Analysis. *Environmental Modelling and Software*, 70:80–85, 2015. 158

I. Podlubny. *Fractional Differential Equations: An Introduction to Fractional Derivatives, Fractional Differential Equations, to Methods of Their Solution and Some of Their Applications*. Academic press, 1998. 84

I. Podlubny. Matrix approach to discrete fractional calculus. *Fractional Calculus & Applied Analysis*, 3(4):359–386, 2000. 84

T. Poinsot and S. Lele. Boundary conditions for direct numerical simulations of compressible viscous flows. *Journal of Computational Physics*, 101:104–129, 1992. 125

J. P. Powell and R. Palacín. Passenger Stability Within Moving Railway Vehicles: Limits on Maximum Longitudinal Acceleration. *Urban Rail Transit*, 1(2):95–103, 2015. 176

A. D. Quinn, M. Hayward, C. J. Baker, F. Schmid, J. A. Priest, and W. Powrie. A full-scale experimental and modelling study of ballast flight under high-speed trains. *Proceedings of the Institution of Mechanical Engineers, Part F: Journal of Rail and Rapid Transit*, 224(2):61–74, 2010. 54

R. S. Raghunathan, H. D. Kim, and T. Setoguchi. Aerodynamics of high-speed railway train. *Progress in Aerospace Sciences*, 38(6):469–514, 2002. 48, 252

S. Raghunathan, H. Kim, and T. Setoguchi. Impulse Noise and Its Control. *Progress in Aerospace Sciences*, 34(1-2):1–44, 1998. 49, 252

Railway Gazette. Chuo maglev route announced, 2013. URL `http://www.railwaygazette.com/news/single-view/view/chuo-maglev-route-announced.html`. 50

J. Rhoads. Effects of grid quality on solution accuracy. In *OpenFOAM Workshop*, pages 1–8, 2014. 126

O. Richoux, B. Lombard, and J. F. Mercier. Generation of acoustic solitary waves in a lattice of Helmholtz resonators. *Wave Motion*, 56:85–99, 2015. 86, 100, 116, 131

S. Rienstra and A. Hirschberg. *An Introduction to Acoustics*. Eindhoven University of Technology, 2004. 39, 42, 43, 175

P. Roe. Characteristic-Based Schemes for the Euler Equations. *Annual Review of Fluid Mechanics*, 18:337–365, 1986. 128

S. Saito, T. Miyachi, and M. Iida. Reduction of Micro-pressure Wave Emitted from Portal of Side Branch of High-speed Railway Tunnel. *Quarterly Report of RTRI*, 51(3):146–150, 2010. 34, 196

S. Saito, T. Miyachi, and M. Iida. Countermeasure for Reducing Micro-pressure Wave Emitted from Railway Tunnel by Installing Hood at the Exit of Tunnel. *Quarterly Report of RTRI*, 54(4):231–236, 2013. 196

K. Sakurai, K. Saeki, Y. Takakuwa, and A. Watanabe. Development of New Tunnel Entrance Hoods. *JR EAST Technical Review*, 12(12):58–63, 2008. 49, 53

D. Salane. Adaptive routines for forming Jacobians numerically. 1986. 99

A. Sasoh, K. Matsuoka, K. Nakashio, E. Timofeev, K. Takayama, P. Voinovich, T. Saito, S. Hirano, S. Ono, and Y. Makino. Attenuation of weak shock waves along pseudo-perforated walls. *Shock Waves*, 8(3):149–159, 1998. 140, 166

H. Schlichting and K. Gersten. *Boundary Layer Theory*. McGraw-hill, New York, 2000. 41

A. Selamet and Z. L. Ji. Circular asymmetric Helmholtz resonators. *Journal of the Acoustical Society of America*, 107(5):2360–2369, 2000. 70

A. Selamet, M. B. Xu, I. J. Lee, and N. T. Huff. Helmholtz resonator lined with absorbing material. *The Journal of the Acoustical Society of America*, 117(2): 725–733, 2005. 113

L. F. Shampine and C. W. Gear. A User's View of Solving Stiff Ordinary Differential Equations. *SIAM Review*, 21(1):1–17, 1979. 63

L. F. Shampine and M. W. Reichelt. The MATLAB ODE Suite. *SIAM Journal on Scientific Computing*, 18(1):1–22, 1997. 99

N. Z. Shor. *Minimization Methods for Non-Differentiable Functions*, volume 3. Springer Science & Business Media, Berlin, 2012. 88

J. Skulina. *A Study of Non-linear Acoustic Flows at the Open End of a Tube using Particle Image Velocimetry*. PhD thesis, University of Edinburgh, 2005. 39

I. M. Sobol. On the distribution of points in a cube and the approximate evaluation of integrals. *Zh. Vychisl. Mat. i Mat. Fiz. 7*, 7(4):784–802, 1967. 149

M. Srinivas and L. M. Patnaik. Adaptive Probabilities of Crossover and Mutation in Genetic Algorithms. *IEEE Transactions on Systems, Man and Cybernetics*, 24(4):656–667, 1994. 154

G. Strang. On the Construction and Comparison of Difference Schemes. *SIAM Journal on Numerical Analysis*, 5(3):506–517, 1968. 100

J. C. Strikwerda. *Finite difference schemes and partial differential equations*. Society for Industrial and Applied Mathematics, 2004. 59

N. Sugimoto. Burgers equation with a fractional derivative; hereditary effects on nonlinear acoustic waves. *Journal of Fluid Mechanics*, 225:631–653, 1991. 81, 84

N. Sugimoto. Propagation of nonlinear acoustic waves in a tunnel with an array of Helmholtz resonators. *Journal of Fluid Mechanics*, 244:55–78, 1992. 45, 55, 71, 74, 75, 77, 81, 118, 136

N. Sugimoto, M. Masuda, J. Ohno, and D. Motoi. Experimental Demonstration of Generation and Propagation of Acoustic Solitary Waves in an Air-Filled Tube. *Physical Review Letters*, 83(20):4053–4056, 1999. 133

N. Sugimoto, M. Masuda, K. Yamashita, and H. Horimoto. Verification of acoustic solitary waves. *Journal of Fluid Mechanics*, 504:271–299, 2004. 118, 131

P. K. Sweby. High Resolution Schemes Using Flux Limiters for Hyperbolic Conservation Laws. *SIAM Journal on Numerical Analysis*, 21(5):995–1011, 1984. 207

K. Takayama, A. Sasoh, O. Onodera, R. Kaneko, and Y. Matsui. Experimental investigation on tunnel sonic boom. *Shock Waves*, 5(3):127–138, 1995. 53, 55, 120, 140, 178

The Engineering Toolbox. Ventilation Ducts - Roughness & Surface Coefficients, 2016. URL `http://www.engineeringtoolbox.com/surface-roughness-ventilation-ducts-d{_}209.html`. 80, 122

T. Tielkes. Aerodynamic Aspects of Maglev Systems. In *19th International Conference on Magnetically Levitated Systems and Linear Drives*, 2006. 55

T. Tielkes, H. J. Kaltenbach, M. Hieke, P. Deeg, and M. Eisenlauer. Measures to counteract micro-pressure waves radiating from tunnel exits of DB's new Nuremberg-Ingolstadt high-speed line. *Notes on Numerical Fluid Mechanics and Multidisciplinary Design*, 99:40–47, 2008. 55

Tokyo Railway Labyrinth. N700A: Advanced Shinkansen Train, 2013. URL `http://tokyorailwaylabyrinth.blogspot.co.uk/2013/11/n700a-advanced-shinkansen-train.html`. 52

L. N. Trefethen. *Spectral Methods in Matlab*, volume 10. Society for Industrial and Applied Mathematics, Philadelphia, 2000. 98

M. Ueno, S. Usui, H. Tanaka, and A. Watanebe. Technological overview of the next generation Shinkansen high-speed train Series N700. In *8th World Congress on Rail Research*, 2008. 52

UIC. Report no. 779-11: Determination of railway tunnel cross-sectional areas on the basis of aerodynamic considerations. Technical report, Paris, 2005. 50

H. A. van der Vorst. Bi-CGSTAB: A Fast and Smoothly Converging Variant of Bi-CG for the Solution of Nonsymmetric Linear Systems. *SIAM Journal on Scientific and Statistical Computing*, 13(2):631–644, 1992. 126

B. van Leer. Towards the ultimate conservative difference scheme. II. Monotonicity and conservation combined in a second-order scheme. *Journal of Computational Physics*, 14(4):361–370, 1974. 93, 128, 206

B. Van Leer. Towards the ultimate conservative difference scheme III. Upstream-centered finite-difference schemes for ideal compressible flow. *Journal of Computational Physics*, 23(3):263–275, 1977. 93

B. van Leer. Towards the ultimate conservative difference scheme. V. A second-order sequel to Godunov's method. *Journal of Computational Physics*, 32(1): 101–136, 1979. 91

A. Vardy. Aerodynamic drag on trains in tunnels part 1: synthesis and definitions. *Proceedings of the Institution of Mechanical Engineers, Part F: Journal of Rail and Rapid Transit*, 210(1):29–38, 1996. 45

A. Vardy. Generation and alleviation of sonic booms from rail tunnels. *Proceedings of the ICE - Engineering and Computational Mechanics*, 161(3):107–119, 2008. 33, 45, 47, 48, 53, 54, 55, 144, 196

A. E. Vardy and J. M. B. Brown. Influence of ballast on wave steepening in tunnels. *Journal of Sound and Vibration*, 238(4):595–615, 2000. 54

R. Wang, H. Feng, and R. J. Spiteri. Observations on the fifth-order WENO method with non-uniform meshes. *Applied Mathematics and Computation*, 196 (1):433–447, 2008. 95

Y. D. Wang, X. Y. Cai, W. Zhao, and B. Chen. The Research on Fatigue Damage due to Tunnel Aerodymical Load Acting on the Body of High-Speed Train. In *Proceedings of the 1st International Workshop on High-Speed and Intercity Railways*, pages 285–293, 2012. 33

H. G. Weller and G. Tabor. A tensorial approach to computational continuum mechanics using object-oriented techniques. *Computers in Physics*, 12(6):620–631, 1998. 36, 63, 120

A. Yamamoto. Micro-pressure wave radiated from tunnel exit. In *Preprint of the spring meeting of physical society of Japan*, 1977. 47, 147

L. Yuan and O. P. Agrawal. A Numerical Scheme for Dynamic Systems Containing Fractional Derivatives. *Journal of Vibration and Acoustics*, 124(2):321, 2002. 84

B. T. Zinn. A theoretical study of nonlinear damping by Helmholtz resonators. *Journal of Sound and Vibration*, 13(3):347–356, 1970. 78

Appendix A

Research Placement at RTRI

A.1 Overview of Placement

The author was provided with the opportunity to undertake a research placement at the Railway Technical Research Institute (RTRI) in Japan, during April-May 2014. Japan began operating its famous high speed rail network (Shinkansen) in the 1960s and is considered to be a pioneer in this field. The mountainous terrain in Japan means that the Shinkansen network features many tunnels, which are often close to populated areas. Consequently, RTRI has substantial experience in tunnel aerodynamics.

The placement was carried out under the supervision of Dr Tokuzo Miyachi and Dr Sanetoshi Saito in the Heat and Air Flow Analysis Laboratory, which specialises in open-air and tunnel aerodynamics for both trains and infrastructure. The results in this section, including figures and tables, have been included with the kind permission of Dr Tokuzo Miyachi of RTRI (as of 31 May 2017). The objectives of the placement included:

- The transfer of knowledge and experience in tunnel aerodynamics, which may be useful for the design and analysis of tunnels/trains in the UK.
- Guidance and practical advice on suitable topics for the PhD research project.
- Industrial experience in railway research and development, including exper-

imental experience.

- Develop contacts in Japan for potential future collaborations and technical advice.

As well as carrying out experiments, the author had the opportunity to visit several institutions associated with RTRI:

- **Maibara Large-Scale Low-Noise wind tunnel** is used to investigate aerodynamic noise generated by high speed trains and cars. The wind tunnel has been fitted with sound absorbing panels and acoustic silencers to minimise background noise.

- **Hamamatsu Shinkansen Workshop** is an overhaul facility which oversees the refurbishment of in-service Shinkansen trains. Consequently, the engineers have significant experience with the issues typically experienced by high speed trains.

- **Hitachi Kasado Rolling Stock Works** is one of the main sites for the construction and assembly of the various Shinkansen trains in Japan.

- **Superconducting Maglev Yamanashi Test Track**. JR Central has recently been approved to begin construction of a new magnetic-levitation (maglev) line, which will eventually operate between Tokyo and Osaka (Chuo Shinkansen). A significant proportion of the route planned will be in tunnels. Aerodynamic noise will be greater than the conventional Shinkansen due to the higher operating speeds.

A.2 Experimental Overview

Experiments were carried in order to investigate the pressure transients generated by a scale moving train model in an open environment and inside a short tunnel. The experimental analysis can be divided into three areas of study:

1. **Passage of the train in the open environment**: Comparison of the pressure waveforms along the length of the train between experimental measurements and a proposed analytical model.

2. **Tunnel entry, passage and exit**: Consideration of the propagation of pressure waves and the effect of an entrance/exit hood on MPWs, i.e. the effects of non-linear steepening with train entry speed and propagation distance in the tunnel.

The train model is launched along a guide wire for a short distance in the open before entering a short duct, representative of a tunnel. Pressure transients were obtained using transducers in the tunnel and microphones in the open, as shown in Figure A.1. Two axisymmetric nose profiles were considered with a ratio of nose length-to-radius, $\theta = l_{\mathrm{zn}}/r_{\mathrm{zn}}$, of 3 and 6. The train model is axis-symmetric with an identical nose and tail. Pressure time-histories were recorded at various distances for a scale model train with the configurations listed in Table A.1. Note that the geometric parameters in this table are approximate values for confidentiality reasons.

An analytical model based on potential flow theory was validated against the experimental data for the train operating in the open. The model can be used to rapidly predict the impact of noise from the train nose and tail on the surrounding environment as a function of its velocity (u_{z}), diameter (d_{z}), and the distance of an observer from the train, r_{o}. Experimental and analytical results for the train in an open environment are not included in this work for confidentiality reasons. Experiments were also carried out on the effect of using a hood at the entrance and exit of the tunnel on the amplitude of MPWs, for different train velocities and nose profiles.

An example of the pressure waveforms generated by the train as it passes the microphones in an open environment is shown in Figure A.2. The spikes in the pressure coefficient correspond to where the train model nose and then the tail passes the microphone position. The maximum absolute pressure coefficient decreases exponentially with the observation distance from the train model.

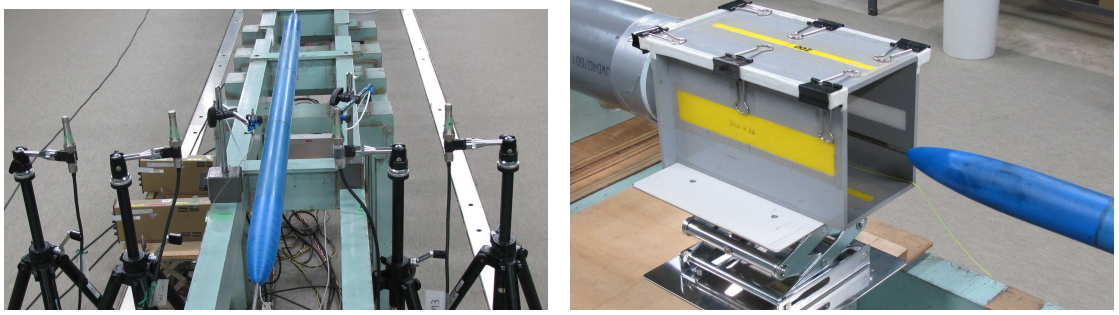
Nose Profile (θ)	u_z (km/r)	Hood
3	250	-
3	300	-
3	300	entrance
3	340	-
3	340	entrance
6	250	-
6	300	-
6	300	entrance
6	300	exit
6	340	-
6	340	entrance
6	340	exit

(a) Model configurations

Variable	Value	unit
l_z	~ 1000	mm
d_z	~ 50	mm
l_{zn}	50-150	mm
l_t	8000	mm
d_t	~ 100	mm
l_h	~ 200	mm
h_h	~ 150	mm
w_h	~ 100	mm
β	~ 0.2	-

(b) Train and tunnel geometry

Table A.1: Model configurations. Approximate values are provided in (b).



(a) (b)

Figure A.1: Scale train model and microphone set-up in the open (a), and the train nose against a simple unventilated tunnel entrance hood (b).

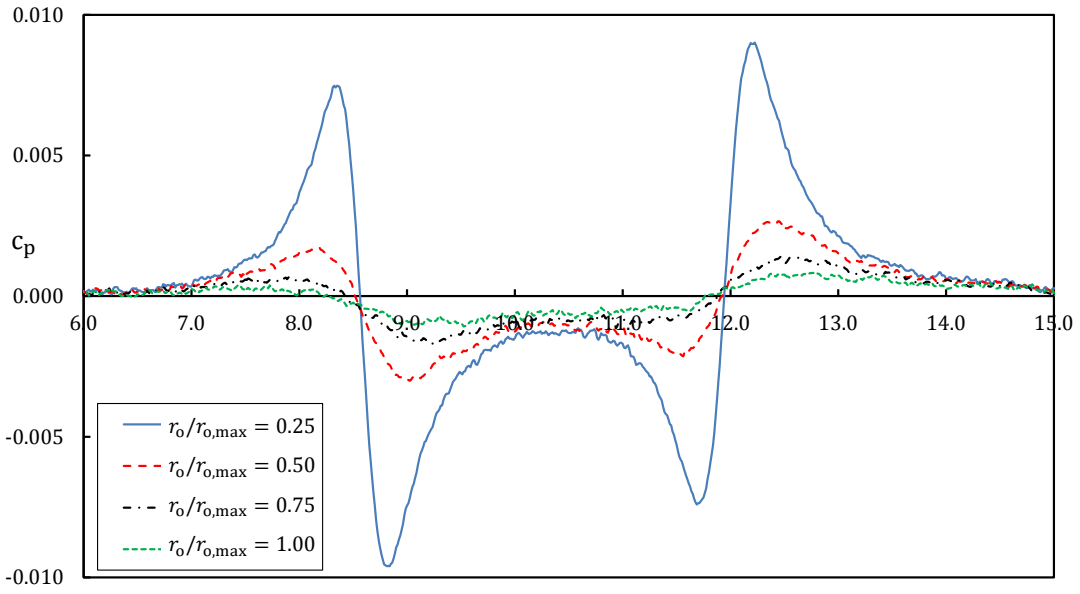


Figure A.2: Pressure coefficient waveforms at various measurement distances from the train model in an open environment. The measurement distance is normalised by the furthest measurement distance.

A.3 Results and Discussion

The model train enters a short cylindrical tunnel after passing an initial open region. Three flush-mounted pressure transducers were fitted at a distance from the tunnel entrance of 1, 5, and 7 m for $\theta = 3$, and 1, 2, and 7 m for $\theta = 6$. A microphone was positioned in-line with the tunnel exit to capture MPWs.

The tunnel has been tested with and without an unventilated hood at the entrance and exit of the tunnel (see Figure A.1). Figure A.3 shows that the maximum amplitude of the MPW approximately follows a power law with the train entry speed (i.e. $\propto u_z^3$), assuming no distortion of the wavefront occurs as it propagates. The true value is slightly closer to u_z^4, due to non-linear steepening of the wavefront over relatively large propagation distances in smooth-walled tunnels.

The use of a simple unventilated tunnel entrance hood significantly reduces the MPW amplitude (also see Equation 5.33). On the other hand, placing a hood at the exit of the tunnel increases the maximum MPW amplitude. The ratio between the maximum MPW amplitude with and without a hood at the tunnel exit is given

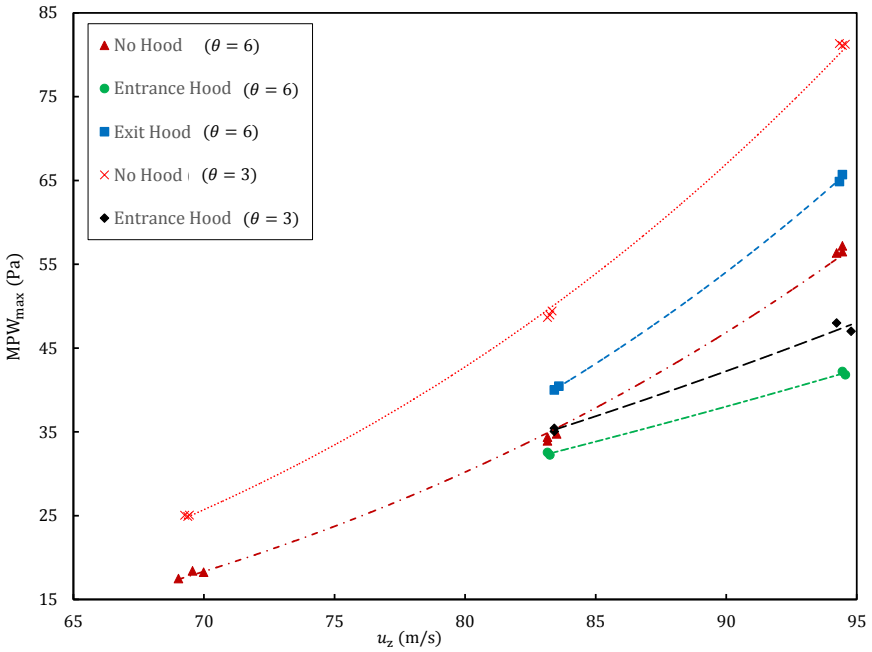


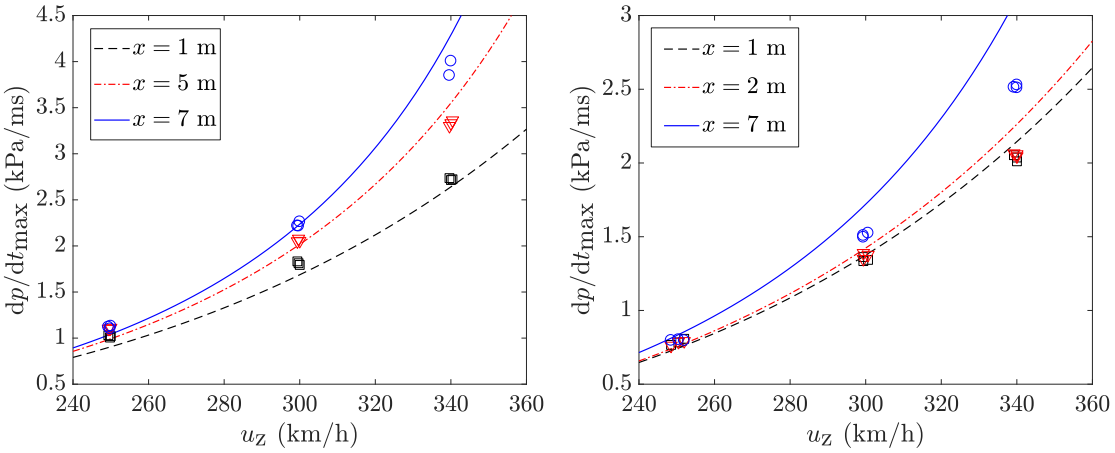
Figure A.3: Variation of maximum MPW amplitude with train entry speed. The fitted curves follow a power law, $\propto u_z^3$.

analytically as $l_h \to \infty$ by (Miyachi, 2017):

$$\alpha_{eh} = \frac{2\theta_h}{1+\theta_h} \tag{A.1}$$

where $\theta_h = S_h/S_t$ and the subscript eh denotes exit hood. For example, $\alpha_{eh} = 1.14$ using Equation A.1 with the dimensions in Table A.1. This value agrees well with the experimental results in Figure A.3, where $\overline{\alpha_{eh}} = 1.12$ for $\theta = 6$. The use of a nose profile with $\theta = 6$, compared to $\theta = 3$, results in a significant reduction in the strength of the MPW for all train speeds considered.

Non-linear steepening of the wavefront with propagation distance from the tunnel entrance is clearly evident from Figure A.4. Good agreement is obtained between the experiments and the semi-empirical model presented in § 5.9. The maximum rate of change of pressure is predicted using Equation 5.28, where the value of L is approximated by Equation 5.7. The empirical factor ϕ, which accounts for the shape of the train nose and tunnel entrance, is found by fitting Equation 5.28 to the experimental data. It is estimated as $\phi \approx 1.2$ and $\phi \approx 1.4$ for $\theta = 3$ and $\theta = 6$, respectively.



(a) $\theta = 3$ (b) $\theta = 6$

Figure A.4: Comparison of experiments and a semi-empirical model for the maximum rate of change of pressure in the duct versus train entry speed. The propagation distance is measured from the tunnel entrance.

The semi-empirical model tends to over-predict the maximum rate of change of pressure, particularly for higher speeds and measurement distances. The steepness of the entry wave increases with train velocity and propagation distance. Therefore, visco-thermal losses due to the tunnel boundary layer and diffusivity of sound can no longer be neglected for strong changes in gradient. The model also appears to be less accurate for larger values of θ.

A.4 Conclusions

Several conclusions are drawn from scale model train experiments in the tunnel:

- The installation of an unventilated entrance hood at the tunnel exit should be avoided, for single-track twin-bore tunnels. Doing so may result in an increase in the strength of MPWs.

- The use of an entrance hood results in a significant reduction in maximum MPW amplitude, for short tunnels at least. Using a long train nose also provided a significant reduction in MPW strength.

- The use of an entrance hood provides a greater relative reduction in MPW

strength than using a longer train nose and is effective in this case against non-linear steepening in the tunnel.

- A simple semi-empirical model (see § 5.9) provides good agreement with experimental data for the maximum rate of change of pressure as a function of train speed and propagation distance.

Appendix B

An Exit Silencer for MPWs

B.1 Introduction

Currently employed MPW countermeasures focus on reducing the steepness of the compression wave generated as the train enters the tunnel (see § 2.5). Alternatively, an array of Helmholtz resonators disperses and attenuates pressure waves as they propagate (see § 2.6.1). This Appendix focuses on the implementation of a reactive silencer (of muffler) installed at the tunnel exit, in order to attenuate MPWs.

A reactive muffler functions by reflecting a significant proportion of the incident acoustic energy back towards the source. The muffler is analogous to a low-pass filter, and so it is expected to be more effective for attenuating higher frequencies (i.e. steep incident wavefronts), compared to a tunnel entrance hood or an array of Helmholtz resonators.

This Appendix serves as the starting point for future work on the optimisation of a tunnel exit silencer. Firstly, a 1-D physical and numerical model is presented for the propagation of pressure waves through the silencer. The geometric variables of the silencer are defined and a parametric study is carried out to investigate their effect on the transmitted wavefront. Finally, an optimisation procedure is proposed

for future work, in order to maximise the attenuation of MPWs.

B.2 Exit Silencer Overview

The phenomena of micro-pressure waves is similar to the noise generated from gun muzzles and the exhaust systems of internal combustion engines. The main differences between these applications is that the gas is essentially ideal in tunnels and the pressure magnitudes are much smaller. However, the tunnel exit and characteristic wavelength are significantly larger than in these systems. A reactive silencer/muffler has been proposed as a countermeasure for MPWs (Aoki et al., 1999; Kim et al., 1997, 2004; Raghunathan et al., 2002, 1998), and is already used in the aforementioned applications for reducing noise levels. The silencer typically consists of an array of expansion chambers and functions by successively reflecting a portion of the incident acoustic power back towards the source, due to a sudden change in acoustic impedance.

Aoki et al. (1999) posited that well-designed hoods at exit portals could be more effective than entrance hoods, for sufficiently high train speeds. The use of an axi-symmetric expansion chamber with a variable height, length, and baffle thickness was investigated through numerical modelling of the inviscid Euler equations and scale experiments using a shock tube. A parametric study was then carried out to find the geometric properties of the silencer which gave the greatest amplitude reduction, based on a quasi-3D axis-symmetric model. It was found that such a silencer could provide around a 30% reduction in the amplitude of MPWs.

This section aims to improve on the optimisation methodology used by Aoki et al. by developing a 1-D model of the silencer. The model can then be used to rapidly optimise the geometry of the silencer and benchmark the predictions against 3-D models.

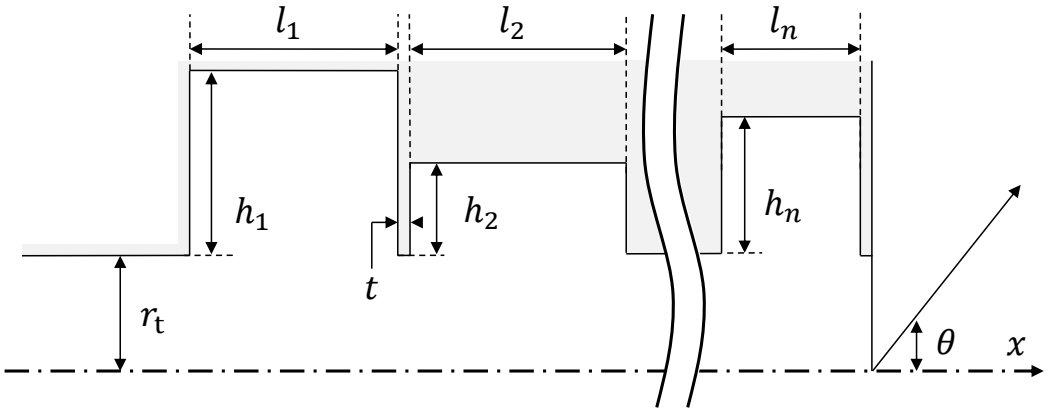


Figure B.1: Cross-section of an axi-symmetric silencer with N_c baffle chambers, with variable heights and lengths. The right-hand side is the exit into atmosphere.

B.3 1-D Model

B.3.1 Physical Model

A time domain treatment, similar to the methodology used for the array of Helmholtz resonators in Chapter 3, is used to model the effect of a series of expansion chambers on an incident compression wave. The acoustic two-port (or four-pole) transfer matrix method (see Munjal, 2014), which is commonly used in heating, ventilation and air conditioning (HVAC) applications and muffler design, is not suitable for this application due to the transient nature of the pressure waves. The transfer matrix method assumes a harmonic solution to the wave equation.

The demonstrative cross-section profile for the silencer is shown in Figure B.1, which is used for both an axi-symmetric profile and a demonstrative silencer at the exit of a tunnel. The PDE system for the propagation of pressure waves through a tunnel with a variable cross-section is derived under the same assumptions as the those used for the treatment of the array of Helmholtz resonators (see § 3.2.3), namely: plane wave propagation under the low frequency approximation and weak-acoustic non-linearity.

The bi-directional form of the equation system is considered as the size of the baffle chambers (in terms of cross-sectional area) is comparable to the size of the tunnel, and so the amplitude of reflected waves cannot be assumed to be

negligible. The bi-directional propagation of pressure waves through a tunnel with a variable cross-section is given by a modified form of the near-field system in Equation 3.62a (see Ozawa et al., 1993):

$$\frac{\partial u^{\pm}}{\partial t} + \frac{\partial \mathcal{F}^{\pm}}{\partial x} = -\frac{a_0}{2S_{\mathrm{t}}}\left[\frac{\partial S_{\mathrm{t}}}{\partial t} + \left(u^{+} - u^{-}\right)\frac{\partial S_{\mathrm{t}}}{\partial x}\right] \tag{B.1}$$

where the two unknowns to be solved are $(u^{+}, u^{-})^{T}$, and $S_{\mathrm{t}} = S_{\mathrm{t}}(x)$ is the axial variation in cross-sectional area of the duct. Therefore, $\partial S_{\mathrm{t}}/\partial t = 0$, assuming a rigid wall for the silencer. The bi-directional advective flux is given by:

$$\mathcal{F}^{\pm} = \pm A u^{\pm} + B\frac{\left(u^{\pm}\right)^{2}}{2} \tag{B.2}$$

where terms A and B for linear and non-linear advection, respectively, are defined in Equation 3.17. The effects of the diffusivity of sound and friction from the tunnel surface have been omitted, as these are assumed to have a negligible effect over the length of the silencer ($l_{\mathrm{s}} < 5d_{\mathrm{t}}$). Acoustic end corrections are incorporated into the thickness of the baffles and the length of the expansion chambers by using Equation 3.7 (see § 3.2.1.2).

This model is expected to be conservative in terms of the predicted maximum rate of change of pressure and the amplitude of the transmitted pressure wave as it does not incorporate dissipative mechanisms, including the high-speed jet which is generated at the discontinuous duct expansions. Jet losses are incorporated in the model for an array of Helmholtz resonators in § 3.2.3.

B.3.2 Numerical Implementation

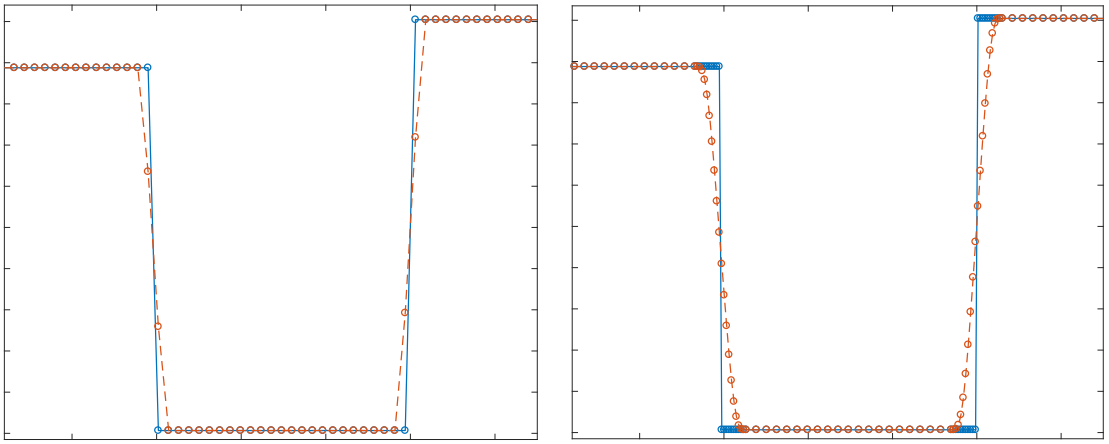
Equation B.1 can be solved by the method of lines (see § 2.7.1), after all spatial derivatives in x have been moved to the right-hand side and discretised (see § 3.3.2). The term for non-linear advection can be discretised using any upwinded shock capturing scheme, such those as employed in § 3.3.3. The 3rd order accurate KT-P scheme is used (see § 3.3.3.1), which permits a non-uniform grid spacing. A flux splitting method is not required, as the wind directions are treated separately.

Other spatial derivatives are discretised using a 2nd order accurate centred finite difference stencil. Higher order schemes are unable to resolve the discontinuous change in cross-sectional area of the baffles, and produce non-physical oscillations in the gradient around the baffle position.

Time marching can be performed using any standard first order ODE solver, such as those based on the explicit Runge-Kutta family, or implicit backwards differentiation formulas (see § 2.7.2). The implicit MATLAB solver `ode15s` (see § 3.3.4) was generally found to have the shortest simulation time, on the condition that a Jacobian sparsity pattern was provided. The Jacobian sparsity pattern is generated using the method described in § 3.3.4.

The source term in Equation B.1 permits an arbitrary area profile to be used for the silencer. However, a limitation was encountered with this modelling approach for the treatment of baffles. The area gradient should in theory become infinite valued in the presence of a discontinuous change in cross-sectional area (i.e. a baffle). In reality, this type of discontinuity does not exist, while the maximum area gradient is numerically restricted by the finite grid spacing. The physical boundedness of the numerical solution is sensitive to term $\partial S_\mathrm{t}/\partial x$ in Equation B.1. For example, the amplitude of reflected pressure waves would sometimes increase to a non-physical value upon encountering a baffle, depending on the amplitude and steepness of the incident wavefront, and the area gradient. This numerical issue persisted when using various shock capturing schemes, such as WENO, KT-L and KT-P (see § 3.3.3), or stiff ODE solvers, i.e. fully implicit BDF, 2nd order trapezoidal rule, 2nd order single-step Rosenbrock formula (see § 2.7.2).

The physical boundedness of the solution was improved by increasing the grid resolution around the baffles and smoothing the function $S_\mathrm{t}(x)$ (see Figure B.2). The `smooth` MATLAB function (MathWorks, 2017a) is used with local regression using weighted linear least squares and a 1st degree polynomial model. However, the degree of smoothing (as determined by the effective axial length of the smoothed baffle) required to maintain boundedness is dependent on the amplitude and steepness of the incident wavefront, as well as the grid resolution and



(a) Regular node spacing (b) Irregular node spacing

Figure B.2: The axial variation of cross-sectional area across a duct contraction and expansion, with the pre (—); and post (– – –) smoothed non-uniform grid.

change in cross-sectional area of the baffle. Consequently, this method of maintaining boundedness is difficult to adapt to a general case for use in an optimisation procedure, where the numerical model must be able to run autonomously. An alternative approach to smoothing $S_t(x)$ and/or increasing the grid refinement around the baffles may be to use a gradient limiter. For example, in OpenFOAM the cell gradient can be limited to maintain physical boundedness (see § 4.3.2.5).

B.3.3 Initial and Boundary Conditions

The initial condition used for this model is a characteristic compression wave generated by a high-speed train entering a tunnel, which has been used previously in this work (see § 5.3). The initial condition is prescribed as a time dependent boundary condition at the upstream boundary for $u^+(0,t) = u_0(t)$ and $u^-(0,t) = 0$, in order to model only downstream wave propagation. The initial fields are $u^+(x,0) = u^-(x,0) = 0$, in order to simulate undisturbed air downstream of the wavefront.

A non-reflective boundary condition is imposed at the downstream boundary by using $u^-(l_s,t) = 0$. The effect of the opening to atmosphere (i.e. an infinite baffle) at the downstream boundary is not modelled. It can be approximated by using $u^-(l_s,t) = u^+(l_s,t)$, so that $p = 0$ at the downstream boundary and an

expansion wave is reflected from the tunnel exit.

B.3.4 Demonstrative Silencer System

The demonstrative cross-section used for the silencer at the exit portal is based on Figure B.1. This section can be fully revolved in the out-of-plane dimension to generate an axi-symmetric silencer, or projected on a semi-circular path in the case of a more representative tunnel exit. The optimisation variables used for this study are shown in Table B.1, where the tilde accent is used to denote a non-dimensional quantity.

Normalised variables are used to simplify the optimisation problem by allowing lower and upper bounds to be used in place of non-linear inequality constraints. The geometric variables are shown in Table B.1 and are dimensionalised as follows:

$$t = \tilde{t} \cdot d_\mathrm{t} \tag{B.3}$$

$$l_i = l_0 + \left(\frac{l_1 - l_0}{N_\mathrm{c} - 1}\right)(i-1)\,, \qquad l_0 = \tilde{l_0} d_\mathrm{t}, \qquad l_1 = \tilde{l_1} d_\mathrm{t} \tag{B.4}$$

$$h_i = h_0 + \left(\frac{h_1 - h_0}{N_\mathrm{c} - 1}\right)(i-1)\,, \qquad h_0 = \tilde{h_0} d_\mathrm{t}, \qquad h_1 = \tilde{h_1} d_\mathrm{t} \tag{B.5}$$

where $i = 1, N_\mathrm{c}$, is the baffle chamber index. The cross-sectional area of the sections, based on a semi-circle (excluding any other features such as side walkways), are then $S_\mathrm{t} \approx \frac{1}{8}\pi d_\mathrm{t}^2$ and $S_{\mathrm{b}i} \approx \frac{1}{8}\pi(r_\mathrm{t} + h_i)^2$, for the baffle chamber and baffles, respectively. The total length of the silencer is the sum of the baffle thickness and chamber lengths.

The variables in Table B.1 allow for a variable baffle cavity length and height, based on linear scaling with the baffle chamber index. In the case of equispaced

Symbol	Definition	LB	UB
N_c	number of silencer baffle chambers	1	10
$\tilde{t}$	Normalised baffle thickness	0.01	1.0
$\tilde{l_0}$	Normalised first baffle cavity length	0.05	1.0
$\tilde{l_1}$	Normalised end baffle cavity length	0.05	1.0
$\tilde{h_0}$	Normalised first baffle cavity height	0.05	1.0
$\tilde{h_1}$	Normalised end baffle cavity height	0.05	1.0

Table B.1: Summary of normalised optimisation variables and corresponding lower and upper bounds, with reference to Figure B.1.

and identical chambers (i.e. $\tilde{l_0} = \tilde{l_1}$ and $\tilde{h_0} = \tilde{h_1}$) the calculation of the variables reduces to $l_i = l_0,\ h_i = h_0$. The baffle thickness and expansion chamber length are modified to account for acoustic end corrections, which are calculated using Equation 3.7. Therefore, the effective chamber length is:

$$l_{\text{eff},i} = l_i - \delta_{\text{e},i} - \delta_{\text{c},i} \tag{B.6}$$

where δ_e and δ_c are the expansion and contraction end corrections, respectively. Similarly, the effective baffle thickness is:

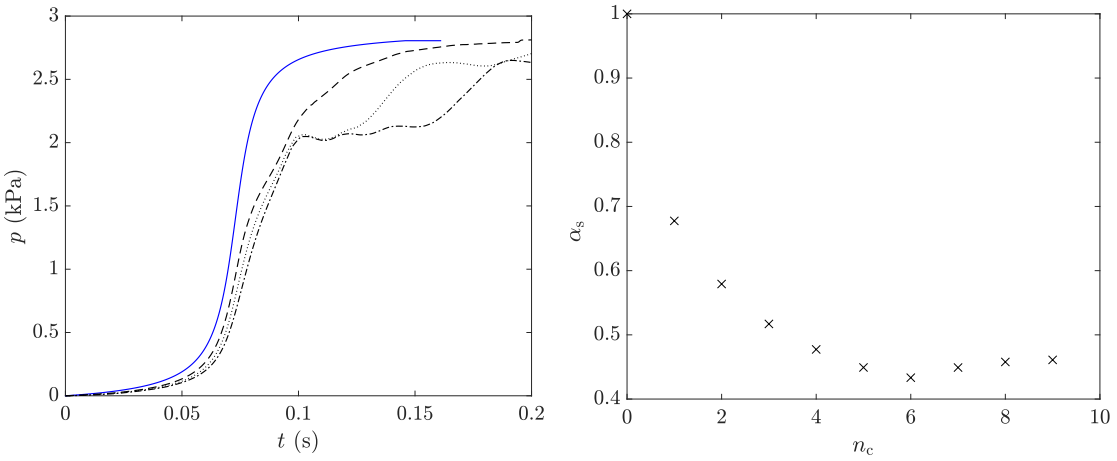
$$t_{\text{eff},i} = t_i + \delta_{\text{c},i} + \delta_{\text{e},i+1} \tag{B.7}$$

B.4 Parametric Study

A parametric study has been carried out to investigate the effect of the different geometric variables defined in § B.3.4 on the objective function, α_s. It is assumed that the expansion chambers are identical for $N_c > 1$ (i.e. $\tilde{h_0} = \tilde{h_1}$ and $\tilde{l_0} = \tilde{l_1}$), while $\tilde{L} = 1$ and $u_z = 400$ km/h for the initial condition. The fixed geometric parameters of the tunnel and physical properties of air are provided in Table 3.1. The variable geometric parameters of the silencer are provided in Table B.2.

Figure	N_c	$\tilde{t}$	$\tilde{l_0}$	$\tilde{h_0}$
B.3a	1-3	0.1	0.5	0.5
B.4	1	0.1	0.0-1.4	0.5
B.5	1	0.1	0.5	0.0-1.0

Table B.2: Normalised geometric variables used for the silencer in the parametric study for regular expansion chamber geometry.

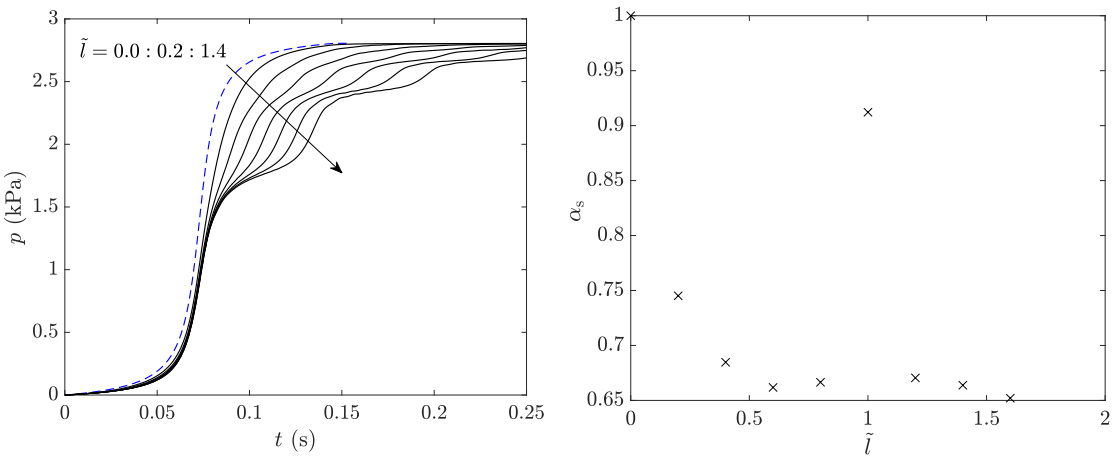


(a) (b)

Figure B.3: Effect of the number of expansion chambers on (a) the transmitted pressure waveform and (b) α_s, for N_c= 0 (—); 1 (– – –); 2 (····); 3 (–·–·–).

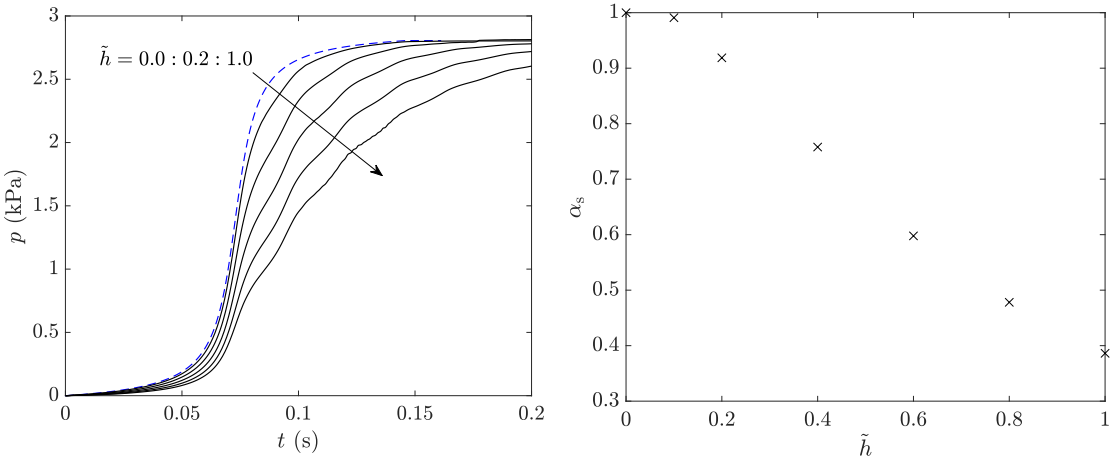
From Figure B.3, increasing the number of expansion chambers provides diminishing returns for the objective value above $N_c \approx 6$, resulting in a very long silencer. However, the length may vary depending on the other dimensions of the silencer chamber. It has not been investigated whether using irregular chamber geometry can provide a greater reduction in the objective value with an increasing number of chambers.

Figure B.4 shows that increasing the length of the expansion chamber has a comparatively small effect on the initial portion of the pressure rise, which becomes the critical factor in the maximum rate of change of pressure. For example, α_s decreases up to $\tilde{l} \approx 0.5$, and then plateaus. The wavy behaviour seen in Figure B.4a for the longer chamber lengths is due to the reflection of pressure waves inside the chamber. Figure B.5 shows a significant reduction in the slope across the entire wavefront with increasing chamber height. The reduction in α_s with $\tilde{h}$ is nearly



(a) (b)

Figure B.4: Effect of $\tilde{l}$ on (a) the transmitted pressure waveform and (b) α_s.



(a) (b)

Figure B.5: Effect of $\tilde{h}$ on (a) the transmitted pressure waveform and (b) α_s.

linear, at least up to $\tilde{h} = 1$. The cross-sectional area and acoustic impedance of the cavity increases with its height, resulting in a greater degree of acoustic power which is reflected by the duct expansion.

B.5 Optimisation strategy

The optimisation strategy proposed for the geometry of the array is nearly identical to the one used in § 5.5. The first objective is the ratio of the maximum absolute rate of change of pressure, with and without the silencer (α_s), which is adapted

from Equation 5.18. In this case, only one model evaluation is needed to evaluate the objective function, as the initial incident pressure waveform is used as the reference waveform. The second objective is chosen as the length, or total volume of the silencer, in order to minimise construction costs and the size of the silencer. Non-linear constraints are imposed, based on the methodology in § 5.5.3, to ensure that the following conditions are met:

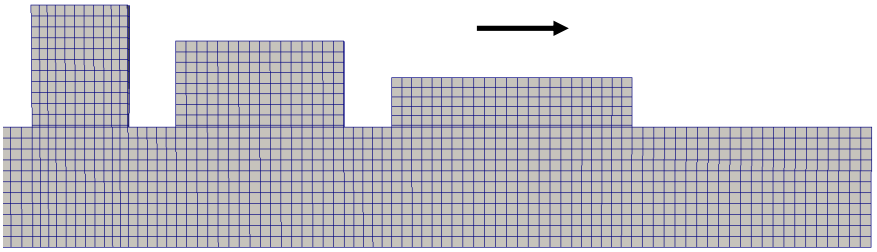
- A maximum and possibly a minimum silencer length (or volume), e.g. $l_\mathrm{s} < l_\mathrm{s,max}$ and $l_\mathrm{s} > l_\mathrm{s,min}$, respectively.
- A minimum length for each expansion chamber, so that the end corrections do not exceed the cavity length, i.e. $l_i > \delta_{\mathrm{e},i} + \delta_{\mathrm{c},i}$.

The first constraint is usually set to $0 < l_\mathrm{s} < \infty$, i.e. it is unbounded. The optimisation procedure may avoid some effective geometric configurations which do not satisfy these constraints.

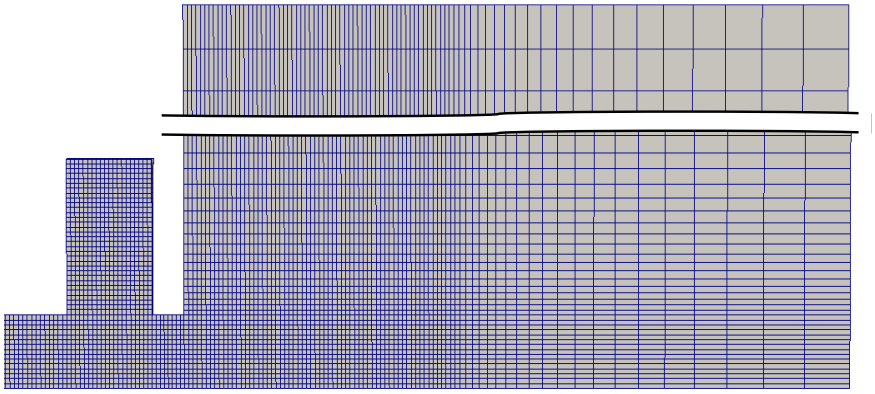
B.6 3-D Benchmarking

The 1-D numerical model can be benchmarked against quasi-3-D predictions in OpenFOAM for a range of test cases. An axis-symmetric silencer is considered for simplicity and computational efficiency. A MATLAB script is used to automate the generation of the blockMesh file based on the user-defined parameters in Table B.1. The proposed modelling strategy is based on the one used for an array of Helmholtz resonators in § 4.3. A non-reflective boundary condition (NRBC) is used at the upstream boundary to avoid unwanted reflections. It is suggested that the following BCs are used at the downstream boundary:

1. A NRBC at the end of the silencer, in order to avoid the reflected expansion wave generated at the opening to atmosphere (see Figure B.6a). The area weighted average pressure is measured across the downstream boundary (see § 4.3.5). This BC is used for the parametric study in § B.4.



(a) Options 1 & 2. The arrow is in the downstream direction.



(b) Option 3. The mesh is coarsened away from the exit portal of the silencer.

Figure B.6: Example of 2-D axis-symmetric meshes for the silencer model in OpenFOAM. The upstream boundary is at the left-end.

2. Identical to Option 1, however the NRBC is replaced by a Dirichlet BC for pressure ($p = p_0$) and Neumann BC for velocity. This pressure release BC is in theory equivalent infinite baffle expansion to atmospheric conditions (Option 3), resulting in a reflected expansion wave from the outlet.

3. A discontinuous opening to atmosphere (see Figure B.1 and B.6b) with NRBCs after a certain distance outside of the silencer. This is representative of an infinite baffle. The transmitted pressure waveform is measured using a probe at a specified distance from the end of the silencer.

Options 2 and 3 are more physically representative of a reactive silencer, whilst Option 1 isolates the effect of the expansion chambers on the transmitted pressure wave.

B.7 Proposed Work

The parametric study in the previous section shows that it may be possible to provide significant reductions in the amplitude of MPWs from the tunnel exit by using a reactive silencer. It is proposed that optimisation could provide even greater reductions, whilst minimising the size, and hence the cost and environmental impact of the silencer. It is proposed that the following steps are carried out, which are closely based on Chapter 5:

1. Numerical benchmarking of the 1-D model against quasi-3-D predictions and experimental validation (started in § B.6).

2. Sensitivity analysis of the objective function to the geometric variables in Table B.1 using the elementary effects test (for example see § 5.6).

3. Multi-objective optimisation considering both regular and irregular geometry for the expansion chamber length and height, with $N_c > 1$. A Pareto front can be generated in order to trade-off the length or volume of the silencer with its effectiveness for attenuating MPWs. For example, see § 5.6.

4. Sensitivity analysis of the optimised silencer configurations to train operating conditions, i.e. entry speed and characteristic wavelength of the initial condition, in order to assess their robustness.

5. The combined effectiveness of the silencer with an array of resonators and a tunnel entrance hood, in order to attenuate MPWs in long tunnels.

Additional attenuation of MPWs may be possible if a deformable material is used for the silencer, as the source term $\partial S_t/\partial t$ in Equation B.1 would no longer be null-valued. A physical model for the deformation of the silencer wall would need to be incorporated and coupled to the gas flow in the silencer (via variables S_t and p). The physical model could provide varying levels of complexity, from simple elastic deformation to visco-elastic effects. However, from a practical and cost viewpoint, a deformable material would be unlikely to have the durability

of a solid concrete or metal wall. Furthermore, it is expected that the change in cross-sectional area due to wall deformation would likely be small (i.e. less than a few percent from the un-deformed shape).

Appendix C

Continuum Model with Wave Reflection

C.1 Introduction

The continuum model for an array of Helmholtz resonators presented in § 3.2.4 considers only downstream wave propagation under the assumption of negligible reflection and interaction between neighbouring resonators ($\kappa \ll 1$). This assumption allows the size, and hence the complexity, of the equation system to be reduced. The far-field model is extended in this section to account for bi-directional wave propagation due to reflection from the resonators, in order to study the effect of increasing the value of κ and provide some indication about the point where the uni-directional propagation model can no longer be considered to be valid.

The bi-directional far-field model is included as an Appendix, as its numerical implementation was found not to work reliably. The model would often fail to converge (i.e. the ODE solver step size $\Delta\mathcal{X} \to 0$) before reaching the final space step when considering large values of κ, particularly when the value of N_l is also increased (see § 3.3.1.2). These convergence issues are most likely related to the increased numerical stiffness of the bi-directional system when there is significant

wave reflection. Consequently, it is expected that the near-field model is better suited for the consideration of bi-directional wave propagation.

C.2 Physical Model

The bi-directional far-field system under the continuum approximation is derived using the same steps as in § 3.2.4, but instead considers the bi-directional form of the continuum near-field system (see Equation 3.62). The substitution for the spatial derivatives in terms with coefficients B, C and D is made using the bi-directional linear advection equation, $\partial u^{\pm}/\partial x = \mp(1/a_0)\partial u^{\pm}/\partial t$. The left and right running wave equations are coupled in the resonator response, which assuming linearity gives:

$$p_{\mathrm{t}} = p_{\mathrm{t}}^{+} + p_{\mathrm{t}}^{-} = \frac{\gamma p_0}{a_0}\left(u^{+} - u^{-}\right) \tag{C.1}$$

Therefore, the bi-directional far-field system is given by:

$$\frac{\partial f^{\pm}}{\partial \mathcal{X}} - \frac{\partial \mathcal{F}^{\pm}}{\partial \mathcal{T}} = -\bar{\delta}_{\mathrm{t}}\frac{\partial^{1/2} f^{\pm}}{\partial \mathcal{T}^{1/2}} - \bar{\tau} f^{\pm}|f^{\pm}| \pm \beta\frac{\partial^2 f^{\pm}}{\partial \mathcal{T}^2} - \bar{K}\left(1 - 2U\epsilon g\right)\frac{\partial g}{\partial \mathcal{T}} \tag{C.2a}$$

$$\frac{\partial^2 g}{\partial \mathcal{T}^2} + \delta_{\mathrm{n}}\frac{\partial^{3/2} g}{\partial \mathcal{T}^{3/2}} + \Omega g = \Omega\left(f^{+} - f^{-}\right) + \epsilon\left[U\frac{\partial^2 g^2}{\partial \mathcal{T}^2} - W\left|\frac{\partial g}{\partial \mathcal{T}}\right|\frac{\partial g}{\partial \mathcal{T}}\right] \tag{C.2b}$$

where the equation coefficients remain unchanged from Equation 3.24 and the bi-directional advective flux is given by:

$$\mathcal{F}^{\pm} = \begin{cases} \frac{\left(f^{+}\right)^2}{2} \\ \frac{\left(f^{-}\right)^2}{2} + \frac{2}{\epsilon} f^{-} \end{cases} \tag{C.3}$$

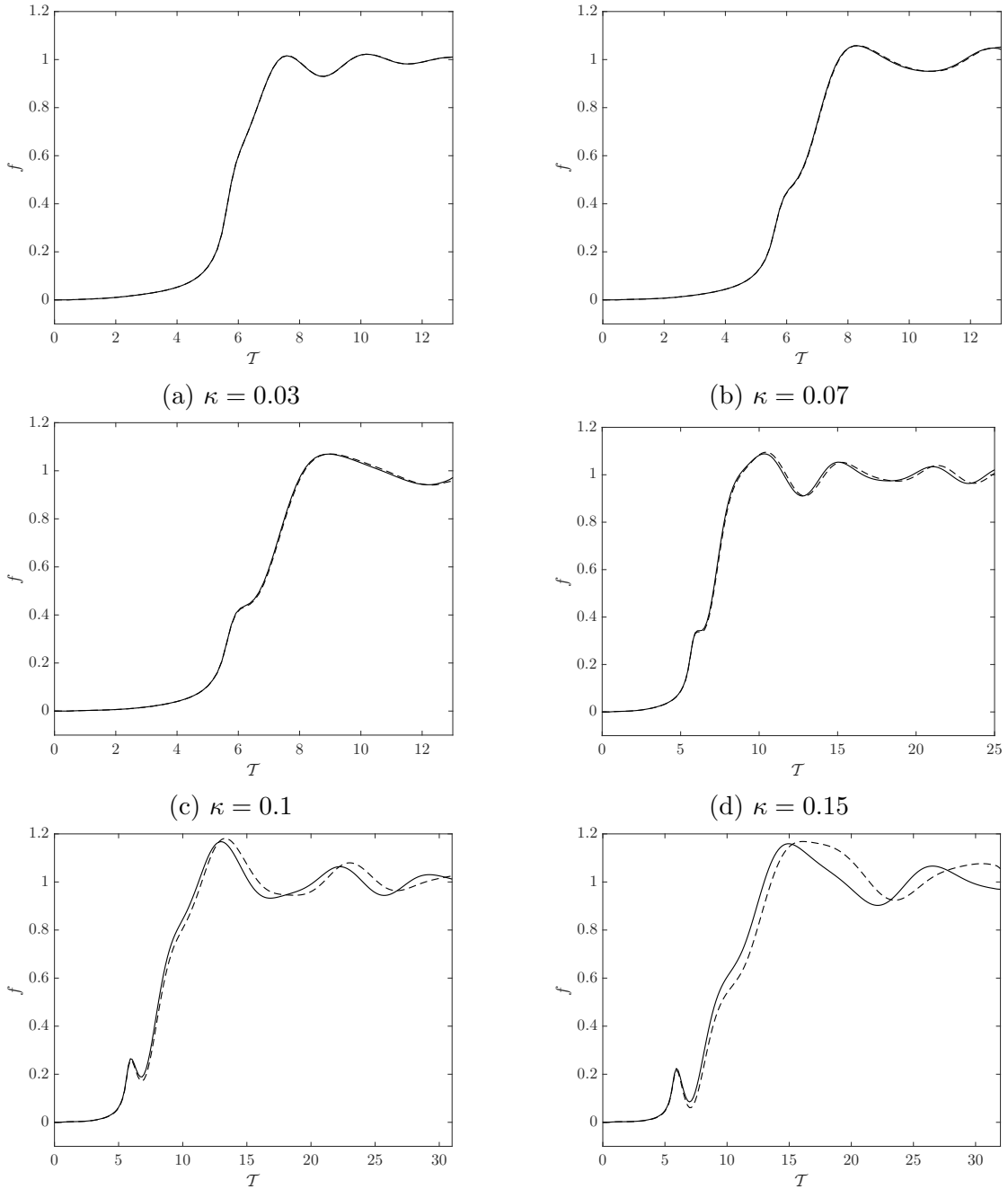
The downstream direction is flipped when changing from the near to far-field variables, i.e. the downstream direction (+) now points from $\mathcal{T} = \mathcal{T}_{\mathrm{N}}$ to $\mathcal{T} = 0$. There are now $(4 + 3N_l)\,N_{\mathcal{T}}$ equations to be solved, compared to $(3 + 2N_l)\,N_{\mathcal{T}}$ for the uni-directional system in § 3.3.2. The bi-directional system is discretised based on the procedure in § 3.3.2, where the unknowns are now

$\left(f^+, f^-, g, q, \xi_1, \cdots, \xi_{N_l}, \psi_1^+, \cdots, \psi_{N_l}^+, \psi_1^-, \cdots, \psi_{N_l}^-\right)^T$.

C.3 Comparison of One and Two-way Propagation

A comparison of the two models is provided in Figure C.1 for a 60 m long array with 20 identical and equispaced cavities, with $u_z = 500$ km/h and $L = d_t$. The value of κ is modified by changing the values of h_1 and w_1 in Figure 3.2. The predicted waveforms indicate that the uni and bi-directional propagation models provide good agreement up to $\kappa \approx 0.15$. Reasonable agreement, at least qualitatively, is still obtained after this point around the initial pressure rise.

Combining this threshold value of κ with the worst-case approximation of κ in Equation 3.13 indicates that the maximum cross-sectional area ratio between the cavities and tunnel in order to satisfy the assumption $\kappa \ll 1$ is $S_c/S_t \approx \kappa_{crit} \approx 15\%$. It is expected that the value of S_c/S_t will be much smaller than this for most tunnel systems, due to the restricted availability of space. Therefore, the uni-directional propagation model is adequate for this application.



(a) $\kappa = 0.03$ (b) $\kappa = 0.07$

(c) $\kappa = 0.1$ (d) $\kappa = 0.15$

(e) $\kappa = 0.31$ (f) $\kappa = 0.49$

Figure C.1: Dimensionless pressure waveforms for an arbitrary array using the uni-directional (—); and bi-directional (– – –) continuum far-field models. The value of κ is varied through w_1 and h_1 in Figure 3.2.

Appendix D

OpenFOAM Pseudo-Code

This Appendix provides an overview of the Bash scripts which have been created in order to automate the configuration of the OpenFOAM models used in Chapters 4 and 6.

D.1 OpenFOAM 3-D Model Configuration

The following is an overview of the Bash script used to automate the case set-up and simulation for the 3-D model for an array of Helmholtz resonators in OpenFOAM (see § 4.3.2). This script is then ran for different array geometries (based on different STL files) and initial condition settings (values of L, p_1). All of the functions used below are provided with OpenFOAM (unless stated otherwise).

1. Copy the reference `0.org` directory containing the boundary condition files for pressure, velocity, temperature.

2. Copy the reference `blockMeshDict.m4` file, which is parameterised by the length and diameter of the tunnel section, and the maximum grid size (see § 4.3.2.2). This file generates the `blockMeshDict` file using the `m4` command.

3. `blockMesh` is invoked to generate the base cuboid hex mesh of size $l_\mathrm{a} \times d_\mathrm{t} \times d_\mathrm{t}$ m, which encompass the entire tunnel and array section.

4. Decompose the mesh using `decomposePar`. The detailed 3-D mesh around the tunnel geometry is then generated using `snappyHexMesh n`, where n is the number of processors/cores. This utility retains the base mesh region which is enclosed by the STL geometry (i.e. the interior of the tunnel and resonator cavities). The mesh is refined at the STL faces. `snappyHexMesh` also assigns the boundary patches for the inlet and outlet and the wall of the tunnel.

5. The command `renumberMesh` is used to renumber the cell list, in order to reduce the bandwidth and memory requirements of the linear equation solvers.

6. The decomposed mesh is reconstructed (i.e. reassembled) using `reconstructParMesh`, so that the initial fields for pressure and velocity at $t = 0$ s can be prescribed using a custom `setPressureFields` tool (see § 4.3.2.3).

7. The fields (pressure, velocity, temperature) are decomposed using `decomposePar -fields`, so that they are assigned to the correct decomposed mesh regions.

8. Run the simulation in MPI parallel using `runParallel 'getApplication'`, which invokes the solver specified in the `controlDict` file, e.g. `pisoCentralFoam`.

9. Reconstruct the completed simulation using `reconstructPar`, which combines the separate fields. The results are viewed and post-processed in Kitware ParaView. A file is also generated containing the pressure-time histories at the inlet and outlet boundaries of the tunnel.

D.2 OpenFOAM 2-D Model Configuration

D.2.1 Top-Level Parametrised Script

This top-level script sequentially loops through the different parameters being studied in the parametric study and invokes the automation scripts for the Primary and Secondary Branch wave models (see Chapter 6). For time-efficiency this script is ran on the HPC in sequential-parallel configuration, i.e. several models are solved simultaneously, each on a single processor core.

1. Loop through parameter 1, $\tilde{r_{\mathrm{b}}}$.

   (a) Loop through parameter 2, u_{z}.

      i. Make a copy of the reference case folder and rename appropriately based on the current values of u_{z} and $\tilde{r_{\mathrm{b}}}$, which contains the all the files needed for the simulation.

      ii. Use unix commands `find` and `sed` to replace the parameters in the copied reference case directory with the current values of u_{z}, $\tilde{r_{\mathrm{b}}}$ in the for-loop, as well as for other fixed parameters, i.e. θ and $\tilde{L}$.

      iii. Invoke the bash script in the copied reference case directory, which is used to pre-process and run the case (see § D.2.2 and D.2.3).

D.2.2 Primary Branch Wave

The following is an overview of the Bash script used to automate the case set-up and simulation for the 2-D mesh for the Primary branch wave in OpenFOAM.

1. Run `cleanCase` to clean current case folder after previous simulations.

2. Copy reference boundary conditions files in `0.org` directory.

3. Invoke `m4` command on `blockMeshDict.m4` to generate `blockMeshDict`, which parametrised. Run `blockMesh` to generate the mesh

4. Invoke `smoothMesh` which uses Laplacian smoothing to reduce non-orthogonality and mesh skewness (available in the FOAM-extend fork).

5. Invoke `m4` command on `controlDict.m4` to generate `controlDict`, which is parametrised so that the correct CFL condition, run-times and step size are used.

6. Invoke `m4` command on `setPresssureFields.m4`, which is parametrised by the initial condition settings (L and p_1). Run `setPressureFields` to generate initial fields for velocity and pressure.

7. Initiate solver

D.2.3 Secondary Branch Wave

The following is an overview of the Bash script used to automate the case set-up and simulation for the 2-D mesh for the Secondary branch wave in OpenFOAM.

1. Clean case folder by removing any existing simulation files (i.e. mesh, boundary conditions, etc.).

2. Invoke `m4` command for `blockMeshDict` for the static and translating mesh regions, which are parametrised by the geometry of the branch, tunnel and train. Run `blockMesh` for the separate mesh regions. The translating mesh is divided into three meshes: (1) upstream of the train, (2) the train, (3) downstream of the train, which have different levels of mesh refinement.

3. Run `snappyHexMesh` on the central translating mesh around the train, to generate a fine mesh in this region.

4. Merge the three translating mesh regions using `mergeMeshes` and `stitchMesh` commands.

5. Use `extrudeMesh` to extrude the 2-D mesh from the front face to remove the 3-D thickness created by `snappyHexMesh`.

6. Run `renumberMesh`, to improve linear solver efficiency.

7. Run `topoSet`, `createBaffles`, `createPatch` to generate face zones for the ACMI boundary, the overlapping boundary conditions for patch switching and finally removing zero-sided patches, respectively.

8. Invoke `m4` command to generate `controlDict`, `dynamicMeshDict` and `initialConditions` files which are parametrised by the tunnel and branch geometry.

Appendix E

Array Optimisation - Additional Results

E.1 Initial Condition Parameters

The optimisation and sensitivity study carried out in § 5.7 is presented in this section for the more severe case of $\tilde{L} = 1$ (see Table E.1). This is in order to identify if the array is more robust under these conditions. This is representative of more extreme operating conditions, e.g. significant non-linear steepening for very high entry speeds ($u_z \approx 500$ km/h).

E.2 Results

The Pareto fronts for with regular and irregular array geometry are plotted in Table E.1a and E.1b, respectively. The corresponding sensitivity analyses of the

Optimisation Regime	Typical	Extreme		Extended Extreme				
Point no.	1	1	2	1	2	3	4	5
$\tilde{L}$	1.0	1.5	0.5	0.5	1.0	1.5	0.5	1.5
u_z (km/h)	400	300	500	300	400	300	500	500

Table E.1: Optimisation points for evaluation of the objective function for reference $\tilde{L} = 1$.

no. opt	1	2	5
min	0.476	0.559	0.481
max	0.703	0.703	0.694
mean	0.564	0.610	0.562
stdev	0.049	0.024	0.044

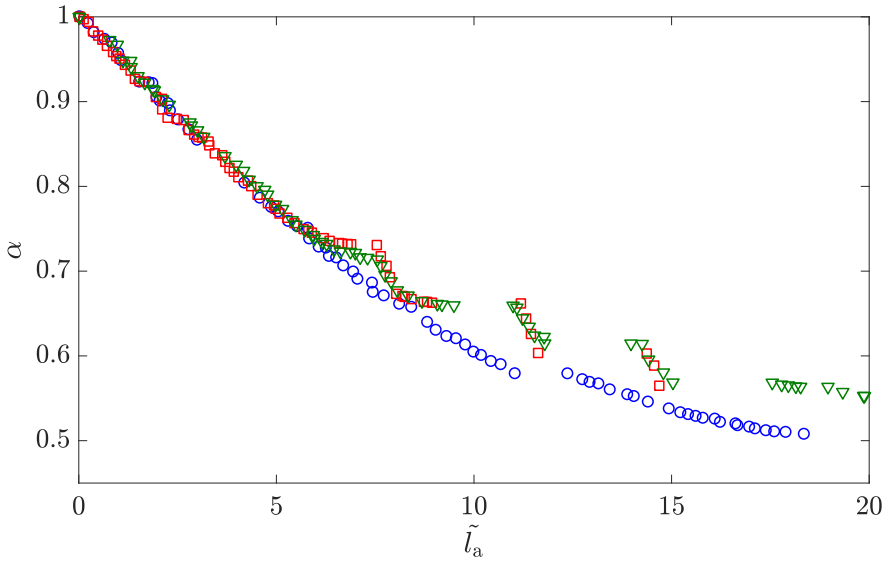
(a) Figure E.2

no. opt	1	2	5
min	0.533	0.546	0.533
max	0.689	0.694	0.683
mean	0.593	0.600	0.589
stdev	0.025	0.025	0.025

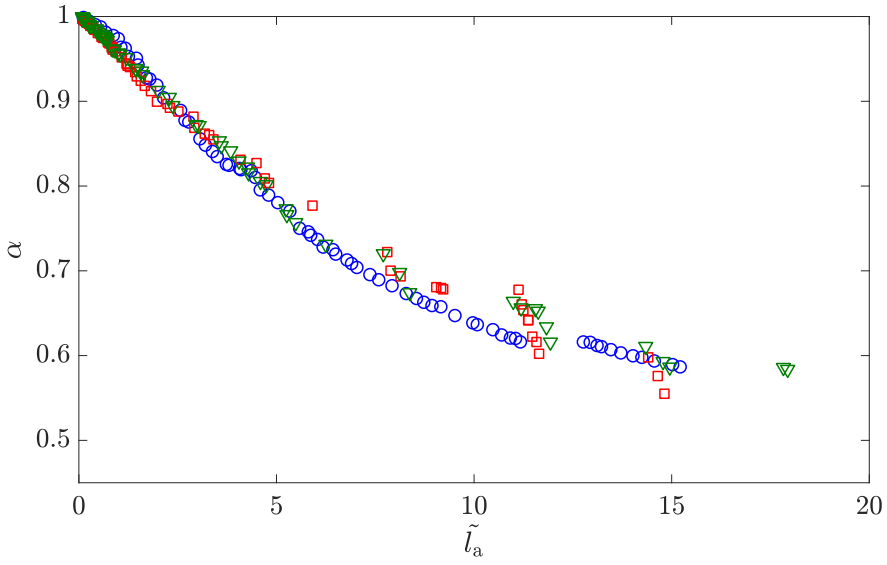
(b) Figure E.3

Table E.2: Statistics for the sensitivity of the different operating regimes as a function of the number of optimisation points.

optimised array configurations (for $\tilde{l_{\mathrm{a}}} \approx 15$) to the variation in the initial condition (in terms of $\tilde{L}$ and u_{z}) are shown for regular and irregular geometry in Figures E.2 and E.3, respectively.



(a) Regular array



(b) Irregular array

Figure E.1: Pareto set under the: typical regime (○); extreme envelope (□); and extended extreme envelope (▽), for reference $\tilde{L} = 1$.

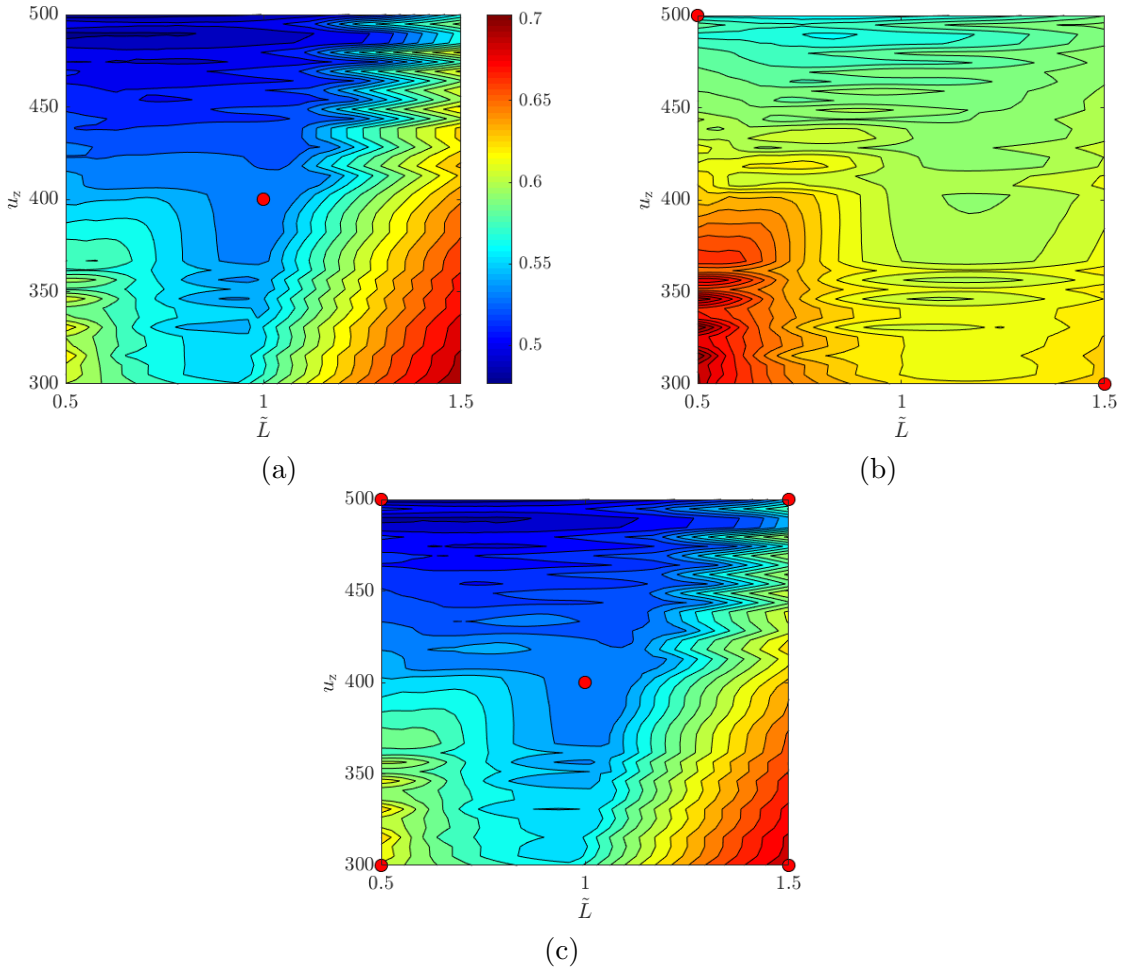


Figure E.2: Sensitivity of the objective function to the initial condition, for $\tilde{l_a} \approx 15$ and $\tilde{L} = 1 \pm 50\%$, optimised with: (a) one; (b) two and (c) five optimisation points (see Table. E.1), with regular resonator geometry.

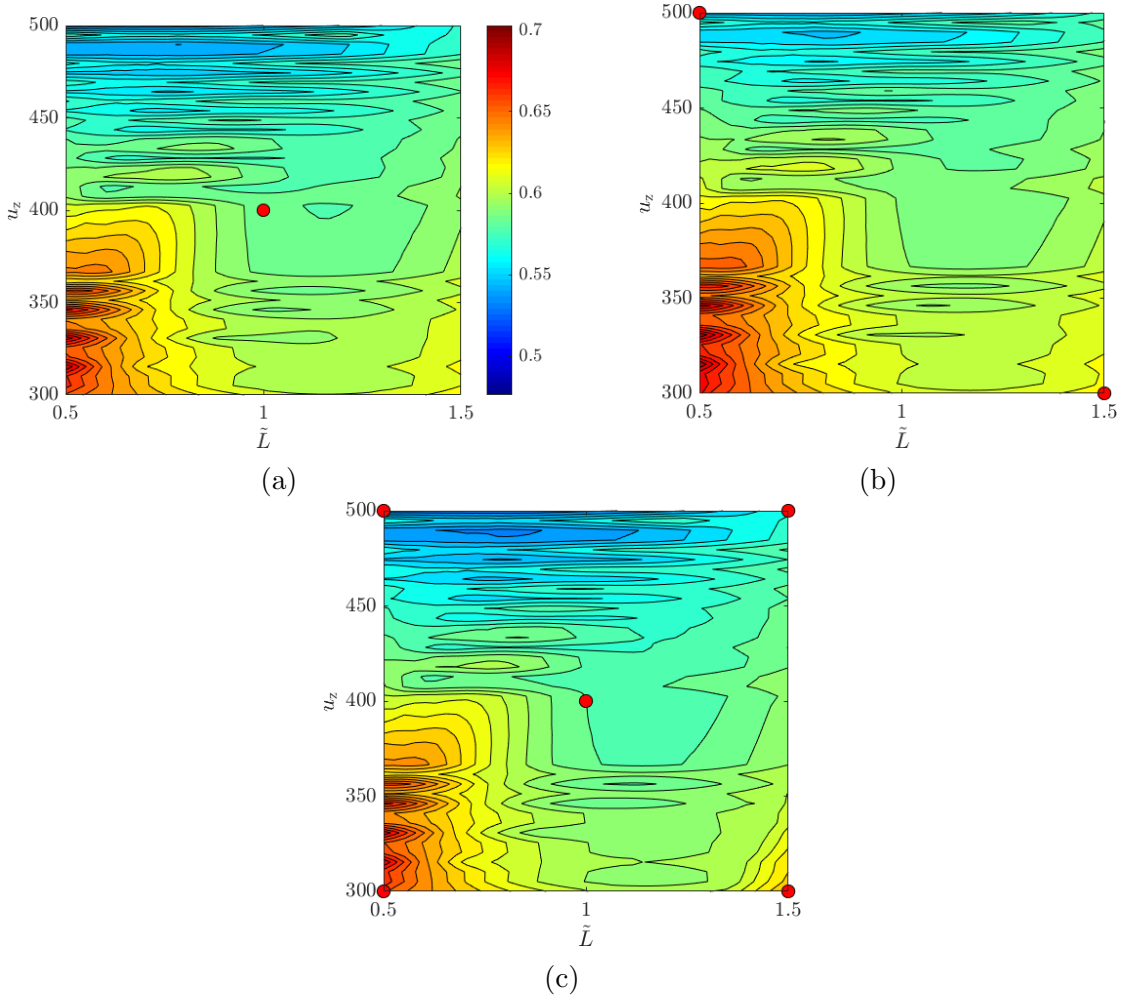


Figure E.3: Sensitivity of the objective function to the initial condition, for $\tilde{l_a} \approx 15$ and $\tilde{L} = 1 \pm 50\%$, optimised with: (a) one; (b) two and (c) five optimisation points (see Table. E.1), with irregular resonator geometry.